Millimeter-Wave Dynamics and Control of Rydberg-Rydberg Transitions

by

David Darrah Grimes

Submitted to the Department of Chemistry
in partial fulfillment of the requirements for the degree of

Doctor of Philosophy

at the

MASSACHUSETTS INSTITUTE OF TECHNOLOGY

June 2017

Author .....
Department of Chemistry
May 1, 2017

Certified by .....
Robert W. Field
Haslam and Dewey Professor of Chemistry
Thesis Supervisor

Accepted by .....
Robert W. Field
Chairman, Department Committee on Graduate Theses

Millimeter-Wave Dynamics and Control of Rydberg-Rydberg Transitions

by

David Darrah Grimes

Submitted to the Department of Chemistry
on May 1, 2017, in partial fulfillment of the
requirements for the degree of
Doctor of Philosophy

Abstract

In this thesis, I report on the design and construction of a new atomic and molecular beam source that exploits the unique capabilities of a buffer gas cooled ablation source. Buffer gas cooled atomic and molecular beams generate samples with $> 1000\times$ more particles and $10\times$ slower translational velocities than typical ablation seeded supersonic expansions. This increase in number density provides an ideal system for the observation of qualitatively new cooperative emission effects. I describe the detection of single-shot free space superradiance in a buffer gas cooled beam of barium atoms. The frequency of this emission is shifted and broadened by a factor of $\sim 10^6\times$ greater than the natural lifetime, indicating the presence of quantum many-body dipole-dipole effects in the cooperative emission. Additionally, the smaller lab-frame velocity reduces the Doppler broadening enough to allow for coherent manipulation of Rydberg states and a coherent coupling of an optical and millimeter-wave photon. I demonstrate this coherent coupling in an ensemble of barium atoms, and provide a theoretical description of how to provably perform complete STImulated Raman Adiabatic Passage (STIRAP).

Thesis Supervisor: Robert W. Field
Title: Haslam and Dewey Professor of Chemistry

Acknowledgments

First amongst the people that I would like to acknowledge is my boss, Bob Field. During my time at MIT, his enthusiasm for science and spectroscopy has been nothing short of infectious. He has always been available to discuss current experiments and difficulties in the lab. Further, he has the faith in his students to let them investigate the problems that interest them. For me, this took the form of allowing myself and fellow student Yan Zhou build a buffer gas cooled molecular beam, and trusting me that investigations of cooperative effects were a valuable use of time. Finally, his ability and desire to explain complex scientific and spectroscopic phenomena with nothing more than his hands is an inspiration. If one cannot explain a concept without need for complex visual aids, one often does not fully understand said concept.

I would also like to deeply thank Prof. John Muenter for the advice and support he has provided through my PhD. Shortly after I began in Bob's group, John began periodically visiting Cambridge to offer advice on a variety of topics, scientific or otherwise. His perspective, often wildly different from my own, has always been valuable, and his suggestions (both in lab and out of lab) have always been thoughtful and thoroughly appreciated.

I only interacted closely with Prof. Susanne Yelin for the last few years of my PhD, but her explanations of cooperative radiative phenomena, superradiance, and subradiance, were crucial to my own understanding of many of my experimental results. The depth and breadth of her knowledge on these topics as well as knowledge of how to present them to the physics community were essential in understanding and preparing the superradiance data for publication.

Profs. John Doyle, Dave Patterson, Dave DeMille, and Dr. John Barry were all extraordinarily helpful and generous as Yan Zhou and I were designing our buffer gas cooled molecular beam. Profs. Doyle and Patterson allowed us to borrow an early prototype of a beam source in order to ensure that the technique would work for our applications, while Prof. DeMille and Dr. Barry gave us comprehensive blueprints of their beam source and expert instruction in the details of its construction.

Prof. DeMille went above and beyond by allowing me to spend 7 weeks in his lab working on the photoassociation of Rb and Cs into ultracold heteronuclear molecules so I could further learn about CW diode laser technology and long-pulse laser technology and bring this experience back to MIT. Scientifically, this period was one of the most exciting of my entire PhD and helped fuel my desire to research cold and ultracold molecules and chemistry.

My fellow members of the Field group were a constant source of companionship and comradery during my time at MIT. Tony Colombo and Yan Zhou were senior students on the Rydberg project when I arrived, and taught me everything they knew in the years that we overlapped. Both were incredibly knowledgeable on any number of topics, and I learned from them how best to approach experiments, unexpected difficulties in lab, and publication of scientific papers. The most important lesson I learned, both from them and from my own error, was the necessity to not fall prey to the temptation to skip steps to move faster in the lab. If something works after skipping a step, you've gotten lucky; if something doesn't work after skipping a step, you don't know why and have to go back to where you were to begin with. Tim Barnum, the last Rydberg, has done nothing but impress me in his time here. Most students need significant hand-holding near the beginning of their time in lab, but Tim was fearless from the beginning and ready to work independently after just a few short months in lab. I have valued his companionship, suggestions, and attention to detail. Holger Herburger only visited our lab for eight months, but his dedication and creativity helped propel the Rydberg project forward during the end of my time here.

Josh Baraban and Barratt Park were senior students on the Singlet project and Dr. Kirill Kuyanov-Prozument was a post-doc on the Singlet project when I began. All three of them were valuable for (often wildly) different perspectives on experimental difficulties and approaches in lab. Jun (JJ) Jiang, Trevor Erickson, Alex Hull, and Dr. Carrie Womack, the recent generation of Singlet experimentalists have filled this role perfectly, and brought a new focus to the singlet project and the lab as a whole.

Finally, amongst fellow students, I would like to acknowledge two undergradu-

ates, Bryan Changala and Ethan Klein. While I did not work directly with Bryan Changala, he was perhaps the most impressive undergraduate I have encountered, in terms of working directly alongside the graduate students. He has nothing but a bright future in front of him and I wish the best for him. Ethan Klein worked alongside Yan Zhou, Tim Barnum, and myself for the entirety of his time at MIT, and made a number of important contributions to the Rydberg project including the LabView control of the buffer gas cooled molecular beam. He had a knack for asking innocent sounding questions that often cut to the heart of the matter and showed my own gaps in understanding, a skill that he never wanted to acknowledge in himself.

Dr. Steve Coy was also a constant contributor to the group over my time at MIT. His calculations and attention to detail about CaF and superradiance were just as important as his experience with microwave and millimeter-wave double-resonance experiments. Discussions with him always led to me considering results from another angle.

I would like to also acknowledge all of the other students, post-docs, and visiting professors that I have interacted with in our group: Rachel Shaver, Monika Ciuba, Chris Camara, Peter Richter, Joshua Middaugh (Green Group), Dr. AJ Vasiliou (Green Group), Mikael Matrat (Green Group), Zachary Buras (Green Group), Paul Romer, Nola Mulugeta, Julia Berk, Clare Keenan, Tal Scully, Prof. Zhenhui Du, and Prof. Bryan Lynch.

Last, and certainly not least, I would like to acknowledge my family and my wife, Maureen. Although my father passed away early during my PhD, I know that he was proud of my decision to pursue a PhD and only hope that my path forward will continue to make him proud. My mother and sister have provided endless support and, from my sister, invaluable advice about pursuing an academic career. Finally, I both met and married Maureen during my time at MIT, and I can no longer imagine my life without her. She has provided more support for me during this time than perhaps even she realizes, and it is highly unlikely that I would be in the same position I am today without her.

This doctoral thesis has been examined by a Committee of the Department of Chemistry as follows:

Professor Robert Guy Griffin .....
Chairman, Thesis Committee
Professor of Chemistry

Professor Robert W. Field .....
Thesis Supervisor
Haslam and Dewey Professor of Chemistry

Professor Keith Adam Nelson .....
Member, Thesis Committee
Haslam and Dewey Professor of Chemistry

Contents

List of Figures

List of Tables

Chapter 1

Introduction

In Section 1.1 I introduce the basic properties of Rydberg states, with particular emphasis on core-nonpenetrating (CNP) states and their properties important for chirped pulse millimeter wave (CPmmW) spectroscopy. In Sec. 1.2 I discuss the techniques that I helped to develop of CPmmW spectroscopy and buffer gas cooled beam formation and their applications to spectroscopy of Rydberg states. In Sec. 1.3 I outline future potential applications of Rydberg states using both CPmmW spectroscopy and a buffer gas cooled beam. Finally, I outline each chapter of this thesis in Sec. 1.4.

1.1 Properties of Rydberg states

A Rydberg state of an atom or molecule is a highly excited electronic state, defined as a state with one electron, the Rydberg electron, in an excited state that can be described as being formed from atomic orbitals of larger principal quantum number than those of the ground state(s) of the constituent atom(s) [5]. This loosely bound electron has an outer turning point that lies well outside of the ion core, and so it only interacts weakly with the ion-core and the remaining core electrons. The Rydberg electron/ion-core interaction is described to zeroth-order by the Coulomb interaction,

$$V(r) = -\frac{Ze^2}{4\pi\epsilon_0 r}, \tag{1.1}$$

where Z is the effective charge of the ion-core, e is the elementary charge carried by the electron, ϵ_0 is the vacuum permittivity, and r is the distance between the electron and the ion-core. The allowed bound energies of the system therefore follow the Rydberg equation

$$E = IP - \frac{Ry}{(n - \delta_\ell)^2} \tag{1.2}$$

where IP is the ionization potential, Ry is the Rydberg constant, n is the principal quantum number, and δ_ℓ is the n and ℓ dependent quantum defect (ℓ is the orbital angular momentum) that is exactly zero for hydrogen. For molecular systems, the quantum defect is a function not just of n and ℓ, but also λ (the projection of the orbital angular momentum on the internuclear axis), N^+ and v^+ (the rotational and vibrational quantum numbers of the molecular ion-core where properties of the ion core are denoted by a superscript $+$) [6].

It is often more convenient to label Rydberg states by the effective principal quantum number

$$n^* = \sqrt{\frac{Ry}{IP - E}} = n - \delta_\ell. \tag{1.3}$$

This notation is useful because n^* gives direct information about the energy of a Rydberg state, and because the many properties of Rydberg states that are typically said to scale with n more accurately scale with n^*. A table of some of these quantities is given in Table 1.1 [7, 4]. These quantities scale non-linearly with n^*, allowing for investigation of states with properties very different from the low-lying states.

Of particular interest for the purpose of mm-wave spectroscopy is that the spacing between adjacent Rydberg states scales as n^{*-3}, the electric dipole transition moment between adjacent ($n^* \rightarrow n^* \pm 1$) Rydberg states scales as n^{*2}, the electric polarizability of a Rydberg state scales as n^{*7}, and the radiative lifetime of a Rydberg state (summed over all potential lower states) scales as n^{*3}. The large electric dipole transition moments and polarizabilities at moderate n^* ($n^* \sim 30$) provide a large handle for driving transitions between Rydberg states, and the transition energy lies

Property	Scaling	Typical value for n = 30
Binding Energy	n^{*-2}	150 cm^{-1}
Transition energy for $\Delta n^* = 1$	n^{*-3}	10 cm^{-1}
Orbital Radius	n^{*2}	900 a_0
Geometric Cross Section	n^{*4}	$2.5 \cdot 10^6$ a_0^2
Electric Dipole Transition Moment for $\Delta n^* = 1$	n^{*2}	2300 D
Electric Polarizability	n^{*7}	400 MHz cm^2/V^2
Radiative Lifetime	n^{*3}	2 ms
Fine Structure Interval	n^{*-3}	3.5 MHz

Table 1.1: n^*-dependence of the properties of atomic Rydberg states. Adapted from Ref. [4]

in the mm-wave regime. Additionally, the long radiative lifetimes of Rydberg states enable long observation times and high-resolution spectroscopy [8, 9, 10]. These large electric dipole transitions moments can interact with each other through long-range dipole-dipole collisions at easily achievable Rydberg number densities ($\rho \approx 10^7$ cm^{-3}), and these interactions can induce significant changes in the absorption and emission profiles of an ensemble of Rydberg states [11, 1, 2]. One primary focus of this thesis is the investigation of these long-range dipole-dipole effects by the study of the cooperative radiation that occurs at these Rydberg number densities.

Rydberg states exist in all molecules as well as all atoms, and follow the same scaling rules and general behaviors [12, 13, 14, 6]. However, one complication that exists in the Rydberg states of molecules that in general does not exist in the Rydberg states of atoms is fast non-radiative decay. In particular, predissociation and autoionization operate on timescales of ns or faster [15, 16, 17, 18, 19]. Predissociation occurs when the Rydberg electron is excited above the thermodynamic energy threshold to dissociation of the molecule. Energy exchange between the electron and ion-core leads to a de-excitation of the Rydberg electron, and dissociation of the molecule into two atoms (for the case of diatomic molecules). Autoionization involves the opposite flow of energy, and occurs when the excited Rydberg state converges on an (electronically, vibrationally, or rotationally) excited state of the ion-core. In this case, energy exchange between the electron and ion-core leads to de-excitation of the ion-core and

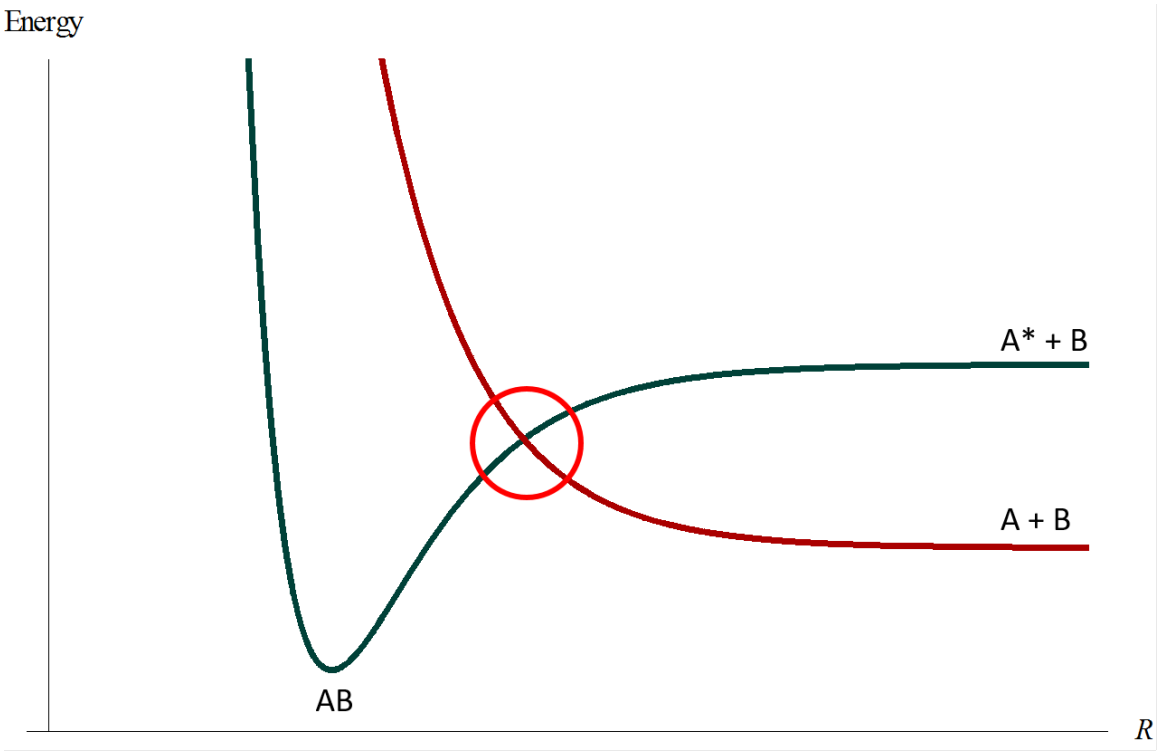

Figure 1-1: A schematic representation of predissociation in Rydberg states of molecules. The blue, bound molecular potential energy surface corresponds to a Rydberg state above the thermodynamic energy threshold to dissociation of the molecule, while the red, dissociative molecular potential energy surface corresponds to the dissociating state. The two states mix in the region of state space indicated by the red circle, coupling the Rydberg state to the dissociation continuum.

ejection of the election. While rotational and vibrational autoionization can only occur in molecules, electronic autoionization can occur in both atoms and molecules [6]. These two processes (predissociation and autoionization) are schematically displayed in Figures 1-1 and 1-2.

Rydberg states can be divided into core-penetrating (CP) and core-nonpenetrating (CNP) states. Due to the $\ell(\ell+1)/2r^2$ centrifugal barrier between the electron and ion-core, the semi-classical inner turning point of the Rydberg electron orbital is controlled almost entirely by the value of ℓ. As such, for relatively low values of ℓ ($\ell < 4$), the Rydberg electron wavefunction has significant overlap with the ion-core and is called core-penetrating. For higher values of ℓ, the Rydberg electron wavefunction has essentially zero overlap with the core and is called core-nonpenetrating. The exchange

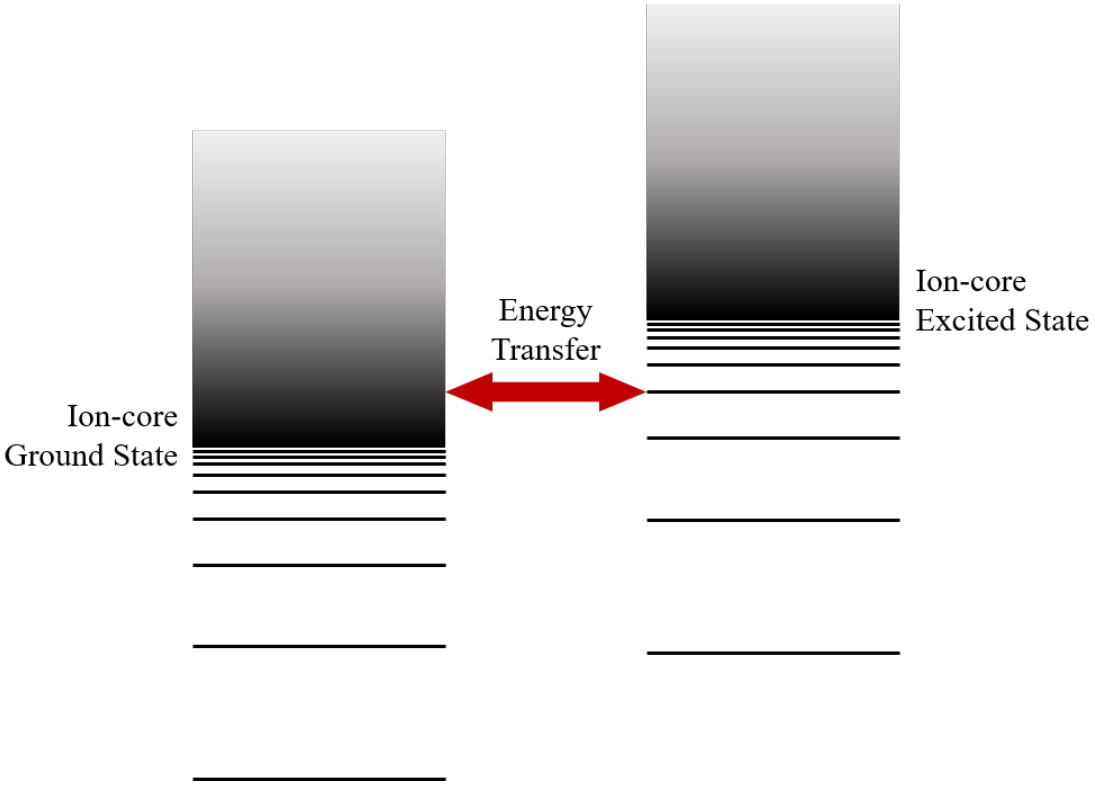

Figure 1-2: A schematic representation of autoionization in Rydberg states of both atoms and molecules. The left-hand level diagram illustrates a Rydberg series converging on the ground state of the ion-core, while the right-hand level diagram illustrates a Rydberg series converging on an excited (rotational, vibrational, or electronic) state of the ion-core. Rydberg states excited in the right-hand manifold above the ground state ionization potential can couple to the ionization continuum, as indicated by the red double-headed arrow.

of energy that causes predissociation and autoionization requires overlap between the Rydberg electron and ion-core, thus CNP states escape the fast non-radiative decay present in molecular Rydberg states [6].

In molecular Rydberg states, due to the lack of spherical symmetry, ℓ is generally not a good quantum number. However, in CNP states, the Rydberg electron is essentially decoupled from the ion-core, which leads to an atom-like structure with $\delta_\ell \approx 0$, and an "almost good" quantum number ℓ. This allows for a simpler assignment of CNP states due to the "pure electronic" transition selection and propensity rules that govern the spectrum ($\Delta\ell = \pm 1$, $\Delta N^+ = 0$, $\Delta v^+ = 0$, $\Delta N = 0, \pm 1$, $+ \leftrightarrow -$, where N is the total angular momentum excluding spin of the total molecule and

+/− represent parity) [10].

Accessing molecular CNP states, however, can be difficult due to their relative remoteness (primarily in angular momentum) from ground/valence electronic states. In general, multiple photons are required to reach the required angular momentum of CNP states, and at least one intermediate short-lived CP state must be traversed. While a small number of molecules have long-lived CP states converging to the lowest ionization potential (due to either an abnormally low ionization potential or atypically weak coupling to predissociating states), in order to access CNP states in a wide variety of molecules, advanced population transfer methods such as STIRAP (STImulated Raman Adiabatic Passage) or Stark switching are required [20, 21]. The other primary focus of this thesis is to demonstrate a proof-of-principle of a generalizable method to robustly populate molecular CNP states in large number densities via a coherent population transfer scheme.

These two goals, taken together, describe the fundamental goal of the research that comprises this thesis: investigation, description, and control of the interaction between mm-waves and Rydberg states of atoms. The long-term aim is to apply the techniques pioneered here in atomic Rydberg states to Rydberg states of molecules. The experiments described in this thesis provide the basis for future experimental work on molecular systems and highly cooperative light-matter interactions.

1.2 Chirped pulse millimeter wave spectroscopy and buffer gas cooling

Millimeter wave spectroscopy is a powerful alternative to the typically performed laser-based spectroscopic experiments [22, 23, 24, 25, 26, 27, 28, 29, 30, 31, 32, 33, 34, 35]. One of the major advantages of mm-wave spectroscopy over laser spectroscopy is the $> 1000\times$ higher resolution and accuracy of the mm-waves. Intracavity etalon-narrowed pulsed dye lasers of the sort typically used in laser spectroscopy generally have a spectral resolution of 1 GHz and high pulse energy [36]. Continuous wave

(CW) lasers can be stabilized to have a much narrower spectral bandwidth, typically on the order of 1 MHz, but can suffer from relatively low power. Mm-waves combine relatively narrow bandwidth with relatively high pulse energy. Typical mm-wave sources can routinely achieve $\sim$ 100 kHz (Doppler-limited) resolution, and due to the large electric dipole transition moment for Rydberg-Rydberg transitions, can saturate transitions with nJ of energy.

Conventional frequency-stepping spectroscopy can require days of experimental time to cover 20 GHz of frequency with 100 kHz resolution [37]. Thankfully, the recent development of Chirped-Pulse Fourier-Transform Microwave (CP-FTMW) spectroscopy by Pate and co-workers, and the extension to CPmmW spectroscopy in our group, allows for the acquisition of a high resolution broadband spectrum in seconds [38, 39, 34, 8, 9, 10, 40]. This technique combines a broadband pulse to polarize all possible transitions within the frequency range of a broadband pulse in a single shot, and time-domain detection to record the Free Induction Decay (FID). In addition to combining broadband spectral coverage with high spectral resolution, direct detection of electric fields in highly advantageous. Typical methods for detection of Rydberg states exploit detection of ions, which requires high-voltage ion-optics near the active volume, which can cause shifts and broadenings of the spectra. Electric field detection does not require any high-voltage components and can more easily achieve low levels of stray electric fields. Additionally, the direct field detection preserves both amplitude and phase information, which can provide important information about the time-dependent emission frequency. CPmmW spectroscopy is the primary method used for interrogating Rydberg states in this thesis.

The atoms of interest in this thesis are the alkaline earth atoms, calcium and barium. The conventional sources for atomic beams of these species are either oven-based sources or supersonic expansions coupled to laser ablation [41]. Neither of these techniques are well suited to Rydberg spectroscopy as they result in relatively fast beam velocities and low atom flux, leading to reduced signal-to-noise ratios and significant Doppler broadening. I use the buffer gas cooling technique, as pioneered by the DeLucia group in the 1980s [42, 43, 44], and further developed into a beam

expansion by the Doyle and DeMille groups in the mid-2000s [45, 46, 47, 48, 49, 50, 51, 52]. Compared to a supersonic expansion coupled to a laser ablation source, the buffer gas cooled atomic beam achieves a smaller beam velocity (decreased by up to a factor of ten) and a much larger number density (increased by up to a factor of 1000). This typically corresponds to an effective increase in signal strength of 10^4. This increase not only aids the sensitivity of standard spectroscopy experiments, but enables access to a regime of very optically dense ensembles which behave in a qualitatively different manner than dilute atomic ensembles, including such behaviors as superradiance.

1.3 Applications of Rydberg spectroscopy

The primary applications of Rydberg spectroscopy that utilize CPmmW spectroscopy and buffer gas cooled atomic beams center around the selective preparation of molecular CNP states and the investigation of optically dense ensembles. Selective preparation of CNP states allows for Rydberg-State-Enabled Stark deceleration and trapping of molecules by exploiting the enormous electric dipole moments and polarizabilities of Rydberg states, while additionally making use of the long lifetimes of CNP states [53, 54, 55, 56, 57, 58, 59, 60, 61]. Similarly, CNP states can be used to prepare molecular cations in single, selected quantum states by selective autoionization or photoionization methods [15, 62, 63, 64, 65, 66, 67]. These state-selected cations can then be used for investigations of ultracold chemistry or in novel quantum computing schemes [68, 69, 70]. Stroboscopic resonances between internal and electronic motions in molecular CNP states can provide insight into the mechanisms of energy transfer between light, fast electrons and heavy, slow nuclei [71, 72, 73, 74, 75, 19, 76, 77]. Additionally, in CNP states with relatively low ℓ ($4 \leq \ell \leq 8$), the Rydberg electron can act as a sensitive probe of the electronic structure (e.g. multipolar moments and polarizabilities) of the molecular ion-core [78, 79, 80, 30, 31, 81, 82, 83, 84, 85, 86, 87, 88]. Finally, molecular CNP states enable investigations of fundamental quantum mechanics through the creation of exotic states such as pendular quantum states that combine

permanent and induced electric dipole interactions [89, 90, 91].

Optically dense ensembles are interesting because the physics that governs their collective radiative properties is described by the same physics as many areas of condensed phase photochemistry and laser physics [1]. Intermolecular interactions can induce or modify photochemical reactions, such as in the case of J-aggregates [92]. Collective radiation from dense ensembles of Rydberg states is fundamentally the same process as a mirrorless laser, and allows for investigation of light propagation through a highly nonlinear medium [23, 25, 26, 28, 93, 94, 95, 96]. Finally, the dynamics of many-body quantum states can be investigated at a fundamental level at both high time and frequency resolution [97, 98, 34, 35, 99, 100, 10, 101, 102, 2].

1.4 Thesis outline

In Chapter 2, I describe the experimental apparatus used in my experiments in this thesis. I present the hydrodynamics of the buffer gas cooled atomic beam expansion and outline the requirements for creating a beam that combines high flux and low velocity. I discuss the lasers involved in the experiment and discuss their coherence properties. Finally, I address the construction of two CPmmW spectrometers that operate in two different frequency ranges, how to apply CPmmW spectroscopy to Rydberg states, and provide a comparison of the pros and cons of each frequency range.

In Chapter 3, I build up a description of the phenomenon of superradiance in a stepwise fashion. First I describe the situation purely classically and show that explicit inclusion of cooperative radiation effects is essential to a treatment that conserves energy in a two-dipole system. Then I present the Dicke model of simplified superradiance in a purely quantum mechanical system. I follow this with a more complete semi-classical derivation based on the Bloch-Maxwell equations. Finally, I present three separate fully quantum-mechanical approaches to calculating the effects of superradiance that provide different trade-offs between computational complexity and extraction of useful information.

In Chapter 4, I present results that show collective and cooperative emission in dense sample of Rydberg atoms. First I discuss the utility of extended samples of Rydberg states in studying superradiance. Then I present my initial observations of untriggered superradiance in the buffer gas cooled beam source. Finally I present observations of externally triggered superradiance and describe how it matches semi-classical theory, but also where it diverges from the semi-classical theory and requires a fully quantum theoretical description.

In Chapter 5, I discuss a variety of population transfer methods that involve both two- and three-level systems, with the ultimate goal of describing STIRAP. First I present three methods of population transfer in two-level systems: incoherent population transfer, coherent population transfer, and adiabatic rapid passage. I then draw parallels between these methods and Stimulated Emission Pumping (SEP), coherent π-pulse transfer, and STIRAP in three-level systems. Finally, I develop the theory required to describe STIRAP in both an ideal experiment and a realistic non-ideal experiment, and provide examples of the effects of each non-ideality, in particular the convenient but generally not Fourier-transform limited pulsed dye laser.

In Chapter 6, I present results that demonstrate coherent coupling between an optical and a mm-wave photon en route to STIRAP. First I describe the level structure required for a proof of principle demonstration of optical-mm-wave STIRAP in atomic systems. Then I present results from both the low Rabi frequency regime that demonstrate the onset of coherent population transfer, and the high Rabi frequency regime that demonstrate the evolution to full STIRAP. Finally, I describe some of the difficulties in applying STIRAP to molecular systems and how to overcome them.

Chapter 2

Experimental Design

In this chapter, I discuss the experimental details associated with the results presented in my thesis. Section 2.1 broadly covers the vacuum system and buffer gas cooled beam, Sec. 2.2 provides details on the pulsed laser systems used to populate Rydberg states, and Sec. 2.3 covers the mm-wave systems used in the work described in my thesis, both the W-band (70 - 100 GHz) and high frequency (260 - 300 GHz) systems.

2.1 Vacuum system for the buffer gas cooled molecular beam

Rydberg experiments in this research group have traditionally been performed on atomic beams formed either from an effusive oven source or through ablation coupled into a supersonic expansion [103, 104, 105, 106, 107, 108, 109, 82, 77, 110, 8, 9]. While both techniques are well-suited to various aspects of Rydberg spectroscopy, but neither is well-suited to performing millimeter-wave (mm-wave) spectroscopy of Rydberg states of molecules and investigating cooperative radiation effects (such as superradiance) in ensembles of Rydberg states. Therefore, I (along with former graduate student Yan Zhou) constructed a completely new class of system based on the hydrodynamic expansion of a buffer gas cooled atomic or molecular beam. This system better matches the requirements of mm-wave spectroscopy of Rydberg states of

molecules and investigations of collective effects. In this section, I first describe the fundamental fluid dynamics associated with the buffer gas cooled molecular beam source. Most theoretical work on this topic comes from the Doyle, DeMille, and Morse groups [52, 51, 111]. Then I give an overall description of the buffer gas cooled beam chamber as designed by myself and Yan Zhou [10]. Additionally, I present a description of the optimization of laser ablation as well as future possibilities for seeding the expansion with a wide variety of atomic and molecular species.

There are three important processes that describe the performance of a buffer gas cooled atomic or molecular beam apparatus: the beam expansion process, the process of thermalization of the species of interest with the buffer gas atoms, and the process of extracting the beam from the chamber in which it was produced. Each of these processes is most sensitive to a different set of experimentally controllable parameters, and I will treat each process in the above order.

2.1.1 Beam expansion characteristics

The fundamental physical picture that I will use to describe each of the three regimes of beam expansions (effusive, hydrodynamic, and supersonic) will be that of a seeded buffer gas. This means that I consider two distinguishable types of particles, a, the species of interest and b, the buffer gas. In the limit of a seeded buffer gas, I assume that these two particles have number densities n_a and n_b such that $n_b \gg n_a$. This allows for the assumption that collisions involving either two a particles or an a and a b particle are vanishingly unlikely, and so we can write the mean free path of each particle as:

$$\lambda_a = \frac{1}{n_b \sigma_{ab} \sqrt{m_a/m_b + 1}} \tag{2.1}$$

$$\lambda_b = \frac{1}{\sqrt{2} n_b \sigma_{bb}} \tag{2.2}$$

where σ_{ab} is the elastic collision cross section between species a and b, σ_{bb} is the elastic collision cross section between two b particles, and m_a and m_b are the masses

of a and b, respectively. In practice, particle b is usually a noble gas, either helium or neon. In my chamber, either helium or neon can be used, but I used exclusively neon for the experiments in this thesis. Typically, $m_a > m_b$ and $\sigma_{ab} \approx \sigma_{bb}$. Cross-sections depend strongly on temperature when T < 10 K, and can be very difficult to measure. I use typical values of $\sigma_{HeHe} = 1 \times 10^{-14}$ cm^2 at 4 K, and $\sigma_{NeNe} = 2 \times 10^{-14}$ cm^2 at 20 K [112, 113]. Collisional cross sections for rotational and vibrational cooling collisions in molecules are discussed in detail below, in the context of thermalization.

The mean free paths of the particles in the cell, along with the diameter of the aperture leading out of the cell, daperture, are the physical quantities that most directly control the behavior of the beam expansion. The mean free paths can be easily controlled by changing n_b, while the aperture diameter is typically set for a particular cell geometry by the requirements of thermalization of particle a and extraction of the beam into vacuum, as I will consider later. Since particle b is generally a noble gas, n_b cannot typically be directly measured in the cell, but it can be determined from the controllable flow rate through the cell, $f_{0,b}$. Typical flow rates for buffer gas beams are $f_{0,b} = 1 - 100$ SCCM (Standard Cubic Centimeters per Minute 1 SCCM $\approx 4 \times 10^{17}$ particles/s) and can be varied using a mass flow controller. Since the buffer gas flow is continuous and under steady state conditions (denoted by the subscript 0), the output flow rate, f_{out}, determined by the conductance of the aperture and the mean exit velocity, v_b^{exit}, of particle b, must be equal to the steady state input flow rate, $f_{0,b}$.

$$f_{out} = \frac{n_{0,b} v_b^{exit} A_{aperture}}{4} = f_{0,b} \tag{2.3}$$

$$n_{0,b} = \frac{4 f_{0.b}}{A_{aperture} v_b^{exit}} \tag{2.4}$$

where $A_{aperture}$ is the area of the aperture of the cell output orifice, with typical values of $5 - 25$ mm^2. The mean exit velocity depends slightly on flow rate, and is fundamentally related to the thermal mean of the magnitude of the velocity of particles b inside the cell

$$\bar{v}_{0,b} = \sqrt{\frac{8k_bT_0}{\pi m_b}} \tag{2.5}$$

where T_0 is the temperature of the cell (4 K for helium buffer gas and 20 K for neon buffer gas). Typical values for the mean thermal velocity of the buffer gas are around 145 m/s for both 4K helium and 20 K neon. When the flow rate is small, the expansion is effusive, and the exit velocity can be determined by integrating the classical velocity distribution in the beam, $f(v)$, over all velocities

$$f(v) = \frac{32}{\pi^2 \bar{v}_{0,b}^4} v^3 e^{-4v^2/\pi\bar{v}_{0,b}^2} \tag{2.6}$$

$$v_b^{exit} = v_b^{eff} = \int_0^\infty v f(v) dv = \frac{3\pi}{8}\bar{v}_{0,b}. \tag{2.7}$$

This provides a lower bound of $\sim 1.2\bar{v}_{0,b}$ on the mean exit velocity. As the input flow rate is increased, collisions in and around the aperture begin to occur and boost the forward velocity of the buffer gas atoms above the mean thermal velocity. When the flow rate is very large, the velocity is boosted to the maximum value given by the fully supersonic velocity

$$v_b^{exit} = v_{\parallel,b}^{ss} = \sqrt{\frac{2\gamma k_B T_0}{(\gamma-1)m_b}} = \sqrt{\frac{\pi\gamma}{4(\gamma-1)}}\bar{v}_{0,b} \tag{2.8}$$

where γ is the Poisson constant, or the ratio of specific heats, and is 5/3 for a monatomic ideal gas. This provides an upper bound of $\sim 1.4\bar{v}_{0,b}$ on the mean exit velocity of the gas. As the flow rate is increased, v_b^{exit} evolves smoothly from the effusive toward the supersonic limit.

It is convenient to define the Reynolds number, Re, as describing the overall behavior of the beam expansion. The Reynolds number is defined as the ratio of inertial to viscous forces in a fluid flow

$$Re = \frac{F_{inertial}}{F_{viscous}} \approx 2Kn^{-1} = \frac{2d_{aperture}}{\lambda_b} \approx \frac{8\sqrt{2}f_{0,b}\sigma_{bb}}{d_{aperture}v_b^{exit}} \tag{2.9}$$

where Kn is the Knudsen number, which is a gas kinetic quantity expressed by the ratio of the aperture size to the mean free path, and is related the Reynolds number by the von Kármán relationship, and where I have made the substitution $A_{aperture} \approx d^2_{aperture}$. The variation in mean exit velocity as a function of flow rate causes a small uncertainty in the exact value of the Reynolds number, but the variation is a slow function of flow rate, and the uncertainty is smaller than the uncertainties introduced by the approximation inherent in the von Kármán relationship and by approximating $A_{aperture} \approx d^2_{aperture}$. The possible types of flow can be roughly divided into three Reynolds number regimes. I discuss each regime in order.

- $Re \lesssim 1$: In this regime, the *effusive* regime, the mean path length of both particles is longer than the aperture, generally on order of the size of the cell. In this case, the resultant beam simply samples the thermal distribution of particles in the cell.

- $100 \lesssim Re$: In this regime, the *supersonic* regime, there are many collisions near the aperture, and the buffer gas begins to behave like a fluid with properties similar to those cooled in a fully isentropic supersonic expansion.

- $1 \lesssim Re \lesssim 100$: In this regime, the intermediate or *hydrodynamic* regime, there are a sufficient number of collisions near the aperture to significantly alter the properties of the beam and result in an approximately isentropic expansion. The experiments described in my thesis all take place in the hydrodynamic regime, although the chamber that I built can operate in any of the three regimes.

Effusive sources are defined by the mean free path of the buffer gas being much larger than the aperture diameter, such that no collisions occur as the molecules pass through the aperture. The behavior of the beam expansion is then entirely determined by the geometry of the cell and the thermal behavior of the species in the cell. The number density of particles in the beam at a given position moving at a given velocity can be described by a semi-isotropic spatial distribution and a normalized velocity distribution

$$n^{eff}(R, v, \theta) = n^{eff}(R, \theta)\frac{\bar{v}_{0,a/b}}{v}f(v) \tag{2.10}$$

$$n^{eff}(R, \theta) = \frac{n_0 \cos\theta}{4\pi R^2}dA \tag{2.11}$$

where R is the distance from the aperture, θ is the angle from the vector normal to the aperture, n_0 is the steady state number density of the gas in the cell, and dA is the aperture area differential. Note that since the buffer gas particles, b, and the particles of interest, a, do not interact during the extraction, the spatial distribution of each is the same, but the velocity distribution of each is different. The mean forward velocity of the buffer gas particles, b, is given by Eq. 7, and the mean forward velocity of the particles of interest, a, are identical to within a factor of$\sqrt{m_a/m_b}$. Due to the thermal equilibrium of the beam, the velocity spreads in the forward and transverse directions are identical, and follow 1-D Maxwell-Boltzmann distributions

$$\Delta v^{eff}_{\parallel,a/b} = \Delta v^{eff}_{\perp,a/b} = \sqrt{\frac{8\ln 2 k_B T_0}{m_{a/b}}} \approx 1.5\bar{v}_{0,a/b}. \tag{2.12}$$

The full width half maximum (FWHM) of the angular spread, $\Delta\theta^{eff}$, and characteristic solid angle, $\Delta\Omega^{eff}$, can be determined by solving

$$n^{eff}(R, \Delta\theta^{eff}) = (n^{eff}(R, 0))/2, \tag{2.13}$$

which yields:

$$\Delta\theta^{eff} = \frac{2\pi}{3} \tag{2.14}$$

$$\Delta\Omega^{eff} = 2\pi(1 - \cos(\Delta\theta/2)) = \pi \tag{2.15}$$

Effusive beams can be formed from the output of a buffer gas cell, but are also commonly formed from the output of an oven operated at 500 - 1000 K in order to interrogate certain metal atoms or low-reactivity molecules with high vapor pressure.

In this latter situation there is no buffer gas, b, only the species of interest, a.

Supersonic sources are defined by a mean free path much smaller than the aperture diameter, which leads to many collisions between particles as they exit through the aperture. In this case the simple gas kinetic theory that governs the effusive expansion is no longer applicable, as the gas behaves more like a compressible fluid. The beam properties in this case are governed both by the thermal equilibrium in the cell and the dynamical flow of the gas. There are, in principle, two intertwined approaches often used to treat these supersonic expansions: one can thermodynamically treat the expansion as adiabatic and isentropic and fit adjustable parameters in the resultant equations to the numerical solutions of the Navier-Stokes equation. Numerically solving the Navier-Stokes equation is beyond the scope of this thesis, therefore the following discussion will focus on the thermodynamic relationships.

The assumptions of adiabaticity and reversibility (equivalent to the requirements for an isentropic expansion) implies that the sum of the enthalpy and kinetic energy of the expansion is constant

$$H(x) + \frac{m_b v_b(x)^2}{2} = \text{constant} \tag{2.16}$$

where $H(x)$ is the position-dependent molar enthalpy of the gas at position x measured from the point of expansion, and $v_b(x)^2$ is the average flow velocity at that position. One can calculate the maximum velocity of the expansion

$$v_b^{max} = \sqrt{\frac{2H(T_0)}{m_b}} = \sqrt{\frac{2C_pT_0}{m_b}} = \sqrt{\frac{2\gamma k_B T_0}{(\gamma-1)m_b}} \tag{2.17}$$

where $H(T_0)$ is the molar enthalpy of the gas at the temperature of the cell, and I have assumed the expansion is that of an ideal gas, so C_p is independent of temperature. Assumption of an ideal gas and use of the ideal gas law allows calculation of the conditions (p_1, T_1, $n_{1,b}$) at any point compared to those in the cell (p_0, T_0, $n_{0,b}$), where p is pressure

$$\frac{T_1}{T_0} = \left(\frac{p_1}{p_0}\right)^{(\gamma-1)/\gamma} \tag{2.18}$$

$$\frac{n_{1,b}}{n_{0,b}} = \left(\frac{p_1}{p_0}\right)^{1/\gamma} \tag{2.19}$$

$$\frac{n_{1,b}}{n_{0,b}} = \left(\frac{T_1}{T_0}\right)^{1/(\gamma-1)} \tag{2.20}$$

These equations are important primarily because they imply that an expansion from a high pressure source will lead to a large reduction in temperature. This is true for any expansion that is close to adiabatic and reversible, and applies to both the supersonic case and the hydrodynamic case I treat next. I can also calculate the speed of sound, a_b, in an ideal gas, as

$$a_b(T) = \sqrt{\frac{\gamma RT}{m_b}} \tag{2.21}$$

where R is the ideal gas constant. The Mach number, $M(x)$, can then be defined as the ratio of the average flow velocity of the expanding gas at any position, $v_b(x)$, to the local speed of sound of the gas, such that $M(x) = v_b(x)/a_b(x)$. The cooling described by the thermodynamic equations 2.18 - 2.20, above, also implies a large reduction of the local speed of sound in the expanding gas, while the average flow velocity increases as the molar enthalpy is converted into directed kinetic energy. The gas expansion is described as supersonic when the Mach number becomes larger than one. Combining equations 2.18 - 2.21, above, I can describe the temperature, pressure, and number density of the expansion at any position in the expansion in terms of the Mach number

$$\frac{T(x)}{T_0} = \left(1 + \frac{\gamma-1}{2}M(x)^2\right)^{-1} \tag{2.22}$$

$$\frac{p(x)}{p_0} = \left(1 + \frac{\gamma-1}{2}M(x)^2\right)^{-\gamma/(\gamma-1)} \tag{2.23}$$

$$\frac{n_b(x)}{n_{0,b}} = \left(1 + \frac{\gamma - 1}{2} M(x)^2\right)^{-1/(\gamma-1)} \tag{2.24}$$

The only information left to be determined is the Mach number at each position, a non-trivial task. This has been done by developing a fitting formula and fitting parameters to match the numerical results of the Navier-Stokes equation; only the results are presented here

$$M(x) = A\left(\frac{x - x_0}{d_{aperture}}\right)^{\gamma-1} - \frac{(\gamma+1)(\gamma-1)}{2A\left[(x - x_0/d_{aperture})\right]^{\gamma-1}} \tag{2.25}$$

where A and $x_0/d_{aperture}$ are the unitless fitting parameters, and depend on γ. For a monatomic ideal gas, $\gamma = 5/3$, $A = 3.26$, and $x_0/d_{aperture} = 0.075$ [111]. In the far field, when $x \gg d_{aperture}$, equations 2.22 - 2.25 can be simplified to express general scaling laws for the behavior of a supersonic expansion of a monatomic ideal gas

$$T(x) \propto x^{-4/3} \tag{2.26}$$

$$p(x) \propto x^{-10/3} \tag{2.27}$$

$$n_b(x) \propto x^{-2} \tag{2.28}$$

The temperature, pressure, and density of the beam decrease rapidly as the particles fly away from the nozzle. The density decrease is consistent with an inverse-square law, as expected when particles expand in straight lines but diverging paths. The temperature decrease continues until the mean free path of the buffer gas particles becomes larger than the average distance between neighboring particles and the gas ceases to act like a fluid, generally on the order of $x \approx (10 - 20) \times d_{aperture}$ for supersonic expansions.

I can use this limiting distance to calculate spatial and velocity distributions, similar to as I did for the effusive beam case above. The forward velocity in an ideal monatomic gas expansion is given in equations 2.8 and 2.17, above, while the forward

velocity spread is given as

$$\Delta v_{\parallel,b}^{ss} = \sqrt{\frac{\gamma R T_{final}}{m_b}} = \sqrt{\frac{T_{final}}{T_0}} \bar{v}_{0,b} \approx 0.08 \bar{v}_{0,b} \tag{2.29}$$

where T_{final} is the final temperature achieved by the beam expansion. The angular spread (FWHM) $\Delta\theta^{ss}$ and beam divergence $\Delta\Omega^{ss}$ can be calculated by solving the equation $n^{ss}(R, \Delta\theta^{ss}) = (n^{ss}(R, 0))/2$ where

$$n_{ss}(R, \theta^{ss}) \approx n_{ss}(R, 0) \cos^2\left(\frac{\pi\theta}{2.8}\right). \tag{2.30}$$

The solution to this equation gives the angular spread and beam divergence

$$\Delta\theta^{ss} \approx 0.4\pi \tag{2.31}$$

$$\Delta\Omega^{ss} \approx 0.4\pi \tag{2.32}$$

All of the equations above for a supersonic expansion have been explicitly written only in terms of the buffer gas mass, density, and velocity. This is because, in the case of a seeded buffer gas beam, there are a sufficient number of collisions in the region of the aperture that species a will always remain in thermal equilibrium with the buffer gas. This means that the equations above apply equally well to particle a as to particle b, without any changes at all. The primary advantage of this analysis is that it allows essentially any target species to have a well-defined lab frame velocity and velocity distribution. Additionally, if the species of interest is a molecule, and has sufficiently large collisional cross sections for cooling rotational and vibrational motions, these internal motions can be thermalized to the translational temperature as well. In general, rotational cooling cross-sections are approximately an order of magnitude smaller than σ_{ab}, the elastic collision cross section, while vibrational cooling cross-sections are three or four orders of magnitude smaller [114, 115]. In practice this means that the rotational temperature of a molecule in a supersonic expansion can be easily thermalized to the translational temperature, but the vibrational temperature

can only rarely be cooled as efficiently.

The final category of beam expansions is the regime intermediate between effusive and supersonic beams, called the hydrodynamic regime. In this category of beam expansions, the rate of collisions between particles as they exit the cell is large enough to modify the final velocity and temperature of the beam, but not enough to behave in a truly fluid manner, as in a supersonic expansion. The forward velocity and beam temperature can be determined by interpolation between the effusive and supersonic limits, but the transverse velocity spread, angular spread, and divergence of the beam cannot be interpolated in this manner and must be calculated independently. For the purposes of high resolution spectroscopy, this type of expansion is preferred because it achieves both a narrow velocity distribution as in a supersonic expansion as well as a low lab-frame velocity as in an effusive expansion. Additionally, under the proper circumstance, a hydrodynamic expansion can operate with a narrower angular spread than either an effusive or supersonic expansion. In the experiments described in this thesis, I operate our buffer gas cooled beam entirely within the hydrodynamic regime.

In order to interpolate between the forward velocity of an effusive beam ($\sim 1.2\bar{v}_{0,a}$) and the forward velocity of a supersonic beam ($\sim 1.4\bar{v}_{0,b}$), I first consider the few-collision regime. Intuitively, when there are few collisions, I expect the velocity to increase linearly with the number of collisions, and saturate as the number of collisions increases. As the particles exit through the aperture, each undergoes roughly $Re/2$ collisions. Each of these collisions gives the particles a momentum boost of $\sim m_b\bar{v}_{0,b}$ in the forward direction, corresponding to a net velocity boost of $\sim m_b\bar{v}_{0,b}Re/2m_a$. This provides the linear portion of the interpolation

$$v_{\parallel,a}^{hydro} \approx 1.2\bar{v}_{0,a} + 0.6\bar{v}_{0,b}\frac{m_b Re}{m_a} \tag{2.33}$$

which is empirically accurate for Reynolds numbers $1 \lesssim Re \lesssim 10$. As the Reynolds number increases further, this model breaks down, and a new model must be used. The most common model used is a "sudden freeze" model, where particles a are in equilibrium with the buffer gas until the density of buffer gas molecules becomes so

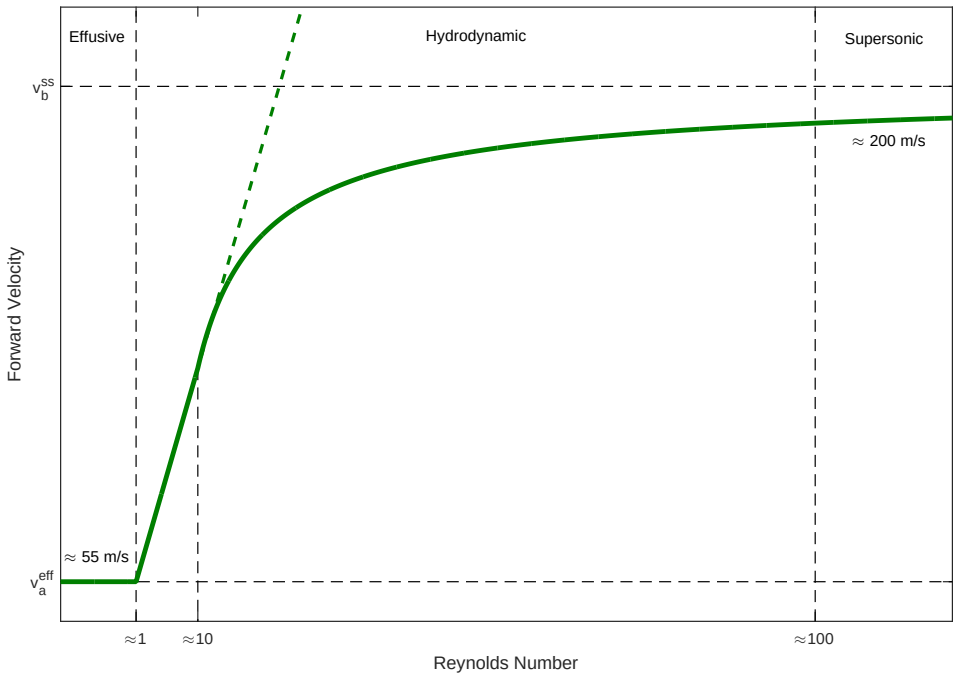

Figure 2-1: A schematic representation of the forward velocity of the beam expansion vs. Reynolds number

small that there are no more collisions. The functional form that this takes is

$$v_{\parallel,a}^{hydro} \approx 1.4\bar{v}_{0,b}\sqrt{1-4Re^{-4/5}} \tag{2.34}$$

which is empirically accurate for Reynolds numbers $10 \lesssim Re \lesssim 100$. The velocity of a buffer gas beam as a function of Reynolds number across all three beam expansion regimes is given in Figure 2-1.

The velocity spread of a hydrodynamic expansion can be similarly interpolated. Again, intuitively, I expect an initial linear dependence on Reynolds number as collisions in the area of the aperture begin to occur, followed by saturation as the expansion approaches the limit of an ideal isentropic supersonic expansion. The final translational temperature (and hence the forward velocity distribution) can be calculated using the thermodynamic techniques described above for a supersonic expansion. Empirical formulas can be constructed similar to those for the mean forward velocity

$$\Delta v_{\parallel,a}^{hydro} \approx 1.5\bar{v}_{0,b} - \bar{v}_{0,b}\frac{m_b Re}{m_a} \tag{2.35}$$

$$\Delta v_{\parallel,a}^{hydro} \approx 0.4\bar{v}_{0,b}\sqrt{1 - 4Re^{-4/5}} \tag{2.36}$$

which are empirically accurate for Reynolds numbers $1 \lesssim Re \lesssim 10$ and $10 \lesssim Re \lesssim 100$, as above. The final translational temperature dependence on Reynolds number, across all three beam expansion regimes, is shown in Fig. 2-2. However, the behavior of the transverse velocity distribution is more complicated and cannot be cleanly interpolated. In the region near the aperture, empirical equations similar to equations 2.35 and 2.36 are reasonably accurate, but I am concerned with the behavior far from the cell, after collisions have ceased. Empirically, the behavior far from the cell is that the transverse velocity is almost a constant for $1 \lesssim Re \lesssim 10$, and then increases significantly, approaching the supersonic limit ($\sim 2.2\bar{v}_{0,b}$) as Re approaches ~ 100. A variety of hydrodynamic simulations have been performed to accurately describe this behavior, which are beyond the scope of this thesis. Further, this behavior has been observed in experiments with both helium and neon buffer gases [45, 49].

The angular spread (FWHM) of the beam can be computed from the transverse velocity spread of the beam and the forward velocity by the relation

$$\Delta\theta_a^{ss} \approx 2\sqrt{\frac{m_b}{m_a}} \tag{2.37}$$

$$\Delta\Omega_a^{ss} \approx \frac{\pi m_b}{m_s}. \tag{2.38}$$

The divergence can be much smaller ($\sim 0.1\pi$) than either the effusive (π) or supersonic (0.4π) limits. Additionally, seeding the beam with heavier particles leads to ever smaller angular spreads and solid angles. The divergence of an atomic beam of calcium, for example, is $\sim 0.5\pi$, while the divergence of an atomic beam of barium is $\sim .14\pi$.

As a visual comparison of the properties of each of the regimes of molecular beam

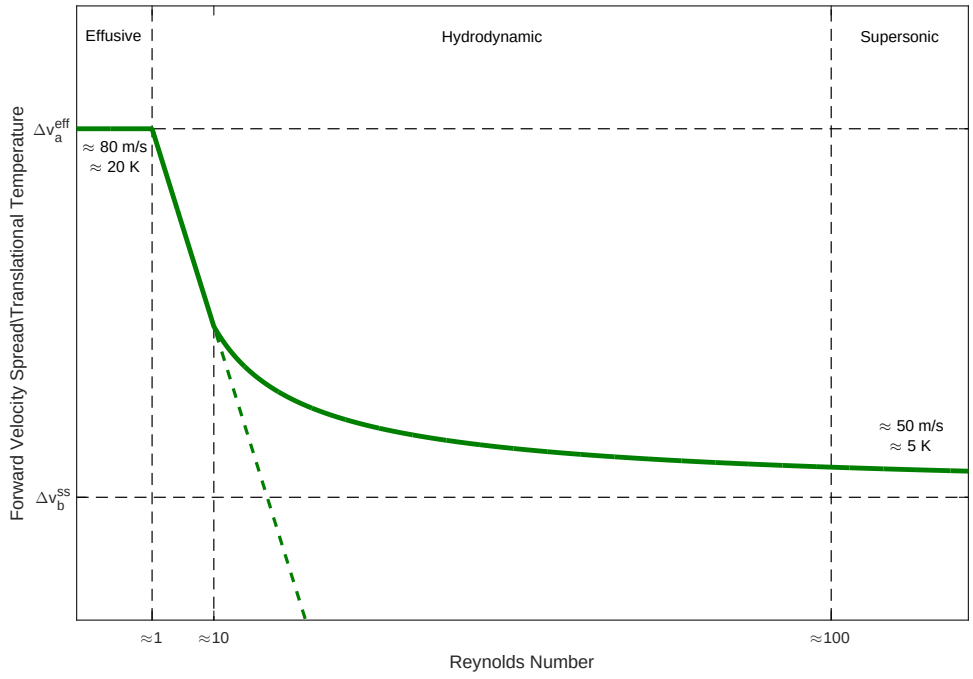

Figure 2-2: A schematic representation of the temperature of the beam expansion vs. Reynolds number

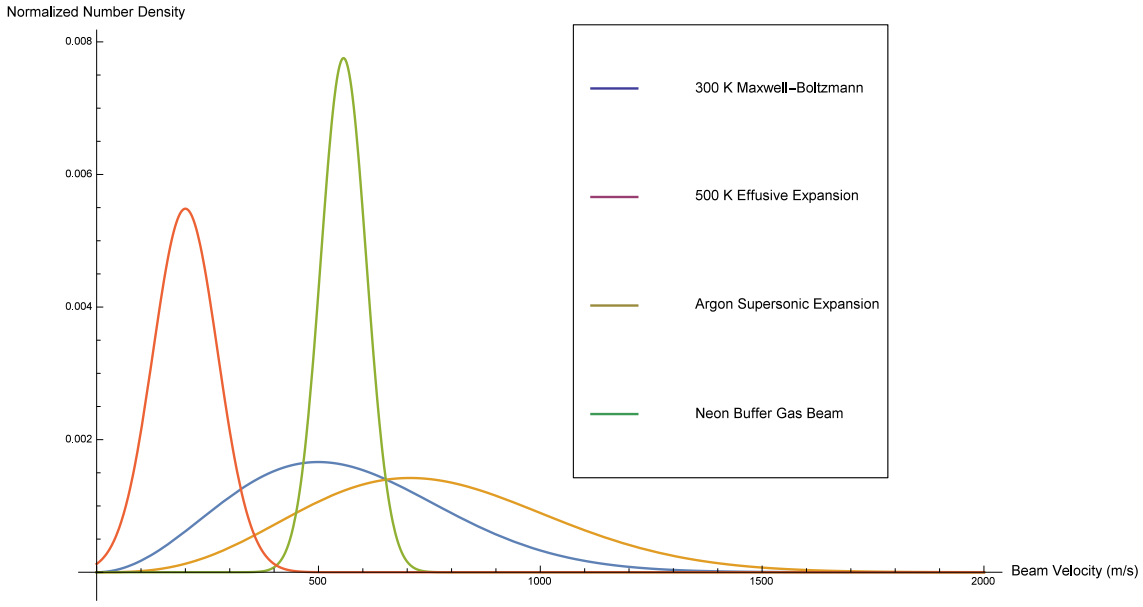

Figure 2-3: A comparison of the forward velocity and velocity spread of an effusive beam, a supersonic beam, and a hydrodynamic beam.

expansion, I have plotted an example of each in Fig. 2-3. The effusive beam source is considered at 500 K (typical of many oven sources), the supersonic source uses argon as the buffer gas, while the buffer gas source (like mine) uses neon as the backing gas. Only the buffer gas beam has both a low forward velocity and a low translational temperature. Additionally, with the proper tuning of the flow rate, the buffer gas beam can have a much smaller divergence than either effusive or supersonic expansions. A comparison of the relevant parameters from each of the three types of beam expansion is given in Table 2.1.1. The values for transit time and Doppler broadening are given for a 300 GHz mm-wave beam spot of 1.75 cm^2.

2.1.2 Thermalization

Up until now I have focused on a pair of particles assumed to already be in thermal equilibrium in the cell. However, in many methods of introducing the species of interest (such as ablation of a solid precursor target) the particles a are introduced at

	Effusive Oven Expansion	Supersonic Expansion	Hydrodynamic Expansion
Beam Velocity	200 - 800 m/s	500 - 2000 m/s	150 - 200 m/s
Translational Temperature	500 - 2000 K	1 - 5 K	1 - 5 K
Rotational Temperature	500 - 2000 K	1 - 5 K	1 - 5 K
Particles/Pulse	CW	$\sim 10^{10}$	$\sim 10^{12}$
Number Density	$\sim 10^{6}$ cm^{-3}	$\sim 10^{5}$ cm^{-3}	$\sim 10^{8}$ cm^{-3}
Number Density/Quantum State	$\sim 10^{3}$ cm^{-3}	$\sim 10^{4}$ cm^{-3}	$\sim 10^{7}$ cm^{-3}
Transit Time Broadening	60 kHz	150 kHz	15 kHz
Doppler Broadening	600 kHz	600 kHz	60 kHz

Table 2.1: Comparisons of effusive, supersonic, and hydrodynamic expansions.

a higher temperature, either room temperature (for high vapor pressure species) or significantly higher ($\sim 1000 - 10000$ K, typical of ablation products). Before forming a beam, there should be a sufficient number of collisions between the cold buffer gas and the hot species of interest in order to decrease the temperature of the target species to that of the cold cell (20 K). The average temperature change of the species of interest per collision with a buffer gas particle is given by

$$\Delta T_a = -\left(T_a - T_b\right)/\kappa \tag{2.39}$$

$$\kappa \equiv \frac{\left(m_a + m_b\right)^2}{2 m_a m_b} \tag{2.40}$$

where T_a and T_b are the temperatures of the species of interest and the buffer gas. I can then write the temperature of the species after N collisions as

$$T_a(N) - T_A(N-1) = -(T_a(N-1) - T_b)/\kappa \tag{2.41}$$

and iteratively solve to find the temperature. However, if I treat N as large and the temperature change per collision as small, I can approximate this as a differential

equation

$$\frac{dT_a(N)}{dN} = -(T_a(N) - T_b)/\kappa \tag{2.42}$$

which yields a solution that provides a ratio between the species and buffer gas temperatures

$$\frac{T_a(N)}{T_b} = 1 + \left(\frac{T_a(0)}{T_b} - 1\right) e^{-N/\kappa} \approx 1 + \frac{T_a(0)}{T_b} e^{-N/\kappa} \tag{2.43}$$

The approximation made in this final step is equivalent to assuming that the species is introduced to the cell at a temperature much larger than the buffer gas temperature. For typical parameters, the target species can be expected to thermalize to the temperature of the buffer gas within 50 - 100 collisions, and in a time of a few milliseconds and a distance of a few centimeters. In order to ensure that the cell is large enough to provide enough time and distance for a particle to thermalize to the buffer gas bath before exiting, the cell should be designed to be larger than the required thermalization distance.

The above discussion focuses entirely on translational thermalization. For molecular targets, rotational and vibrational motions are cooled slightly differently. Rotational collisional cross sections are approximately one order of magnitude smaller than elastic collisional cross sections [114, 115]. However, due to the lack of a relative mass factor ($\sqrt{m_a/m_b}$) in the rotational cooling process, the thermalization efficiency can be comparable to or greater than that of the translational thermalization which is most efficient when $m_a \approx m_b$. Vibrational collisional cross sections are generally quite small, three or four orders of magnitude smaller than elastic collisional cross sections, thus the vibrational temperature of the final beam is typically similar to that of the introduction temperature [114, 115].

2.1.3 Extraction from the cell

After the target species is cooled to the temperature of the buffer gas bath, it needs to be efficiently moved towards the output aperture and entrained in the formed

molecular or atomic beam. There are two competing processes that must be considered for in-cell dynamics, the diffusion of the target species to the walls of the cell that ends with the target species frozen to the cell walls, and the extraction of the target species from the cell. I define a dimensionless parameter to characterize the competition between these two processes

$$\gamma \equiv \frac{\tau_{diff}}{\tau_{extract}} \tag{2.44}$$

where τ_{diff} is the timescale for diffusion to the walls, and $\tau_{extract}$ is the timescale for extraction from the cell. Using a Brownian motion model, I can calculate the diffusion constant as

$$D = \frac{3}{16 n_{0,b} \sigma_{ab}} \left(\frac{2\pi k_B T_0}{m_b} \right)^{1/2} = \frac{3\pi}{32} \frac{\bar{v}_{0,b}}{n_{0,b}\sigma_{ab}}. \tag{2.45}$$

In order to determine the timescale for diffusion to the walls, I simply need to equate the mean-squared displacement of the target particle to the internal surface area of the cell

$$\left\langle \Delta x^2 \right\rangle (t) = 6Dt = d_{cell}^2 \approx A_{cell} \tag{2.46}$$

where d_{cell} is the diameter of the cell interior, and A_{cell} is the surface area of the cell interior. This allows me to calculate the timescale for diffusion to the walls as

$$\tau_{diff} = \frac{16}{9\pi} \frac{A_{cell} n_{0,b} \sigma_{ab}}{\bar{v}_{0.b}}. \tag{2.47}$$

The diffusion time is typically 1-10 ms. The extraction time is determined primarily by the conductance of the cell aperture

$$\dot{N}_b = \frac{N_b \bar{v}_{0,b} A_{aperture}}{4 V_{cell}} \tag{2.48}$$

where V_{cell} is the interior volume of the cell, N_b is the total number of buffer gas particles in the cell, and $\dot{N}_b$ is the rate at which the buffer gas particles are flowing out of the cell. The solution to this differential equation is a single exponential decay

with a characteristic time

$$\tau_{extract} = \frac{4V_{cell}}{\bar{v}_{0,b}A_{aperture}}. \tag{2.49}$$

The extraction time is also typically around 1-10 ms. The extraction time also sets the total duration of the target of interest in the beam expansion, in the case of pulsed loading.

Both diffusion to the walls and extraction into the beam occur at the same time, and their relative importance is given by

$$\gamma = \frac{4}{9\pi}\frac{n_{0,b}\sigma_{ab}A_{aperture}}{L_{cell}} \approx \frac{\sigma_{ab}f_{0,b}}{L_{cell}v_b^{exit}} \tag{2.50}$$

where L_{cell} is the characteristic length of the cell.

For $\gamma \lesssim 1$, diffusion to the walls is faster than extraction into the beam, thus most of the species of interest will be lost. In order to combat this effect, the main experimental parameters that I adjust are the flow rate of the buffer gas and the overall size of the buffer gas cell. For $\gamma \gtrsim 1$, molecules are mostly extracted from the cell before diffusing to the walls, in what is known as "hydrodynamic enhancement." Diffusion alone extracts a fraction of molecules on the order of $A_{aperture}/A_{cell} < 0.1\%$, whereas when $\gamma \gtrsim 1$, the maximum efficiency plateaus and can be as large as 40%. Typical experiments operate with an extraction efficiency of around 10%. In order to form a cold beam as well, the thermalization time given above must also be smaller than either $\tau_{extract}$ or τ_{diff}.

The fluid dynamics of the buffer gas inside the cell are mostly described by laminar flow. An investigation of the precise dynamics inside the cell was performed by the Hinds group and confirms that this description is generally correct [116]. One feature that was revealed by this calculation is that there are significant eddies located in the corners of the cell, and it is these eddies that account for the plateau in extraction efficiency - the eddies get larger and trap more target molecules as the flow rate is increased, counteracting the decrease in flyout time.

2.1.4 Beam loading

The primary method that I use to introduce the target species to the cell is laser ablation. The experiments in this thesis focus on atomic calcium and barium. Ablation of metals is typically much easier than the ablation of inorganic salts, which is covered in detail in Yan Zhou's thesis, Sect. 2.4. While it is possible to achieve satisfactory yields of calcium and barium with minimal optimization, there are two important optimizations that allow for the largest, longest-lived signal. First, unlike the inorganic case where the high power density requirements necessitate the use of a nearly diffraction-limited laser spot, the laser can be defocused to a $\gtrsim 1\text{mm}^2$ spot in order to ablate a larger overall area and create a denser beam. Second, the direction of the plasma generated in an ablation process is normal to the surface being ablated. Because of this, after the target has been ablated at relatively low power (~ 5 mJ/pulse), the surface of the target becomes craggy, and any individual ablation shot can lead to the ablation plume expanding at a large angle relative to the normal to the surface of the target. This both effectively reduces the dimensions of the cell and causes some of the ablatant to be caught in eddies in the corners of the cell, unavailable for extraction into the beam.

The use of higher laser intensity does not lead to higher ablation efficiency, but it does allow for localized melting of the metal targets, thus effectively smoothing the surface of the target, which minimizes this effect in the ablation plume. In this thesis project, the ablation was performed with an Nd:YAG laser (Spectra-Physics Quanta-Ray GCR-130). This laser produces up to 25 mJ/pulse of 532 nm light and 50 mJ/pulse of 1064 nm light. I use the full output of the 532 nm light to ablate calcium, and the full output of the 1064 nm light to ablate barium.

2.1.5 Details of the buffer gas cell and vacuum chamber

Considerations of beam expansion properties, thermalization times, and extraction efficiencies all must be taken into account when designing the buffer gas cell, as all three depend on the physical dimensions of the buffer gas cell. A photo of the cell

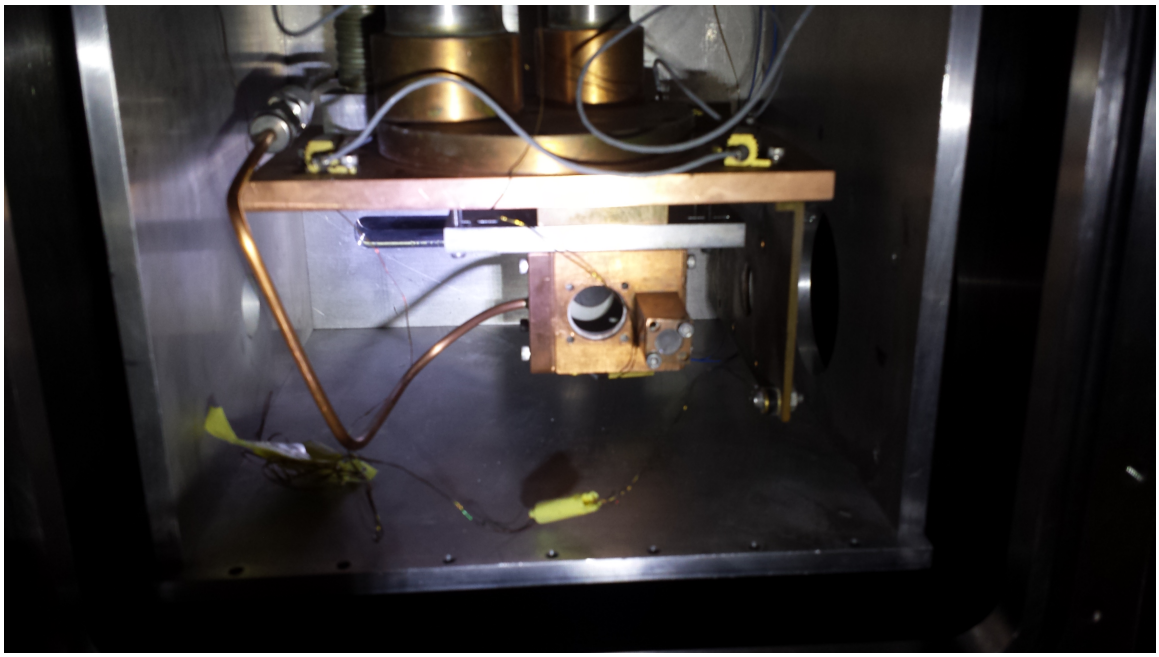

Figure 2-4: A photograph of the buffer gas cell.

that Yan Zhou and I designed is shown in Fig. 2-4. The internal dimensions of the cell are 1.20 inches in diameter and 1.50 inches long, with an exit aperture 3.0 mm in diameter. The distance between the ablation spot and the exit aperture is ~ 3 cm, which is both long enough to ensure thermalization of the ablatant to the buffer gas temperature, but also to extract more than 10% of the target species into the beam.

A second buffer gas cell is attached to the backside of the main cell that is preloaded with buffer gas in a ring, which then flows into the main cell through an annulus. The back of the cell is left open, so approximately half of the buffer gas flows backward out of the cell. However, due to the annular flow, all of the buffer gas that enters the main buffer gas cell continues forward and contributes to forward laminar flow out of the cell. The reason for doing this is that it allows a permanent gas (or high vapor pressure species) to be directly loaded into the cell from the rear. Some of this inserted gas will be deflected out of the cell by the backward flowing buffer gas, but any that survives to enter the cell will be drawn out into the hydrodynamic expansion. This allows for the possibility of creating molecular targets (such as CaF and BaF) through ablation of calcium and barium metal while flowing fluo-

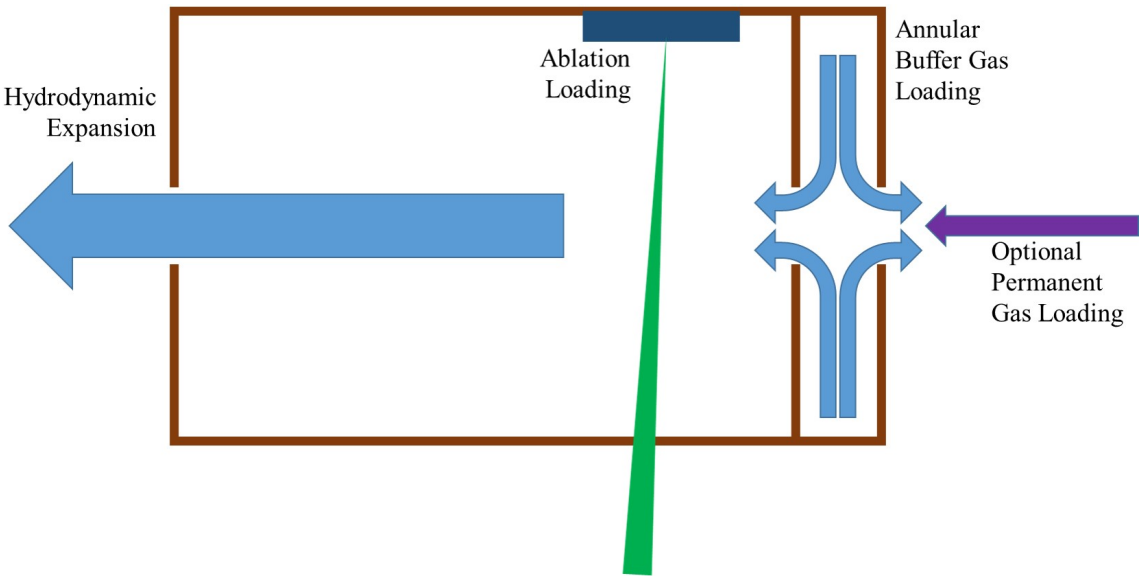

Figure 2-5: A schematic representation of the buffer gas cell.

rinating agents (such as SF_6) into the cell in a method analogous what is commonly done in standard Smalley-type supersonic expansions. It also allows for immediate investigation of permanent gases, such as NO. A schematic of the annular flow is shown in Fig. 2-5.

The vacuum chamber that houses the buffer gas cell was designed jointly by myself and Yan Zhou, and was thoroughly described in his thesis, Sect. 2.3.3. I provide here a brief review of the primary features of the vacuum chamber, and note all significant changes to the overall operation of the system. A photo of the complete system is shown in Fig. 2-6.

The buffer gas cooled beam chamber is fundamentally built around a 2-stage closed cycle pulse tube refrigerator (Cryomech PT410-RM) with a remote reservoir. This refrigerator has a cooling capacitance of ~ 1 W at 4 K, easily cooling the system to the required 20 K (for neon buffer gas) and allowing for potential experiments at 4 K (for helium buffer gas). The vacuum shields consist of two chambers: a cryostat/beam formation chamber and a detection chamber. The cryostat chamber contains the pulse tube refrigerator head, with eight vacuum ports allowing access for temperature monitoring and control, neon gas feedthroughs, pressure monitoring, and vacuum connections and gauges. A radiation shield is connected to the first stage of

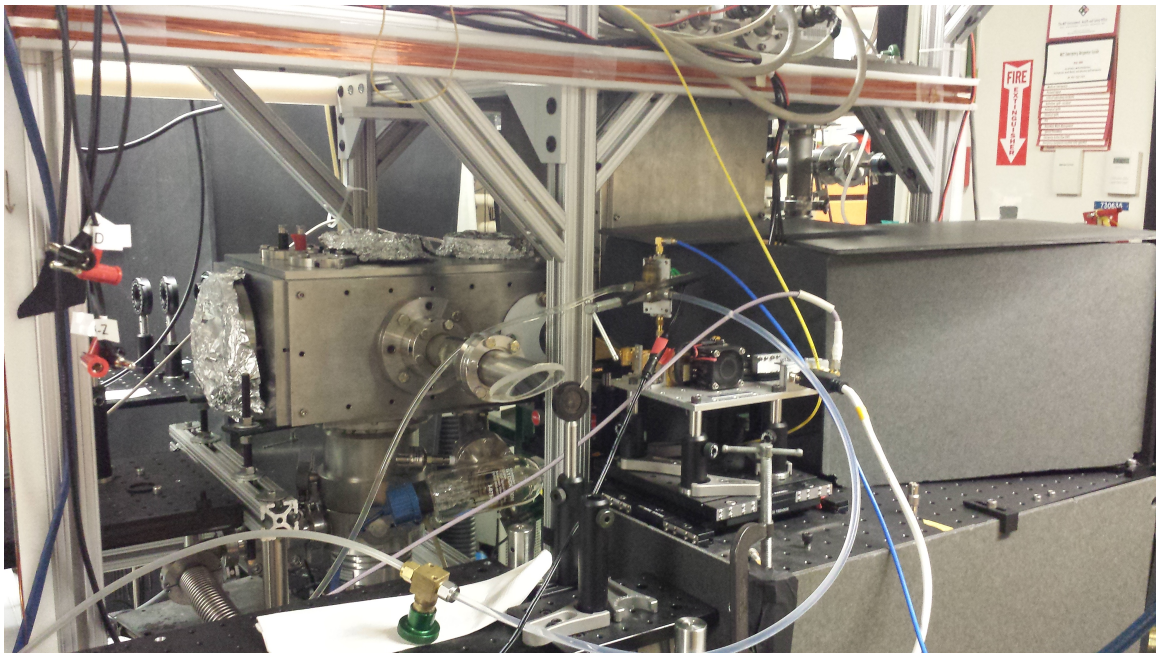

Figure 2-6: A photograph of the vacuum chamber.

the refrigerator ($\sim$ 40 K) and serves to reduce the blackbody heat load on the second stage ($\sim$ 4 K) and the buffer gas cell ($\sim$ 20 K). The buffer gas cell is offset from the cold plate of the second stage and held at 20 K with a series of resistive heaters and a Labview PID control program. Rectangular windows on either side of the vacuum shield and radiation shield allow optical access to the cell for ablation and diagnostics. A 4 K cold plate directly in front of the cold cell acts as a cold skimmer, collimator, and additional cryopumping for the cryostat chamber.

Room temperature neon gas (99.999% purity) flows into the cell through a series of 1/8 inch stainless steel and copper tubes. It is thermalized first to the radiation shield temperature, and then the buffer gas cell temperature through wrapping around a pair of copper cylinders. The second stage of thermalization is also controlled by the Labview PID control program. High purity neon must be used, because any impurities other than helium (the most common impurity) will freeze in the tube, while helium will degrade the vacuum in front of the cell. Excessive helium in the beam reflects backwards towards the cell off the cold skimmer and prevents the hydrodynamic beam expansion from occurring as described above.

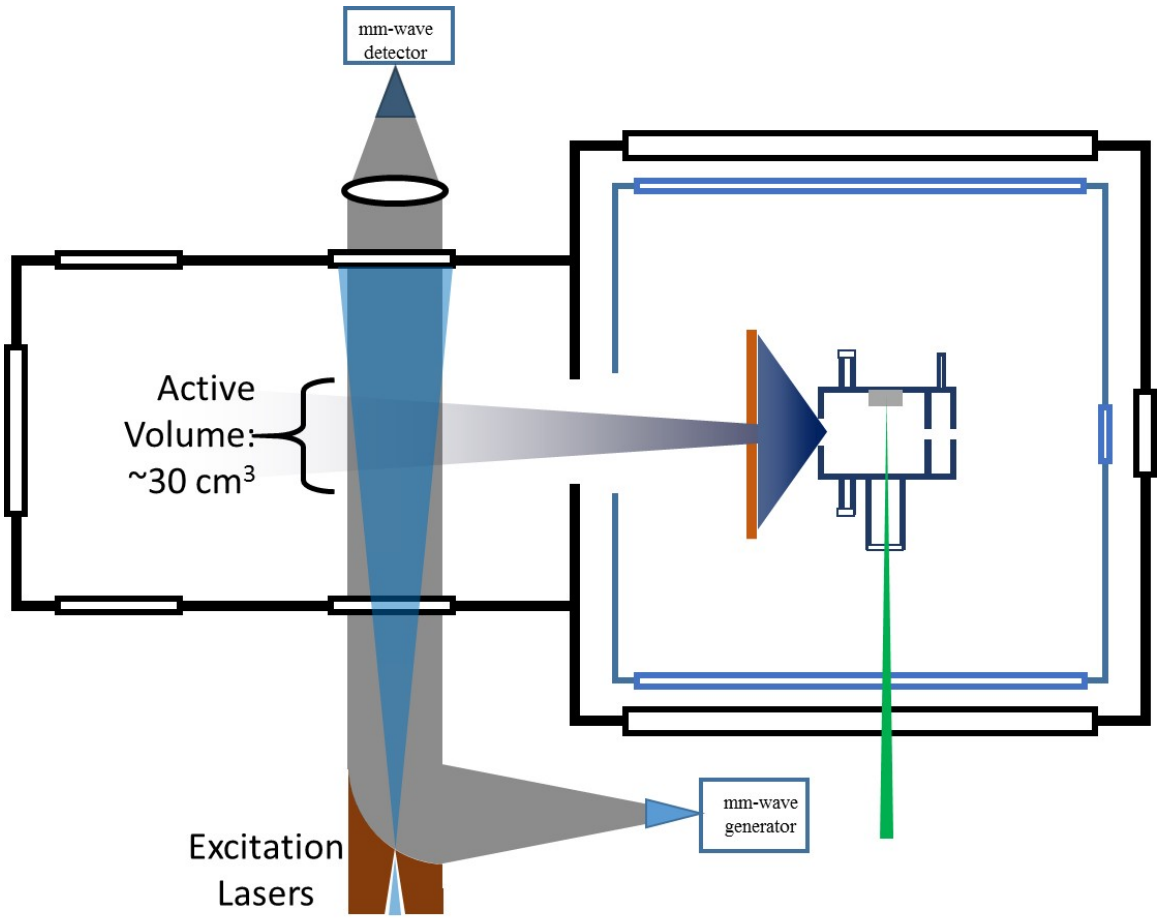

Figure 2-7: A schematic representation of the buffer gas cooled molecular beam chamber.

The buffer gas beam expands into vacuum, is skimmed and loosely collimated by the aforementioned 4K cold plate, and proceeds into the detection chamber. There it is transversely crossed by lasers and millimeter waves for both diagnostic and experimental purposes. A schematic diagram of the entire vacuum system and relevant radiation sources is shown in Fig. 2-7.

To minimize the Earth's magnetic field, the entire vacuum apparatus is surrounded by three orthogonal pairs of rectangular Helmholtz coils. The strength of each pair is controlled by varying the voltage of a current-limited power supply. Rough calibration of these voltages is performed with a Honeywell HMC5883L 3-axis magnetometer chip to eliminate the stray magnetic field in each direction. Any residual field, detectable as splittings in the mm-wave spectrum, is removed by fine adjustment using the

mm-wave spectrum as a guide.

2.2 Pulsed laser system

Rydberg states, existing at high excitation energies near (or above) the first ionization potential, require a large amount of energy to populate. We choose to use pulsed tunable laser excitation to balance state selectivity and resolution with total number of Rydberg states created. There are several details associated with the laser excitation process that are important for both cooperative effects (such as superradiance) and coherent population transfer experiments (such as STIRAP). I describe first the details of how the lasers are used in the experiment, then the details of the longitudinal cavity modes of each laser and how they affect the experiments at hand, and then fine details that are important for planning future experiments on Rydberg-Rydberg transitions.

We use one or two pulsed dye lasers to selectively populate individual Rydberg states in all of the following experiments. A sample two-photon scheme for populating ns or nd states of calcium atoms for mmwave interrogation is shown in Figure 2-8. Both lasers are pumped by the same 20 Hz injection-seeded Spectra-Physics GCR-290 with either ∼200 mJ/pulse, 7.5 ns duration 532 nm light or ∼100 mJ/pulse, 6 ns duration 355 nm light.

For the sample two-photon scheme, the first transition, from the $4s^2\ ^1S_0$ ground state to the 4s5p $^1P_1$ state, is driven with 544.4 nm radiation, doubled in a β-BBO crystal to 272.2 nm, generated in a Sirah Cobra-Stretch pulsed dye laser pumped by the third harmonic of the Nd:YAG. The second transition, from the 4s5p $^1P_1$ state to a 4sns $^1S_0$ or a 4snd $^1D_2$ Rydberg state is driven with ∼800 nm radiation generated in an intracavity etalon-narrowed Scanmate pulsed dye laser pumped by the second harmonic of the Nd:YAG. Both lasers are vertically polarized so all of the optical transitions follow the selection rule $\Delta m = 0$. In certain experiments, only a single UV photon is required, and in those cases it is generated with the intracavity etalon-narrowed Scanmate pumped by the third harmonic of the Nd:YAG.

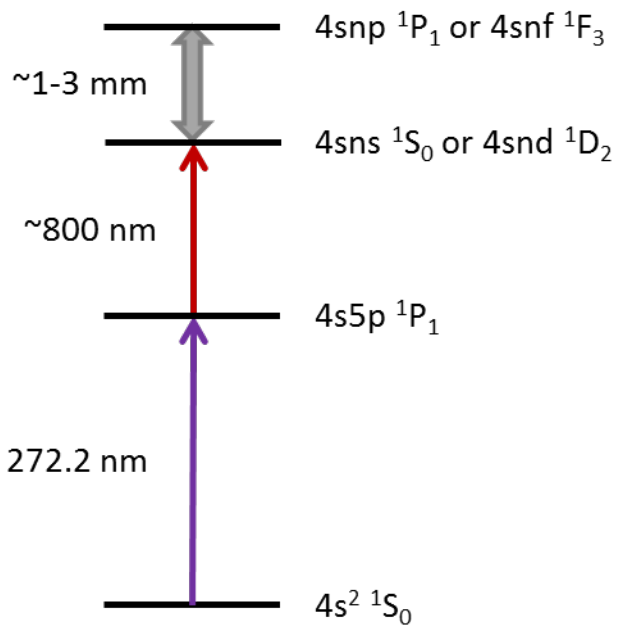

Figure 2-8: A sample two-photon excitation scheme to Rydberg states.

In order to perform high-resolution spectroscopy with a high signal to noise ratio, I aim to generate a large population of Rydberg states, while maintaining a low enough density to avoid solely observing collective effects. To this end, I allow the laser beams to be diverging upon entrance into the chamber in order to create a large active volume for the experiment. In practice, I combine the radiation from both lasers (if using two) using a Semrock 325 nm BrightLine dichroic beamsplitter (average reflectance $> 90\%$ $\lambda < 300$ nm, average transmittance $> 90\%$ $\lambda > 336$ nm) and send both beams through a short focal length (f = 50 mm) convex lens. The focused light passes through a small hole in the center of a gold coated copper off-axis parabolic mirror in order to co-propagate the mm-waves with the superimposed laser beams. The mm-wave radiation is allowed to diverge after passing through the mirror. The laser beams have typically expanded to an area of ~ 1.5 cm^2 at the beginning of the interaction with the atomic beam and continue to expand throughout the sample. When using two colors, the focal length is slightly different for the two, but the primary goal is large sample volume. Slight differences in beam diameter are acceptable.

Calibrating the wavelengths of the lasers, when necessary, is done in two ways. First, the laser can be scanned to compare the wavelength at any given step to a known spectral source, typically a heated sample of tellurium for $\lambda < 550$ nm, and iodine, potentially heated, for $\lambda > 550$ nm. This allows precise determination of the absolute wavelength of the laser. For less stringent applications, the laser radiation is fed via optical fiber to an Angstrom WS-7 Fizeau wavemeter to determine the wavelength interferometrically. The original purpose of the wavemeter, and primary advantage in this manner of measurement, is nearly instant feedback as to the wavelength without having to record and calibrate a spectrum. The absolute accuracy of the wavemeter is, when calibrated, 50 MHz and, in principle, sufficient to use as the sole calibration source for an experiment, although it is wise to use a secondary source for confirmation. The second advantage of the wavemeter is that it displays the interferogram directly in its associated software, which can aid in determining the longitudinal mode structure of a laser beam, which had previously only been accessible at low resolution by measurement of etalon fringes.

The longitudinal modes of the intracavity etalon-narrowed Scanmate behave in a qualitatively different manner than those of the double grating-narrowed Sirah Cobra-Stretch, or any other solely grating-narrowed dye laser that we have tested. When properly aligned, the intracavity etalon-narrowed Scanmate lases primarily on a single longitudinal mode on any given shot, shown in Fig. 2-9a, while grating-narrowed lasers lase on multiple longitudinal modes on any given shot, shown in Fig. 2-9b. The multimode character is evident in the double peak structure observed on the wavemeter, circled in red in Fig. 2-9b. This is an essential distinction when attempting to perform coherent population transfer experiments such as STIRAP.

In principle, single longitudinal mode lasing should be possible in both the Scanmate and the Sirah. The cavities of the Scanmate and Sirah are similar in longitudinal mode spacing and bandwidth. The mode spacing in each is $\sim$500 MHz ($\sim$0.015 cm^{-1}), while the FWHM of each mode is $\sim$250 MHz. Thus three modes can be supported in the nominal bandwidth of each, 0.03 cm^{-1}. In both cases, the first mode to begin lasing reduces the gain available in the dye to the other two modes in the process known

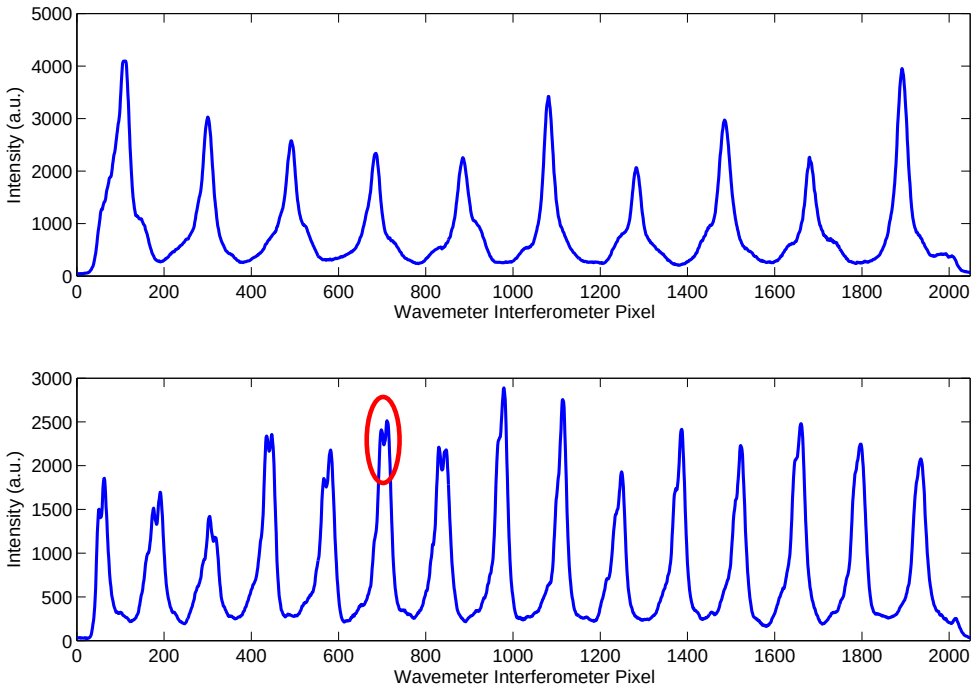

Figure 2-9: Examples of detected mode structure in the pulsed laser systems.

as mode-competition. Different longitudinal modes can acquire gain from spatially separate portions of the gain medium, and so improper pump laser alignment (specifically an improperly placed cylindrical focusing lens) can lead to multimode behavior. Similarly, increasing pump power past the point of saturation for a single longitudinal mode can lead to multimode behavior. However, I have never been able to achieve single longitudinal mode lasing in the Sirah, while it has been a routine accomplishment with the Scanmate. This may be a consequence of an unexamined small difference in the cavity structures, alignment procedures, or manufacturing quality. Even though I do not understand the fundamental reason behind this difference in lasers, it makes the Scanmate the natural choice for performing any coherent experiments (such as STIRAP).

Unfortunately, the cavity mode FWHM of the Scanmate, 250 MHz, is still much larger than the Fourier-transform limited 59 MHz bandwidth for a 7.5 ns pulse, by a factor of $\sim$4, creating a remaining obstacle to coherent interactions, as examined

in detail in Section 6.2. Therefore, an attempt to narrow this cavity mode width is highly desirable for coherent experimentation. While there have been some demonstrated successes at narrowing dye laser outputs by, for example, introducing an additional frequency discriminator into the cavity, a simpler path forward is to use pulse-amplified radiation from a single-mode stabilized CW laser.

The power density required to pump sufficient population to Rydberg states is on the order of GW/cm^2, which is out of the reach of almost all CW tunable laser systems. On the other hand, pulse amplification of a CW laser can provide the power density required, albeit often at the cost of degrading the resolution of the seed laser. Pulse amplified systems, with proper alignment, can provide Fourier-transform limited pulses of radiation, which is a significant step toward using coherent interactions in future experiments. Timothy Barnum is currently implementing pulse amplified systems for use in future coherent population transfer experiments.

One large complication with Nd:YAG pumped dye laser systems is the large intensity fluctuations in their output. Both the Scanmate and the Sirah have been measured to have a Standard Deviation of 0.025 when compared to the mean power. These variations in intensity cause fluctuations in the shot-by-shot Rydberg state population densities, which is important both to determine the signal level of each shot, but also in any collective effects of each shot.

Additionally, care must be taken when determining the paths of the laser beams interacting with the atomic beam inside the chamber. We have copropagated the lasers with the mm-waves in all of the experiments covered in this thesis, primarily for ease of alignment (the details associated with aligning the mm-waves are covered in Sec. 2.3). However, for certain experiments, primarily those associated with cooperative effects, the exact geometry of the interaction volume is important, and introducing the lasers from another direction could be extremely useful in precisely designing the active volume (through the use of laser pulse spatial shaping). It is possible to propagate the lasers and mm-waves perpendicular to each other and obtain signals roughly as strong as copropagation, but there are details beyond difficulties concerning alignment, such as termination and polarization of the laser beams that

must be considered before doing so.

First, the laser beams must be terminated on a material with a larger work function than the highest photon energy in order to prevent the generated photoelectrons from creating an inhomogeneous electric field that would artificially broaden the spectrum. This had been a problem, for example, when the experiment was set up in a double pass retroreflected scheme [10]. In the copropagation setup used in this thesis, the laser-beams terminate on a Teflon window, which minimizes the production of photo-electrons. If the laser beams must be terminated on a conductor (such as the walls of the chamber), it is ideal for this termination to be located as far from the active volume as possible.

Second, the polarizations of the laser beams must be carefully considered. In the copropagating experiments described above, both lasers are vertically polarized so that that can only drive $\Delta m = 0$ transitions. Other polarization combinations can be useful in molecular spectroscopy to determine the rotational state of the populated Rydberg state, as demonstrated initially by Vladimir Petrović and expanded on by Tim Barnum [110]. If the lasers are not copropagating with the mm-waves the possibilities for relative polarizations are more complicated, primarily due to the fact that (in the case of perpendicular relative propagation), one potential polarization state of the laser beams corresponds to the wavevector of the mm-waves, and vice versa. In these cases one may not be able to drive solely the desired Δm for a given experiment.

Finally, the transverse mode structure of the beam spot of both laser beams must be taken into account. Neither laser produces a beam with a TEM_{00} transverse mode, and once the beams have been expanded the asymmetries and dead spots of the beams can make uniform overlap of the beams difficult. Example beam spots for the UV and IR lasers are shown in Figs. 2-10 and 2-11. Spatial filtering can be performed, but presents significant difficulties. The power required to pump to Rydberg states, especially in a coherent population transfer scheme, can be quite large due to the unavoidably large interaction volume. Spatial filtering can reduce the power output of a dye laser by as much as 50%, and the high dye laser pulse energy required can burn

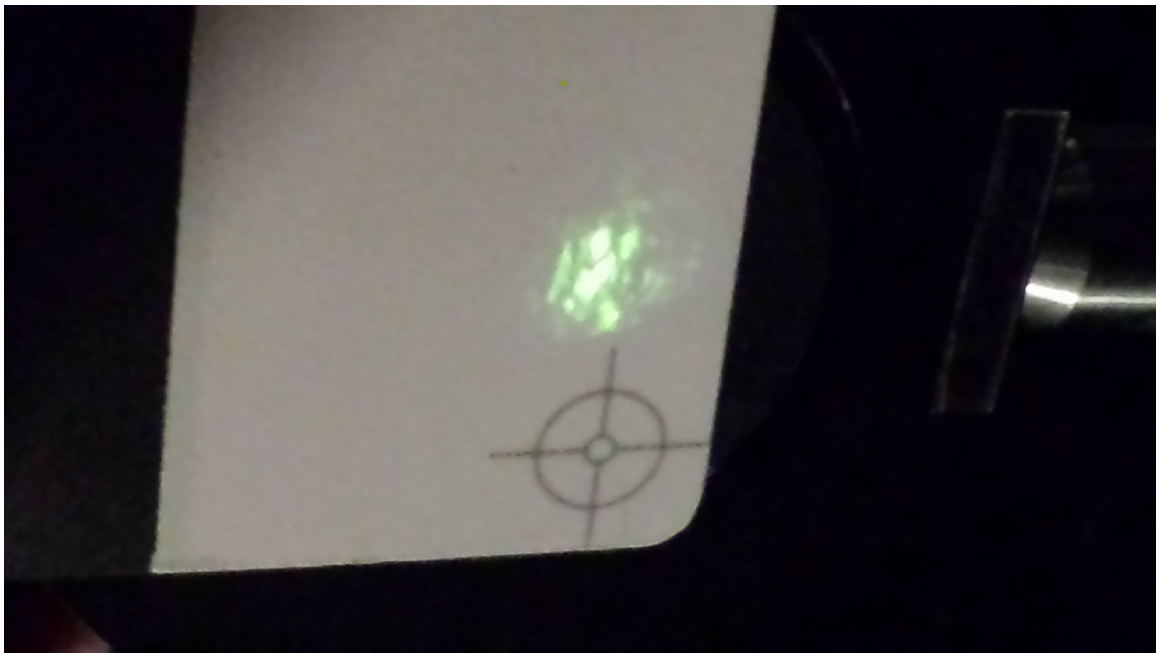

Figure 2-10: Example of the IR beam spot generated by the Scanmate pulsed dye laser.

and destroy the pinholes used for filtering. Pulse amplified cw dye lasers generally have far better spatial properties and do not require additional spatial filtering.

2.3 Chirped-pulse millimeter-wave spectrometers

While laser spectroscopy continues to be the primary technique used in the study of Rydberg states, we choose to use millimeter wave spectroscopy for three related reasons. First, the frequency resolution and accuracy of millimeter wave spectrometers is much higher than those provided by our pulsed dye lasers and the coherence properties of the millimeter wave source is vastly superior to that of pulsed dye lasers. Second, the recent invention of the Chirped-Pulse Fourier-Transform Microwave (CP-FTMW) spectroscopy by Pate and co-workers, and expansion to the millimeter wave regime by our group, provides the ability to scan rapidly broad swathes of frequency space [38, 39, 34, 8, 40]. Third, the exceptionally large electric dipole transition moments for Rydberg-Rydberg transitions allow for a variety of novel experiments that exploit mm-wave radiation, including those described later in this thesis, such as coherent

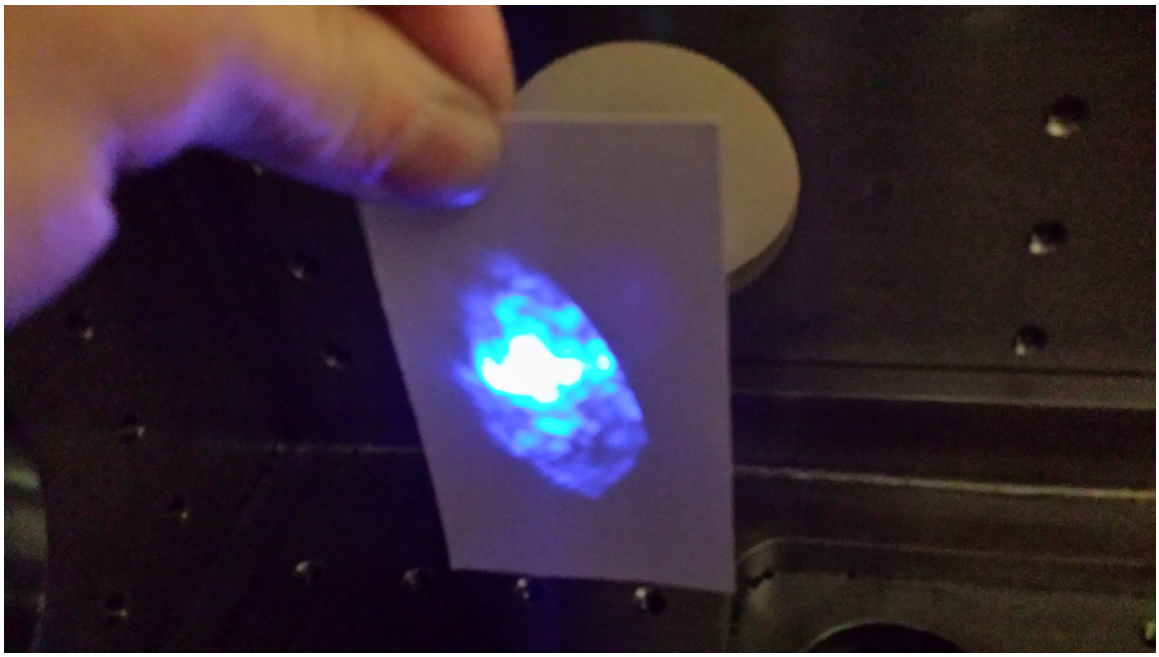

Figure 2-11: Example of the UV beam spot generated by the Sirah pulsed dye laser.

population transfer and investigations of cooperative radiation.

I employed two separate mm-wave spectrometers in the course of this work: a W-band (70 - 100 GHz) system and a THz (260 - 300 GHz) system. Contrary to the common belief that the specific frequency regime does not matter in the Rydberg manifold due to the well-known Rydberg scaling laws, each of these spectrometers has unique strengths and weaknesses when for Rydberg-Rydberg spectroscopy. In this section I first describe the construction of the two spectrometers, then I briefly outline the procedure for careful alignment of the mm-waves through free space. Finally, I discuss the relative advantages and disadvantages of each frequency range.

2.3.1 W-band spectrometer

A schematic of the W-band spectrometer is given in Figure 2-12. The core of the spectrometer is a 4.2 GS/s arbitrary waveform generator (AWG) (vi), clocked by a 4.2 GHz phase-locked oscillator (ii). This AWG generates a user-defined RF pulse with frequency components in the range of 0.2-2.0 GHz. This RF is mixed (vii) with the output of a 6.2 GHz phase-locked oscillator (iii), and band-pass filtered to

select the upper sideband (ix), in order to create a user-defined microwave pulse with frequency components in the range of 6.4-8.2 GHz. This pulse is sent through a variety of microwave filters, isolators, amplifiers, and frequency multipliers (viii, x âĂŞ xviii) described in the next section, with the end result being the same user-defined pulse now at the mm-wave frequencies of 76.8-98.4 GHz. The two active frequency multipliers in the circuit (xiv, xviii) multiply the frequency of the pulse, the bandwidth of the pulse, and the phase of the pulse, providing a 12x larger bandwidth in the mm-wave regime than generated originally in the RF region. This mm-wave pulse is coupled into free space by a 24 dBi (decibel increase over isotropic broadcast) standard rectangular gain horn (xx), collimated, and directed to the molecular beam chamber by either a set of Teflon lenses (xxi) or an off-axis parabolic mirror (not displayed). The remaining input pulse, along with any resultant FID, is refocused through a similar set of Teflon lenses or an identical off-axis parabolic mirror into a standard rectangular gain receiving horn, and mixed with the sextupled (xxvii) output of a microwave frequency synthesizer (iv). The down-converted signal is amplified by a low-noise amplifier (xxix) and directly digitized and averaged on a 12.5 GHz oscilloscope (xxx). All frequency sources used in this spectrometer are locked to the same 10 MHz Rb frequency standard (i). The part list for this spectrometer is given in Yan Zhou's thesis, Sect. 2.3.2, and the specifications in Sect. 2.3.4.

This spectrometer required several optimizations in order to improve its phase stability and decrease its frequency noise. The majority of the isolators and filters in the source arm of the spectrometer (v-xviii) were included to maintain frequency purity before entering the two active multipliers (xiv, xviii). Active multipliers function fundamentally as amplified mixers, so if even a weak sideband is present (10-20 dB below the main frequency in power), it will be amplified and mixed with the fundamental frequency at each step, leading to numerous unwanted side bands in the final output.

In order to avoid this, the output of the AWG was first filtered with a 2.2 GHz low pass filter (v) in order to remove the Nyquist frequency ($f_{samplerate} - f_{RF}$) and higher harmonics. Spurious frequencies could be introduced in the triple-balanced

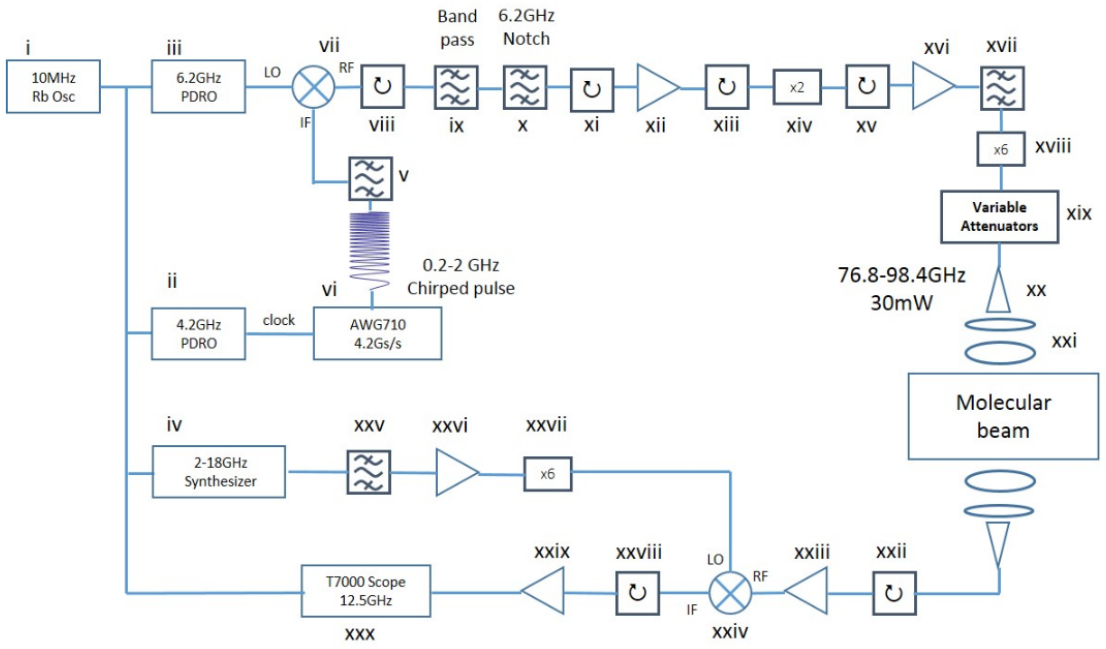

Figure 2-12: Schematic diagram of the W-band millimeter-wave spectrometer.

mixer (vii) as the result of leakage of either non-mixed LO or IF frequencies. As the IF was broadband and difficult to filter effectively, while the LO was a single known frequency, we opted to oversaturate the LO power input to the mixer so that the spurious transmitted frequency was almost entirely 6.2 GHz, and then used a custom 6.2 GHz notch filter (x) to remove the excess LO frequency.

RF and mm-wave reflections at coaxial connections can be formed by impedance mismatches caused by improperly tightened SMA connectors, or improperly driven active components. Similarly, large angle bends of coaxial cable can stress the internal conductor and cause frequency dependent attenuation and reflection in the cable itself. These reflections can remix with the original RF and microwave frequencies in the mixer (vii) and active multipliers (xiv, xviii), resulting in a complex noise spectrum. Two steps are taken to reduce this noise spectrum. First, significant care is taken when constructing and placing the low frequency components of the spectrometer to prevent excessive torque in either the tightening of the SMA connectors and in the coaxial cables connecting distant components of the experiment. In order to reduce coaxial noise and attenuation, the majority of the RF and microwave components

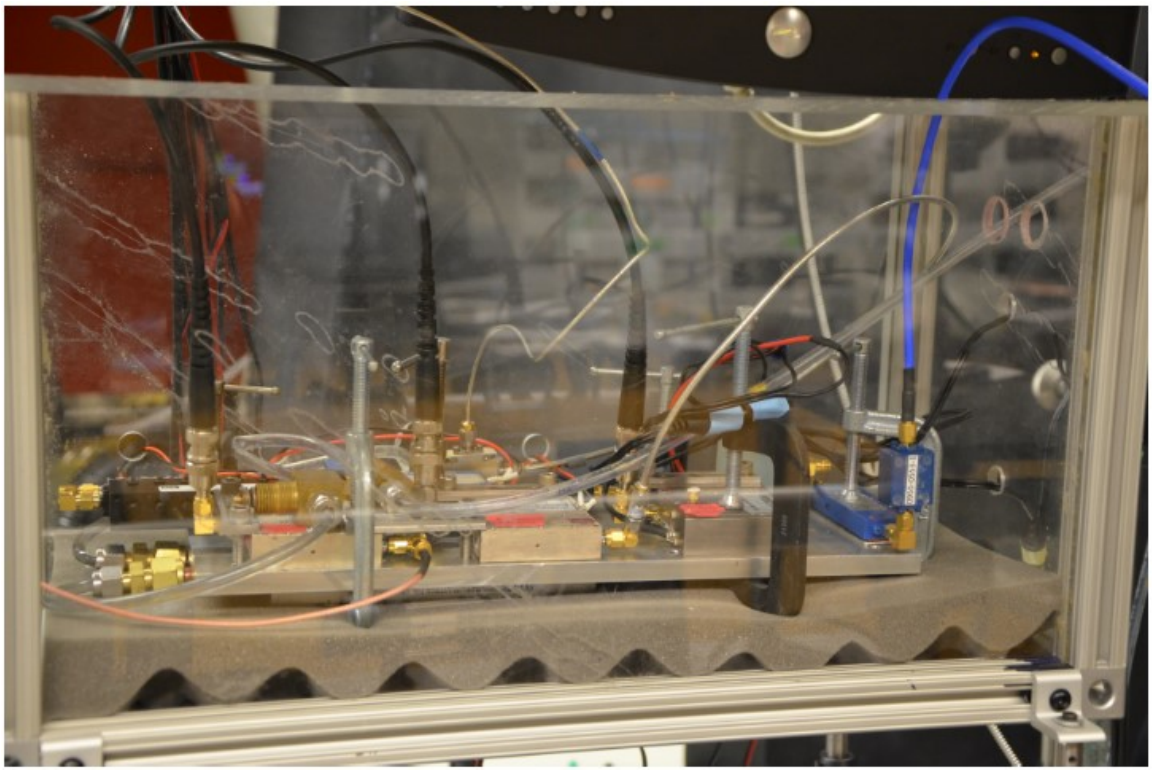

Figure 2-13: Photograph of the low-frequency components of the W-band spectrometer.

(ii, iii, v, vii-xvii) are placed in the same area and connected by small solid state SMA male-male connectors, as all of the components are connectorized with SMA female inputs and outputs. Second, numerous isolators (viii, xi, xiii, xv, xxii, xxviii) are installed before and after any active components, to prevent reflections due to impedance mismatching caused by power supply fluctuations.

The relative stability of the phase locked oscillators with respect to each other is strongly dependent on pressure and temperature, and the efficiency of all active components, such as amplifiers and multipliers (xii, xiv, xvi, xviii, xxvii, xxiii, xxix) depends strongly on temperature. Without active cooling, these components are all subject to the varying ambient temperature and pressure. In order to reduce these effects, we actively cool each component to 12 °C with a chilled water circulator. Additionally, the majority of the RF and microwave components (ii, iii, v, vii-xvii) are housed in an unsealed plastic case in order to minimize pressure fluctuations, as seen in Fig. 2-13.

2.3.2 High-frequency spectrometer

The high frequency spectrometer operates on principles to very similar to those of the W-band spectrometer. A schematic of the high frequency spectrometer is given in Figure 2-14. The core of this spectrometer is a 12 GS/s AWG (ii) clocked directly by the 10 MHz Rb frequency standard (i). This AWG produces a user-defined RF pulse with frequency components ranging from 2.0 - 3.5 GHz, as well as a single frequency LO signal in the same frequency range. The RF pulse is mixed (iii) with the output of an 8.8 GHz phase-locked oscillator (vii) and bandpass filtered (v) to select the upper sideband, thus producing a user-defined 10.8 - 12.3 GHz microwave pulse. This microwave pulse is filtered (viii), amplified (ix), and isolated (x) before being fed into an x24 active multiplier chain (xi) to produce a user-defined 260-300 GHz pulse. This high frequency pulse is again coupled into free space using a 24 dBi standard rectangular gain horn, and collimated into the detection chamber using an off-axis parabolic mirror. After interacting with the sample, the remaining radiation and any resultant FID is focused with a series of Teflon lenses into a receiving standard rectangular gain horn. The LO signal from the AWG is mixed (iv) with the output of the same 8.8 GHz phase-locked oscillator, similarly filtered (xiii), amplified (xiv), and isolated (xv), before being fed into an x12 active multiplier (xvi) and used as the LO in a subharmonic mixer (xvii) to down-convert the captured signal and the FID. The RF output of this subharmonic mixer is then sent through a low-noise amplifier (xix) before being read out directly on a 50 GS/s, 20 GHz oscilloscope. The part list for this spectrometer is as follows:

(i) 10 MHz Rubidium frequency standard (Stanford Research Systems FS725)

(ii) 12 GS/s arbitrary waveform generator (Agilent M8190A)

(iii) Triple-balanced mixer (MITEQ M/N-DM0416LW2)

(iv) Triple-balanced mixer (MITEQ M/N-DM0416LW2)

(v) Band-pass filter (Lorch 7CF7-8800/A150-S)

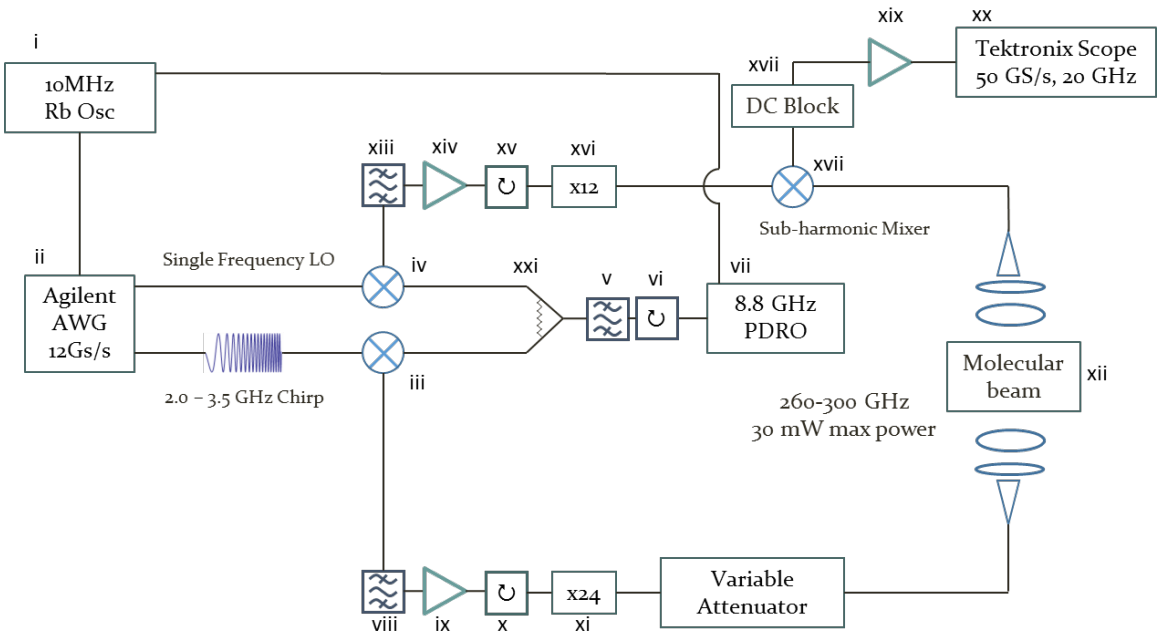

Figure 2-14: Schematic diagram of the high-frequency millimeter-wave spectrometer.

(vi) Isolator (Unknown)

(vii) 8.8 GHz phase-locked dielectric resonator oscillator (Microwave Dynamics PLO-4000-08.80)

(viii) Band-pass filter (Lorch 13EZ5-11450/A1500-S)

(ix) Power amplifier (WT ASG-183020)

(x) Isolator (Ditom DM16018)

(xi) Active multiplier chain x24 (Virginia Diodes AMC291)

(xii) 24 dBi, W-band standard rectangular gain horn (Millitech)

(xiii) Band-pass filter (Lorch 13EZ5-11450/A1500-S)

(xiv) Power amplifier (WT ASG-183020)

(xv) Isolator (Ditom DM16018)

(xvi) Active multiplier chain x12 (Virginia Diodes MixAMC156)

(xvii) Subharmonic mixer (Virginia Diodes MixAMC156)

(xviii) DC Block (Pasternack PE8250)

(xix) Low-noise amplifier (MITEQ AMF-70-00101800-24-10P)

(xx) 50 GS/s, 20 GHz high-speed oscilloscope (Tektronix DPO72004)

(xxi) Power divider (SERNO-0176 292481P1)

This spectrometer required a different set of optimizations than the W-band spectrometer, although the fundamental philosophy and goals (minimize phase and frequency noise) were the same. The frequency purity requirements for the x24 and x12 active multiplier chains were much more stringent than those of the x2 and x6 active multiplier chains used in the W-band experiment. As such, the frequency purity achieved through a combination of filters and isolators as in the W-band spectrometer was insufficient. The Agilent (now rebranded as Keysight Technologies) AWG (ii), at the time of purchase, had the best specifications for frequency purity (-60 dBc [decibels relative to the carrier frequency]) and was therefore chosen to be used as the central AWG. Further, the Agilent AWG was supplied with two output channels, allowing both the chirp and the LO to be generated by the same instrument, which eliminates the need for a separate synthesizer.

Since the AWG provided an RF pulse with superb frequency purity characteristics in the range of 2.0 - 3.5 GHz (far from DC), we were able to perform the same trick of overdriving the triple-balanced mixer (iii) with the output of the 8.8 GHz phase-locked oscillator (vii), and filter to isolate both the lower sideband and the residual LO frequency with the same band-pass filter (viii). The remaining frequency noise was dealt with by installing an isolator between the power amplifier (ix) and the x24 active multiplier chain (xi).

The high-frequency spectrometer requires the same physical constraints as the W-band spectrometer, therefore all of the RF and microwave components (iii-x, xiii-xv) are kept in the same location, connected with SMA male-male connectors and coupled to the active multiplier chains (xi, xvi) with highly shielded, kink-free coaxial cables.

All active components (vii, ix, xiv, xix) are actively cooled to 12 °C with a chilled water circulator, aside from the active multipliers which are supplied with their own built-in forced air cooling systems.

The use of a single AWG to generate the signal and LO, and a single 8.8 GHz phase-locked oscillator to mix with both the signal and the LO eliminates a large portion of the phase noise in the experiment. In the W-band spectrometer, the majority of the phase noise comes from uncorrelated phase fluctuations between the three frequency sources (6.2 GHz phase-locked oscillator, 4.2 GHz phase-locked oscillator, and 2-18 GHz frequency synthesizer) despite synchronization by the common fundamental 10 MHz clock. In the high-frequency spectrometer, all fluctuations in the signal channel are exactly reproduced in the LO channel, because they are both generated from the same AWG, and mixed with the same 8.8 GHz phase-locked oscillator. To prove this, the system can be run unlocked from the 10 MHz Rb standard and observed to still possess satisfactory (although not as great) phase stability, whereas the W-band system becomes completely unlocked. Hence, we cool the 8.8 GHz phase-locked oscillator to prevent damage to the oscillator, not to maintain phase coherence, and do not use a plastic case to minimize pressure fluctuations, as that has been found to be unnecessary.

The two active multiplier chains require at least 10 dBm each of input power to generate the necessary high harmonics. The currently used power amplifiers in the system are the minimum required to supply this level of power to the active multiplier chains, and limit the addition of more components to the circuit. If higher levels of frequency purity or phase stability are required, in addition to components to stabilize the frequency and phase, it will be necessary to replace the power amplifiers by more powerful models.

The specifications of the high-frequency spectrometer are similar those of the W-band spectrometer. The output power of the spectrometer can be measured by a calibrated Virginia Diodes thermal power detector. The maximum output power of the spectrometer is 30 mW, with minor variations over the output bandwidth; the output power as a function of frequency is given in Fig. 2-15. Despite the manu-

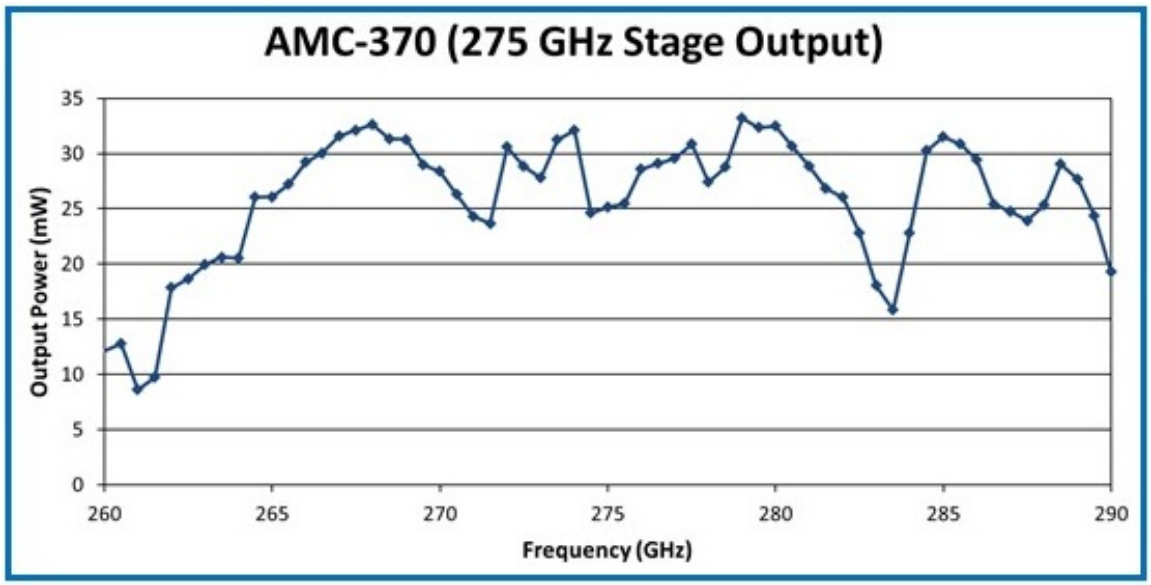

Figure 2-15: Nominal power output of high-frequency spectrometer as a function of frequency.

facturer provided specifications, the spectrometer will produce power at frequencies greater than 290 GHz, although with a slow decrease in power that becomes more pronounced at frequencies above 300 GHz. Figure 2-16 displays the detected power in a full bandwidth 1 μs 260-300 GHz chirp averaged 1000 times. The apparent gap at the center of the chirp is where the chirp passes through the LO frequency, and the detected frequency passes through DC. Note that the low-noise amplifier has an 18 GHz bandwidth, so the frequencies on the edges of the chirp (260-262 GHz, 298-300 GHz) are additionally attenuated. The typical detection sensitivity of the spectrometer (S:N $>$ 3 in 5000 averages) is $\sim$10 nW, although sensitivity for signals near the edges of the band ($\sim$260-265 GHz, 292-300 GHz) is poorer, typically $\sim$50-100 nW.

While most of the fluctuations observed in Fig. 2-16 are due to the frequency dependent output and detection sensitivity of the spectrometer, there are additional variations caused by standing waves and unintentional etalons formed between focusing and collimating elements in the system. In order to reduce the effects of these, the Teflon focusing lenses are rotated slightly away from perpendicular to the propagation direction of the mm-waves. The remaining sources of unintentional cavities come from the windows on the chamber (one UV-quartz, one Teflon) and the broad-

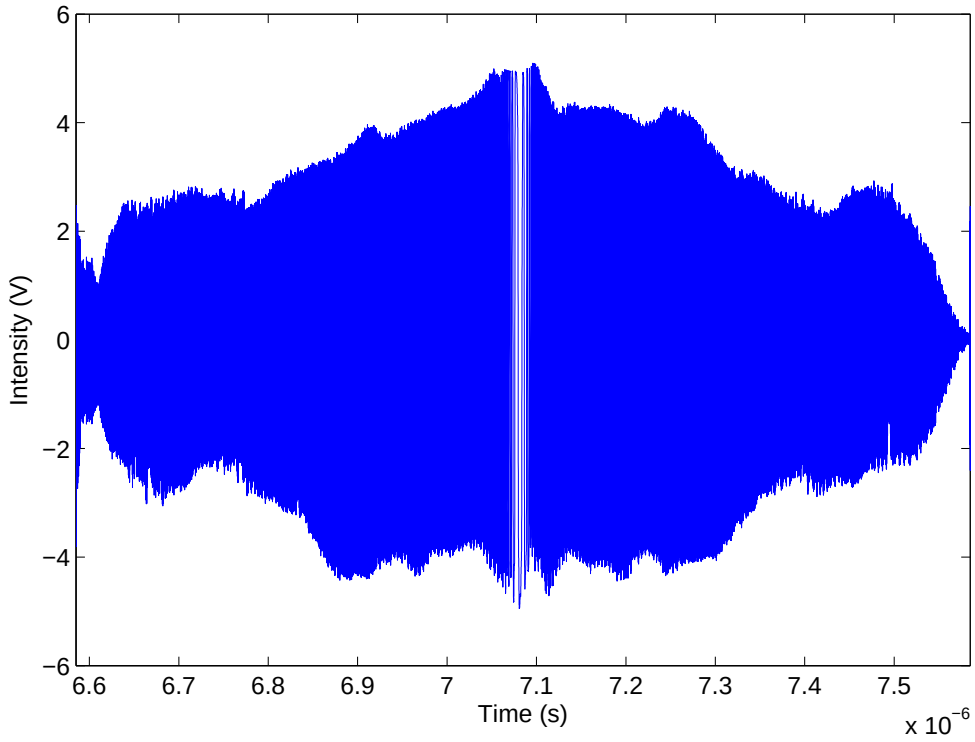

Figure 2-16: Example of a full bandwidth chirp produced in the high-frequency spectrometer.

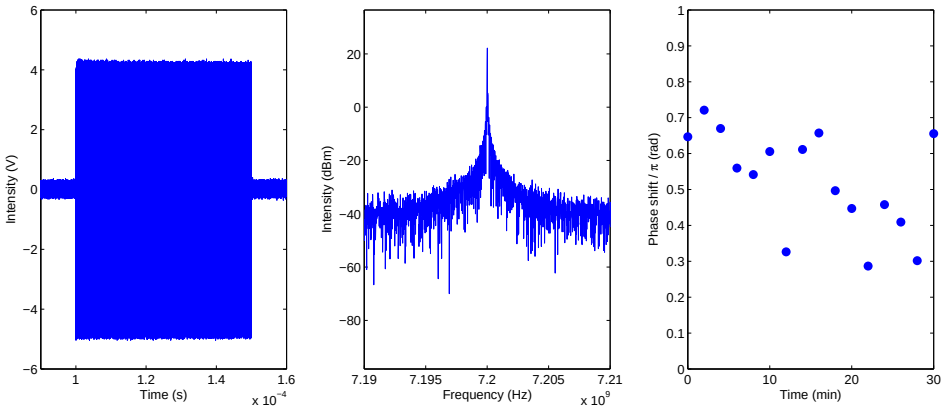

Figure 2-17: Example of a single frequency pulse produced in the high-frequency spectrometer.

cast horns themselves. The effects of these two sources of cavities can be separated by slightly shifting the position of the receiving or broadcast horn and noting how the cavity fluctuations in the spectrum change. In the current setup, the primary source of standing waves is the broadcast horns themselves, and these horns produce broad modulations typically on the order of no more than $\sim 30\%$. This corresponds to a cavity of length 90 cm, free spectral range of $\sim$150 MHz, and a quality factor $Q < 1$.

To evaluate the frequency purity and phase noise associated with the spectrometer, Fig. 2-17a shows the time domain trace of a 1 μs pulse at 280 GHz, and Fig. 2-17b shows the frequency-domain power spectrum of the same pulse. The FWHM of the frequency is $\sim$ 20 kHz, consistent with a Fourier-transform-limited pulse of 50 μs. Figure 2-17c shows the overall phase shift of the output power that occurs in observations over one hour, which defines the achieved long-term phase stability, and shows that over the course of half an hour, the phase does not shift by more than $\sim 0.2\pi$ in either direction.

While the W-band spectrometer can be outfitted with a voltage controlled attenuator (VCA) to produce user-selected amplitude modulations with a rise time of 10 ns, broadband VCAs in the 260-300 GHz region are not currently commercially available. Therefore, in order to perform high-speed attenuation, either to smooth a pulse shape over 10s of ns, or to attenuate one pulse of a pulse sequence with respect to another,

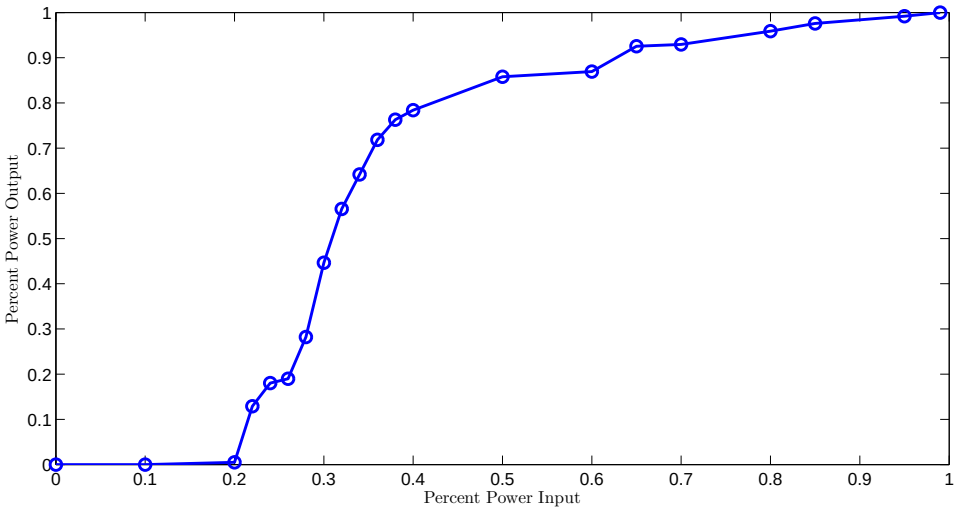

Figure 2-18: Variation of high-frequency spectrometer output power as a function of AWG input power.

we must modulate the output amplitude of the AWG. This is made complicated by the numerous stages of amplification and multiplication that make up the spectrometer. Fig. 2-18 shows the output power of the spectrometer at 282 GHz as a function of AWG generated power. This curve is, in general, extremely frequency dependent and must be measured at the exact frequency that is to be amplitude-modulated. However, the broad features of the curve, no signal until a requisite input power is met followed by a sharp turn on with a long tail to full power, are the same across all frequencies.

The complete laser-CPmmW setup is shown in Fig. 2-7. The millimeter wave radiation from the source arm is both collimated by and reflected from a 30 cm off-axis parabolic mirror through the chamber before being collimated by a 10 cm Teflon lens and input into the receiving arm. The active volume is determined by the overlap of the laser and mm-wave radiation and the atomic beam. The mm-wave radiation determines two dimensions of the overlap region, as it is collimated to a $\sim$1.5 cm beam diameter through the detection chamber. The divergence of an atomic beam of barium is calculated using the relationship given in Hutzler et al [52]:

$$\Delta\theta \approx 2\sqrt{\frac{m_b}{m_a}} = 43.6\,\mathrm{deg} \tag{2.51}$$

Using the width of the cold skimmer as a reference point, we calculate that the atomic beam has diverged to ∼15 cm diameter in the detection region, leading to an active volume of $1.5 \times 1.5 \times 15 \approx 30$ cm^3.

The alignment of the millimeter waves both through the chamber and to overlap with the laser beams is a nontrivial process, and proper alignment is essential to obtain high quality spectra. In order to align the millimeter waves through the chamber with as high transmission as possible, the following procedure should be followed.

1. The components should be set up in roughly their correct positions. Any collimation or reflection optics should take into account that given the relatively long wavelength of millimeter waves as compared to lasers, millimeter waves are better described as propagating following Gaussian optics instead of ray optics. As such, the horns should be $2\sum f$ apart from each other, where the fs are the focal lengths of all collimating optics in the system. For example, the current system has a 30 cm off-axis parabolic mirror and a 10 cm lens, thus the horns should be placed 80 cm apart. Due to geometric constraints of the chamber, it is currently impossible to perfectly match the horn distance to the optics included, and they are instead 90 cm apart.

2. The source horn should broadcast a full power CW signal, and the receiving horn should be attached to a calibrated power detector in the same location where the down-conversion arm will eventually be located. Carefully adjust the position of the source horn and all collimating optics to maximize power transmission through the system. This can end up being as high as 90% transmitted power. If using an off-axis parabolic mirror with a hole for laser propagation, the modal structure of the millimeter waves may be disrupted, leading to an apparent loss due to poor impedance matching to the detection waveguide. As such, the measured value may be as much as an order of magnitude smaller than the actual value. To compare, replace the mirror with a smooth, hole-less mirror

for alignment before inserting the actual mirror for experiments.

3. In order to locate the active volume in the chamber, and ensure intersection with the atomic beam, one can image the beam by using a large iris and the same power detector setup as in Step 2. The large iris should be placed in the path of the millimeter-wave radiation with a small aperture ($\sim$1 cm diameter). The location of the millimeter-wave radiation can be determined by finding the iris position where the transmission is maximized, while the beam waist of the millimeter-wave radiation can be determined by adjusting the aperture of the iris. The vertical position of the millimeter wave radiation should be aligned with the axis of the atomic beam expansion in order to ensure signal.

4. All lasers should be aligned through the chamber at this stage to ensure overlap with the millimeter waves. A standard alignment procedure can be used, using the hole in the center of the off-axis parabolic mirror and the iris from Step 3 to determine of the propagation axis of the millimeter waves. It is also recommended to choose the focal length of the laser focusing lens to match the diameter of the millimeter waves near the entrance to the chamber.

5. If you can now observe FID, fine adjustment of the alignment should be performed iteratively and empirically using the FID signal strength as a guide. Note that as the alignment becomes better, collective effects may begin to come into play, leading to unexpected frequency modifications. Hence, these adjustments should be performed at relatively low laser powers to avoid creating cooperatively interacting samples.

2.3.3 Comparison of W-band and high-frequency spectrometers

Despite the strict quantum number scaling laws of Rydberg states and the similarities that Rydberg states have to each other over their energy range, there are distinct advantages and disadvantages to choosing to use the W-band spectrometer over the

	Advantages	Disadvantages
W-Band Spectrometer	• Larger accessible electric transition dipole moments • Chirp covers entire n^* to n^*+1 region • Access to more of the common stroboscopic resonances in molecules	• Requires advanced lasers to routinely access Rydberg states involved • Higher sensitivity to collective effects
High-Frequency Spectrometer	• Larger accessible laser transition dipole moments • Shorter wavelength leads to weaker collective effects for high resolution spectroscopy	• Lack of high speed hardware (e.g. VCA) • Higher sensitivity to blackbody radiation

Table 2.2: Comparisons of the W-band and high-frequency spectrometers.

high-frequency spectrometer, and vice versa. These advantages and disadvantages are laid out briefly in Table 2.3.3, and discussed below.

The W-band spectrometer drives transitions with $\Delta n^* \approx 1$ when $n^* \approx 44$, and can drive specific transitions with $\Delta n^* < 1$ down to $n^* \approx 30$, depending on the details of the quantum defects of a given system. The high-frequency spectrometer drives transitions with $\Delta n^* \approx 1$ when $n^* \approx 28$, and can drive specific transitions with $\Delta n^* < 1$ down to $n^* \approx 25$. Both spectrometers can drive transitions with $\Delta n^* > 1$ at a variety of principal quantum numbers, although the transition dipole moments for those transitions decrease rapidly as Δn^* increases.

The electric dipole transition moment for a $\Delta n^* = 1$ transitions scales like n^{*2} for Rydberg states, which means that the millimeter-wave electric dipole transition moments accessible to the W-band spectrometer are much larger than those to the

high-frequency spectrometer. In general, the 30 mW of power available in both bands is sufficient to easily polarize these transitions and perform most experiments. However, $\Delta n^* \geq 2$ transitions have significantly smaller transition dipole moments, scaling roughly as $(\Delta n^*)^{-2}$. The available power in the W-band allows easy polarization of up to $\Delta n^* \sim 3$, while the power available in the high-frequency band only reaches $\Delta n^* \sim 2$.

Larger transition moments allow for larger absolute signal strengths and greater coherent control, but also a greater susceptibility to collective and cooperative effects (which is itself a bonus if those effects are the goal of the experiment). The density of Rydberg states therefore requires significantly more control in W-band experiments than in high-frequency experiments.

Blackbody radiation becomes a less important factor at large n^* values due to the n^{*-3} scaling of the frequency for $\Delta n^* = 1$ transitions. In the high temperature limit, blackbody radiation can directly dephase a transition at a rate

$$\gamma_{bb,1} = \frac{4\pi k_B T}{3\epsilon_0 c^3} \left(\frac{\mu\nu}{\hbar}\right)^2 \tag{2.52}$$

where μ is the electric dipole transition moment for the transition and ν is the transition frequency. Blackbody radiation can also drain population away from either the group or excited state of a transition at a rate

$$\gamma_{bb,2} = \frac{4\alpha^3 k_B T}{3\hbar n^{*2}} \tag{2.53}$$

where α is the fine structure constant. To avoid double counting, we can estimate the total blackbody dephasing as

$$\gamma_{bb} = 2\gamma_{bb,2} - \gamma_{bb,1} \tag{2.54}$$

Both terms scale as n^{*-2}, and rapidly become smaller as n^* increases. If the experiment were to take place inside a cooled vacuum shield at liquid He temperatures (4K), however, then the high-frequency spectrometer would become competitive as the peak of the blackbody spectrum scales like $\nu_{max} = 58.8/\text{T GHz/K}$, thus the

blackbody radiation would be at too low frequency to interact with the 300 GHz transitions associated with the high-frequency spectrometer.

The optical electric dipole transition moment for transferring population from a low-lying or ground state to a Rydberg state scales as n^{*-2}, so populating the lower n^* states required for the high-frequency spectrometer requires less laser power. Additionally, the Doppler width of these laser transitions in our buffer gas cooled atomic beam is generally $\sim$100 MHz, narrower than the spacing between longitudinal cavity modes in our pulsed dye lasers. This means that it is possible to jump accidentally over a transition because the cavity modes lase only on opposite sides of the transition, with no fluence at the actual transition wavelength. The easiest way to avoid this is to power broaden the transitions to Rydberg states to a width of several hundred MHz. This requires less power when exciting to levels at lower n^*. As a point of reference, it requires $\sim$1 mJ of pulse energy to broaden the 4s5p-4s30d transition in Ca to an acceptable level. Pulse amplified dye lasers are both narrower and more precise in their continuously scannable frequencies, thus can avoid this problem entirely.

The transition wavelength between two adjacent-n^* Rydberg states scales as n^{*-3}, thus at higher values of n^* the same bandwidth covers a larger relative fraction of the spectrum. For example, a 40 GHz bandwidth chirp (260 - 300 GHz) allows interrogation of all transitions with $\Delta n^* = 0.91 - 1.05$ at $n^* = 30$, while a smaller bandwidth chirp (70 - 100 GHz) allows interrogation of all transitions with $\Delta n^* = 0.93 - 1.35$ at $n^* = 44$. Table 2.3.3 shows the allowable transitions in a 30 GHz bandwidth centered at 285 GHz and 85 GHz. A transition with $\Delta n^* = 1$ can only be observed from the $n^* = 28$ state when using the high frequency spectrometer, while it can be observed from any state with $40 \leq n^* \leq 44$ with the W-Band spectrometer. As such, reliably being able to observe transitions even from two adjacent n^* states with the high frequency spectrometer is not possible. This is shown schematically in Fig. 2-19.

The ability to observe transitions with similar Δn^* at adjacent principle quantum number is important for two reasons. First, assignment of molecular spectra relies on observing the same transitions from different n^* in order to obtain high-precision

n^* (High-Freq)	Range of Δn^*	n^* (W-band)	Range of Δn^*
26	0.72 - 0.84	40	0.70 - 1.01
27	0.81 - 0.94	41	0.75 - 1.08
28	0.91 - 1.05	42	0.81 - 1.17
29	1.01 - 1.18	43	0.87 - 1.26
30	1.13 - 1.31	44	0.93 - 1.35

Table 2.3: Ranges of Δn^* accessible by the W-band and high-frequency spectrometers at different n^*

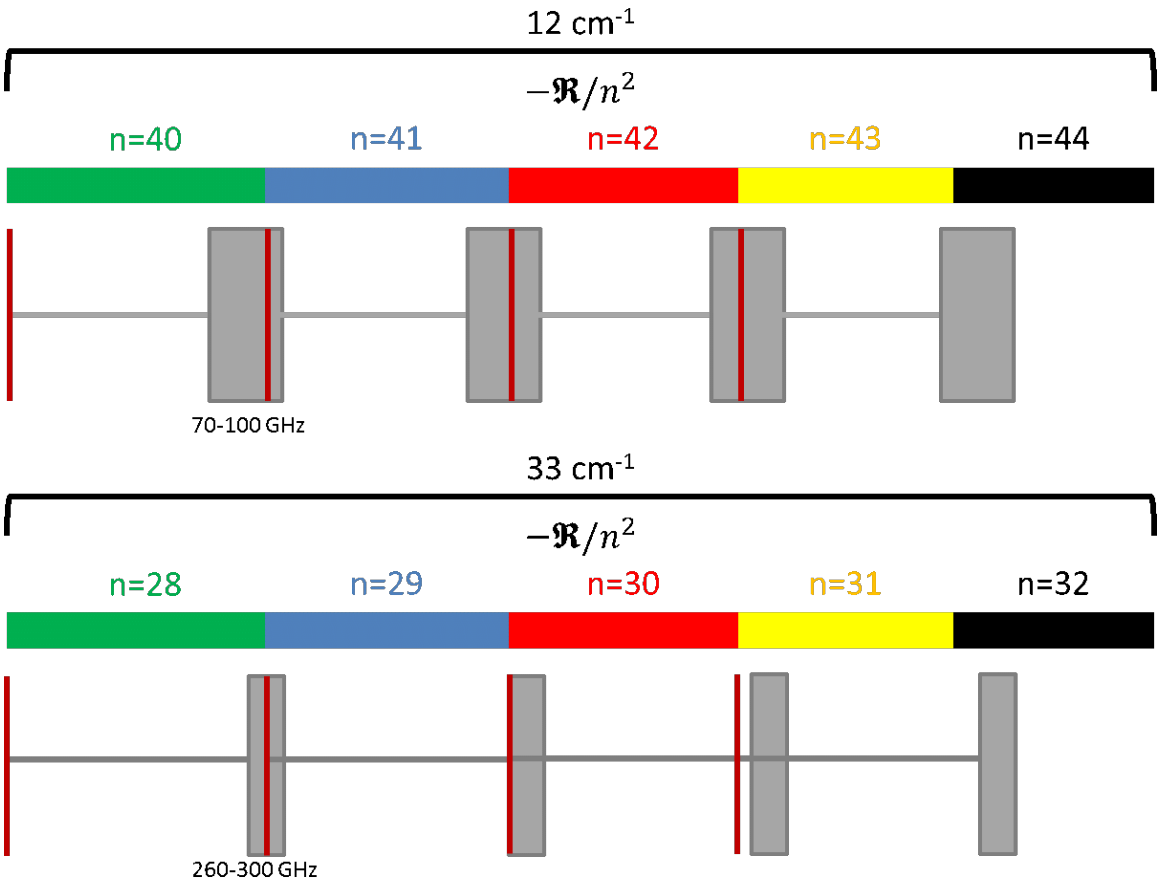

Figure 2-19: Schematic diagram of the dependence of Δn^* coverage of the W-band and high-frequency spectrometers.

values of the state energies. Transitions observed from a single initial n^* are limited by the uncertainty in the laser energy, while those observed from several initial n^* can be related to each other in order to determine their relative energies with mm-wave precision. Second, the determination the core electric multipolar moments and polarizabilities of molecules as laid out by Jeff Kay is greatly simplified by observing transitions with similar Δn^* at adjacent principle quantum numbers [82]. In particular, due to the scaling of effective Hamiltonian parameters with n^* and ℓ, one must either observe transitions with several different ℓ at a single n^*, or transitions at a single ℓ at several different n^*.

One disadvantage to the high-frequency spectrometer that may be solved simply as a matter of time is the lack of high speed, broadband hardware for controlling the millimeter-wave radiation. In particular, the lack of a high speed VCA across the band makes certain pulse sequence experiments far more complicated with the high-frequency spectrometer than with the W-band spectrometer.

Chapter 3

Superradiance Theory

In this chapter I discuss the theory of cooperative radiative effects, in particular the phenomena of superradiance and subradiance. In Section 3.1 I provide a brief introduction to the concepts essential to superradiance, a proof that much of superradiance is described by classical electrodynamics, and a review of Dicke superradiance, which is the simplest quantum mechanical model of superradiance. In Section 3.2 I derive a semi-classical model of superradiance using the Bloch-Maxwell equations and a Bloch-angle representation. In Section 3.3 I describe a fully quantum model of superradiance, as formulated in both the Schrödinger and Heisenberg representations, as well as in a master equation model.

3.1 An introduction to superradiance

Superradiance is fundamentally the modification of the emission properties of a particle by neighboring particles [117, 118, 119, 1, 120]. Intuitively, one particle emitting a photon (either through spontaneous or stimulated emission) is seen in a phase coherent manner by a neighbor, which then releases a photon through stimulated emission. This coherence is created first in a small volume and propagates through the entire system by radiative coupling. Coherence that is built up in this way is called "cooperative".

In contrast to the familiar monotonic exponential decay with lifetime τ associated

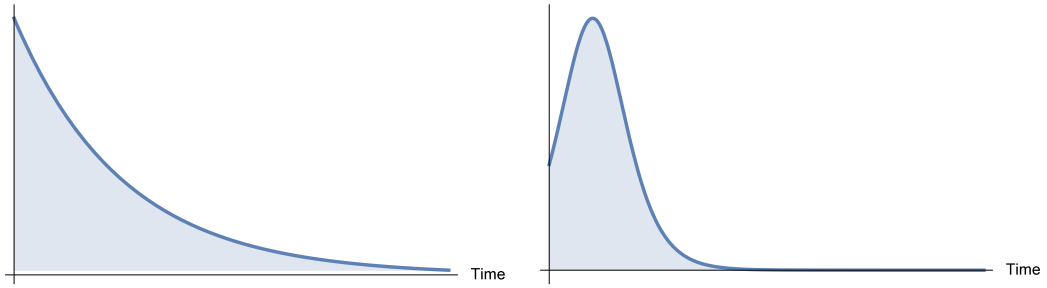

Figure 3-1: The left plot displays the typical emission behavior of a *dilute* ensemble of emitters. The right plot displays the typical superradiant emission behavior of a *dense* ensemble of emitters.

with fluorescent emission of incoherent radiation from dilute samples, the superradiant emission from dense samples is manifest as a short, intense *burst* of coherent radiation. This distinction is shown schematically in Figure 3-1. This coherent burst of radiation, which scales in intensity as N^2 and in lifetime as N^{-1}, where N is the number of emitters, is a characteristic feature of superradiance [1].

The phenomenon of superradiance is often described as a mirror-less laser, and many of the approaches describing superradiance are grounded in laser physics [121, 122, 123, 124, 118, 119, 125, 126, 127, 128, 1]. In some respects, superradiance is a simpler phenomenon to analyze than lasing, because the only parameters that need to be considered are the evolution of the superradiant medium and its own generated electric field. However, a detailed analysis of superradiance requires a complex blend of concepts from quantum electrodynamics, non-linear optics, and many-body problems[1].

An additional collective effect is subradiance. Whereas, in superradiance emitters *constructively* interfere with each other to produce a coherent burst of radiation, in subradiance emitters *destructively* interfere with each other and emit on timescales much longer than the fluorescence lifetime of dilute particles [129, 130, 131, 132, 133, 93, 134, 135]. Subradiance is theoretically derived in a similar manner to superradiance, although it is much more difficult to provably observe experimentally [136, 137, 138, 139].

In order to develop the theory needed to describe the experiments presented in

Chapter 4, I first demonstrate how much of the superradiant phenomenon occurs in a classical two-particle system in Section 3.1.1. In Section 3.1.2, I introduce Dicke superradiance for a many-particle system and use a two-particle system to demonstrate the points of equivalence with the classical results. In Section 3.1.3, I briefly introduce the concepts of non-fully symmetric quantum mechanical states and subradiance.

3.1.1 Superradiance in classical electrodynamics

The importance of collective decay in classical electrodynamics has not been widely appreciated. In approaching the calculations, I follow the general outline presented by Berman [140]. To illustrate the fundamental phenomenon, I consider a pair of dipole oscillators with the same radiative lifetime and resonance frequency and separated by a distance R_{12}, as shown in Figure 3-2. At time $t = 0$, both oscillators are impulsively excited, with potentially different initial speeds. The phase of each excitation impulse may also be different, but for simplicity, I assume the phases to be identical. The behavior of each dipole can be described as a damped oscillator

$$\ddot{z}_i + 2\gamma\dot{z}_i + \omega^2 z_i = 0 \tag{3.1}$$

$$z_i(0) = 0, \dot{z}_i(0) = v_i, \tag{3.2}$$

where $i = 1, 2$ denotes each individual oscillator, $z_i(t)$ is the displacement of the i^{th} oscillator, γ is the radiative decay rate of an isolated oscillator, ω is the resonant frequency of both oscillators, $\omega \gg \gamma$, and v_i is the initial speed of the i^{th} oscillator. For a single oscillator, γ can be determined classically to be

$$\gamma = \frac{1}{3}\frac{q^2\omega^2}{4\pi\epsilon_0 mc^3}. \tag{3.3}$$

where q is the effective charge of both oscillators and m is the effective mass of both oscillators, and both q and m are only important as they provide a means of calculating γ. The solution for z_i can be written as the product of an oscillating field

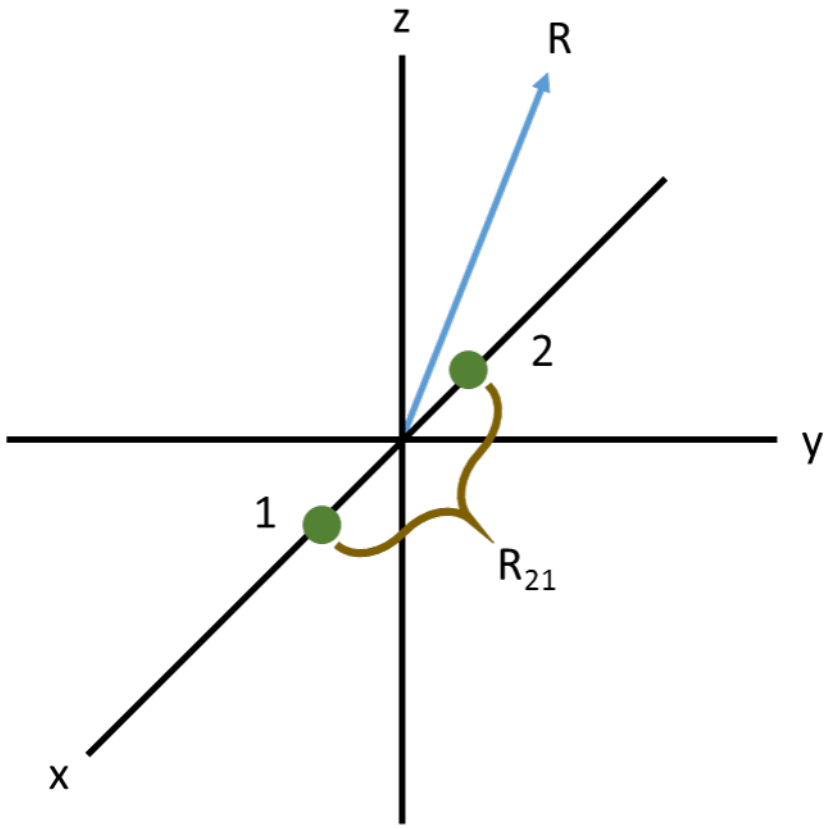

Figure 3-2: Schematic diagram of a pair of classical dipoles, 1 and 2, separated by a distance R_{21}.

and an envelope function A_i:

$$z_i = A_i(t)e^{-i\omega t} \tag{3.4}$$

$$\dot{A}_i = -\gamma A_i \rightarrow A_i(t) = \frac{iv_i}{2\omega}e^{-\gamma t}. \tag{3.5}$$

The initial total energy of these two individual oscillators is the kinetic energy $W_0 = 1/2\ m\,(v_1^2 + v_2^2)$. The final emitted energy of the two individual oscillators can be obtained by integrating the radiated power over solid angle and time

$$W_f = \int dt \int R^2 d\Omega \langle \vec{S} \rangle \cdot \hat{R} \approx W_0 \left(1 + \frac{3\beta \sin\xi}{2\xi}\right) \tag{3.6}$$

where $\langle \vec{S} \rangle$ is the time-averaged Poynting vector, R is the distance between the center of coordinate system and an observation point in a direction $\hat{R}$ and is defined graphically in Figure 3-2, $\xi = kR_{21}$ (with k the wavevector of the radiation ω/c and R_{21} the dsitance between the two dipoles) is the dimensionless distance between the two oscillators and the result is expressed to first order in ξ^{-1}, and $\beta = \frac{2v_1v_2}{v_1^2+v_2^2}$.

In general, $\frac{3\beta\sin\xi}{2\xi} \neq 0$, so the radiated energy is not equal to the initial energy, which leads to a violation of energy conservation. In order to satisfy energy conservation, I introduce a cooperative decay term $\gamma_{12}(\xi)$ that accounts for the modification of the decay of each oscillator produced by the field of the other oscillator. This coupling modifies Equation 3.5 to yield the coupled differential equations

$$\dot{A}_1 = -\gamma A_1 - \gamma_{12}(\xi)A_2 \tag{3.7}$$

$$\dot{A}_2 = -\gamma A_2 - \gamma_{12}(\xi)A_1 \tag{3.8}$$

$$\gamma_{12}(\xi) = \gamma \frac{3e^{i\xi}}{2i\xi}\left(1 + \frac{i}{\xi} - \frac{1}{\xi^2}\right), \tag{3.9}$$

where $\gamma_{12}(\xi)$ can be derived analytically from classical electrodynamics for the two-

particle case. This derivation is beyond the scope of this thesis. The solution to these differential equations is

$$A_1(t) = e^{-\gamma t}\left[\frac{iv_1}{2\omega} - \frac{iv_2\gamma_{12}(\xi)t}{2\omega}\right] \tag{3.10}$$

$$A_2(t) = e^{-\gamma t}\left[\frac{iv_2}{2\omega} - \frac{iv_1\gamma_{12}(\xi)t}{2\omega}\right]. \tag{3.11}$$

The modification of the emitted radiation arises entirely from the second term in the brackets, and is time-dependent. When the two oscillators are close to each other ($\xi < 1$), this additional decay rate can be of the same order of magnitude as the natural decay rate. As the distance between the oscillators increases, the value of $\gamma_{12}(\xi)$ oscillates about zero, where positive coupling increases the decay rate and negative coupling decreases the decay rate. This oscillation is due to competing constructive and destructive interference between the two dipoles. The increase in decay rate corresponds to superradiance, while the decrease in decay rate corresponds to subradiance. Thus, both superradiance and subradiance can be reproduced in classical electrodynamics.

When I include these envelope functions in the calculation of the total radiated power, I obtain

$$W_f = \int dt \int R^2 d\Omega \langle \vec{S} \rangle \cdot \hat{R} = W_0 \tag{3.12}$$

as desired. The decay rate of the radiation when the two oscillators are placed at the same position ($\xi = 0$) and orientation can be evaluated as

$$\frac{\partial W_f}{\partial t} = 2\gamma e^{-2\gamma t}(1 - 2\gamma t) \tag{3.13}$$

The effective decay rate of the power for the two oscillators with $\xi = 0$ is approximately 4γ instead of 2γ, matching the expectation of scaling with N, the number of particles, from before.

3.1.2 Dicke superradiance

Both superradiant and subradiant decay are present in classical electrodynamic systems, but the details of the field evolution require quantum mechanics to accurately describe the microscopic behavior of the quantized emitters. I first introduce a general formulation and then I specialize to the two-particle case to demonstrate equivalence to the classical result, loosely following Gross and Haroche [1].

I consider an ensemble of N two-level particles all located at the same position, with an energy separation between the ground, $|g\rangle$, and excited, $|e\rangle$, states of $\hbar\omega_0$. The only interaction between the atoms that I will consider is the electric dipole coupling between them via their own generated electric field. The raising and lowering off-diagonal operators $D_i^{\pm}$ are defined as

$$D_i^+ = |e\rangle \langle g| \tag{3.14}$$

$$D_i^- = |g\rangle \langle e| \tag{3.15}$$

and the diagonal operator $D_{i,3}$ describing the population inversion is defined as

$$D_{i,3} = \frac{1}{2} \left[|e\rangle \langle e| - |g\rangle \langle g| \right] \tag{3.16}$$

where all three operators follow angular momentum commutation rules:

$$\left[D_{i,3}, D_j^{\pm} \right] = \pm \delta_{ij} D_i^{\pm} \tag{3.17}$$

$$\left[D_i^+, D_j^- \right] = 2\delta_{ij} D_{i,3}. \tag{3.18}$$

where δ_{ij} is the standard Kroenecker delta function.

The raising and lowering operators can be used to define the electric dipole operator

$$\mathcal{D}_i = \left(D_i^+ + D_i^-\right) d \tag{3.19}$$

where $d = \langle e| - \mu\mathcal{E}|g\rangle$ is the electric dipole matrix element of the transition (μ is the electric dipole transition moment, $\mathcal{E}$ is the electric field magnitude, and the phases of the eigenstates have been chosen such that d is real). Collective operators can also be defined as the sum over individual atomic operators

$$D^{\pm} = \sum_i D_i^{\pm} \tag{3.20}$$

$$D_3 = \sum_i D_{i,3} \tag{3.21}$$

$$D^2 = \frac{1}{2}\left(D^+D^- + D^-D^+\right) + D_3^2 \tag{3.22}$$

I assume that at time $t = 0$, all of the atoms are instantaneously prepared in the excited state,

$$|\psi(t=0)\rangle = |e, e, e \ldots e\rangle\,, \tag{3.23}$$

and that the atoms are motionless. Since the atoms are assumed to all be located at the same position, I note that the radiation coupling is *symmetric* with respect to the exchange of any two atoms in the system. This assumption follows from the fact that there is no way of discerning from which atom any given photon originated. As such, I can treat the system as identical to a symmetric superposition of N spin-1/2 states. There are $(N+1)$ such states that can be formed by applying the collective lowering operator to the initial state

$$|JM\rangle = \sqrt{\frac{(J+M)!}{N!(J-M)!}}(D^-)^{(J-M)}\,|e, e, e \ldots e\rangle\,, \tag{3.24}$$

where $J = N/2$, and $-J \leq M \leq J$ are analogous to standard angular momentum and projection quantum numbers. This state represents the fully symmetric state

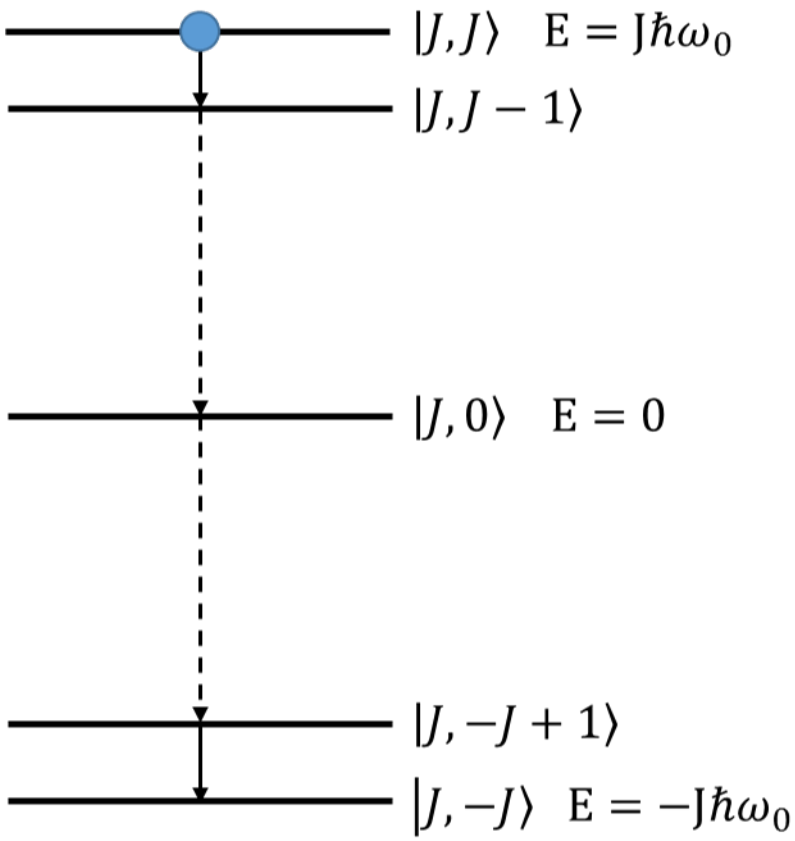

Figure 3-3: Schematic diagram of the fully symmetric levels in N-atom Dicke superradiance. The $|J,J\rangle$ state is initially populated and the population cascades through electric dipole transitions to $|J,-J\rangle$. The energies of the $M = J, 0$, and $-J$ states are indicated.

that contains $(J+M)$ atoms in the upper level and $(J-M)$ atoms in the lower level. The energy of this state is $M\hbar\omega_0$, with the energy of the $M = 0$ state taken as zero. The system therefore is a ladder-type system of evenly separated levels, as shown in Figure 3-3. There are 2^N possible combinations of N two-level systems, and I deal with the non-fully symmetric combinations in the next section.

The rate of photon emission for this N-atom system in any given $|J,M\rangle$ state can be written as

$$W_N = \Gamma \left\langle D^+ D^- \right\rangle = \Gamma(J+M)(J-M+1), \tag{3.25}$$

where Γ is the natural linewidth of an individual atom. The initial decay rate, there-

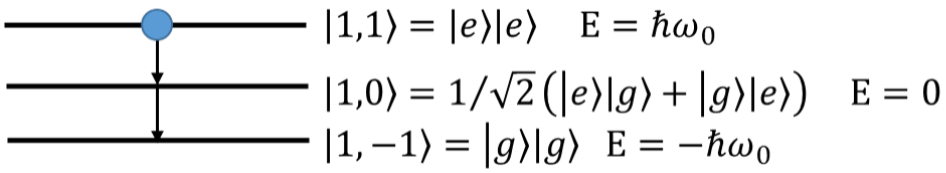

Figure 3-4: Schematic diagram of the fully symmetric levels in 2-atom Dicke superradiance. The $|1,1\rangle$ state is initially populated and the population cascades through electric dipole transitions to $|1,-1\rangle$. The energies and wavefunctions of the $M = 1, 0,$ and -1 states are indicated.

fore, is $2J\Gamma = N\Gamma$ as expected for an N-atom system. As the system loses excitation, however, the rate of emission increases to a maximum of $J(J+1)\Gamma$ for $M = 0$ before decreasing to zero when $M = -J$. At $M = 0$, the decay rate scales as N times that of the non-interacting case, as expected.

In the case $N = 2$, it is simple to compare to the classical results. In this case, $J = 1$, $M = -1, 0, 1$, as shown in Figure 3-4. Using Equation 3.25, it is easy to see that the rate of photon emission from $|1,1\rangle$ and $|1,0\rangle$ are both 2Γ, while the emission from $|1,-1\rangle = 0$. The rate of photon emission at time t is therefore

$$W_2(t) = 2\Gamma \left[\Pi_1(t) + \Pi_0(t)\right], \tag{3.26}$$

where $\Pi_M(t)$ is the probability at time t that the system is in state $|1,M\rangle$. At time $t = 0$, $\Pi_1 = 1$ and $\Pi_0 = \Pi_{-1} = 0$. We can use this along with the rate of decay from $|1,1\rangle$ to write

$$\frac{d\Pi_1}{dt} = -2\Gamma\Pi_1 \rightarrow \Pi_1(t) = e^{-2\Gamma t}. \tag{3.27}$$

In order to determine the rate of decay from Π_0, I invoke energy conservation. The average number of excited atoms intuitively is $2\Pi_1 + \Pi_0$. Energy conservation mandates than any decrease in the atomic excitation should be accompanied by an increase in radiation, such that

$$2\frac{d\Pi_1}{dt} + \frac{d\Pi_0}{dt} = -2\Gamma \left[\Pi_1(t) + \Pi_0(t)\right]. \tag{3.28}$$

Combining this with Equation 3.27, $\Pi_0(t)$ I arrive at

$$\Pi_0(t) = 2\Gamma t e^{-2\Gamma t}. \tag{3.29}$$

and the probability of the system residing in the ground state can be written as

$$\Pi_{-1}(t) = 1 - \Pi_0(t) - \Pi_1(t) = 1 - e^{-2\Gamma t}(1 + 2\Gamma t). \tag{3.30}$$

The rate of photon emission at time t from Equation 3.26 is then

$$W_2(t) = 2\Gamma e^{-2\Gamma t}(1 + 2\Gamma t) \tag{3.31}$$

which is nearly identical to the classical result derived in Section 3.1.1.

3.1.3 The importance of non-fully symmetric states

I have so far only considered the $(N+1)$ fully symmetric Dicke states. However, there are $(2^N - N - 1)$ additional non-fully symmetric states that contribute to subradiant effects [117]. In the two-atom system, the remaining singlet antisymmetric state,

$$|-\rangle = \frac{1}{\sqrt{2}} \left(|e\rangle |g\rangle - |g\rangle |e\rangle \right), \tag{3.32}$$

does not emit at all. For larger atom numbers, N, there can be multiple manifolds of these non-fully symmetric states. Each state can be assigned to a given level of symmetry, and for even N, the lowest symmetry states will similarly not emit at all. A schematic diagram of the complete state-space for an N-atom system is shown in Figure 3-5.

Each manifold contains a ladder of states of effective angular momentum J', separated by $\hbar\omega_0$ in energy, and connected by electric dipole transitions. However, the total rates of emission are slower than for the fully symmetric case. The rate of photon emission of each state is given again by Equation 3.25, with J' replacing J. Each manifold only has electric dipole transitions to states within the same manifold. Under the assumptions made above, only the fully-symmetric, highest-spin manifold

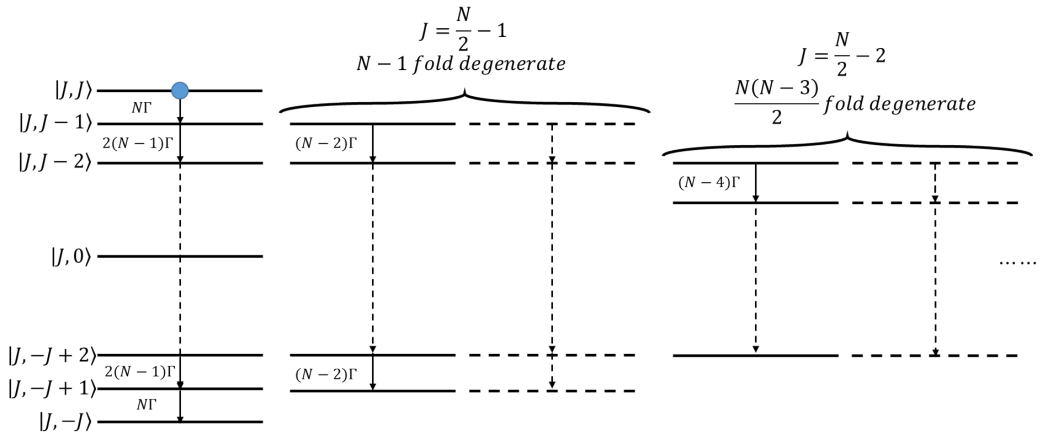

Figure 3-5: Schematic diagram of all states in N-atom superradiance. Each lower-symmetry manifold only has electric dipole transitions to other states within the same manifold at lower rates than the full symmetry manifold. The rates of decay are displayed next to the indicated electric dipole transitions (solid arrows).

can ever be populated.

However, actual experiments suffer from sources of decoherence that can populate and de-populate the non-fully symmetric manifolds. In particular, the breakdown of the exchange symmetry assumed at the beginning of Section 3.1.2 leads to dipole-dipole dephasing between the various particles which results in population of all subradiant manifolds [136]. Similarly, state-changing collisions can destroy the coherence that is required for superradiant states to remain in the fully symmetric manifold. Finally, in analogy to the classical example above becoming subradiant at certain emitter separations, extended samples of particles (ensembles with volume greater than λ^3) can emit both super- and subradiantly from different spatial regions. Extended samples and the importance of sample geometry are treated in Section 3.2.3.

3.2 Semi-classical approach to superradiance

The Dicke superradiance model is very useful as an intuitive starting point for describing superradiance. However, the number of approximations involved makes it

not useful for anything beyond a qualitative description of the process. In particular, the approximations of all emitters being located at the same spatial location and the symmetry with respect to exchange of any two atoms are significant departures from experimental reality. One way to proceed in the absence of these approximations is to treat the field classically while continuing to treat the atoms in a quantum mechanical manner. This semi-classical method ignores the effect of dipole-dipole exchange symmetry, and is based on the Bloch-Maxwell equations, which I introduce in Section 3.2.1. It is convenient to approach the system in the Bloch-angle representation, which I describe in Section 3.2.2. With these ideas established, it is straightforward to calculate the time-evolution of the emission intensity of a superradiant sample. Finally, I discuss the ramifications of an extended sample and the sample geometry in Section 3.2.3. I deal with fully quantum mechanical methods in Section 3.3.

3.2.1 Introduction to the Bloch-Maxwell equations

The Bloch-Maxwell equations are a system of coupled differential equations that describe the evolution of an electric field and the population difference and the polarization of an atomic sample. I again consider a collection of N two-level atoms now located in a volume of any size. I assume that the sample size is significantly larger in one direction than the other two, which leads to the approximation that the system can be approximated as a one-dimensional system. I discuss the ramifications of this approximation in Section 3.2.3. The density matrix associated with the i^{th} atom is given by

$$\rho^i = \left|\psi^i\right\rangle \left\langle\psi^i\right| \tag{3.33}$$

where ρ is the density matrix. This is a 2×2 matrix where the diagonal terms (ρ_{gg} and ρ_{ee}) describe the population in the ground and excited state, respectively, and the off-diagonal terms (ρ_{eg} and ρ_{ge}) describe the coherences between the ground and excited state. The population difference and the polarization of the system are given by

$$\mathcal{N}(z,t) = \frac{1}{\Delta z} \sum_{i \in [z, z+\Delta z]} \left[\rho^i_{ee} - \rho^i_{gg}\right] \tag{3.34}$$

$$\mathcal{P}^{\pm}(z,t) = \frac{d}{\Delta z} \sum_{i \in [z, z+\Delta z]} \rho^i_{eg} e^{\pm \omega_0 t} \tag{3.35}$$

where ω_0 is the resonant angular frequency for the transition between the $|g\rangle$ and $|e\rangle$ states, and I have divided the sample along the z-axis into small slabs of thickness Δz ($\Delta z \ll \lambda$) where the z-axis is defined as the direction in which the sample has the longest spatial extent. The radiated electric field is given by

$$\mathcal{E}^{\pm}(z,t) = \mathcal{E}^{\pm}_0(z,t) e^{\pm i(\omega_0 t - kz)} \tag{3.36}$$

where k is the wavevector of the radiation, and $\mathcal{E}^{\pm}_0(z,t)$ is the slowly-varying envelope function of the electric field. The Bloch-Maxwell equations are then

$$\frac{\partial \mathcal{N}}{\partial t} = \frac{i}{\hbar}\left[\mathcal{P}^+\mathcal{E}^+ - \mathcal{P}^-\mathcal{E}^-\right] \tag{3.37}$$

$$\frac{\partial \mathcal{P}^+}{\partial t} = \frac{2id^2}{\hbar}\mathcal{E}^-\mathcal{N} \tag{3.38}$$

$$\frac{\partial \mathcal{E}^+}{\partial z} = \frac{i\omega_0}{2\epsilon_0 c}\mathcal{P}^- \tag{3.39}$$

where I have made the approximation,

$$\frac{L}{c} < \frac{1}{N\Gamma m}, \tag{3.40}$$

where L is the characteristic length of the system, and $m = \frac{3\Omega_0}{8\pi}$ (where Ω_0 is the solid angle of emission that will be discussed in Section 3.2.3) is a geometric factor that describes the overall shape of the system. This approximation is known as the Arrechi-Courtens condition, which states that the envelope of the electric field varies more slowly than the time it takes for light to propagate from one end of the sample to

the other. The Arrechi-Courtens condition applies to all superradiance experiments discussed in this thesis.

The initial conditions of the Bloch-Maxwell equations are

$$\mathcal{E}_0^{\pm}(z,0) = 0 \tag{3.41}$$

$$\mathcal{P}^{\pm}(z,0) = 0 \tag{3.42}$$

$$\mathcal{N}(z,0) = \frac{N}{\Delta z}, \tag{3.43}$$

which describes the system in which all the atoms are in the excited state. This is an unstable equilibrium state, and the system will not evolve unless either an outside field acts on it (either a blackbody photon or a tipping pulse) or a spontaneous emission event occurs. The time evolution of these equations is discussed in Section 3.2.2.

The Bloch-Maxwell equations can be further simplified by making the approximation that all atoms play an identical role in the superradiance process, essentially disregarding all propagation effects. This is equivalent to assuming the same average field, polarization, and population ($\bar{\mathcal{E}}^{\pm}$, $\bar{\mathcal{P}}^{\pm}$, and $\bar{\mathcal{N}}$) at every point in the system. The Bloch-Maxwell equations then become the mean-field equations

$$\frac{\partial \bar{\mathcal{N}}}{\partial t} = \frac{i}{\hbar}\left[\bar{\mathcal{P}}^{+}\bar{\mathcal{E}}^{+} - \bar{\mathcal{P}}^{-}\bar{\mathcal{E}}^{-}\right] \tag{3.44}$$

$$\frac{\partial \bar{\mathcal{P}}^{+}}{\partial t} = \frac{2id^2}{\hbar}\bar{\mathcal{E}}^{-}\bar{\mathcal{N}} \tag{3.45}$$

$$\bar{\mathcal{E}}^{+} = \frac{i\omega_0}{4\epsilon_0 c}L\bar{\mathcal{P}}^{-} \tag{3.46}$$

3.2.2 Conversion to the Bloch angle representation

While the mean-field Bloch-Maxwell equations can be solved directly, physical insight can be gained by making a transformation to the Bloch angle representation. As earlier, when considering Dicke superradiance, I can represent the N two-level atom system as a single spin-$N/2$ system. This system can be described by the Bloch vector, a vector of norm N, the direction of which describes the population inversion and the polarization of the system. The axis system is set up such that the z-axis corresponds to the population of the atomic system, and the x- and y-axes correspond to the phase of the polarization of the system. The population inversion and the polarization can therefore be expressed as functions of two characteristic angles θ and ϕ

$$\bar{\mathcal{N}}(t) = \frac{N}{2}\cos\theta(t) \tag{3.47}$$

$$\bar{\mathcal{P}}^{\pm}(t) = \frac{N}{2}\sin\theta(t)e^{\pm i\phi}. \tag{3.48}$$

The axis system and these angles are displayed schematically in Figure 3-6. The mean-field Bloch-Maxwell equations can then be written as

$$\frac{d\theta}{dt} = \frac{1}{2N\Gamma m}\sin\theta \tag{3.49}$$

$$\frac{d\phi}{dt} = 0, \tag{3.50}$$

with the initial condition

$$\theta(0) = \theta^i, \tag{3.51}$$

where the angle θ^i is an initial tip value as caused either by spontaneous emission, blackbody radiation, or an external resonant electromagnetic field [1, 128, 141, 142, 143]. As ϕ does not change and merely provides a phase shift of the overall polarization, I ignore it in the following.

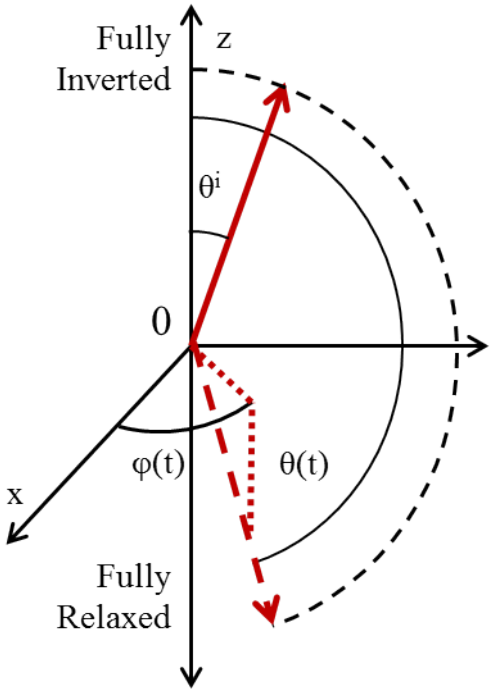

Figure 3-6: Schematic representation of the Bloch angle representation of mean-field superradiance. The solid red arrow is the Bloch vector after the initial tipping pulse, and the dashed red arrow is the Bloch vector after a time t. The Bloch angles θ and ϕ are displayed with the thin solid arcs.

The evolution of this system is formally analogous to the evolution of a damped pendulum in a viscous fluid. If $\theta(0) = 0$, this system would not evolve away from the unstable equilibrium point. With a small initial tip angle, the Bloch vector evolves irreversibly from pointing in the positive z-direction to pointing in the negative z-direction. This evolution occurs over a time scale of $N\Gamma m \equiv T_R$, the characteristic superradiance time.

It is straightforward to calculate the radiated intensity,

$$I(t) = -\hbar\omega_0 \frac{\partial \bar{\mathcal{N}}}{\partial t} = \frac{\hbar\omega_0 N}{2T_R} \operatorname{sech}^2 \left[\frac{1}{2T_R} \left(t - T_D(\theta^i) \right) \right], \tag{3.52}$$

where $T_D = -2T_R \ln(\theta^i/2)$ is the characteristic delay time of the superradiant pulse. The superradiant pulse displayed in Figure 3-1 is an example of a hyperbolic-secant pulse.

In the absence of an external electric field, T_D is determined by the blackbody temperature of the surroundings and spontaneous emission rate of the atomic system. When both are considered, the average delay is

$$\langle T_D \rangle = T_R \ln \left[\frac{N}{1+\bar{n}} \right] \tag{3.53}$$

where $\bar{n}$ is the average photon number of blackbody photons at the resonant frequency, and the variance of the delay is

$$\Delta T_D = \sqrt{\langle T_D^2 \rangle - \langle T_D \rangle^2} = 1.3 T_R. \tag{3.54}$$

However, the delay can be made much shorter and have much smaller variance by introducing an external resonant field to tip the Bloch vector by a known amount.

3.2.3 Sample size and geometry dependence

I made several approximations in my derivation of the mean-field Bloch-Maxwell equations (Equations 3.44 - 3.46) all of which fundamentally relate to the size and geometry of the sample. The approximation of one dimension of the sample being

larger than the others turns out to be a very minor approximation. This geometry is the natural geometry of any laser pumped atomic beam experiment. A collimated laser typically intersects an atomic beam that has a width larger than the beam waist of the laser, leading to this "pencil-shaped" geometry. The formal definition of this geometry states that it is a cylinder satisfying $L \gg w \gg \lambda$, where w is the radius of the cylinder.

However, as the exact values of L, w, and λ are varied, the behavior of the superradiant emission undergoes several qualitative changes. The Fresnel number F of the emitting cylinder is the critical determinant of the qualitative regime of emission,

$$F = \frac{w^2}{L\lambda}. \tag{3.55}$$

The qualitative change in behavior occurs as the Fresnel number becomes larger or smaller than unity. For $F > 1$, the geometric angle of emission of the sample, determined by $\theta_G = w/L$, is larger than the diffraction angle, determined by $\theta_D = \lambda/w$. This means that the sample supports multiple diffraction-limited modes within the geometric angle of emission, each evolving separately. On the other hand, for $F < 1$, the emission occurs in a single diffraction limited mode that has a much broader spatial extent than the geometric angle of emission. In the discussion in Section 3.2.2, I have taken the sample size to satisfy $F = 1$ in order to compromise between excess off-axis emission and excess diffraction. Figure 3-7 displays the effects of Fresnel number larger or smaller than 1. The solid angle of the emission used in m (from Equation 3.40) is determined entirely from the diffraction angle, $\Omega_0 \sim \theta_D^2 = \lambda^2/w^2$.

Fresnel numbers far from 1, however, begin to cause the assumption of one-dimensional emission to fail. This includes the case of $w \approx L$ when the sample is relatively spherical. The primary difference is that the treatment of the electric field must include its behavior in the transverse directions, and so Equation 3.39 must be replaced by

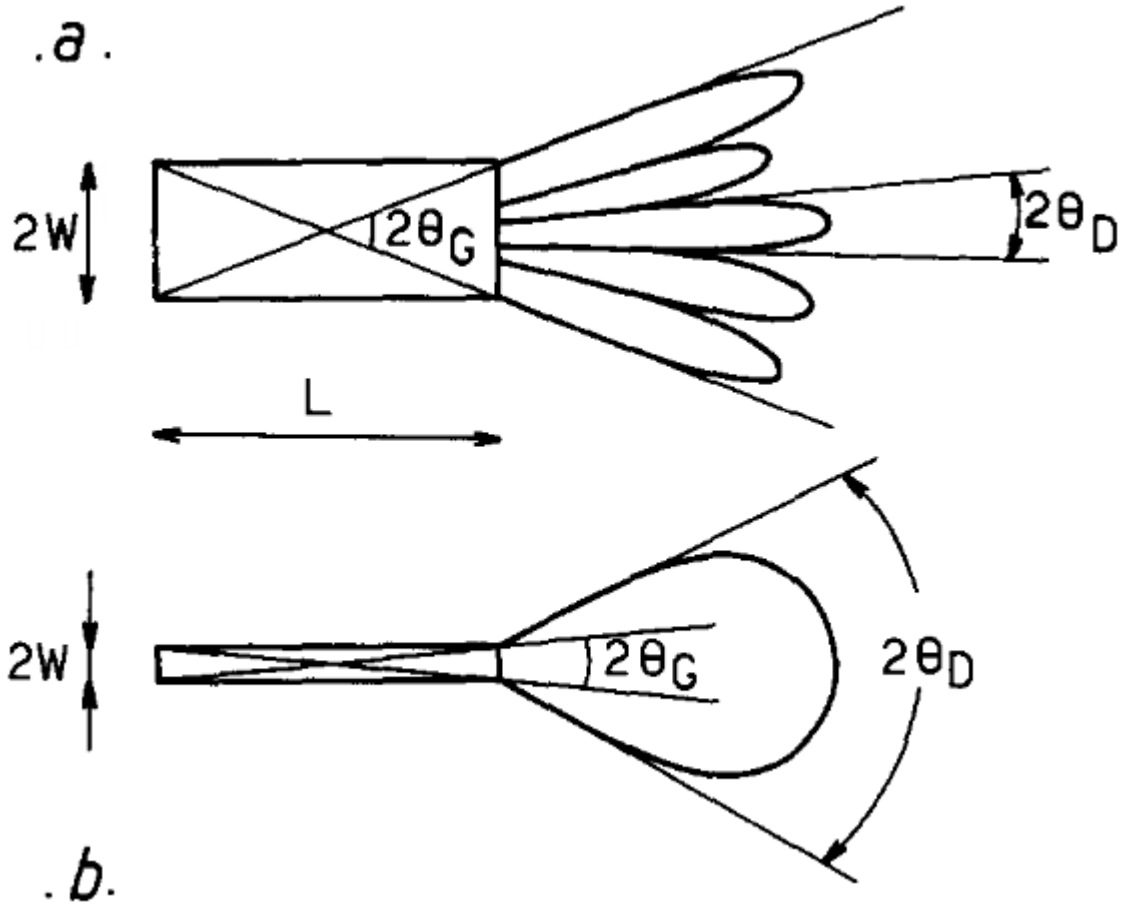

Figure 3-7: Schematic representation of the transverse directions of the superradiant field given by a sample with a) Fresnel number $F > 1$ and b) Fresnel number $F < 1$. Figure from Ref [1].

$$\frac{\partial \mathcal{E}^+}{\partial z} - \frac{i}{2k_0}\left(\frac{\partial^2}{\partial x^2} + \frac{\partial^2}{\partial y^2}\right)\mathcal{E}^+ = \frac{i\omega_0}{2\epsilon_0 c}\mathcal{P}^-, \tag{3.56}$$

while the expressions for the number of excited atoms and polarization remain identical. The meaning of the transverse terms here depends on whether $F \gg 1$ or $F \ll 1$. For $F \gg 1$, typical of geometric optics, this term describes the potential off-axis diffraction limited modes supported in the geometric angle of emission θ_G. For $F \ll 1$, typical of Frauenhofer diffraction, this term describes the off-axis emission that is diffracted through the angle θ_D.

While these extreme cases seem like a relatively small change to the Bloch-Maxwell equations, it is impossible to derive an analytical solution and the equations must be solved numerically. The experiments described in this thesis operate with $F \approx 1$, typical of Fresnel diffraction, therefore numerical solutions to these three-dimensional equations are beyond the scope of this thesis.

Another approximation made in Section 3.2.2 is the mean-field approximation, which is to ignore all propagation effects. The full ramifications of discarding this approximation require a full quantum treatment of the system, discussed in Section 3.3. However, one qualitative change is that distinct spatial segments of the sample can destructively interfere with the emission originating from other spatial segments. This has the effect of replacing Equation 3.49 by

$$\frac{d\theta}{dt} = \frac{1}{2T_R}J_1(\theta) \tag{3.57}$$

where J_1 is the first-order Bessel function of the first kind. The radiated emission as a function of time is then

$$I(t) = \frac{\hbar\omega N}{2T_R}\operatorname{sech}^2\left[\frac{1}{4T_R}\left(t - T_D(\theta^i)\right)\right]. \tag{3.58}$$

The final approximation that I made in Section 3.2.2 is that the radiation only propagates in a single direction. When an external electric field triggers the superradiance, it travels in the exact direction of the triggering field. When the superradiance is triggered by spontaneous emission or a blackbody photon, any given superradiant

event can propagate in either the positive or negative z-direction. The equations listed above work equally well for either direction in this untriggered case.

In an extended sample, however, emission can be triggered in different directions at different locations in the extended sample, leading to complicated emission modes in both the positive and negative z-direction that interfere with each other. This can be accounted for by including additional electric field and polarization terms in the Bloch-Maxwell equations and numerically solving, as shown in Reference [1]. All of the experiments described in this thesis use an external electric field to trigger the superradiance. Thus, they always have a single direction of emission.

3.3 Full quantum mechanical approach to superradiance

The approximations made in the semiclassical approach above, while minor, still fail to describe some fundamental effects of superradiance. In particular, propagation effects and variations in the dipole-dipole interaction throughout the sample are neglected in the mean-field approximation. These effects lead to important frequency domain effects that cannot be accurately represented by the semi-classical method. First I introduce two conventional fully quantum mechanical calculation methods in Sections 3.3.1 and 3.3.2, using the Schrödinger and Heisenberg representations as described by Gross and Haroche [1]. While both operate formally in the interaction representation, the Schrödinger representation method focuses on the collective wavefunction of the sample and the Heisenberg representation method focuses on the collective observables of the sample. In Section 3.3.3, I present a master-equation model developed by Susanne Yelin that maintains the full richness of the quantum mechanical picture while retaining ease of calculation [120].

3.3.1 Schrödinger representation

In both the Schrödinger and Heisenberg representation approaches, the Hamiltonian is the same

$$H = H_{at} + H_{rad} + V \tag{3.59}$$

where H_{at} is the Hamiltonian of the N-atom system, H_{rad} is the Hamiltonian of the electromagnetic field, and V is the term that describes the light-matter dipole interactions

$$H_{at} = \hbar\omega_0 \sum_i D_{i,3} \tag{3.60}$$

$$H_{rad} = \sum_{k,\varepsilon} \hbar\omega_k \left(a^\dagger_{k,\varepsilon} a_{k,\varepsilon} + \frac{1}{2} \right) \tag{3.61}$$

$$V = -\sum_i \left(E^+(r_i) + E^-(r_i) \right) \cdot \mathcal{D}_{i,\varepsilon}, \tag{3.62}$$

where i labels the atoms, k and ε label the mode and the polarization of the electric field, $a^\dagger$ and a are the creation and annihilation operators of the electric field, and E^+ and E^- are the positive and negative frequency portions of the electric field

$$E^+(t) = -i \sum_{k,\varepsilon} \mathcal{E}_{k,\varepsilon} a_{k,\varepsilon} e^{ik\cdot r} \tag{3.63}$$

$$E^-(t) = i \sum_{k,\varepsilon} \mathcal{E}_{k,\varepsilon} a^\dagger_{k,\varepsilon} e^{-ik\cdot r} \tag{3.64}$$

$$\mathcal{E}_{k,\varepsilon} = \sqrt{\frac{\hbar c k}{2\epsilon_0 \mathcal{V}}} \varepsilon. \tag{3.65}$$

$\mathcal{V}$ is an arbitrarily chosen quantization volume that is much larger than the atomic ensemble.

The entire atom-field system is described by its total density matrix $\Phi(t)$, which

evolves according to the Liouville-von Neumann equation

$$i\hbar\frac{d\Phi}{dt} = [H, \Phi]. \tag{3.66}$$

It is simpler to solve this equation in the Interaction representation, such that

$$\tilde{\Phi}(t) = e^{i(H_{at}+H_{rad})t/\hbar}\Phi e^{-i(H_{at}+H_{rad})t/\hbar} \tag{3.67}$$

$$\tilde{V}(t) = e^{i(H_{at}+H_{rad})t/\hbar}V e^{-i(H_{at}+H_{rad})t/\hbar} \tag{3.68}$$

$$i\hbar\frac{d\tilde{\Phi}}{dt} = [\tilde{V}, \tilde{\Phi}]. \tag{3.69}$$

Similarly, the observables that I am interested in are generally the atomic observables, and so I take the partial trace of the density matrix over the field variables

$$\tilde{\rho}(t) = \mathrm{Tr}_{rad}\tilde{\Phi}. \tag{3.70}$$

This makes it possible to express the time evolution of the atomic system by

$$\frac{d\tilde{\rho}}{dt} = -\frac{1}{\hbar^2}\mathrm{Tr}_{rad}\int_0^t d\tau \left[\tilde{V}(t), \left[\tilde{V}(t-\tau), \tilde{\Phi}(t-\tau)\right]\right] \tag{3.71}$$

where the initial condition, $\tilde{\Phi}(0)$, is the field in its vacuum state with all the atoms in their upper level. This expression, however, is not particularly useful, as it requires knowledge of the entire previous history of the atom-field system, as represented by $\tilde{\Phi}(t-\tau)$. The Born-Markov approximation, which neglects the build-up of correlation between the atoms and the field, however, reduces this equation to a more tractable form. The evolution of the atomic variables can then be expressed as

$$\left[\frac{d\tilde{\rho}}{dt}\right]_{BM} = -\frac{1}{\hbar^2}\mathrm{Tr}_{rad}\int_0^\infty d\tau \left[\tilde{V}(t), \left[\tilde{V}(t-\tau), \tilde{\rho}\otimes|0\rangle\langle 0|\right]\right], \tag{3.72}$$

where $|0\rangle\langle 0|$ is the vacuum state of the field. This expression can be transformed back to the Schrodinger representation, which results in a superradiance master equation,

$$\frac{d\rho}{dt} = \frac{1}{i\hbar}\left[\sum_j H_j, \rho\right] - \frac{cd^2}{16\epsilon_0\pi^3\hbar}\int_0^\infty d\tau \int_0^\infty k^3 dk \int d\Omega \varepsilon^2 \sum_{i,j} e^{ik\cdot(r_i - r_j) - ick\tau} \times \left[D_i^+ e^{-\frac{iH_j\tau}{\hbar}} D_j^- e^{\frac{iH_j\tau}{\hbar}}\rho - e^{-\frac{iH_j\tau}{\hbar}} D_j^+ e^{\frac{iH_j\tau}{\hbar}}\rho D_i^+\right] + h.c. \quad (3.73)$$

In order to solve this equation, I need to know the exact distribution of the atoms in space, which in general I cannot know. However, there are two useful limiting cases that reveal some of the details that the fully quantum approach provides. In the first case, if I assume that the atoms are distributed as in Dicke superradiance, all at a single point, the dephasing factor $e^{ik\cdot(r_i - r_j)}$ can be replaced by 1, and the master equation becomes solvable. The solution is involved and beyond the scope of this thesis, but the results are instructive. The evolution is in general complex, and the real part describes the decay of the system

$$\left(\frac{d\rho}{dt}\right)_{real} = -\frac{\Gamma}{2}[D^+D^-, \rho] + \Gamma D^-\rho D^+. \quad (3.74)$$

When starting at $t = 0$ in the fully excited state of the ensemble, this describes evolution downwards in the symmetric manifold as in Dicke superradiance. To evaluate the matrix elements, I project the operators onto the Dicke states, and obtain the evolution

$$\frac{d\rho_M}{dt} = -\Gamma(J+M)(J-M+1)\rho_M + \Gamma(J+M+1)(J-M)\rho_{M+1}, \quad (3.75)$$

where ρ_M is the probability of finding the system in the state $|JM\rangle$. The imaginary part of the evolution describes the effect of off-resonant photon processes, and corresponds to a frequency shift of the emission

$$\left(\frac{d\rho}{dt}\right)_{imag} = -\frac{1}{i\hbar}\left[\sum_i D_i^- D_i^+, \rho\right]. \quad (3.76)$$

This frequency shift is generally called the "collective Lamb shift," because in the

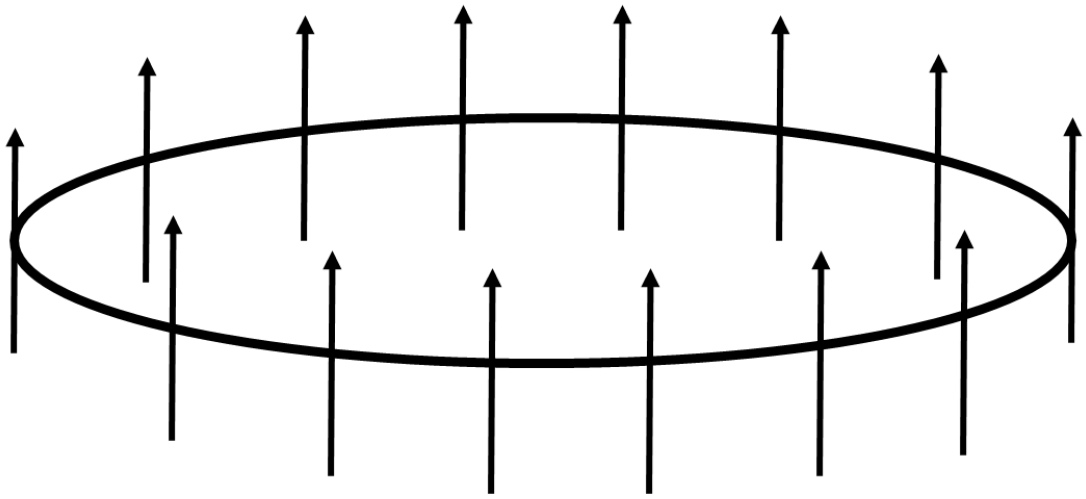

Figure 3-8: Schematic representation of dipoles aligned and equally spaced on a ring, one of the few cases where the dipole-dipole interaction is symmetric with respect to exchange.

limit of $N = 1$ atoms, this shift converges to the ordinary Lamb shift.

When the atoms are not all located at the same position, then even if the sample ensemble size is smaller than a wavelength, then in general the system will not be symmetric with respect to exchange. There are a few special geometries where the atoms are symmetric to exchange that are described by solvable master equations, and one of them is the case of regularly spaced atoms on a ring, as shown in Figure 3-8. The real part of the evolution is still given by Equation 3.74. The imaginary part, on the other hand, varies as the system emits, leading to a chirped emission. The energy of a given $|JM\rangle$ state is given by

$$\langle JM|\hbar\Omega|JM\rangle = \frac{d^2}{4\pi\epsilon_0 r^3}\frac{J^2 - M^2}{J - \frac{1}{2}}. \tag{3.77}$$

Therefore, the frequency shift can be obtained by differentiating, to obtain

$$\hbar\delta\omega_s = -\frac{d^2}{4\pi\epsilon_0 r^3}\left[1 - \frac{2s}{N}\right] \tag{3.78}$$

where $s = J - M$ is the s^{th} photon in the cascade. Therefore, the system chirps from the red to the blue of the expected emission frequency. A level diagram for this is shown in Figure 3-9.

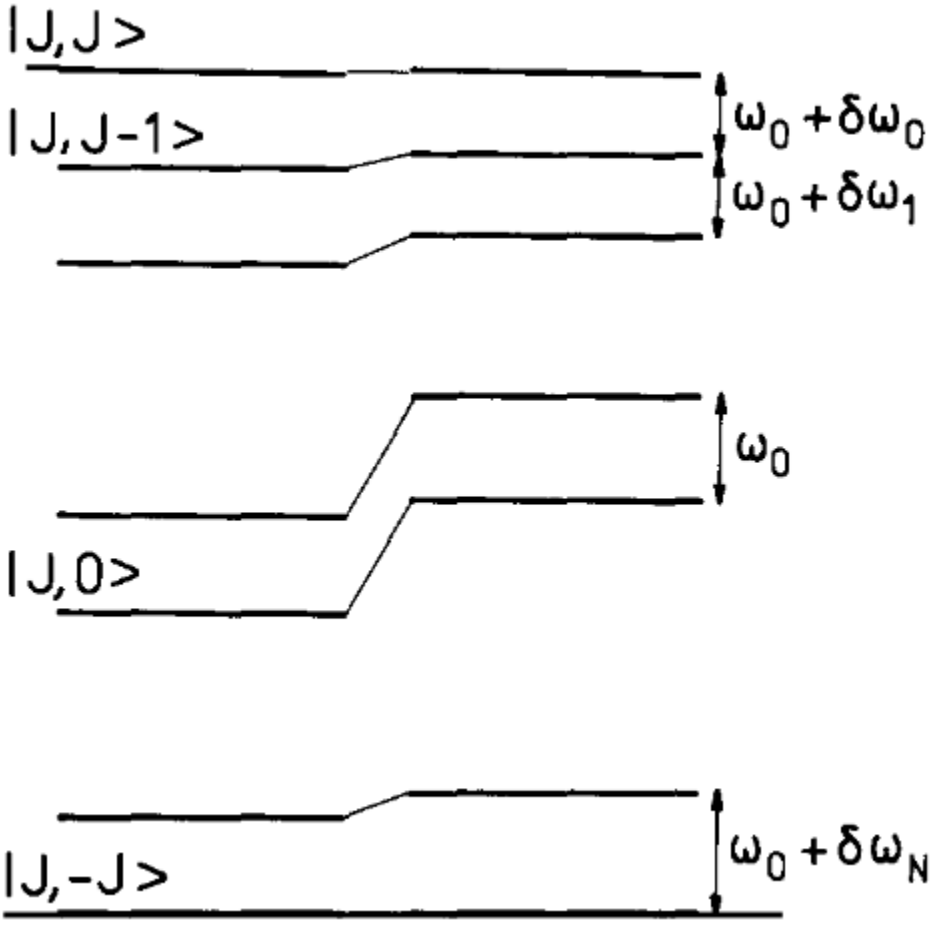

Figure 3-9: Energy diagram of the Dicke states from an ensemble of an evenly spaced ring of atoms. The left side represents the evenly spaced energy levels of single-point Dicke superradiance, while the right side shows those levels shifted by the varying dipole-dipole interaction. Figure from Ref [1].

3.3.2 Heisenberg representation

The Schrödinger representation is very convenient for relatively small sample sizes, in particular when the ensemble is restricted to a fully symmetric manifold of Dicke states. When the sample size is larger than a wavelength, however, the Dicke description of the system fails. In this case the Schrödinger representation, while still accurate, is much less convenient. In such cases, the Heisenberg representation, which naturally allows for extensions to large volumes, is far more convenient. The overall structure of the approach in the Heisenberg representation is nearly identical to that of the semi-classical treatment in Section 3.2, but with no approximations.

For a sample of any size and dimension, the population difference N and polarization $P^{\pm}$ are defined as

$$N(r) = \sum_i \delta_\zeta(r - r_i) D_{i,3} \tag{3.79}$$

$$P^{\pm}(r) = d\varepsilon \sum_i \delta_\zeta(r - r_i) D_i^{\pm} \tag{3.80}$$

where the δ_ζ functions are three-dimensional analogues of Heaviside step functions with value 1 over a volume ζ^3, and value 0 outside of that volume, where ζ is large compared to an atomic radius, but small compared to λ. The evolution for N, $P^{\pm}$, and the positive and negative frequency components of the electric field E are given by the Heisenberg equations

$$\frac{\partial X}{\partial t} = \frac{1}{i\hbar}[X, H] \tag{3.81}$$

where X is any of the three operators above, and H is the Hamiltonian of the system. The following exact Bloch-Maxwell equations are obtained

$$\frac{\partial N}{\partial t} = \frac{i}{\hbar} e^- \cdot (P^+ - P^-) + \frac{i}{\hbar}(P^+ - P^-) \cdot E^+ \tag{3.82}$$

$$\frac{\partial P^+}{\partial t} = i\omega_0 P^+ + 2i\varepsilon\frac{d^2}{\hbar}(E^- N + N E^+) \tag{3.83}$$

$$\frac{\partial^2 E^+}{\partial t^2} - c^2\nabla\times\nabla E^+ = \frac{1}{\epsilon_0}\frac{\partial^2 P^-}{\partial t^2}. \tag{3.84}$$

These equations can be simplified, in the manner shown in Section 3.2, to obtain a semi-classical formalism to describe superradiance. The quantum effects of field quantization are the non-commutation of N and P with E. In the case where superradiance is initialized by spontaneous emission, these exact equations are necessary. If a blackbody photon or external field generates the initial coherence, then the field quantization is not necessary and the semi-classical approach from Section 3.2 is appropriate.

These exact Bloch-Maxwell equations are useful to obtain numerical solutions for large volume or large atom-number superradiance, but extracting information from them about the emission rate and frequency shift is non-intuitive.

3.3.3 Second-order master equation method

Recently, a fully quantum mechanical method has been developed that combines the ability to investigate large and extended samples of atoms with an intuitive approach to determine, for example, collective rates of emission and frequency shifts. In this case, the Hamiltonian specifies two atoms, labeled "1" and "2" such that the entire Hamiltonian can be written as

$$H = H_{field} + \sum_i H^i_{atom} + H_{int} + V \tag{3.85}$$

where H_{field} is the Hamiltonian of the quantized electric field, H_{atom} is the free Hamiltonian of the i^{th} atom at location r_i, H_{int} is the Hamiltonian of the interactions of all atoms other than the two specified atoms, while V is the Hamiltonian of the interactions of the two specified atoms,

$$H_{int} = -\sum_{i\neq 1,2} p_i \cdot (\mathcal{E}_i + E_i) \tag{3.86}$$

$$V = -\sum_{j=1,2} p_j \cdot (\mathcal{E}_j + E_j) \tag{3.87}$$

p_i is the dipole operator of the i^{th} atom, E_i is the quantized field at the position of the i^{th} atom, and $\mathcal{E}_i$ is an external classical driving field at the position of the i^{th} atom. The effective two-atom density matrix equation can be written as

$$\begin{aligned}
\dot{\rho}^{(1,2)}(t) = &\sum_{i=1,2}\left[\sigma_i\Omega_{Li}^{\dagger} + \sigma_i^{+}\Omega_{Li}, \rho^{(1,2)}\right] \\
&- i\sum_{i=1,2}\Delta_{ii}\left[\rho^{(1,2)}, \left[\sigma_i^{+}, \sigma_i\right]\right] - i\sum_{i,j=1,2}\delta_{ij}\left[\rho^{(1,2)}, \left[\sigma_j^{+}, \sigma_i\right]\right] \\
&- \sum_{i,j=1,2}\left(\frac{\Gamma_{ij}}{2}\left(\left[\rho^{(1,2)}\sigma_i, \sigma_j^{+}\right] + \left[\sigma_i, \sigma_j^{+}\rho^{(1,2)}\right]\right)\right. \\
&\left. + \frac{\Gamma_{ij}+\gamma_{ij}}{2}\left(\left[\rho^{(1,2)}\sigma_j^{+}, \sigma_i\right] + \left[\sigma_j^{+}, \sigma_i\rho^{(1,2)}\right]\right)\right),
\end{aligned} \tag{3.88}$$

where Ω_{Li} is the driving field at the location of atom i and σ_i is the lowering operator for atom i, $\sigma_i = |g_i\rangle\langle e_i|$. Importantly, γ_{ij}/Γ_{ij} and δ_{ij}/Δ_{ij} denote the collective spontaneous/induced decay and frequency shift parameters. The spontaneous terms are analogous to the real and imaginary parts of the superradiance master equation from Section 3.3.1. For a single atom in vacuum, the spontaneous decay tends toward the vacuum decay rate γ_0 for $|e\rangle \rightarrow |g\rangle$, and the spontaneous frequency shift tends toward the Lamb shift. The induced terms are analogous to AC Stark effects on the atomic ensemble. All of these parameters result from second-order correlation of the atomic sample

$$\frac{\Gamma_{ij}}{2} - i\Delta_{ij} = \frac{d^2}{\hbar^2}\int_0^{\infty} d\tau \left\langle\left\langle E_i^{-}(t)E_j^{+}(t-\tau)\right\rangle\right\rangle e^{-i\omega t} \tag{3.89}$$

$$\frac{\gamma_{ij}}{2} - i\delta_{ij} = \frac{d^2}{\hbar^2}\int_0^{\infty} d\tau \left\langle\left[E_i^{+}(t-\tau)E_j^{-}(t)\right]\right\rangle e^{-i\omega t} \tag{3.90}$$

where $\langle\langle \ldots \rangle\rangle$ denotes the second-order cumulant as in many-body theory. The full derivation of these equations is well beyond the scope of this thesis, and can be found in Reference [120]. It is important to note that the decay and frequency broadening (the time-dependence of the frequency shift) are not related by the standard Fourier transform relationship, but by a Kramers-Kronig relationship

$$\Delta_{ij} = \frac{1}{\pi}\mathcal{P}\int_{-\infty}^{\infty} d\Delta'_{ij} \frac{\Gamma_{ij}(\Delta'_{ij})}{\Delta_{ij} - \Delta'_{ij}} \tag{3.91}$$

and similarly for γ_{ij}/δ_{ij}, where $\mathcal{P}$ denotes the Cauchy principal part of the integral.

The only assumptions needed to derive these equations are that the atomic sample is a three-dimensional homogeneous atomic gas in free space (i.e. no cavity modes to the radiation). These quantities and the density matrix can then be numerically solved in a self-consistent manner. In general, the two spontaneous parameters (γ and δ) are orders of magnitude smaller than the induced parameters (Γ and Δ), and so only the induced parameters are allowed to vary, while the spontaneous parameters are approximated by their vacuum values.

The key results from this theoretical approach are that it naturally produces a time-dependent frequency shift and shows that all parameters (Γ, average excited state population, etc) except for Δ depend on the optical depth ($OD = \rho\lambda^2 L$). Δ depends nearly exclusively on the relative density ($RD = \rho\lambda^3$). This method of calculating superradiant effects contains all correlations up to second order. This describes most of the physics in the context of cooperative effects. As such, these calculations make what is currently the most effective tradeoff between approximations and accuracy.

The time-dependent frequency shift has not been studied much outside of specific geometries for large excitations and the single-photon collective Lamb shift for general geometries [11, 144, 145, 146, 3, 147, 148, 96, 149, 135, 139, 150]. The single excitation regime is easily approached by any of the three methods provided here, and the specific geometries approachable with the Schödinger and Heisenberg representations are not easily achieved in experiments. However, in the large excitation regime with a pencil-

shaped geometry, as in my experiments, only this master equation methods provides a handle on the induced collective frequency shifts and chirps [2].

Chapter 4

Single-shot observation and characterization of superradiant emission

In this chapter I discuss the single-shot experimental observation of superradiant emission. In Section 4.1, I outline the benefits of the use of Rydberg states for observation of superradiant emission and describe the importance of using an extended sample. In Sec. 4.2, I demonstrate an initial observation of spontaneous superradiance in a dense ensemble of Rydberg states. In Sec. 4.3, I report single-shot detection of superradiance, present a time-domain filtering method for noise removal, and make connections to the semi-classical theory of superradiance. Finally, in Sec. 4.4, I describe the failure of the semi-classical theory to account for the frequency shifts and broadenings I observe in superradiance and make connections to a fully quantum theory that naturally accounts for these frequency effects. The discussion in Sections 4.3 and 4.4 is derived from my publication in [151].

4.1 Advantages of Rydberg states for the observation of superradiance

Rydberg states of atoms appear at first to be well suited to studies of superradiance. Rydberg states have exceptionally large transition dipole moments and long wavelengths for $\Delta n^* \leq 1$ transitions (transition dipole moments scale as n^{*2} and wavelengths scale as n^{*3}). These properties lead to strong interactions at long range and cooperativity over large volumes. This strong cooperativity results in $\Delta n^* \leq 1$ transitions between Rydberg states achieving greater spontaneous emission rates than transitions to the ground state, despite the Einstein A coefficient scaling as ω^3 [98].

Furthermore, when Rydberg states are prepared with pulsed laser excitation, as in my experiments, the initial state is a perfectly symmetric inverted system. In a zeroth-order approximation, an inverted two-level system is formed between the populated single Rydberg state and the next energetically-lowest optically-accessible Rydberg state. For example, a laser populated $30s$ state in hydrogen would form an inverted two-level system with the $30s$ state as the excited state and the $29p$ state as the lower state. The influence of the $28p$ state (and all other lower lying states) becomes less significant as Rydberg number density increases.

However, observing unambiguous superradiant emission requires that the superradiant emission time, T_R, is shorter than any forms of dephasing present in the experiment, where

$$T_R = \frac{8\pi}{A_{21} OD} \tag{4.1}$$

$$OD = \rho \lambda^2 L \tag{4.2}$$

$$A_{21} = \frac{8\pi^2 \mu^2}{3\epsilon_0 \hbar \lambda^3} \tag{4.3}$$

and ρ is the density of Rydberg states, λ is the wavelength of radiation for the

transition between the two states, L is the length of the sample, μ is the electric dipole transition moment between the two states, OD is the optical depth of the sample, and A_{21} is the Einstein A coefficient for the transition. As the transition dipole moment scales as n^{*2} and the wavelength scales as n^{*3}, A_{21} scales as n^{*-5}. However, this is balanced out by the λ^2 factor in the optical depth, which scales as n^{*6}, so the superradiant emission time scales as n^{*-1}.

Dephasing times have a wide variety of dependences on n^*. Geometric dephasing effects, such as flyout broadening, are insensitive to n^*. The Doppler dephasing time depends on the wavelength of the transition, and so the Doppler dephasing time scales as n^{*3}, and quickly becomes much longer than the superradiant emission time.. In my experiment, the Doppler broadening rate is ~ 250 kHz and flyout broadening rate is ~ 10 kHz. The blackbody dephasing time, as discussed in Section 2.3.3, scales as n^{*2} due to the longer wavelength of the transitions, and also becomes longer than the superradiant emission time.

Dephasing effects that arise from interactions with external electric fields generally become the fastest effects at very large n^* ($n^* > 100$). While the electric polarizability of Rydberg states scales like n^{*7}, neither dephasing due to homogeneous fields nor dephasing due to inhomogeneous fields have a generally applicable dependence on n^*. This is because the exact value of the quantum defect of a given level modifies the nature of the Stark effect. States with small quantum defects very quickly mix with the manifold of high-ℓ states at low external fields and broaden in lineshape rapidly in homogeneous fields. On the other hand, states with large quantum defects (s, p, and occasionally d states) require much larger fields before they merge into the manifold of high-ℓ states; thus, at typical values of stray fields, homogeneous fields induce little broadening, only Stark shifts. This behavior is shown schematically in Figure 4-1, and can be used as a diagnostic for determining the quantum defect (and therefore the ℓ-character) of a state. The $28h$ state in Fig. 4-1 has a large broadening at Stark fields of > 10 V/cm, the $28f$ state has a large broadening at Stark fields of > 50 V/cm, and the $29p$ state has negligible broadenings until a very large external electric field. The calculations in Fig. 4-1 were performed using the quantum defects

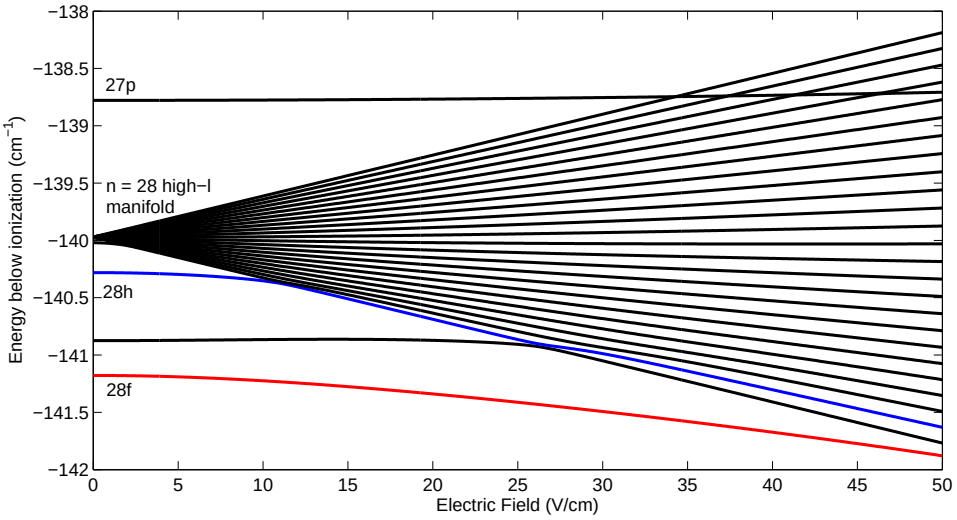

Figure 4-1: Calculated energy dependence of $n = 28$ Rydberg states of barium on the strength of an external electric field. The $28f$ state (red) has a strong Stark shift, but does not mix with the high-ℓ manifold until > 50 V/cm. The $28h$ state (blue) has a stronger Stark shift and mixes with the high-ℓ manifold at ~ 10 V/cm. The $27p$ state (black, top) has essentially no Stark shift and does not interact with the $n = 28$ high-ℓ manifold. As such, of these three states, the $28h$ state is most sensitive to electric fields, while the $27p$ state is least sensitive to electric fields. These 3 states illustrate the universal range of behaviors of Rydberg states in an external electric field.

of atomic barium.

Inhomogeneous electric fields, however, will induce line broadening in both states with large and small quantum defects although again it does not have a characteristic scaling with n^*. In general, due to the nearby high-ℓ states, the inhomogeneous broadening in states with small quantum defects will again be larger than in states with small quantum defects. States with large quantum defects do broaden because each spatial portion of the sample experiences a different electric field and therefore a different Stark shift. In my experiments the entire chamber is grounded, so the primary source of electric field is generated by stray electrons and ions. These charged particles may come from multiphoton ionization by the lasers that excite to Rydberg states, photoelectrons produced by laser beams terminating on conductive surfaces, or from the ablation process and subsequent entrainment of the charged species in the atomic beam. Multiphoton ionization is minimized by carefully reducing the

amplified spontaneous emission from the pulsed dye laser (below 1% of the total output power). The laser spots are also terminated on a Teflon surface to prevent the generation of photoelectrons. Ions formed in the ablation process are unavoidable, but can be reduced through careful tuning of the ablation pulse energy and focal spot size. I monitored the density of Ba^+ ions in the detection chamber using flourescence detection of the $6s - 6p$ transition and measured a density of $< 10^6$ cm^{-3}. This density of ions corresponds to a broadening of 10 kHz due to an inhomogeneous field for the transition I discuss below.

Magnetic fields generally have much smaller effects than electric fields. Homogeneous magnetic fields (assuming an arbitrary alignment) split each Rydberg transition into a triplet with values of Δm of ± 1 and 0. A field of 1 Gauss corresponds to a ~ 1.5 MHz splitting between the $\Delta m = 0$ and $\Delta m = \pm 1$ lines. An inhomogeneous field therefore broadens each of these lines, typically only smearing the three out into a single peak if the magnetic field passes through zero in the experimental volume. In practice, it is simple to maintain the magnetic field < 0.1 Gauss during the experiment, so all three Δm transitions fall within the Doppler envelope.

Collisional effects scale rapidly with n^* and form the most important source of competing dephasing in typical Rydberg experiments. Long range dipole-dipole mediated Rydberg-Rydberg collisions homogeneously dephase individual emitters at a rate of [152]

$$\gamma_{dd} = \frac{\pi \mu^2 \rho}{4\epsilon_0 \hbar} \tag{4.4}$$

compared to a superradant decay rate of

$$\gamma_{SR} = \frac{1}{T_R} = \frac{\pi \mu^2 \rho}{3\epsilon_0 \hbar} \frac{L}{\lambda}. \tag{4.5}$$

The two rates are essentially equivalent to within a geometric factor of L/λ. For extended sample geometries, as in my experiments, $L \gg \lambda$, thus the superradiant decay rate can be orders of magnitude faster than the rate of homogeneous dipole-dipole dephasing. Rydberg superradiance experiments that take place in, for example,

magneto-optical traps may sample larger absolute densities, but do not routinely exhibit superradiance due to this competing dephasing rate [102]. Collisions of Rydberg states with neutral buffer gas atoms from the buffer gas expansion do not scale with n^*. This is because at high enough n^* ($\gtrsim 20$), the elastic collisional cross section (which determines the magnitude of the dephasing) is governed entirely by the collisional cross section between the buffer gas atom and the ion-core [4].

Taking the above shift and broadening mechanisms into account, the optimal experimental parameters to observe superradiance are to use as high n^* as possible without compromising the value of L/λ or suffering too large an effect from electric fields. In the following experiment, $L \approx 15$ cm and $n^* \approx 30$, so $\lambda \approx 1$ mm and $L/\lambda \approx 150$, which means that dipole-dipole mediated collisions are not relevant to these experiments.

In the fully quantum theory developed by Yelin [120, 2], the induced cooperative line shift scales as the relative density

$$RD = \rho\lambda^3. \tag{4.6}$$

This term scales as n^{*9}, significantly faster than the optical depth (n^{*6}), which is the value on which all other observables depend. Therefore, Rydberg states are ideal for observing induced cooperative line shifts, as they will be larger relative to other superradiant effects than in other systems where $L \leq \lambda$.

The energy level diagram relevant for the experiments discussed below is shown in Figure 4-2. A single UV laser pulse (from the Scanmate laser and doubled in a β-BBO crystal) populates the $6s30p\ ^1P_1$ state of Ba. This creates two separate inverted two-level systems. The primary focus of this chapter is on the two-level system formed between the $6s30p$ state and the $6s28d\ ^1D_2$ state. However, a second two-level system, formed between the $6s30p$ state and the $6s30s\ ^1S_0$ state, is more strongly cooperative than the first and can spontaneously decay by superradiance. Unfortunately, the frequency of this transition is outside of the bandwidth of both of the millimeter wave spectrometers I had available. I was, however, able to monitor

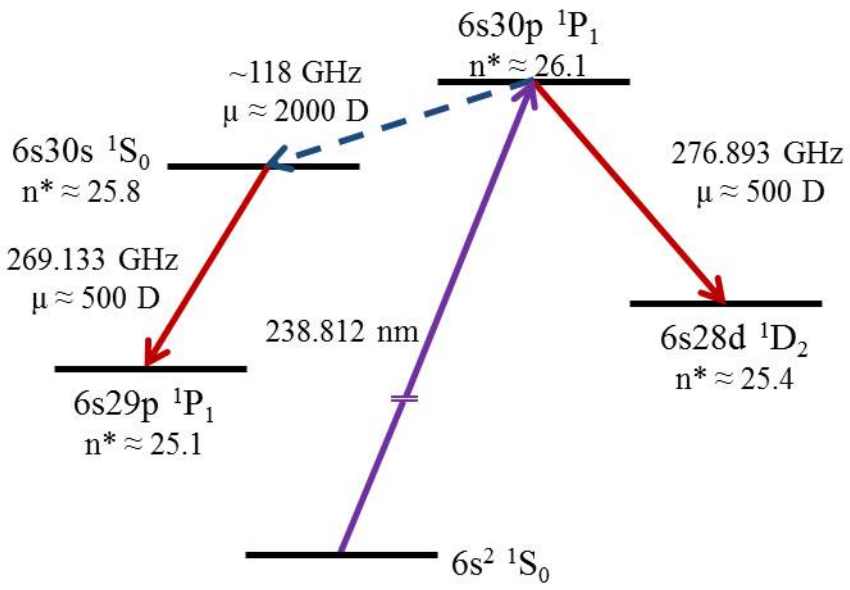

Figure 4-2: Energy level diagram of the relevant states of barium involved in my superradiance experiments. The purple arrow indicates the 238.812 nm laser pump pulse. The two red arrows indicate the two observable transitions corresponding to the $30p \rightarrow 28d$ and $30s \rightarrow 29p$ transitions. The blue dashed line indicates the untriggered superradiant transition $30p \rightarrow 30s$ that was unobservable in my experimental setup.

this spontaneous process by probing the transition between the $6s30s$ and $6s29p$ $^1P_1$ states. Often, enough population was superradiantly transferred to the $6s30s$ state that I could observe cascade superradiance between the $6s30s$ and $6s29p$ states.

4.2 Initial observation of untriggered superradiant decay

While previous experiments had observed superradiance as the leading source of homogeneous broadening in FID experiments [8, 9], and had even directly observed the superradiant burst of emitted radiation in averaged experiments [10], superradiance had not been observed in either a single shot or to occur without an external trigger. Initial experiments observing FID between Ba Rydberg states were made more difficult by the failure to consistently reproduce signal levels and the appearance of several initially unexplained strong transitions. Both of these anomalies are explained

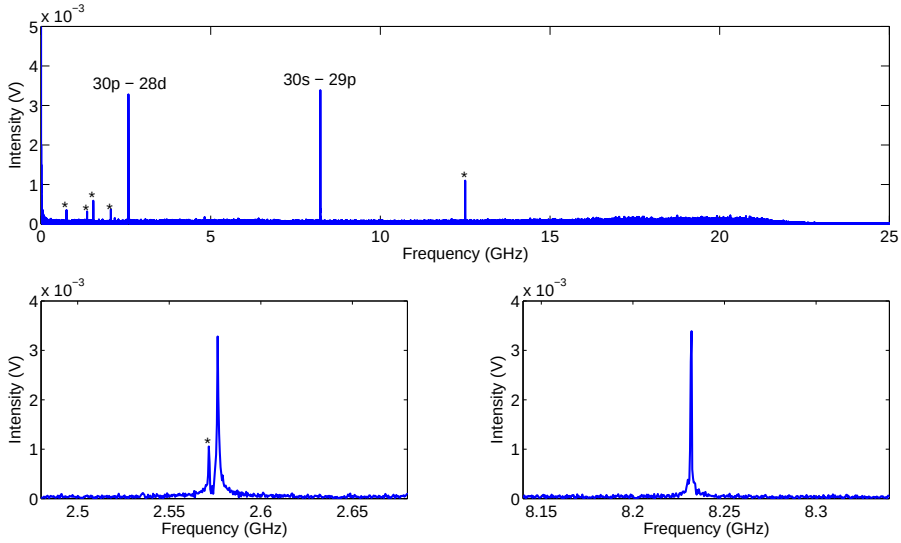

Figure 4-3: Sample spectrum displaying the relative intensities of the $30p \rightarrow 28d$ and $30s \rightarrow 29p$ transitions. The features marked with asterisks (*) are artifacts of the detection system. The frequency axis is the heterodyne-detected frequency, not the actual atomic transition frequencies. This spectrum was performed with a 100 ns delay between the optical preparation and mm-wave probe.

by spontaneous superradiant emission.

A sample spectrum of 100 averages obtained from the Ba system described in Section 4.1 is displayed in Figure 4-3. In these experiments, barium atoms were optically pumped to the $6s30p$ state with a single UV laser, as in Figure 4-2. The mm-wave transitions were then probed by a 100 ns duration 35 GHz chirp (260-295 GHz) after a selected delay (between 10 ns and 1 μs). All resonant transitions in this frequency range then decayed via FID at their resonant frequency with relative intensities related to their absolute populations in the laser populated sample and sample polarizations.

Transitions between the $6s30p$ and $6s28d$ states and the $6s30s$ and $6s29p$ states are both marked in the spectrum. However, the $30s \rightarrow 29p$ transition was not observed in every laser shot. The intensity of the $30s \rightarrow 29p$ transition as a function of time is shown in Figure 4-4 where each point on the x-axis represents a single shot. The fluctuations in the strength of the $30s \rightarrow 29p$ transition indicate that the superradiant decay to the $30s$ state does not always occur at a delay shorter than 100 ns.

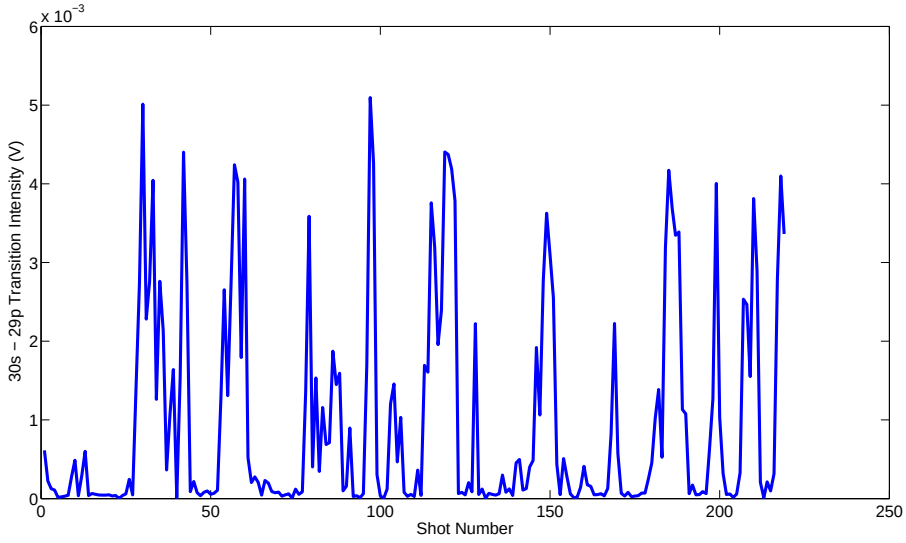

Figure 4-4: Shot to shot variation in the intensity of the $30s \rightarrow 29p$ transitions as a function of time. Each point on the x-axis represents a single shot of the experiment.

The relative intensity of the two transitions can be used as a probe of the extent of the superradiant process. As the delay between laser excitation and mm-wave probe is increased, the intensity of the $30s \rightarrow 29p$ transition becomes larger relative to the intensity of the $30p \rightarrow 28d$ transition, as shown in Figure 4-5. This is due to population in the $6s30p$ state consistently superradiantly decaying into the $6s30s$ state as the delay between the pump and probe pulses increases. The opposite can be observed when increasing the pump laser intensity, as shown in Fig. 4-6. As the energy of the pump laser pulse decreases, the strength of the $30p \rightarrow 28d$ transition decreases, but the strength of the $30s \rightarrow 29p$ transition decreases significantly faster, and becomes essentially unobservable below a pump laser pulse energy of 150 μJ. This is caused by a change in the initial Rydberg density in the $6s30p$ state. The signal intensity of the transition from the $6s30p$ state scales as ρ, but the cooperativity of the transition to the $6s30s$ state (and hence the signal intensity from the $6s30s$ state) scales as ρ^2.

However, investigation of novel cooperative effects (such as cooperative frequency shifts and broadenings) requires direct observation of the emitted superradiant electric field, and not simply indirect observation of states acquiring population as a secondary

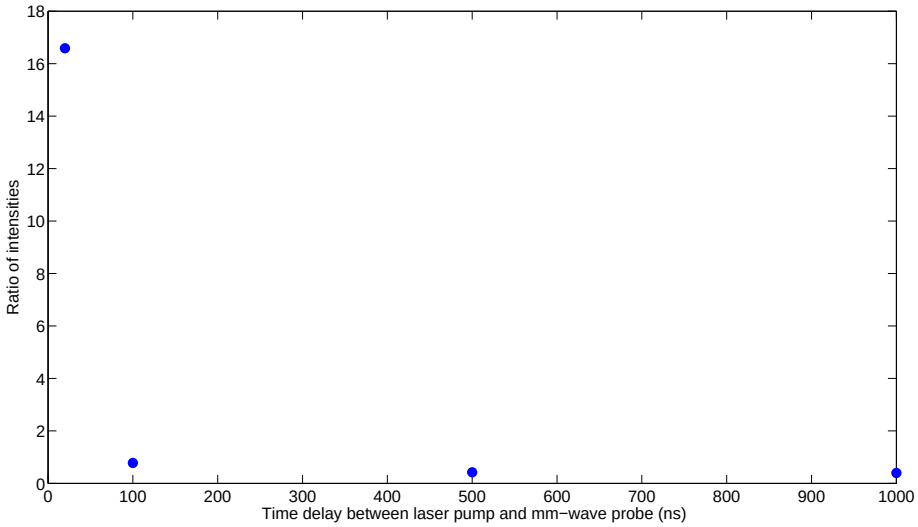

Figure 4-5: Ratio of the intensity of the $30p \rightarrow 28d$ transition to the intensity of the $30s \rightarrow 29p$ as a function of the time delay between the laser pump pulse and mm-wave probe pulse. The ratio decays monotonically with delay time.

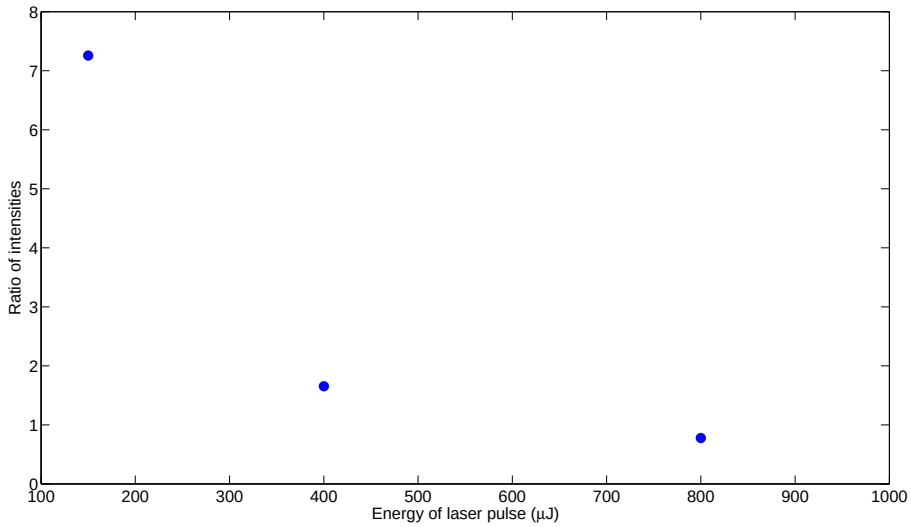

Figure 4-6: Ratio of the intensity of the $30p \rightarrow 28d$ transition to the intensity of the $30s \rightarrow 29p$ as a function of the energy of the pump laser pulse.

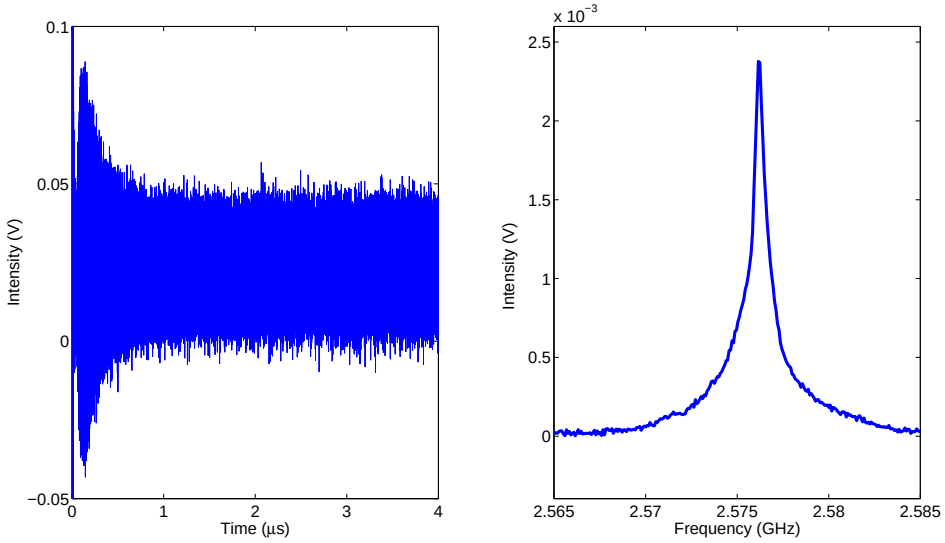

Figure 4-7: Averaged time-domain and frequency domain observation of superradiant emission in dense samples of barium atoms. The time-domain data display a clear initial increase in intensity as opposed to the monotonic decrease typical of a standard FID signal. The frequency-domain data displays an asymmetric line shape with a long tail to the low frequency side.

effect of superradiant decay. As such, I investigated the $30p \rightarrow 28d$ transition to see whether there was sufficient cooperativity to observe superradiant decay. Averaged results from this investigation are displayed in Figure 4-7. Superradiant decay on a time scale ($\ll 1$ μs) faster than any other dephasing process (~ 5 μs) can be clearly seen as an initial increase in the emitted electric field, unlike the typical monotonic decrease of FID radiation in less cooperative systems. However, each averaged shot has a different Rydberg number density due to fluctuations in both the atomic beam loading process and the excitation dye laser intensity. In order to perform a more systematic investigation of cooperative effects, I found it necessary to observe the data on a shot-by-shot basis.

4.3 Single-shot superradiance

An example of the detected emitted electric field from a highly cooperative sample observed in a single shot is displayed in Figure 4-8, along with a zoom-in of the

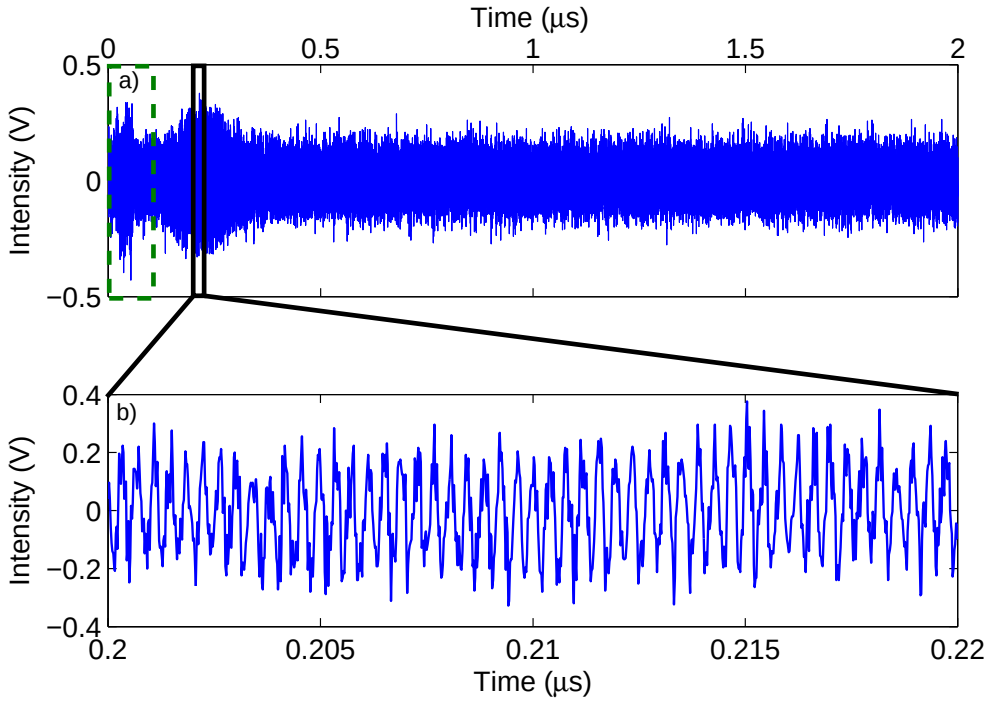

Figure 4-8: a) Raw *single-shot* data trace recorded in the time-domain in my superradiance experiments. The early dashed-boxed feature is the tipping pulse that initiates the superradiance, and the large feature is the superradiant emission. b) A zoom-in of the later solid-boxed portion of the raw data trace from part a. displaying that the signal is visable without filtering, but at a weak S:N ratio.

strongest portion of the signal. While some of the signal is clearly visible, the signal-to-noise (S:N) ratio is not large enough to perform any meaningful analysis. This signal was obtained by using a small 'tipping' mm-wave pulse to initiate the superradiant emission at a well-defined time and phase, and is observable in the boxed region of Fig. 4-8. This tipping pulse induced a $\pi/40$ polarization of the sample, too small to be observable in a single-shot without cooperative enhancement. The characteristic increase of emitted electric field is clearly visible even with the low S:N ratio.

Upon Fourier transformation, however, the S:N ratio is on order of 100:1, as shown in Figure 4-9. The Fourier transform was time-gated to exclude the tipping pulse. The broad peak is due to the superradiant emission, while the narrow peak is caused by other processes, which are discussed in Section 4.4. Due to the ~ 40 GHz detection bandwidth of the mm-wave spectrometer, most of the noise observed in the time-domain occurs at frequencies far from the resonance frequency. In order to combat

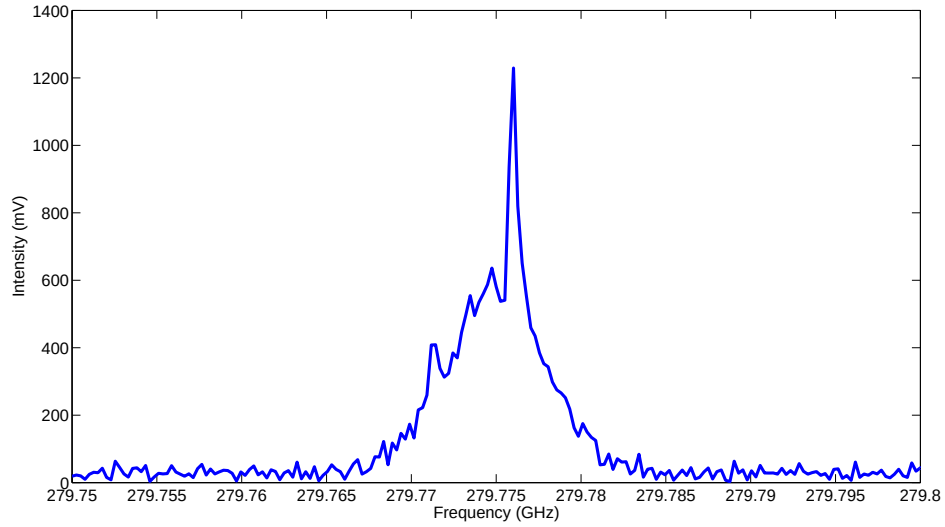

Figure 4-9: The Fourier transform of the raw data from Figure 4-8a. The data from the frequency-domain shows a narrow peak at the low-density resonance frequency and a broad peak shifted to lower frequency.

this effect, I performed post-detection digital filtering of the time-domain data.

In order to filter the data, I first obtained the resonance frequency of the $6s30p \rightarrow 6s28d$ transition from low density samples (276.893 GHz). I then multiplied the superradiant time-domain signals by a sine (cosine) wave at this frequency and employed a 25 MHz classic type I finite impulse response (FIR) zero-phase low-pass filter in order to acquire the in-phase (quadrature) component of the emitted electric field. I then calculated the time-dependent radiated electric field amplitude and phase with $I(t) = s^2 + c^2$ and $\phi(t) = \tan^{-1}(s/c)$, where s and c are the in-phase and quadrature components of the signal. The phase is calculated using a four quadrant arctangent function. An example of the filtered electric field amplitude is shown in Figure 4-10. This filtered amplitude is taken from the same shot as the unfiltered time-domain data of Fig. 4-8. The phase evolution associated with the filtered electric field amplitude from Fig. 4-10 is displayed in Fig. 4-11.

The time-domain signal can be fit to the hyperbolic secant lineshape function predicted by the semi-classical theory discussed in Section 3.2.2, fitting both the superradiance emission time (T_R) and the superradiance delay time (T_D) simultane-

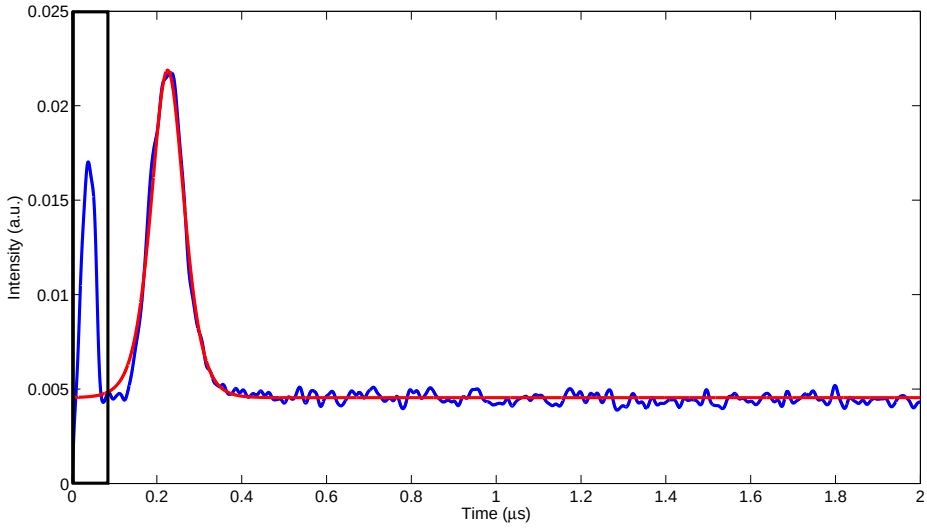

Figure 4-10: The digitally filtered electric field intensity profile from the raw data in Figure 4-8a is shown in blue, and the fit to the mean-field emission functional form is shown in red. The boxed feature is the tipping pulse that triggers the superradiance.

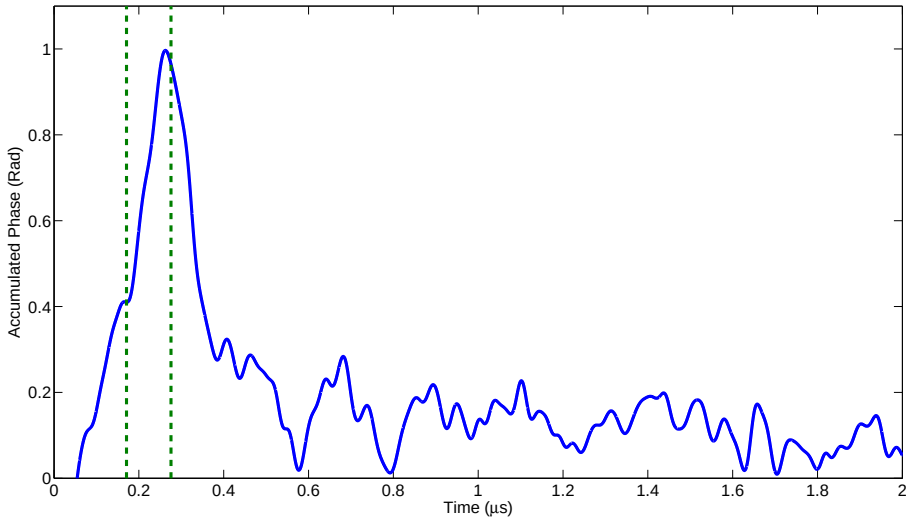

Figure 4-11: The recorded phase as a function of time from the raw data from Figure 4-8a, obtained by demodulation at the low-density resonance frequency. The green dashed lines indicate the time FWHM of the superradiant field amplitude. A positive slope indicates a frequency that is shifted below the resonance frequency, while a negative slope indicates a shift above the resonance frequency.

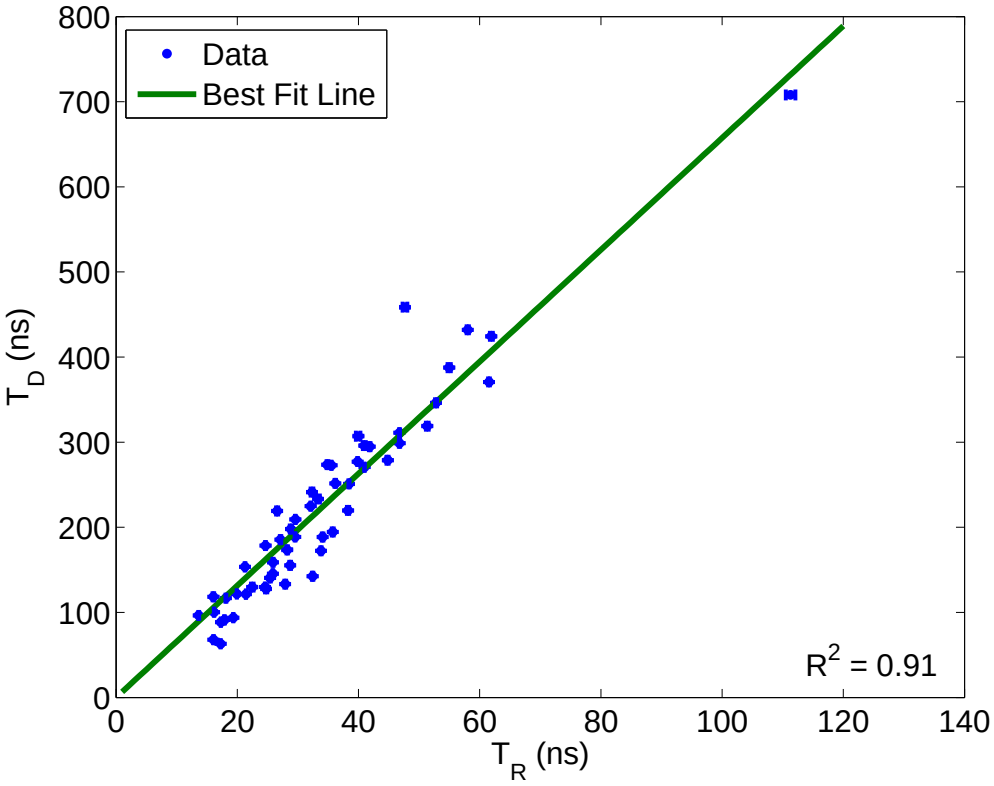

Figure 4-12: Relationship between the separate fitting parameters, T_R (characteristic superradiance emission time) and T_D (superradiance delay time). Blue points are the data and the green line is the best fit to the data. The error bars represent 95% confidence intervals.

ously. An example of this fit is shown as the red curve in Figure 4-10. In order to confirm that the model used to interpret the data is appropriate, I plot T_R vs. T_D in Fig. 4-12. Since $T_D = 2T_R \log(\theta^i/2)$ [1], I expect a linear correlation with a slope that is directly related to the initial tipping angle of the triggering pulse. The linear correlation between T_R and T_D is clear, and the tipping angle extracted from the relationship between T_R and T_D matches the directly measured value of $\theta^i = \pi/40$. This agreement with the semi-classical expectations for the emitted signal implies that I can in principle use the semi-classical theory to determine the optical depth of the sample on each single shot. Optical depth is related to the superradiance emission time T_R through Equation 4.1.

Unfortunately, due to the presence of an uncontrolled and unobserved decay path-

way, I cannot connect optical depth to either absolute or relative density. The uncontrolled decay to the $6s30s$ state occurs at both an unknown time and unknown location in the sample, leading to shot-to-shot fluctuations in the length, L, of the sample. I can detect whether this uncontrolled decay has occurred by probing the $6s30s \rightarrow 6s29p$ transition, which becomes superradiant when significant population is transferred to the $6s30s$ state. I can use the filtering process above in order to determine the electric field amplitude of this second superradiant transition. An example of a pre- and post-filtered shot, where both transitions are superradiant, is displayed in Figure 4-13. The Fourier transform of this shot, with zoom-ins on both transition frequencies, is shown in Fig. 4-14.

Despite knowing *whether* an uncontrolled superradiant decay has occurred, I still lack the information required to determine *where* in the active region such a transition occurred, and *how much* of the original sample decayed. I have attempted to determine the relative populations involved in each superradiant transition from the relative amplitudes of the emitted fields. In principle such a measurement is possible, but simply knowing the number of emitters (obtained from the amplitudes of the emitted fields) does not allow me to separately determine density and optical depth (obtained from comparisons to semi-classical theory).

For future experiments, two changes would be required to separate optical depth from (relative) density. First, a state that only has one superradiant mode should be excited. This can easily be done by exciting to an ns state that can only decay to an $n'p$ state. Second, atomic absorption spectroscopy should be performed simultaneously with the mm-wave experiments in order to determine an accurate *absolute* number density of Rydberg states.

4.4 Superradiance induced frequency shifts

Despite the good agreement of the envelope of the time-domain data with the semi-classical theory, a detailed investigation of the data in the frequency domain reveals several significant departures that can only be explained by a fully quantum calcu-

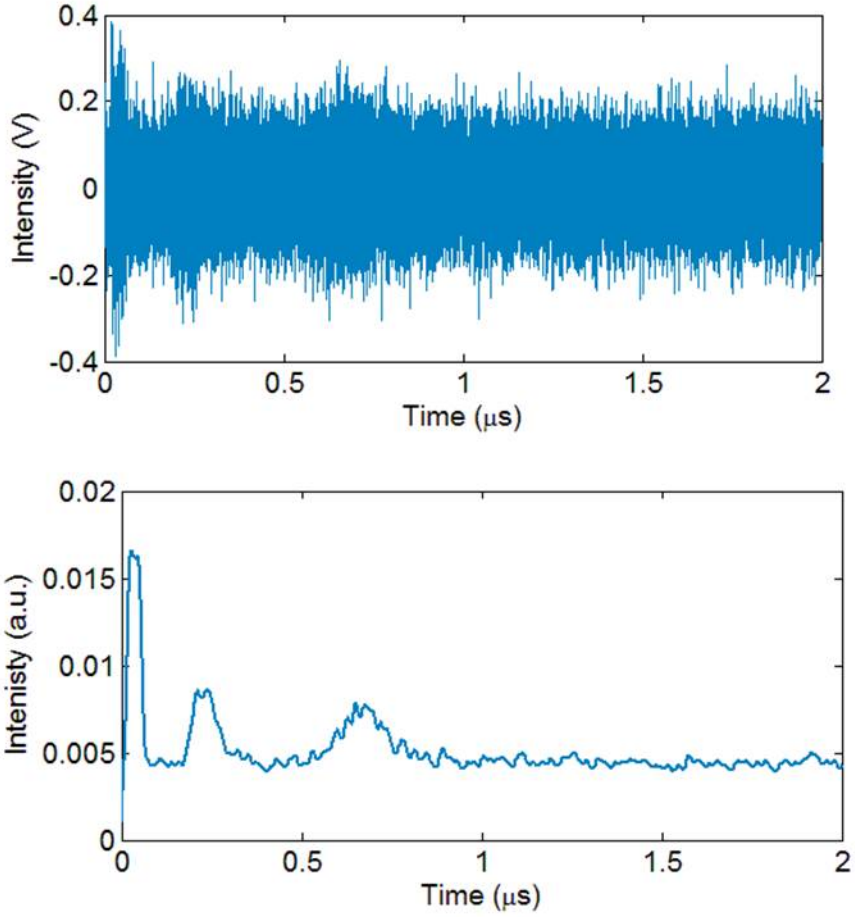

Figure 4-13: The top plot displays the raw *single-shot* data of a sample that superradiantly emits on two separate transitions. The bottom plot displays the digitally filtered electric field intensity profile of the top plot.

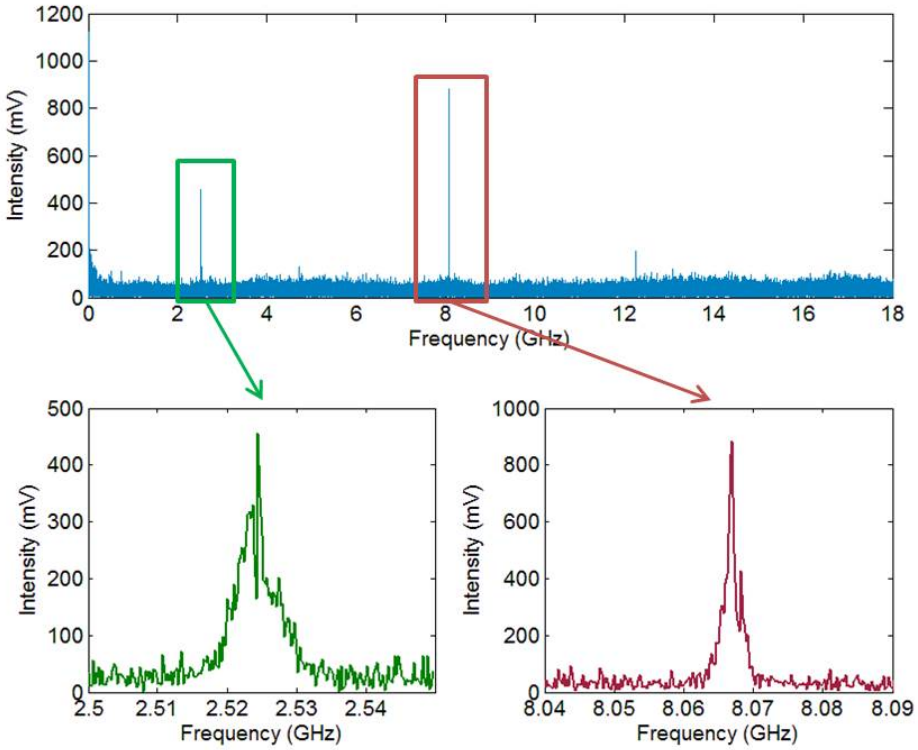

Figure 4-14: The top plot displays the Fourier transform of the single-shot data from Figure 4-13. The bottom plots display the lineshapes of the $30p \rightarrow 28d$ (left, green) and $30s \rightarrow 29p$ (right, red) transitions. The FWHM of the $30p \rightarrow 28d$ transition is ~ 1 GHz and the FWHM of the $30s \rightarrow 29p$ transition is ~ 400 MHz.

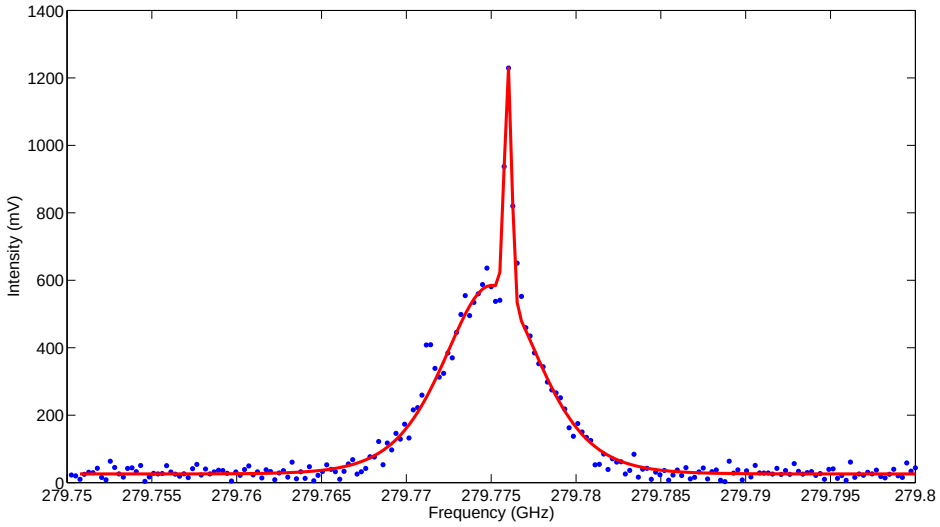

Figure 4-15: The fit (red curve) of the Fourier transform of the data (blue points) from Figure 4-8a. This fit is to a sum of two lineshape functions, a narrow Gaussian centered at the low-density resonance, and a broad hyperbolic secant centered at lower frequency than the low-density resonance.

lation. The Fourier transform of Figure 4-8a, gated to exclude the tipping pulse, shown along with a fitted lineshape, is shown in Fig. 4-15. The fitted lineshape is a sum of a narrow Gaussian peak, centered at the low-density resonance frequency, and a hyperbolic secant peak, the center frequency of which was a fittable parameter. The broad feature is associated with the superradiant emission, has a FWHM of ~ 6 MHz, and is red-shifted ~ 2 MHz below the low-density transition frequency. The narrow feature has a FWHM consistent with Doppler broadening (~ 250 kHz) and no observable shift from the low-density transition frequency. When performing a Fourier transform with a longer time gate that excludes both the initial tipping pulse and the superradiant pulse, only the narrow feature remains.

The integrated area under the broad and narrow lineshapes vary with the same dependence on optical depth. This implies that both signals are fully cooperative in nature. If the narrow feature were generated exclusively in low density regions of the sample, I would expect the area associated with superradiant signal to decrease faster than that associated with the narrow signal, as emitters that were not in a sufficiently dense volume of the sample would contribute to the narrow signal instead of the su-

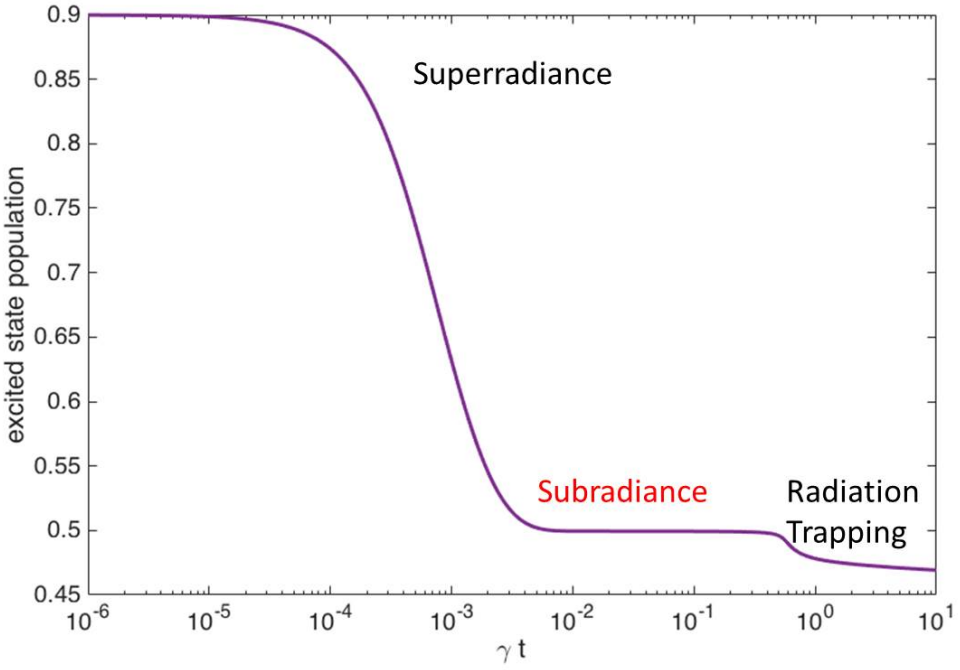

Figure 4-16: The calculated excited state population of a highly cooperative system as a function of time. The calculations were performed by Susanne Yelin and provided for this thesis, following the second-order master equation method described in Section 3.3.3. The x-axis is on a log scale and measured in units of natural lifetimes, γ, for isolated atom emission. The large decrease in excited state population is indicative of superradiance, with the long-plateau following being indicative of subradiance. Radiation trapping occurs at times much longer than a natural lifetime. Note that the final measurable excited state population is still $> 45\%$, even after 10 natural lifetimes.

perradiant signal. This narrow signal is likely due to subradiance. This interpretation is supported by theoretical predictions from the Yelin group [120]. As displayed in Figure 4-16, fully quantum simulations predict a transition from superradiant to subradiant behavior with a long time evolution to radiation trapping behavior (incoherent absorption and re-emission of photons). As my heterodyne detection system only detects coherent radiation, I tentatively assign this narrow feature as subradiance, but given that I cannot measure a linewidth narrower than the radiative lifetime (and in practice, I cannot measure a linewidth narrower than the Doppler broadening, or blackbody broadening in the case of a photon-echo experiment), I cannot state with certainty that this signal is due to subradiance.

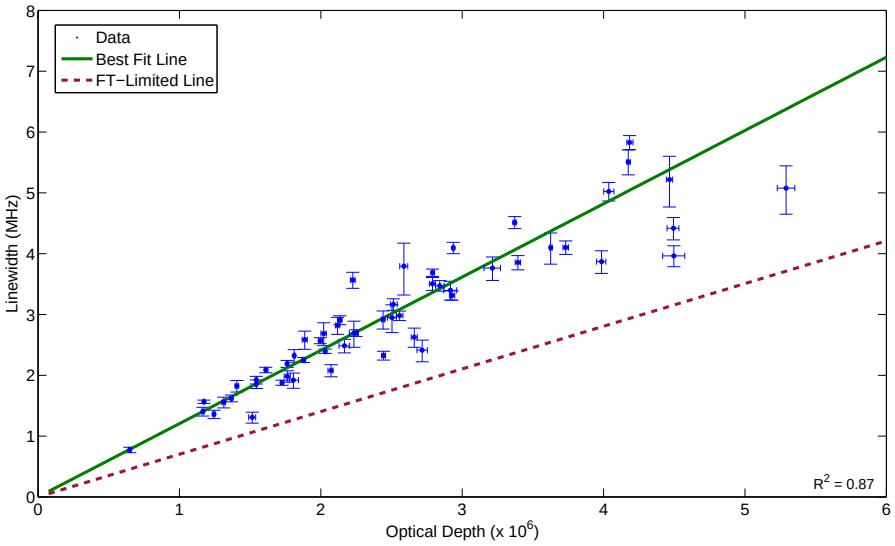

Figure 4-17: The relationship between the optical depth of a superradiant sample and the linewidth of the emitted radiation. Blue points are the data, the green line is the best fit to the data, and the red dashed line is the linewidth expected if the emission were Fourier transform limited. The error bars represent 95% confidence intervals.

There are two important features of the frequency of the superradiant emission: the broadening and the shift. I focus first on the broadening. The relationship between the width of the superradiant emission peak and the optical depth of the sample determined from T_R is shown in Figure 4-17. The green line shows the least-squares linear fit to the data, while the red dashed line shows the value of the Fourier transform limited linewidth associated with a time domain hyperbolic secant signal with characteristic width T_R. The superradiant emission is consistently broader than the Fourier transform limit, and is well correlated with the optical depth. In principle, the observed excess frequency width could be due to either a frequency chirp during the emission process, or a dephasing process (e.g. inhomogeneous dipole-dipole dephasing). Since I directly detect the emitted electric field in the time domain, any dephasing process would be immediately apparent as destructive interference, which shortens the emitted superradiant pulse. Therefore, the excess width implies that the frequency chirps across the linewidth of the emission feature.

This frequency chirp is most directly measured by observing the accumulated phase of the emitted radiation, because the instantaneous frequency is determined

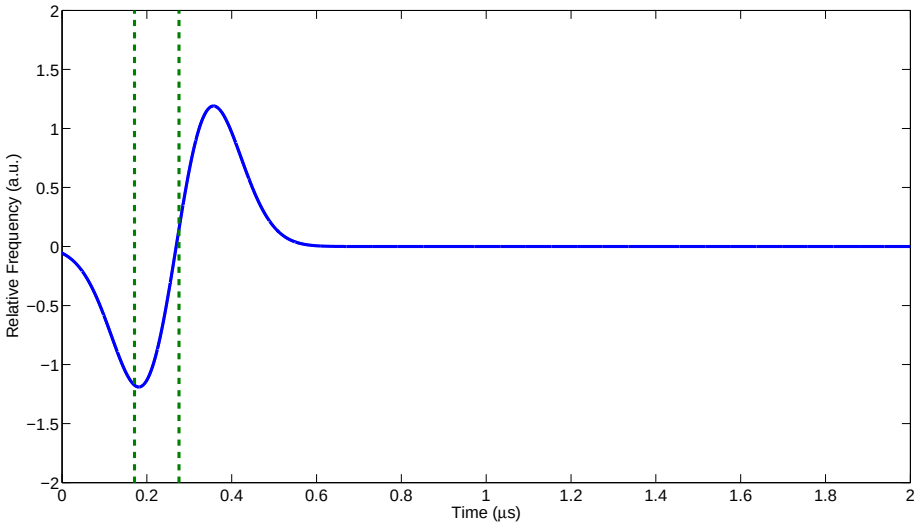

Figure 4-18: The fitted frequency evolution associated with the phase evolution from Figure 4-11 using a Gaussian as a fitting function. The green dashed lines indicate the time FWHM of the superradiant emission amplitude. The frequency is taken relative to the low-density resonance.

by the time derivative of the phase. The accumulated phase is directly sampled by our methods of detection and filtering. The blue solid trace in Figure 4-11 displays the phase evolution of the single-shot data trace in Fig. 4-10. In the absence of a model for the frequency and hence the phase evolution of the sample, I fit the phase evolution to a series of lineshape functions (Gaussian, Lorentzian, hyperbolic secant) and computed the derivative of each in order to determine the frequency as a function of time. Qualitatively, each lineshape fit model produced the same result. The frequency evolution determined from the Gaussian fit is shown in Fig. 4-18, plotted relative to the low-density emission frequency. The previously discussed frequency chirp that is implied by the excess frequency-domain width is clearly present.

Additionally, the time at which the maximum in the phase evolution occurs (and frequency crosses through the low-density resonance frequency) does not coincide with the envelope of the field amplitude in the time domain. The time FWHM of the superradiant emission amplitude is displayed by the vertical green dashed lines in Figs. 4-11 and 4-18 to demonstrate this offset. This mismatch between the phase evolution and the electric field envelope is the cause of the observed frequency shift. I base

this claim on the observation that the emission is most intense while the frequency is shifted away from the low-density value, despite the fact that the frequency chirp is symmetric around the low-density frequency. In a fully quantum mechanical many-body treatment, both a chirp and an overall shift to lower frequencies are predicted during the maximum amplitude of the superradiant emission. These calculations predict a large red shift during the maximum amplitude of the superradiant emission [2]. After the time at which the maximum amplitude occurs, the frequency chirps towards a long-lived blue shift at long times, in qualitative agreement with our observations. The apparent blue chirp in our experiments occurs after the superradiant emission has concluded and is likely an artifact of the filtering method (as the phase of zero signal must be zero). Comparisons can presently be made only at a qualitative level, due to the vastly larger optical depth in our experiment than is currently tractable in simulations. Qualitative results are displayed in Fig. 4-19.

The relationship between the frequency shift of the superradiant emission and the optical depth determined from T_R is shown in Figure 4-20. There is only a weak correlation between the optical depth and frequency shift, showing that some other terms must contribute to the frequency shift. Quantum many-body calculations indicate that the relative density, not the optical depth, has the largest effect on the induced lineshift of the superradiance. The calculated effect of holding the relative density constant while increasing the length (and therefore optical depth) of the sample is shown in Fig. 4-21 [2]. Unfortunately, as discussed in Section 4.3, it was not possible in my experiments to determine either the absolute or relative density of emitters, due to the presence of an uncontrolled decay pathway.

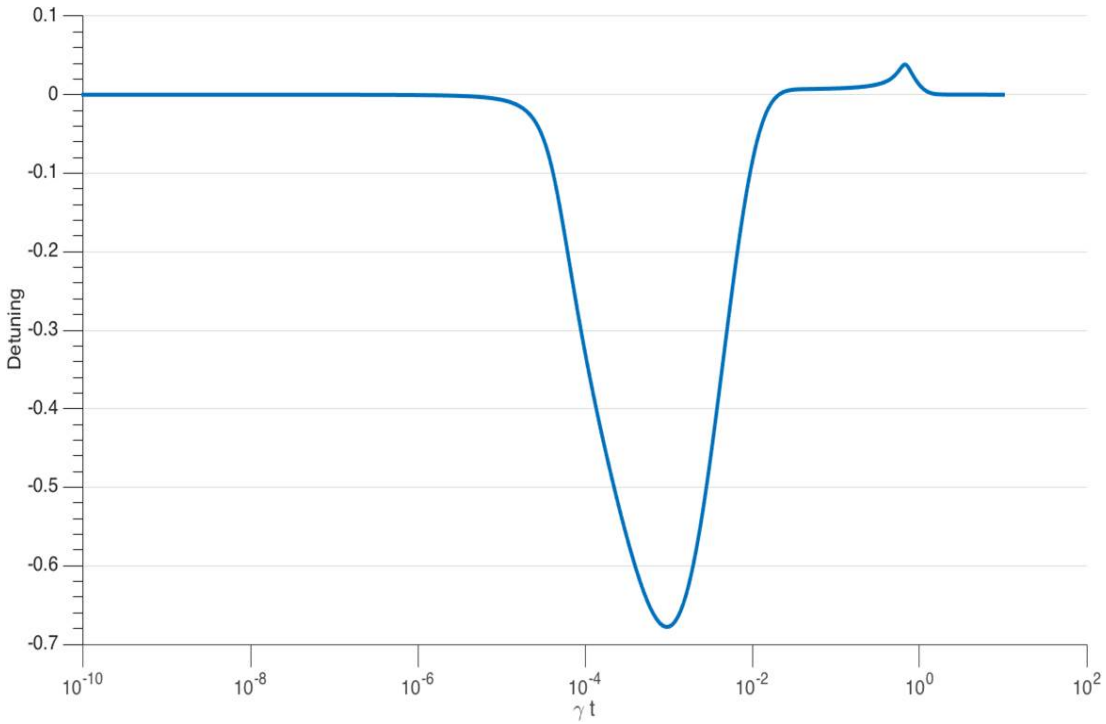

Figure 4-19: The calculated frequency shift of a strongly cooperative system as a function of time. The calculations were performed by Susanne Yelin and provided for this thesis, following the second-order master equation method described in Section 3.3.3. The x-axis is on a log scale and measured in units of natural lifetimes for isolated atom emission. The y-axis is measured in arbitrary units. There is a large red shift during the superradiant emission (at $\sim 10^{-3}$ γt, compare to Fig. 4-16), and a small blue shift during subradiant emission (at ~ 100 γt).

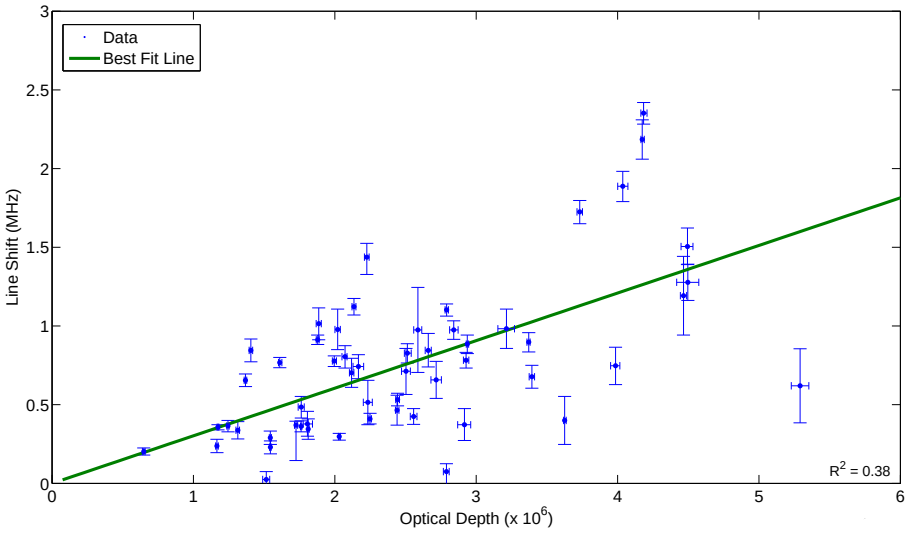

Figure 4-20: Relationship between the optical depth of a superradiant sample and the frequency shift. Blue points are the data and the green line is the best fit to the data. The error bars represent 95% confidence intervals.

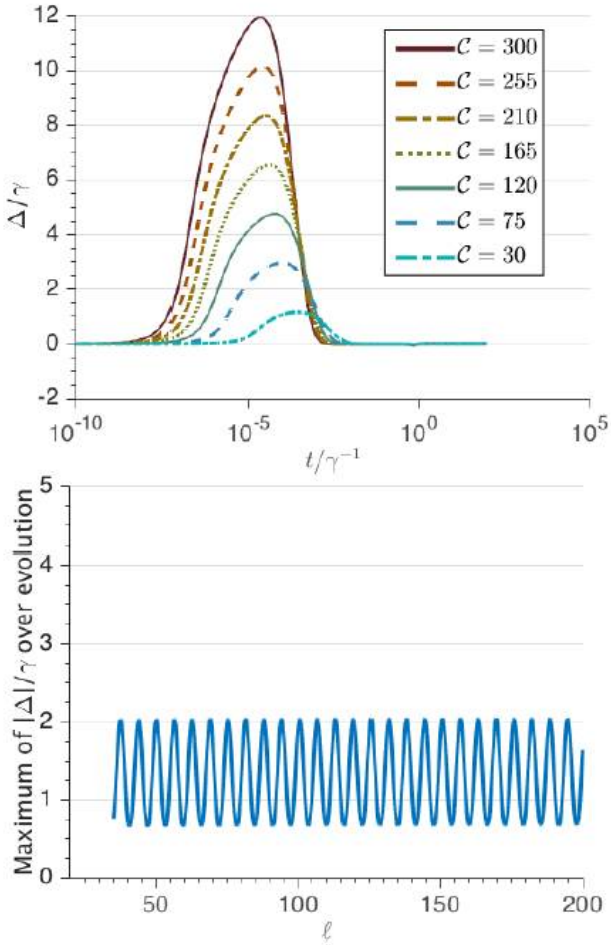

Figure 4-21: The top plot displays the calculated frequency shift as a function of Optical Depth (displayed here as $\mathcal{C}$). The bottom plot displays the calculated frequency shift at a constant density and a varying length. The calculations were performed by Susanne Yelin and provided for this thesis, following the second-order master equation method described in Section 3.3.3. The x-axis of the top plot is on a log scale and measured in units of natural lifetimes for isolated atom emission. The y-axis of the top plot is the frequency shift measured in multiples of the natural linewidth. The y-axis of the bottom plot is the maximum extent of the frequency shift evolution. Note that, in the bottom plot, although the optical depth increases linearly with ℓ, the frequency shift exhibits only a small sinusoidal oscillation. Figure reproduced from Ref. [2]

Chapter 5

STIRAP Theory

In this chapter I discuss the theory behind STImulated Raman Adiabatic Passage (STIRAP) and methods for performing simulations based on the parameters for realistic systems. In Section 5.1 I provide a motivation for robust, high-fidelity methods of population transfer and provide an introduction to one- and two-photon methods of population transfer. In Sec. 5.2 I carefully derive the equations that describe the STIRAP process, explore some instructive analytical results, and outline the basics of the calculations used in simulating STIRAP. In Sec. 5.3 I apply these calculations to realistic systems, adding complexity stepwise until all essential aspects of the real system are accounted for.

5.1 An introduction to population transfer methods

Rydberg states of molecules can be divided into two categories: core-penetrating (CP) and core-nonpenetrating (CNP) states. CP states are those in which the wavefunction of the Rydberg electron has significant amplitude within the ion-core because it possesses a relatively low orbital angular momentum, ℓ. However, owing to multipolar mixing that occurs when the Rydberg electron is near the ion-core, ℓ is typically not a good quantum number in molecules. These CP states are usually easy to access from low-lying electronic states (usually the ground state) because of optical transition selection rules, and have been widely studied. CNP states are those with

relatively large orbital angular momentum ($\ell > 4$, in general) and small quantum defects ($\delta_\ell < 0.05$), and have received considerably less attention, largely due to the difficulty in accessing them via standard optical transitions from low-lying valence states. Owing to the $\ell(\ell+1)/r^2$ centrifugal barrier in the effective radial potential of the Rydberg electron, predissociation lifetimes of CNP states are generally on the order of 10^{-7} to 10^{-4} s, amenable to FID detection (requiring 1-10 μs), compared with 10^{-11} to 10^{-9} s for CP states [16, 17].

Traditional incoherent multiple resonance techniques, by which a system's population is transferred one step at a time, are generally incapable of transferring a detectable population into CNP states by transit through a CP state with a nanosecond or shorter lifetime. Coherent population transfer methods, such as STIRAP, on the other hand, are well suited for efficient transfer of population to CNP states while avoiding the large decay rates associated with the easily accessible CP states. STIRAP has been demonstrated in a variety of systems to be capable of robust 100% population transfer through a short lifetime state (and even roughly 20% population transfer through a continuum).

In order to describe this method of transfer, I briefly describe one- and two-photon methods for population transfer in Sections 5.1.1 and 5.1.2, respectively.

5.1.1 Two-state, one-photon methods

Even for the relatively simple case of a two-state interaction, there are still many ways in which one could transfer population from an initially populated ground state, $|1\rangle$, to a final state, $|2\rangle$. The most obvious method is interaction with a photon the energy of which matches the energy difference between the quantum states. The fidelity and robustness of this process depend on the coherence characteristics of the oscillating electric field of the electromagnetic radiation. Here I use the phrase 'fidelity' to describe how efficiently a process transfers population from state $|1\rangle$ to state $|2\rangle$, and the phrase 'robustness' to describe how strongly a process depends on experimental parameters (e.g. electric field magnitude of the light source) to achieve its maximum fidelity.

Excitation involving incoherent light may be described using differential equations for excitation probabilities with Einstein coefficients as rate constants for absorption and stimulated emission [153]. For the purposes of this introduction, I ignore spontaneous emission from both states. The differential equations that describe this situation are

$$\frac{dN_1}{dt} = -B_{12}^{\omega} F(t) N_1 + B_{21}^{\omega} F(t) N_2 \tag{5.1}$$

$$\frac{dN_2}{dt} = -B_{21}^{\omega} F(t) N_2 + B_{12}^{\omega} F(t) N_1 \tag{5.2}$$

where N_1 and N_2 are the fraction of particles in the initial and final states, B_{12}^{ω} and B_{21}^{ω} are the Einstein coefficients for absorption and stimulated emission, and $F(t)$ is the energy density per unit *angular frequency* (measured in radians/sec) as a function of time, and is assumed to be constant over the frequency range of the transition. The Einstein coefficients can be written as

$$B_{21}^{\omega} = \frac{\pi^2 c^3 A_{21}}{\hbar \omega_{21}^3} = \frac{3\epsilon_0 \hbar^2}{\pi} \mu^2 \tag{5.3}$$

$$B_{12}^{\omega} = \frac{g_2}{g_1} B_{21}^{\omega} \tag{5.4}$$

where g_1 and g_2 are the degeneracy factors of the two levels, ω_{21} is the transition frequency in radians/sec, and A_{21} is the Einstein coefficient for the spontaneous decay rate. Note that, if I had defined $F(t)$ in terms of *regular frequency* (measured in cycles/sec or Hz) instead, there would be an extra factor of 2π in these definitions, such that $B_{21}^{f} = B_{21}^{\omega}/2\pi$. Attention to the difference between angular frequency and regular frequency is essential to performing accurate calculations.

Assuming that all of the particles are in the initial state at $t = 0$, these differential equations have a simple solution that gives the fraction of population in the final state as

$$N_2(t) = \frac{g_2}{g_1 + g_2}\left(1 - e^{-\frac{g_1}{g_1+g_2}B_{21}^{\omega}G(t)}\right), \tag{5.5}$$

where $G(t)$ is the integral of the time-varying energy density per unit angular frequency

$$G(t) = \int_{-\infty}^{t} F(t')dt'. \tag{5.6}$$

Equation 5.5 shows that N_2 increases monotonically as excitation duration and excitation energy density increase, eventually saturating at a value of g_2/g_1+g_2. This form of excitation can be said to lack fidelity (being limited by the ratio of degeneracies of the two states), but is exceptionally robust with respect to experimental changes once the saturated regime has been reached.

The discussion of the interaction of coherent light with a two-level system is fundamentally different, and must begin with the time-dependent Schrödinger equation [154]. I describe the electric field as being monochromatic with constant frequency ω and a slowly-varying envelope $\mathcal{E}(t)$. In the interaction representation and following the Rotating Wave Approximation (RWA), the Hamiltonian used in this case is

$$\hat{H}_I(t) = \frac{\hbar}{2}\begin{bmatrix} 0 & \Omega(t) \\ \Omega(t) & 2\Delta \end{bmatrix} \tag{5.7}$$

$$\Omega(t) = \frac{\mu\mathcal{E}(t)}{\hbar} \tag{5.8}$$

where Ω is the Rabi frequency, and Δ is the detuning from resonance, $\omega - \omega_{21}$. The level structure associated with the Hamiltonian is displayed in Figure 5-1. This Hamiltonian can be solved exactly, and it provides the fraction of particles in the final state as

$$N_2(t) = \frac{A(t)^2}{A(t)^2 + \Delta^2}\sin^2\left(\sqrt{A(t)^2 + \Delta^2}\frac{t}{2}\right) \tag{5.9}$$

where $A(t)$ is the pulse area up to time t,

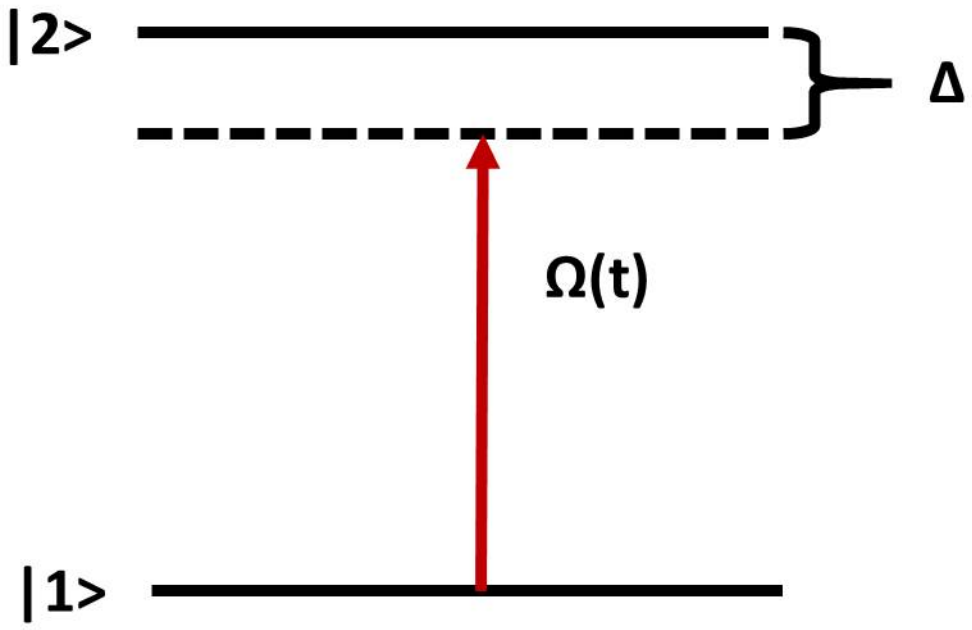

Figure 5-1: Schematic diagram of a two-state, one-photon system, where $\Omega(t)$ is the Rabi frequency and Δ is the detuning from resonance.

$$A(t) = \int_{-\infty}^{t} \Omega(t')dt'. \tag{5.10}$$

Equation 5.9 predicts that population will oscillate sinusoidally and can achieve 100% population transfer in the resonant case ($\Delta = 0$). The excitation reaches a maximum whenever the generalized pulse area, $\sqrt{A(t)^2 + \Delta^2}$, is equal to an odd multiple of π, such that $\sqrt{A(t)^2 + \Delta^2} = (2n+1)\pi$. When $n = 0$, this is known as a π-pulse, and in the case of resonant excitation, 100% of the population is transferred to the final state, leading to a very high fidelity. However, any variations from ideal parameters (fluctuations in either the pulse area or detuning of the pulse) will cause unavoidable losses in transfer efficiency.

If there are spatial inhomogeneities in pulse area (e.g. caused by spatial inhomogeneities of the slowly-varying envelope $\mathcal{E}(t)$), different portions of an ensemble will undergo varying amounts of transfer, leading to only 50% transfer on average in the case of large inhomogeneities. Further, μ depends on the quantum numbers of the states involved, so excitation of multiple degenerate states with different values of

m, for example, will lead to differing Rabi frequencies (and hence pulse areas) for each state and departure from the ideal of 100% population transfer. Therefore, the lack of robustness in performing a π-pulse drastically reduces its utility, despite its potentially very high fidelity.

Thankfully, methods exist that provide both a very high fidelity and strong robustness. The example I give here is that of Adiabatic Rapid Passage (ARP). Adiabatic sweeps are a well-established technique in nuclear magnetic resonance (NMR) spectroscopy and are routinely used to robustly invert population in two-level systems [155, 156, 157, 158, 159, 160, 161]. The fundamental idea behind the technique is that the frequency of a pulse is swept through resonance slowly while maintaining strong coupling between the two levels with a magnetic field. This strong interaction leads to an avoided crossing between the eigenstates of the full Hamiltonian. If this avoided crossing is traversed slowly, or adiabatically, this procedure results in a complete transfer of population from the initial to final state. In general, the Landau-Zener formula predicts the probability of traversing the avoided crossing adiabatically [162].

In order to account for the frequency sweep, the detuning in the Hamiltonian in Eq. 5.7 is replaced with

$$\Delta(t) = \omega(t) - \omega_{21} \tag{5.11}$$

$$\omega(t) = \omega_i - \alpha t \tag{5.12}$$

$\omega(t)$ is the time-varying angular frequency of the electric field, ω_i is the initial frequency of the sweep, and α is the frequency sweep rate in radians/second^2. For the purposes of clarity in this example, the electric field envelope $\mathcal{E}(t)$, and hence the Rabi frequency $\Omega(t)$, will be assumed to be constant. With these adjustments, the Hamiltonian in Eq. 5.7 can be diagonalized to yield eigenstates

$$|+\rangle = \sin\Theta\,|1\rangle + \cos\Theta\,|2\rangle \tag{5.13}$$

$$|-\rangle = \cos\Theta\,|1\rangle - \sin\Theta\,|2\rangle\,, \tag{5.14}$$

where the mixing angle Θ is given by

$$\tan 2\Theta = \frac{\Omega}{\Delta(t)}. \tag{5.15}$$

A two-level system that starts with all of its population in the initial state with a large (compared to Ω), positive detuning, therefore, begins completely in eigenstate $|-\rangle$. As the radiation is brought toward resonance, $\Delta(t)$ decreases and the mixing angle Θ increases. Passing through resonance the sign of $\Delta(t)$ changes and the magnitude once again begins to increase. Once the detuning is again large (compared to Ω) *and now negative*, the entire system, still in eigenstate $|-\rangle$, is now composed completely of state $|2\rangle$. In order for this population transfer to be complete, the sweep rate must follow the adiabaticity criterion of

$$\alpha \ll \frac{(\Omega^2 + \Delta(t)^2)^{\frac{3}{2}}}{\Omega}, \tag{5.16}$$

and in order for the population to begin and end entirely in eigenstate $|-\rangle$, the initial and final detunings must be much larger than the Rabi frequency

$$|\Delta_i|, |\Delta_f| \gg \Omega, \tag{5.17}$$

where Δ_i and Δ_f are the initial and final detunings.

ARP can have both a very high fidelity and be robust with respect to variations in experimental parameters. As long as the adiabaticity criterion is satisfied and one starts and ends far from resonance, in general, due to having a large Rabi frequency and a slow sweep rate, near unity population transfer is achievable [156]. This is possible even in the case of differences in spatial radiation intensity or multiple degenerate states. Figure 5-2 displays an example of the total population transfer achievable with each of these methods.

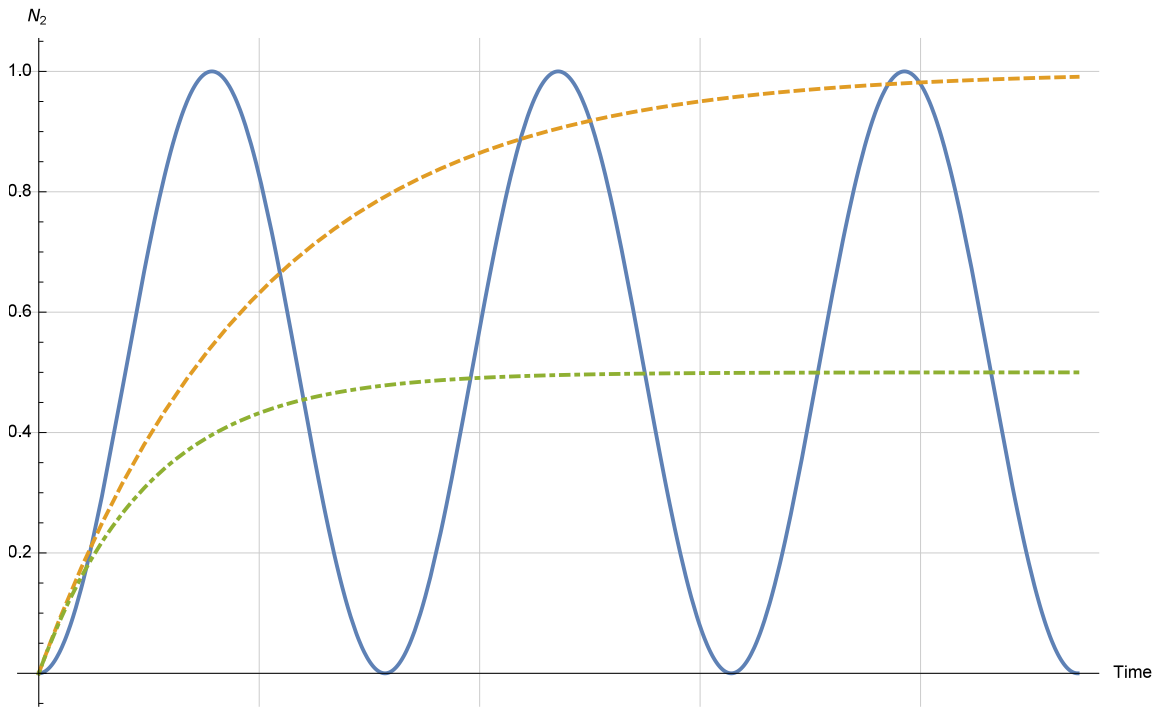

Figure 5-2: Schematic representation of various one-photon population transfer methods as a function of time. The solid blue curve displays coherent transfer, the dashed yellow curve displays adiabatic rapid passage, and the dash-dotted green curve displays incoherent transfer.

5.1.2 Three-state, two-photon methods

In many experiments, single-photon transfer of population is infeasible. This could be due to angular momentum selection rules, as is the case in transferring population to CNP Rydberg states, or due to small Franck-Condon factors in molecular electronic spectroscopy. In both cases the general solution is to transfer population through a third state that has either the correct angular momentum character or vibrational wavefunction overlap with both the initial and final states. In the following discussion, the initial state will continue to be denoted $|1\rangle$, the final state will now be denoted $|3\rangle$, and the intermediate state will be denoted $|2\rangle$. In the spectroscopy of both CNP Rydberg states and highly excited molecular vibronic states, the initial and final states are generally stable on the timescale of the experiment, while the intermediate state may have a short lifetime due to predissociation, autoionization, spontaneous emission, intersystem crossing, internal conversion, or intramolecular vibrational redistribution (IVR).

Stimulated Emission Pumping (SEP) is a well-known method for populating highly-excited vibronic states of molecules [163, 164]. It is fundamentally a straightforward extension of the incoherent two-state scheme described above to a three-state system. Population is first transferred from $|1\rangle$ to $|2\rangle$, and then separately from $|2\rangle$ to $|3\rangle$. Both transfers are incoherent and so have a maximum transfer efficiency of 50%, leading to a 25% total transfer efficiency. 50% of the population remains in the initial state, while the remaining 25% typically decays out of the intermediate state to a variety of final states. If both fields are present at the same time, the population equilibrates between all three states, leading to 33% population transfer. However, when the lifetime of the intermediate state is very short, even this 33% efficiency is difficult or impossible to achieve. Thus, while SEP and incoherent methods in general are quite robust against experimental conditions, their lack of fidelity and potential population of a wide variety of unwanted states makes these incoherent methods undesirable in many situations.

Coherent population transfer can be extended from the two-state discussion above

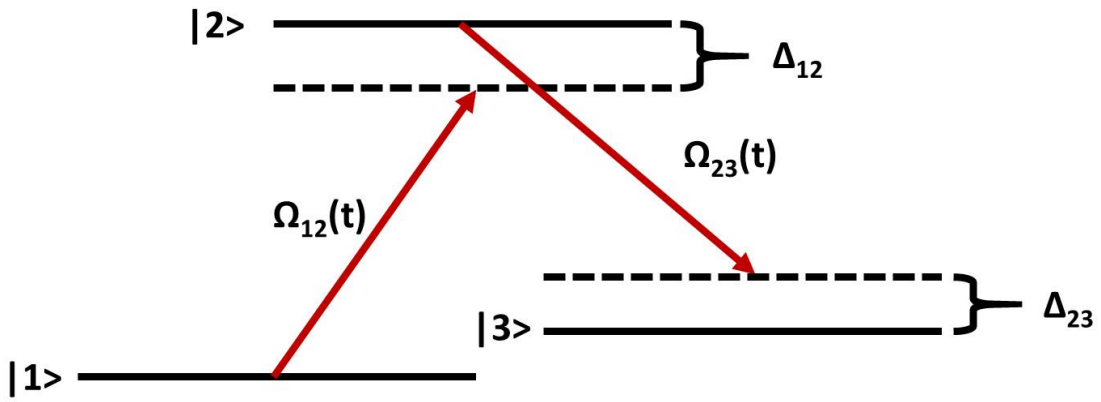

Figure 5-3: Schematic diagram of a Λ-type three-state, two-photon system, where $\Omega_{ij}(t)$ are the Rabi frequencies and Δ_{ij} are the detunings from resonance.

to a three-state model. The interaction Hamiltonian under the RWA is now

$$\hat{H}_I(t) = \frac{\hbar}{2}\begin{bmatrix} 0 & \Omega_{12}(t) & 0 \\ \Omega_{12}(t) & 2\Delta_{12} & \Omega_{23}(t) \\ 0 & \Omega_{23}(t) & 2(\Delta_{12}-\Delta_{23}) \end{bmatrix} \tag{5.18}$$

where Ω_{ij} and Δ_{ij} are the Rabi frequency and detuning associated with the transition between states i and j. A Λ-type level structure associated with this Hamiltonian is displayed in Fig. 5-3. Note that state $|3\rangle$ could in principle lie higher in energy than state $|2\rangle$ in a ladder-type level structure.

The simplest case to first consider, drawing parallels to the two-state case, is when both Rabi frequencies have the same slowly varying electric-field envelope. This can be the case if, for example, both transitions are driven by the same light source, or if they are driven by two different temporally overlapped pulses of the same duration. If Δ_{12} is large (compared to either Rabi frequency), then the system can be approximated as a two-state system transferring population directly between states $|1\rangle$ and $|3\rangle$. In such a case, the *effective* two-photon Rabi frequency for the system is [165, 166]

$$\Omega_{13} = \frac{\Omega_{12}\Omega_{23}}{4\Delta_{12}} \tag{5.19}$$

and the population of state $|3\rangle$ after an interaction time t is

$$N_3(t) = \frac{A_{13}(t)^2}{A_{13}(t)^2 + \delta\omega^2} \sin^2\left(\sqrt{A_{13}(t)^2 + \delta\omega^2}\frac{t}{2}\right), \tag{5.20}$$

where $A_{13}(t)$ is the pulse area up to time t

$$A_{13}(t) = \int_{-\infty}^{t} \Omega_{13}(t')dt', \tag{5.21}$$

and $\delta\omega$ is the two photon detuning $(\Delta_{12} - \Delta_{23})$. If the intermediate state detuning is large, then effectively no population accumulates in state $|2\rangle$, and the entire population oscillates between states $|1\rangle$ and $|3\rangle$. Under ideal conditions, it is possible to achieve 100% population transfer to the final state with a π-pulse (or $(2n+1)\pi$-pulse) despite the possibility of fast decay from the intermediate state. However, this scheme encounters the same difficulties as the two-state coherent π-pulse scheme in terms of spatial inhomogeneities of the pulse area and degenerate states with different transition moments. Two-photon π-pulses, in analogy to the one-photon versions, have potentially very high fidelity for populating the final state, but lack the robustness required for many experiments. The requirements for two-photon π-pulses are even more stringent due to the requirement that Δ_{12} be large compared to *both* Ω_{12} and Ω_{23}, which typically means that Ω_{13} will be relatively small.

Fortunately, there exist three-state, two-photon schemes that, in analogy to ARP, allow for robust, high fidelity transfer of population through a lossy state to a preselected final state. STIRAP is one such scheme [20, 21, 167, 168, 169, 170, 171, 172, 173, 174, 175, 176, 177, 178, 179, 180, 181, 182, 160, 183, 184, 185, 186]. The fundamental concept of STIRAP is that of a three-state, two-photon *Raman* process, where the maxima of the Rabi frequencies occur at separate times. I will now switch to the traditional STIRAP notation referencing the Raman nature of the process, by referring to the transition between states $|1\rangle$ and $|2\rangle$ as the "Pump" transition, and the transition between states $|2\rangle$ and $|3\rangle$ as the "Stokes" transition. When the Pump and Stokes pulses are applied in what is known as the "counter-intuitive" pulse sequence, where the Stokes pulse is applied *before* the Pump pulse, 100% population transfer is

robustly possible, regardless of the lifetime of the intermediate state. I present proof of this and a detailed analysis of the STIRAP process in the next section.

5.2 Detailed theory of STIRAP

In order to provide a more complete description of the STIRAP process, I fully derive the three-state two-photon Hamiltonian, solve for the eigenstates and eigenenergies, and determine the conditions for adiabatic following in Sec. 5.2.1. In Section 5.2.2 I expand upon the basic framework to include non-idealities in the experimental system, including phase fluctuations and intermediate state decay, and then I present and discuss the coupled differential equations that can be numerically solved to provide insight.

5.2.1 Derivation of STIRAP and the adiabatic following condition

The Hamiltonian for a general three-state system soupled by two radiation fields is given by

$$\hat{H}(t) = \begin{bmatrix} E_1 & -\mu_{21}\mathcal{E}_P(t)\cos(\omega_P T) & 0 \\ -\mu_{21}\mathcal{E}_P(t)\cos(\omega_P T) & E_2 & -\mu_{32}\mathcal{E}_S(t)\cos(\omega_S T) \\ 0 & -\mu_{32}\mathcal{E}_S(t)\cos(\omega_S T) & E_3 \end{bmatrix} \quad (5.22)$$

where E_i is the absolute energy of the ith state, μ_{ij} is the electric dipole transition moment between states i and j, $\mathcal{E}_{P/S}(t)$ are the slowly-varying electric field envelopes of the Pump and Stokes fields, and $\omega_{P/S}$ are the frequencies of the Pump and Stokes fields. As before, it is more convenient to work in the interaction representation and make the RWA, which yields the following Hamiltonian

$$\hat{H}_I(t) = \frac{\hbar}{2}\begin{bmatrix} 0 & \Omega_P(t) & 0 \\ \Omega_P(t) & 2\Delta_P & \Omega_S(t) \\ 0 & \Omega_S(t) & 2(\Delta_P - \Delta_S) \end{bmatrix} \tag{5.23}$$

$$\Omega_P(t) = \frac{\mu_{21}\mathcal{E}_P(t)}{\hbar} \tag{5.24}$$

$$\Omega_S(t) = \frac{\mu_{32}\mathcal{E}_S(t)}{\hbar} \tag{5.25}$$

$$\hbar\Delta_P = (E_2 - E_1) - \hbar\omega_P \tag{5.26}$$

$$\hbar\Delta_S = (E_3 - E_2) - \hbar\omega_S \tag{5.27}$$

where $\Omega_{P/S}$ are the Rabi frequencies of the Pump and Stokes laser pulses, and $\Delta_{P/S}$ are the detunings of the Pump and Stokes laser pulses. This Hamiltonian is identical to that of Eq. 5.18, expressed with different notation. Making the assumption of two-photon resonance, this Hamiltonian has eigenstates

$$\left|a^+\right\rangle = \sin(\Theta)\sin(\Phi)\left|1\right\rangle + \cos(\Phi)\left|2\right\rangle + \cos(\Theta)\sin(\Phi)\left|3\right\rangle \tag{5.28}$$

$$\left|a^0\right\rangle = \cos(\Theta)\left|1\right\rangle - \sin(\Theta)\left|3\right\rangle \tag{5.29}$$

$$\left|a^-\right\rangle = \sin(\Theta)\cos(\Phi)\left|1\right\rangle - \cos(\Phi)\left|2\right\rangle + \cos(\Theta)\cos(\Phi)\left|3\right\rangle \tag{5.30}$$

where Θ and Φ are mixing angles defined in terms of Rabi frequencies and detunings

$$\tan(\Theta) = \frac{\Omega_P(t)}{\Omega_S(t)} \tag{5.31}$$

$$\tan(\Phi) = \frac{\sqrt{\Omega_P^2 + \Omega_S^2}}{\sqrt{\Omega_P^2 + \Omega_S^2 + \Delta_P^2} + \Delta_P}. \tag{5.32}$$

Of these two mixing angles, only Θ will be important in the following discussion. The eigenenergies associated with these eigenstates are

$$\omega^0 = 0 \tag{5.33}$$

$$\omega^{\pm} = \Delta_P \pm \sqrt{\Delta_P^2 + \Omega_P^2 + \Omega_S^2}. \tag{5.34}$$

The goal of the STIRAP process is to transfer population from bare state $|1\rangle$ to bare state $|3\rangle$ without placing population even transiently into bare state $|2\rangle$. Therefore, preventing any population from entering eigenstates $|a^{\pm}\rangle$ becomes the goal, as each of those states are linear combinations of all three bare states, including bare state $|2\rangle$. Analogous to ARP, where the goal became to stay entirely in eigenstate $|-\rangle$, the goal of STIRAP is to begin and end in eigenstate $|a^0\rangle$, which is free at all times of contributions from bare state $|2\rangle$.

If the only radiation field present is the Stokes field, then $\Theta = 0$. If the initial population is entirely in the bare state $|1\rangle$, then the system must be entirely in eigenstate $|a^0\rangle$. In order to keep the population in this eigenstate while transferring population, the mixing angle Θ should be changed adiabatically from 0 to $\pi/2$. This is accomplished by slowly turning on the Pump radiation field while slowly turning off the Stokes radiation field. In practice, this is done by delaying (either temporally or spatially) the Pump laser pulse so that it arrives after the Stokes laser pulse. A schematic diagram that displays the temporal evolution of both electric fields, the mixing angle Θ, and the population, is shown in Figure 5-4.

In order for this process to transfer 100% of the population from the initial to the final bare state, the process must be performed adiabatically. In general, for this to be achieved, the nonadiabatic interaction between eigenstate $|a^0\rangle$ and eigenstates $|a^{\pm}\rangle$ must be smaller than the field-induced splitting of the eigenstates [20]. The

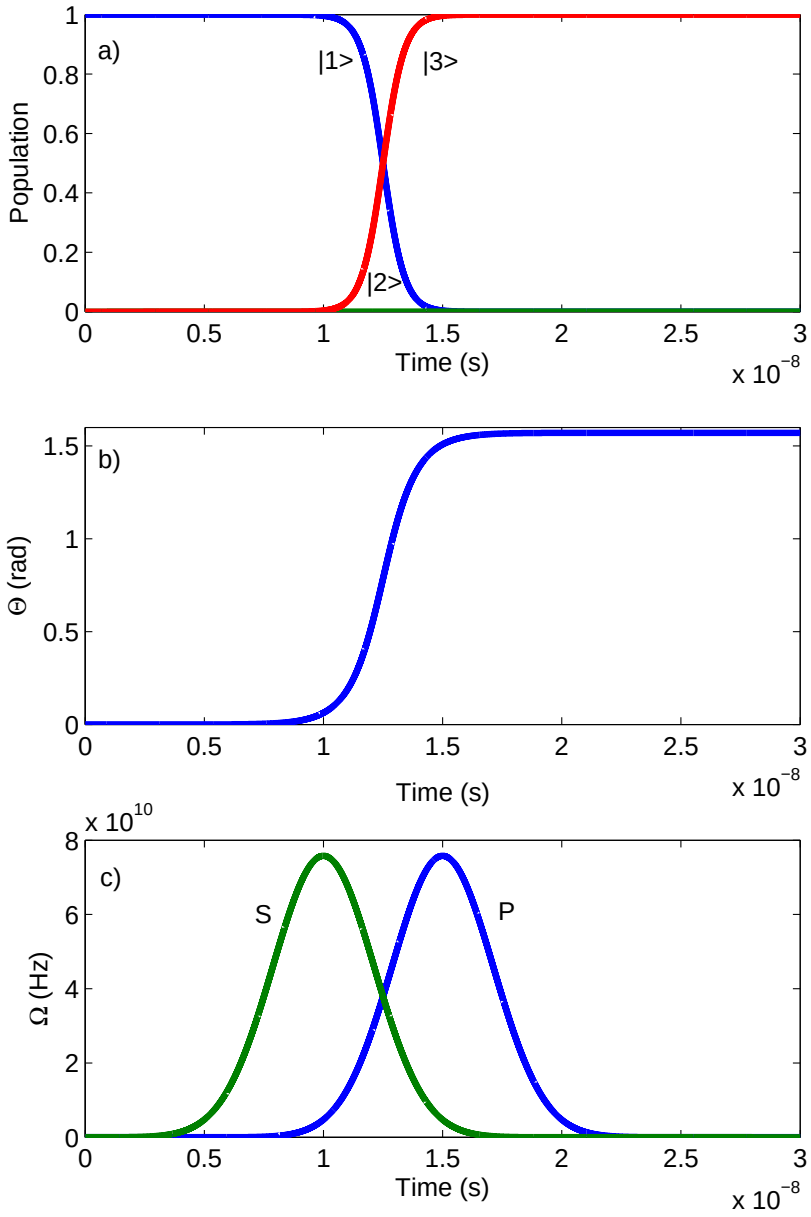

Figure 5-4: Schematic representation of the evolution of the populations, mixing angle Θ, and Rabi frequencies in perfect STIRAP. In this and all future figures, the population of bare state $|1\rangle$ and the Pump Rabi frequency will be shown in blue, the population of bare state $|2\rangle$ and the Stokes Rabi frequency will be shown in green, and the population of bare state $|3\rangle$ will be shown in red.

nonadiabatic interaction matrix element is $\langle a^{\pm}|\dot{a}^0\rangle$, thus the adiabaticity criterion can be expressed as

$$\left\langle a^{\pm}|\dot{a}^0\right\rangle \ll \left|\omega^{\pm} - \omega^0\right|. \tag{5.35}$$

These matrix elements can be written as

$$\left\langle a^{+}|\dot{a}^0\right\rangle = -\dot{\Theta}\sin\Phi \tag{5.36}$$

$$\left\langle a^{-}|\dot{a}^0\right\rangle = -\dot{\Theta}\cos\Phi \tag{5.37}$$

The maximum magnitude of both of these matrix elements is $\dot{\Theta}$. Therefore, a local adiabaticity criterion can be written as

$$\dot{\Theta} = \left|\frac{\dot{\Omega}_P\Omega_S - \Omega_P\dot{\Omega}_S}{\Omega_P^2 + \Omega_S^2}\right| \ll \left|\omega^{\pm} - \omega^0\right|. \tag{5.38}$$

This adiabaticity condition can be evaluated at any time t, but doing so does not provide global insight. If the slowly-varying electric field envelopes are smooth, then a convenient global adiabaticity condition can be derived by taking the time average of $\dot{\Theta}$,

$$\left\langle \dot{\Theta_{av}} \right\rangle = \frac{\pi}{2\Delta\tau}, \tag{5.39}$$

where $\Delta\tau$ is the period during which the pulses overlap. Adiabaticity is most important when each radiation field is on resonance ($\Delta_P = \Delta_S = 0$), and so I can write that in general,

$$\left|\omega^{\pm} - \omega^0\right| \geq \sqrt{\Omega_P^2 + \Omega_S^2} \equiv \Omega_{eff}, \tag{5.40}$$

where Ω_{eff} is the effective Rabi frequency. Combining these expressions, I arrive at a numerical condition to ensure global adiabaticity, which matches well with both experimental experience and numerical simulations

$$\Omega_{eff}\Delta\tau > 10 \tag{5.41}$$

However, this inequality is only accurate for Fourier-transform limited radiation. As discussed in Sec. 2.2, the Nd:YAG-pumped pulsed dye lasers used in my experiments suffer from phase fluctuations during each pulse and are significantly broader than what the Fourier-transform limit of their duration would imply. These phase fluctuations lead to a time-dependent detuning from the two-photon resonance and sudden changes in the values of both mixing angles, which result inevitably in losses due to nonadiabatic coupling to the bare state $|2\rangle$. In general, these phase fluctuations may only be compensated for by a larger effective Rabi frequency,

$$\Omega_{eff}\Delta\tau \gtrsim 10N_{Fourier}^2 \tag{5.42}$$

$$N_{Fourier} = \frac{\Delta\omega_{phase}}{\Delta\omega_{Fourier}}, \tag{5.43}$$

where $\Delta\omega_{phase}$ is the bandwidth of the pulsed laser, and $\Delta\omega_{Fourier}$ is the Fourier-transform limited bandwidth for a given pulse duration, and $N_{Fourier}$ is the ratio between the two.

5.2.2 Numerical calculations including experimental imperfections

In order to accurately simulate the behavior of the STIRAP pulse sequence as performed in my experiments, I explicitly include several experimental imperfections in my calculations: phase and intensity fluctuations in the pulsed dye laser pumped Pump pulse, nonadiabatic losses that are the result of the square-wave nature of the mm-wave pumped Stokes pulse, and the possibility of rapid decay from the intermediate state.

In order to account for the poor phase coherence properties and intensity fluctuations of the pulsed dye laser Pump pulse, I include these fluctuations as pseudo-

random functions modifying the Rabi frequency of the Pump pulse. I then average the simulation results in an attempt to replicate the experimental results. For the phase fluctuations, I include exponentially-correlated colored phase noise (the Ornstein-Uhlenbeck process), equivalent to a phase diffusion model with a non-Lorentzian lineshape, as described in reference [170]. This takes the form of a pseudo-random phase function $\alpha(t)$ modulating the Pump pulse Rabi frequency:

$$\Omega_P = \frac{\mu_P \mathcal{E}_P(t) e^{i\alpha(t)}}{\hbar} \tag{5.44}$$

This phase function $\alpha(t)$ depends on two parameters, the spectral density of the noise, D, and the correlation time of the fluctuations, Γ, defined by

$$\langle \epsilon_P(t) \rangle = 0 \tag{5.45}$$

$$\langle \epsilon_P(t) \epsilon_P(s) \rangle = D\Gamma e^{-\Gamma|t-s|} \tag{5.46}$$

where t and s are two arbitrary times, and ϵ_P is the dynamic detuning of the Pump pulse (a factor in addition to the static detuning Δ_P). These parameters also include the effect of the ratio of the laser bandwidth to the Fourier-transform limited pulse, $N_{Fourier}$ by the relationship,

$$N_{Fourier} = \frac{\Delta\omega_{phase}}{\Delta\omega_{Fourier}} = \Delta t_{laser} \sqrt{\frac{D\Gamma}{2}}, \tag{5.47}$$

Δt_{laser} is the full width half maximum (FWHM) of the duration of the laser pulse. In order to simulate a non-transform limited pulse that matches any mode of our intracavity etalon-narrowed pulsed dye laser (bandwidth ~ 250 MHz, $N_{Fourier} \sim 4$), I set $D = \Gamma = 0.75$ GHz.

In general, different values of D and Γ that maintain a constant value of $(D\Gamma/2)^{1/2}$ are more efficient at population transfer when $D > \Gamma$. This is because nonadiabatic losses from the sudden phase jumps of lifetime $1/\Gamma$ cause greater loss to bare state $|2\rangle$ than the decrease in effective Rabi frequency given by the spectral density of noise,

D.

In order to generate $\alpha(t)$, I use the Box-Müller algorithm [170],

$$\epsilon(0) = \cos(2\pi b)\sqrt{2D\Gamma \ln a} \tag{5.48}$$

$$\epsilon(t + \Delta t) = \epsilon(t)E + h \tag{5.49}$$

$$E = e^{\Gamma \Delta t} \tag{5.50}$$

$$h = \cos(2\pi b)\sqrt{2D\Gamma(1 - E^2) \ln a} \tag{5.51}$$

$$\alpha(t) = \epsilon(t)\Delta t, \tag{5.52}$$

where a and b are evenly distributed random numbers in the interval $0 < a, b \leq 1$, and Δt is the time step for defining the function. In my calculations, $\Delta t = 10^{-12}$ s. A new a, b pair are generated at every time step, and I average over at least 100 different values of $\alpha(t)$ in order to get statistically meaningful results. An example $\alpha(t)$ is displayed in Fig. 5-5.

I included intensity fluctuations by modifying the electric field envelope, and hence the Rabi frequency of the Pump laser pulse. The nominal Pump laser field was multiplied by a pseudo-random number chosen from a Gaussian distribution with a variance of 0.025, chosen to match the intensity fluctuations observed in our laser (see Sec. 2.2). The temporal profile of the dye laser pulse is modeled as a Gaussian pulse with a 7.5 ns FWHM.

The mm-wave Stokes pulse has vastly better coherence properties and fewer intensity fluctuations than the pulsed dye laser Pump pulse. The primary limitation of the mm-wave source is that the electronics have response times on the order of several nanoseconds, thus cannot be easily pulse-shaped on time scales shorter than $\sim$ 10 ns. The Stokes pulse, therefore, takes the form of a 10 ns Fourier-transform

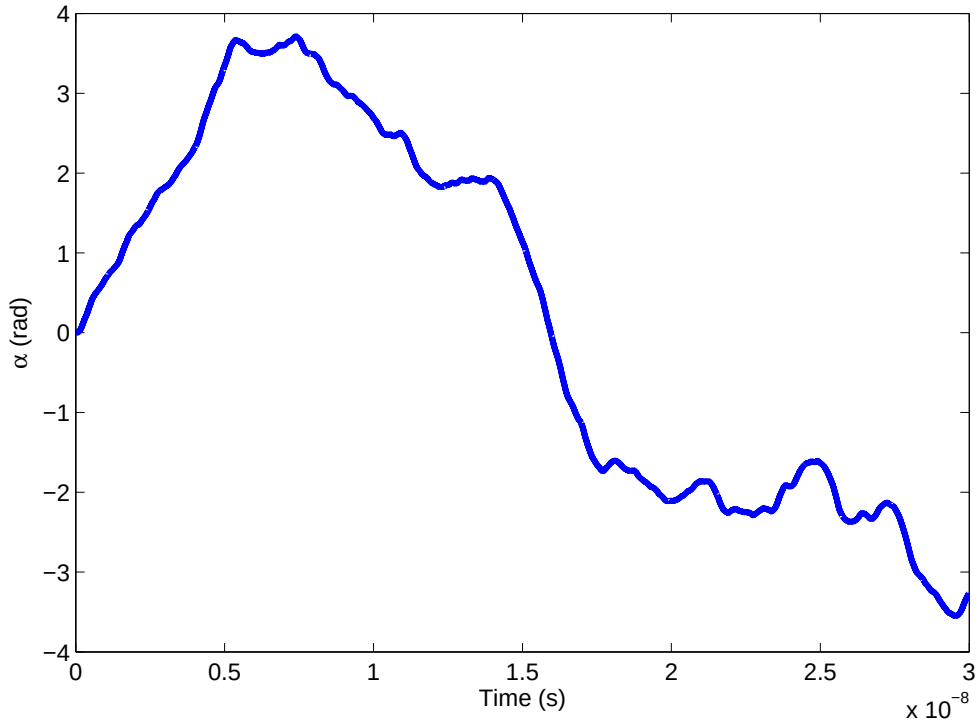

Figure 5-5: Example of the evolution of the pseudo-random phase function $\alpha(t)$ which broadens the Pump pulse beyond its Fourier-transform limit.

limited (Fourier transform limit of $\sim$ 120 MHz) square-wave pulse. In anticipation of more advanced electronic control over the mm-wave pulse shape, I also perform simulations with a Gaussian pulse and a triangular pulse, with identical pulse area to the square-wave case.

Finally, in order to account for losses from the three-state system that originate from the intermediate bare state $|2\rangle$, I introduce a complex term to the Hamiltonian, responsible for draining population from the system. This term drains population with a rate $1/T_2$, where T_2 is typically $\sim$ 100 ps for predissociation. Therefore, the final interaction Hamiltonian that I use for full calculations of STIRAP is

$$\hat{H}_I(t) = \frac{\hbar}{2}\begin{bmatrix} 0 & \Omega_P^{Gauss}(t)e^{i\alpha(t)} & 0 \\ \Omega_P^{Gauss}(t)e^{-i\alpha(t)} & 2\Delta_P - \frac{i}{T_2} & \Omega_S^{Sq}(t) \\ 0 & \Omega_S^{Sq}(t) & 2(\Delta_P - \Delta_S) \end{bmatrix} \tag{5.53}$$

where Ω_S^{Sq} is the square-wave enveloped Stoke pulse Rabi frequency and Ω_P^{Gauss} is the variable-intensity Gaussian-enveloped Pump pulse Rabi frequency. This Hamiltonian cannot be solved analytically, but can be solved numerically in either of two ways: the time-dependent Schrödinger equation,

$$i\hbar\frac{\partial\psi}{\partial t} = \hat{H}_I(t)\psi, \tag{5.54}$$

where ψ is the wavefunction for the three-state system, or the Liouville-von Neumann equation,

$$i\hbar\frac{\partial\rho}{\partial t} = \left[\hat{H}_I(t), \rho\right], \tag{5.55}$$

where ρ is the density matrix. For an n-level system, the density matrix is an $n \times n$ matrix where the diagonal terms represent the populations of the individual levels, and the off-diagonal terms represent the coherences between connected levels. The density matrix and the wavefunction are related by the outer product

$$\rho = |\psi\rangle\langle\psi|. \tag{5.56}$$

For completeness, the explicit set of coupled differential equations from the time-dependent Schrödinger equation are

$$i\dot{c_1} = -\Omega_P(t)c_2 \tag{5.57}$$

$$i\dot{c_2} = -\Omega_P(t)c_1 - \Omega_S(t) - (2\Delta_P - \frac{i}{T_2})c_2 \tag{5.58}$$

$$i\dot{c_3} = -\Omega_S(t)c_2 - 2(\Delta_P - \Delta_S)c_3 \tag{5.59}$$

where $c_i = \langle i|\psi\rangle$. The explicit set of coupled differential equations from the Liouville-von Neumann equation are

$$i\dot{\rho}_{11} = \Omega_P\left(\rho_{21} - \rho_{12}\right) \tag{5.60}$$

$$i\dot{\rho}_{12} = \Omega_P\rho_{22} - \Omega_P^*\rho_{11} - \Omega_S\rho_{13} - \left(2\Delta_P + \frac{i}{T_2}\right)\rho_{12} \tag{5.61}$$

$$i\dot{\rho}_{13} = \Omega_P\rho_{23} - \Omega_S\rho_{12} - 2\left(\Delta_P - \Delta_S\right)\rho_{13} \tag{5.62}$$

$$i\dot{\rho}_{21} = \Omega_P^*\rho_{11} - \Omega_P\rho_{22} + \Omega_S\rho_{31} + \left(2\Delta_P - \frac{i}{T_2}\right)\rho_{21} \tag{5.63}$$

$$i\dot{\rho}_{22} = \Omega_P^*\left(\rho_{12} - \rho_{21}\right) + \Omega_S\left(\rho_{32} - \rho_{23}\right) - \frac{2i}{T_2}\rho_{22} \tag{5.64}$$

$$i\dot{\rho}_{23} = \Omega_P^*\rho_{13} - \Omega_S\left(\rho_{33} - \rho_{22}\right) + \left(2\Delta_S - \frac{i}{T_2}\right)\rho_{23} \tag{5.65}$$

$$i\dot{\rho}_{31} = -\Omega_P\rho_{32} + \Omega_S\rho_{21} + 2\left(\Delta_P - \Delta_S\right)\rho_{31} \tag{5.66}$$

$$i\dot{\rho}_{32} = -\Omega_P^* \rho_{31} - \Omega_S \left(\rho_{22} - \rho_{33}\right) - \left(2\Delta_S + \frac{i}{T_2}\right) \rho_{32} \tag{5.67}$$

$$i\dot{\rho}_{33} = \Omega_S \left(\rho_{23} - \rho_{32}\right) \tag{5.68}$$

These two sets of differential equations provide numerically identical values for the populations of the bare states, but the density matrix approach also facilitates investigation of the coherence between two states. In the optical-mm-wave experiments I describe in Chapter 6, the coherence between bare states $|2\rangle$ and $|3\rangle$, detected as FID, is essential to determine whether I am performing STIRAP. Figure 5-6a displays the numerical results from the Schrödinger equation, Fig. 5-6b displays the numerical results from the Liouville-von Neumann equation, and Fig. 5-6c displays the difference in populations as a function of time. The STIRAP process in this case was, for clarity, performed with the Pump and Stokes transitions each having a 1 D transition dipole moment, 10 ps intermediate state lifetime, and being pumped by a 10 mJ, 7.5 ns Gaussian-envelope radiation field. The relative timing of these two pulses is displayed in Fig. 5-6d.

In order to determine whether I have successfully performed STIRAP in my experiments, I sweep the relative timing of the Pump and Stokes pulses in order to observe the "STIRAP signature" of increased population in the final state, decreased population in the intermediate state, and no residual coherence between the intermediate and final states. This signature is displayed in Figs. 5-7(a-b) using the same parameters as above except for the intermediate state lifetime, which is not included. The solid curves in Figure 5-7a display the population in the intermediate and final states as a function of τ, the variable delay between the Pump and Stokes pulses. Positive values of τ correspond to the Pump pulse arriving after the Stokes pulse, negative values correspond to the Pump pulse arriving before the Stokes pulse, and $\tau = 0$ corresponds to the Pump and Stokes pulses being temporally overlapped. The STIRAP signature is the large peak in the population of the final state at small, positive values of τ. This signature can also be seen in Fig. 5-7b as the coherence

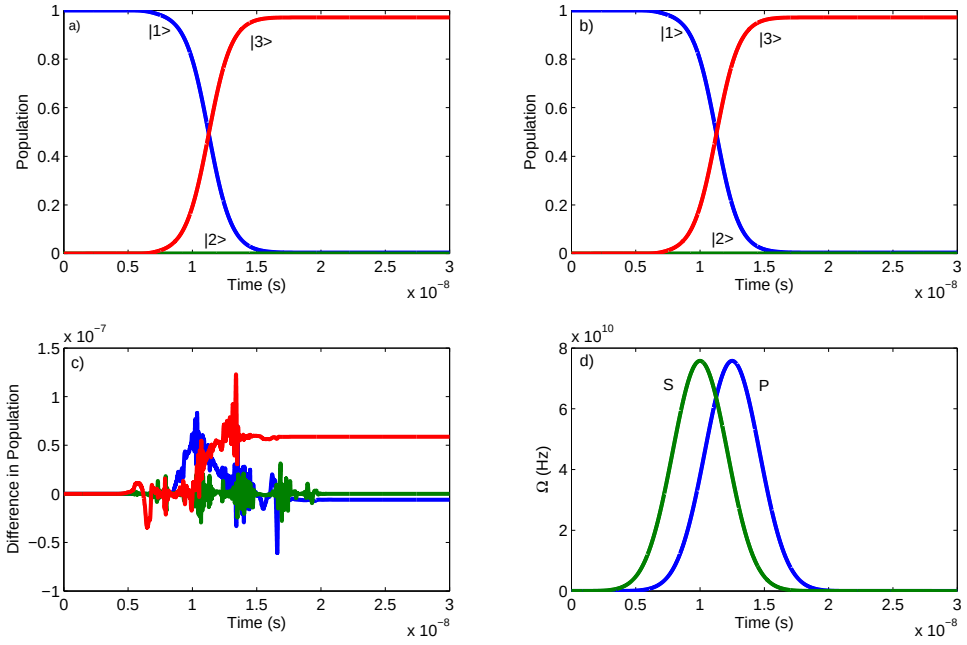

Figure 5-6: Comparison of numerical results from solutions of Schrödinger's equation and the Liouville-von Neumann equation for the same system. Note that the differences in population between the two methods are never more than 1.5 parts in 10^7.

decreases to zero at the same small, positive values of τ. The rapid oscillations seen in Figs. 5-7(a-b) at small, negative delay are two-photon Rabi oscillations related to my discussion of coherent two-photon effects in Sect. 5.1.2, but since $\Delta_P = 0$, they involve transferring population between all three bare states. Figures 5-7(c-f) display the same variation in timing with 10 μJ and 500 nJ pulse energies instead, to display the characteristic signatures of near-STIRAP behavior and non-STIRAP behavior. Note that both the maximum in population transfer and the coherence dip move toward $\tau = 0$ and narrow in time significantly. While it may seem that population can still be transferred efficiently in these cases, in the case of a short intermediate state lifetime, essentially no population is transferred, as seen in Fig. 5-8, which displays the population in the final state as a function of τ, with the same parameters as above, but a 10 ps intermediate state lifetime.

5.3 Characteristic results

In this Section I show the effects of the various experimental imperfections on the process of population transfer via STIRAP. Unless otherwise noted, the Pump pulse is a 2 mJ, 7.5 ns Gaussian-enveloped pulse, the Stokes pulse will be a 10 ns square-wave enveloped pulse of 8 dBm mm-wave power (pulse energy $\sim$ 60 pJ), the Pump transition has a 0.5 D transition dipole moment, and the Stokes transition has a 1000 D transition dipole moment. These pulse energies are easily achievable in lab, and the transition dipole moments are reasonable representations of realistic systems.

In order to determine the best results I can expect, I initially simulate an ideal experimental system, with two Gaussian-enveloped pulses with no decay or fluctuations. The results for this system are shown in Fig. 5-9. Figure 5-9a displays the populations of the intermediate and final states as a function of the delay of the pump pulse τ. Figure 5-9b displays the coherence between the intermediate and final states as a function of τ. There is a clear increase in the population of the final state and decrease both in the population of the intermediate state and the coherence between the intermediate and final states at small, positive values of τ, as expected of

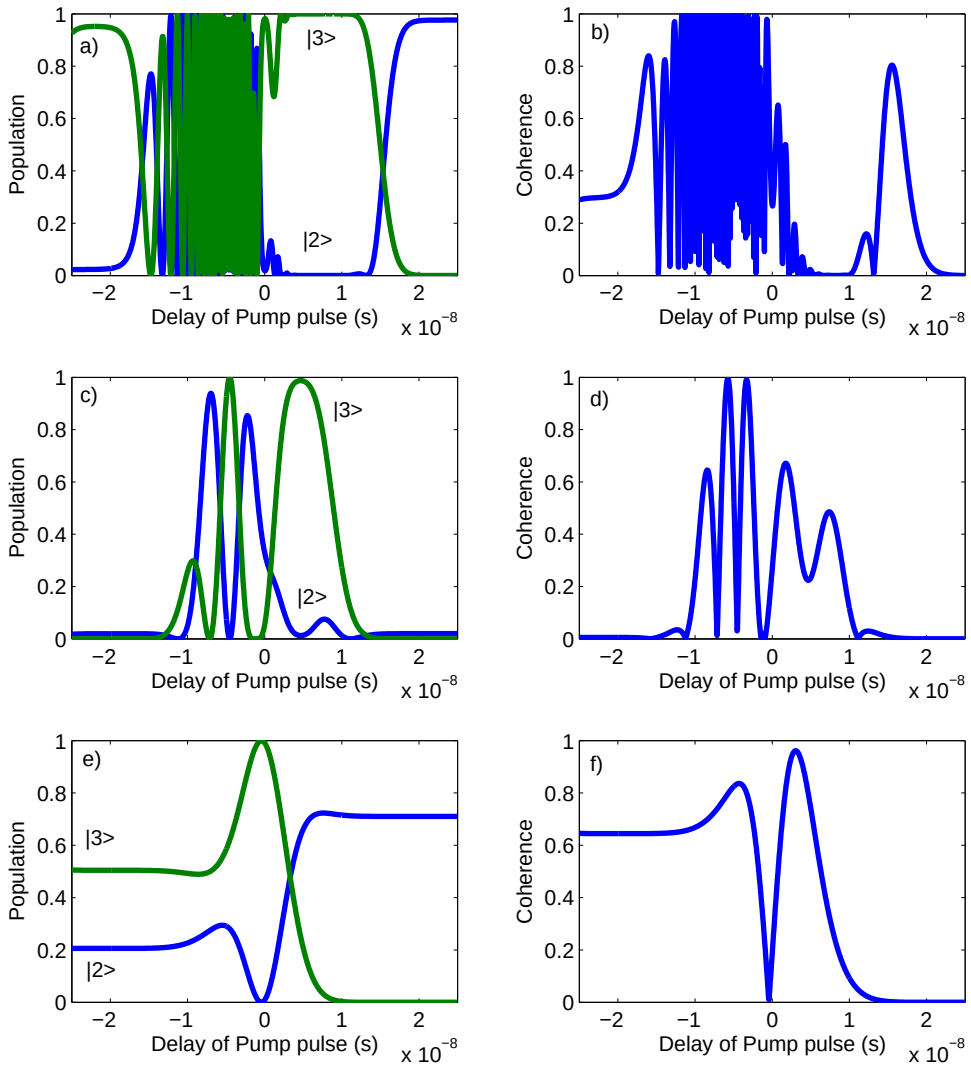

Figure 5-7: Depiction of the STIRAP signature of population transfer from bare state $|2\rangle$ to bare state $|3\rangle$ and decrease in coherence between the two. The curves display the final populations of states $|2\rangle$ and $|3\rangle$ and the coherence between the two as a function of delay between the Pump and Stokes pulses and of pump laser power. Subfigures a,b display 10 mJ Pump and Stokes pulse energies, subfigures c,d display 10 μJ pulse energies, and subfigures e,f display 500 nJ pulse energies.

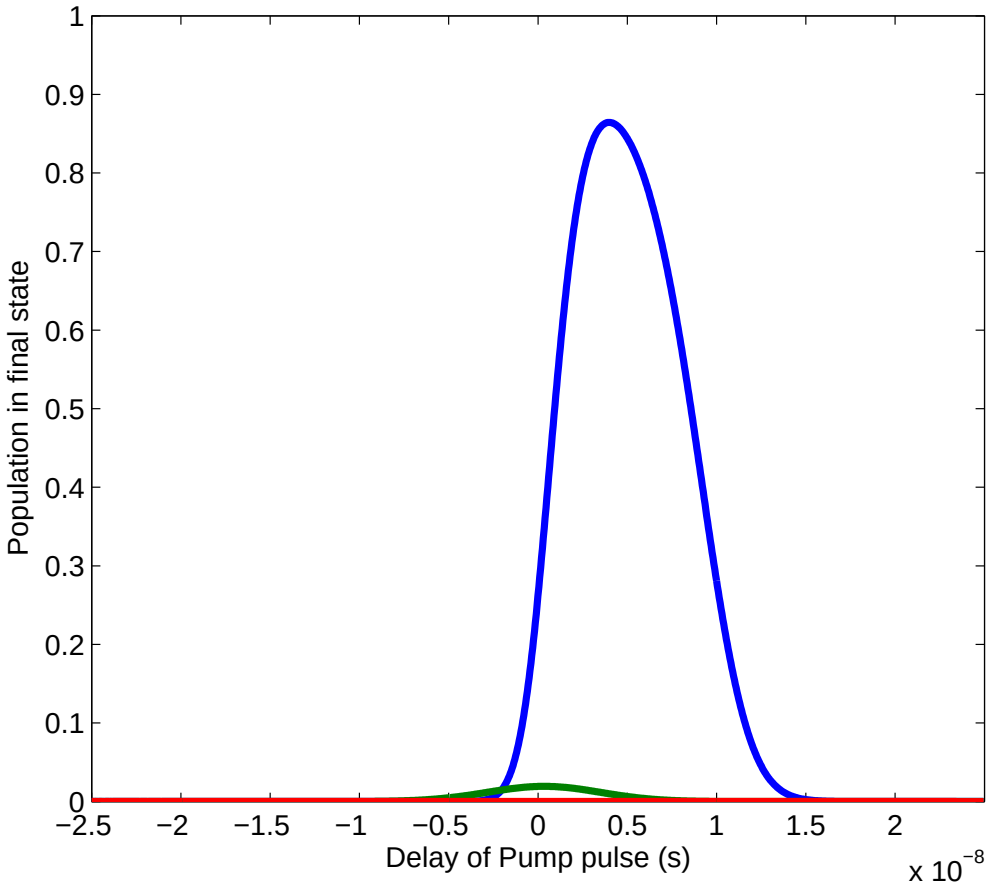

Figure 5-8: Comparison of final state population in the presence of intermediate state decay $T_2 = 10$ ps at three different pulse intensities. The blue trace displays 10 mJ Pump and Stokes pulse energies, the green trace displays 10 μJ pulse energies, and the red trace displays 500 nJ pulse energies.

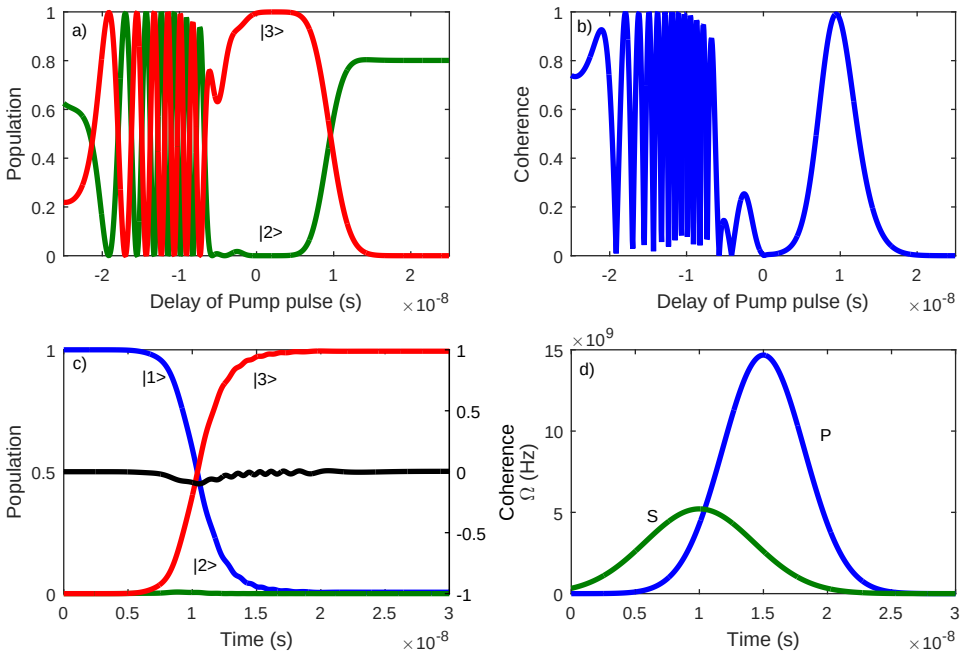

Figure 5-9: Depiction of the STIRAP process for an experimentally ideal system. Subfigure a displays the variation of the population transfer from bare state $|2\rangle$ to bare state $|2\rangle$ as a function of τ and shows a clear peak at the STIRAP timing. Subfigure b displays the coherence between bare states $|2\rangle$ and $|3\rangle$ and shows a clear dip at the STIRAP timing. Subfigure c displays the evolution of the bare state populations at the STIRAP timing, and subfigure d displays the Rabi frequencies of the Pump and Stokes pulse at the STIRAP timing. Again, in this and all future figures, the population of bare state $|1\rangle$ and the Pump Rabi frequency will be shown in blue, the population of bare state $|2\rangle$ and the Stokes Rabi frequency will be shown in green, the population of bare state $|3\rangle$ will be shown in red, and the coherence between the two states will be shown in blue in subfigure b and shown in black in subfigure c.

a STIRAP-type transfer. Figure 5-9c displays the evolution of the population of each bare state and the coherence as a function of time in the STIRAP pulse sequence, and Fig. 5-9d displays the time-dependent Rabi frequencies associated with that pulse sequence. Note that the Rabi frequency of the Pump pulse is much larger than that of the Stokes pulse, in anticipation of the inclusion of phase fluctuations below.

Experimental non-idealities are added on step-by-step in Figs. 5-10 - 5-12 and display the same quantities as Fig. 5-9. Figure 5-10 displays the effect of Pump pulse intensity fluctuations on STIRAP efficiency. As I would hope, due to the robustness

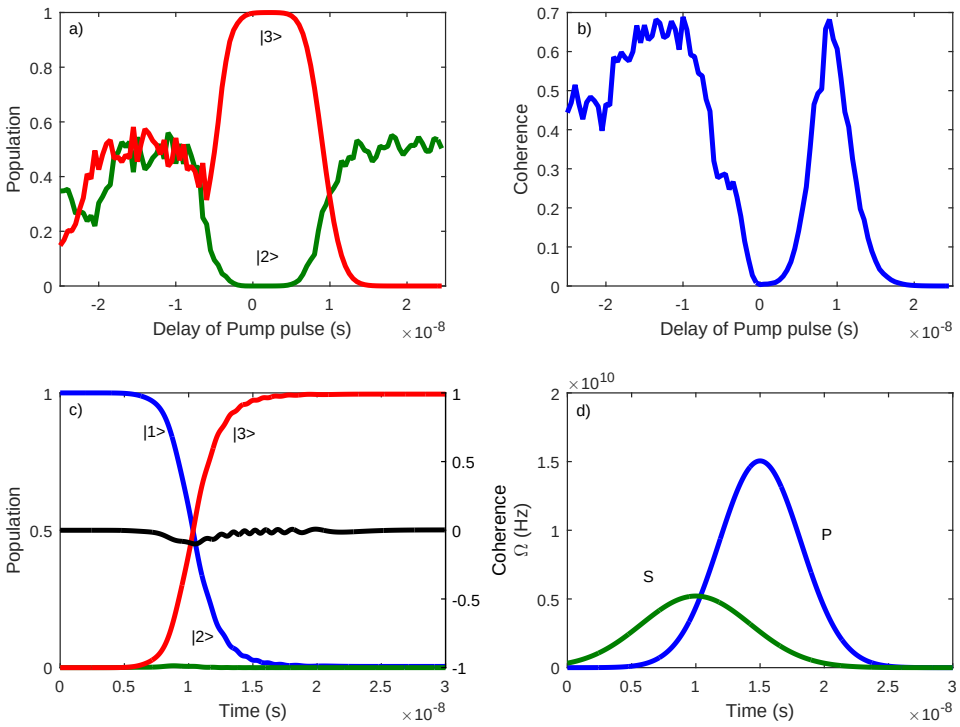

Figure 5-10: Depiction of the STIRAP process for a system with Pump pulse intensity fluctuations. The only significant change induced by intensity fluctuations are that the two-photon Rabi oscillations at small, negative τ are blurred out and average out to 50% population transfer.

of the STIRAP population transfer method, minor fluctuations in the intensity of the Pump pulse have essentially no effect on the population transferred. The well-resolved two-photon Rabi oscillations from Fig. 5-9 at small, negative values of τ are blurred out, providing further evidence of the lack of robustness of the direct π-pulse method.

Figure 5-11 displays the effects of both Pump pulse intensity fluctuations and a square-wave enveloped Stokes pulse on STIRAP efficiency. The total population transferred at the STIRAP pulse sequence is still quite large, although it now exhibits minor dependences on exact pulse timing due to the non-adiabatic turnoff of the Stokes pulse. Additionally, the dip in the coherence is less visible. However, the total population transferred to the final state remains quite high, $> 90\%$.

Finally, Fig. 5-12 displays the effect of Pump pulse intensity and phase fluctua-

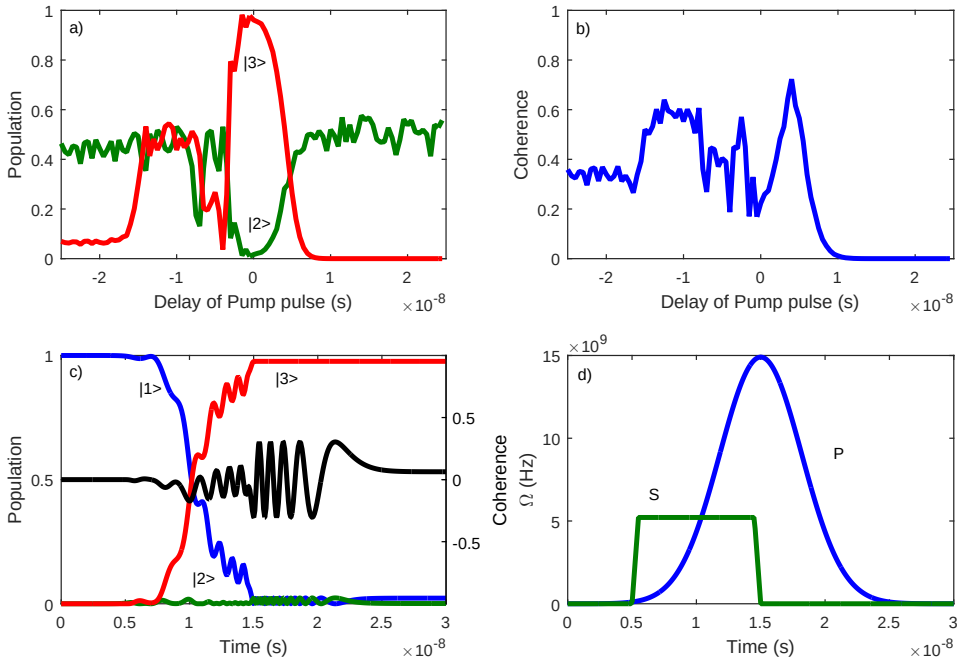

Figure 5-11: Depiction of the STIRAP process for a system with Pump pulse intensity fluctuations and a square-wave enveloped Stokes pulse. The primary effect of adding a square-wave enveloped Stokes pulse is that the STIRAP signature in both the populations and coherence become narrower and less pronounced, as the population transfer is no longer near unity and the coherence no longer dips to exactly zero.

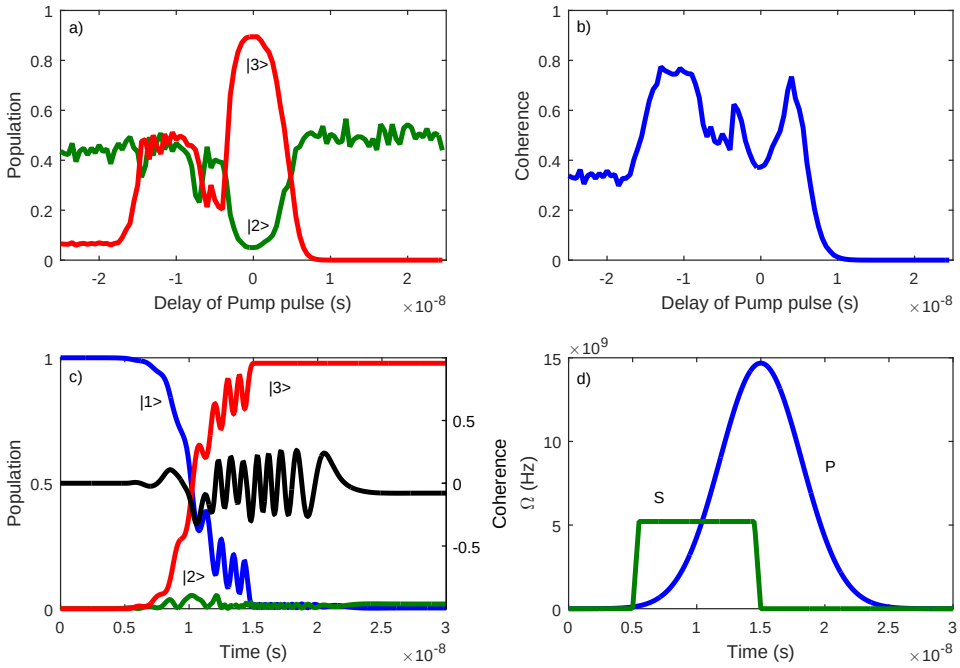

Figure 5-12: Depiction of the STIRAP process for a system with Pump pulse intensity and phase fluctuations and a square-wave enveloped Stokes pulse. The primary change to adding phase fluctuations to the Pump pulse is a further blurring of the STIRAP signature as the population transfer is even weaker than before and the coherence dip is much narrower and even less pronounced. Note, however, that the total population transfer is still quite strong, and the coherence dip is still clearly visible.

tions and a square-wave enveloped Stokes pulse on STIRAP efficiency. The effect of phase fluctuations is primarily to further reduce the overall population transfer efficiency and further reduce the visibility of the dip in the coherence. Total population transferred is not as high as before, $\gtrsim 80\%$, but still more than acceptable for future spectroscopy of CNP states

The effects of an intermediate state decay time of 100 ps is displayed in Fig. 5-13. The curves show the total transfer to the final state as a function of the delay of the Pump pulse τ, for the conditions of Figs. 5-10-5-12 in the solid, dashed, and dash-dotted curves, respectively. The effects of the intensity fluctuations cannot be distinguished from what results from a stable Pump pulse intensity, thus the ideal case is not shown. Even in the case of intensity and phase fluctuations and a square-wave enveloped Stokes pulse, the total transfer as a function of delay reaches 50%. This

relative insensitivity to intermediate state lifetime confirms that STIRAP is indeed possible in a realistic experimental system. Experimental confirmation of this is dealt with in Chapter 6.

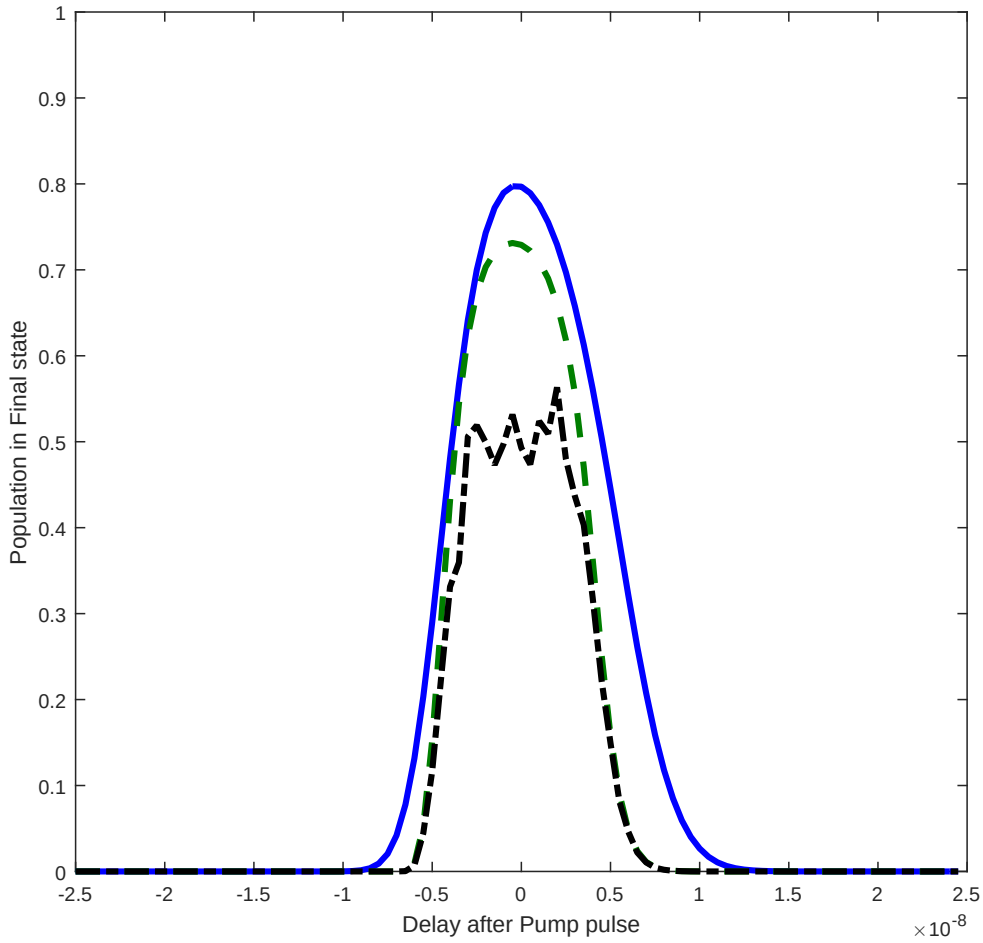

Figure 5-13: The population transfer of STIRAP with varying levels of experimental non-idealities with a 100 ps intermediate state lifetime. The blue curve displays the case with only Pump pulse intensity fluctuations, the green dashed curve displays the case with intensity fluctuations and a Square-wave enveloped Stokes pulse, and the black dash-dotted curve displays the case with all experimental non-idealities.

Chapter 6

Coherent coupling of optical and millimeter-wave photons

In this chapter I discuss the proof-of-principle experiments that demonstrate coherent coupling between an optical and a millimeter-wave photon, both in the low Rabi frequency regime (coherently enhanced population transfer) and the high Rabi frequency regime (STImulated Raman Adiabatic Passage [STIRAP]). In Section 6.1 I describe the atomic systems in which each experiment takes place, and the requirements of an atomic system for proof-of-principle demonstrations of coherent population transfer. In Sec. 6.2 I discuss the low Rabi frequency regime explored in barium. In Sec. 6.3 I discuss the high Rabi frequency regime explored in calcium as an example of full STIRAP. Sec. 6.2 compares experimental results to theoretical calculations while Sec. 6.3 is purely based on calculations. Finally, in Sec. 6.4, I briefly describe the application of these coherent population transfer methods to molecules with typical predissociation lifetimes. I also discuss experimental improvements that facilitate molecular optical-mm-wave STIRAP.

6.1 Atomic systems as proof-of-principle demosntrations of coherent population transfer

Atomic systems are useful as proof-of-principle systems for coherent population transfer methods because population in the intermediate state does not decay, and hence can be measured to ensure high efficiency population transfer. In practical terms this requires a particular level structure of the Rydberg states as compared to the bandwidth of the mm-wave spectrometer used in the experiment. For an optical-mm-wave STIRAP process transferring population from a low-lying ground state through a Rydberg core-penetrating (CP) intermediate state to a Rydberg core-nonpenetrating (CNP) final state, both the intermediate and final state must satisfy several requirements. First and most importantly, the Stokes transition between the intermediate and final state must be within the bandwidth of the spectrometer. Additionally, for diagnostic purposes, both the intermediate and final state must have transitions to secondary probe states that also lie within the bandwidth of the spectrometer.

These requirements for the existence of Stokes and probe transitions within the bandwidth of the spectrometer are generally satisfied, although it may require going to relatively large n^* (and therefore relatively large Δn^* transitions). However, the Stokes transition also requires a large enough electric dipole transition moment to ensure that the Rabi frequency for the Stokes transition is large enough to permit performance of STIRAP. For 10 ns Pump and Stokes pulses with an overlap of ~ 5 ns, this means that the Rabi frequency must be $\gtrsim 2$ GHz (to satisfy the general adiabaticity criterion from Chapter 5). The maximum power output of both the W-band and high frequency mm-wave spectrometers is 30 mW, and so the electric dipole transition moment for the Stokes transition must be $\gtrsim 150$ D in order to satisfy this criterion (for a mm-wave beam waist of ~ 1 cm). In general, this means that only a transition with $\Delta n^* \lesssim 3$ is suitable for use as a Stokes transition. This typically also restricts the potential number of probe transitions.

The level structure of the relevant states in barium is displayed in Figure 6-1. Beginning in the $6s^2\ ^1S_0$ ground state of barium, the Pump pulse is a 238.269 nm

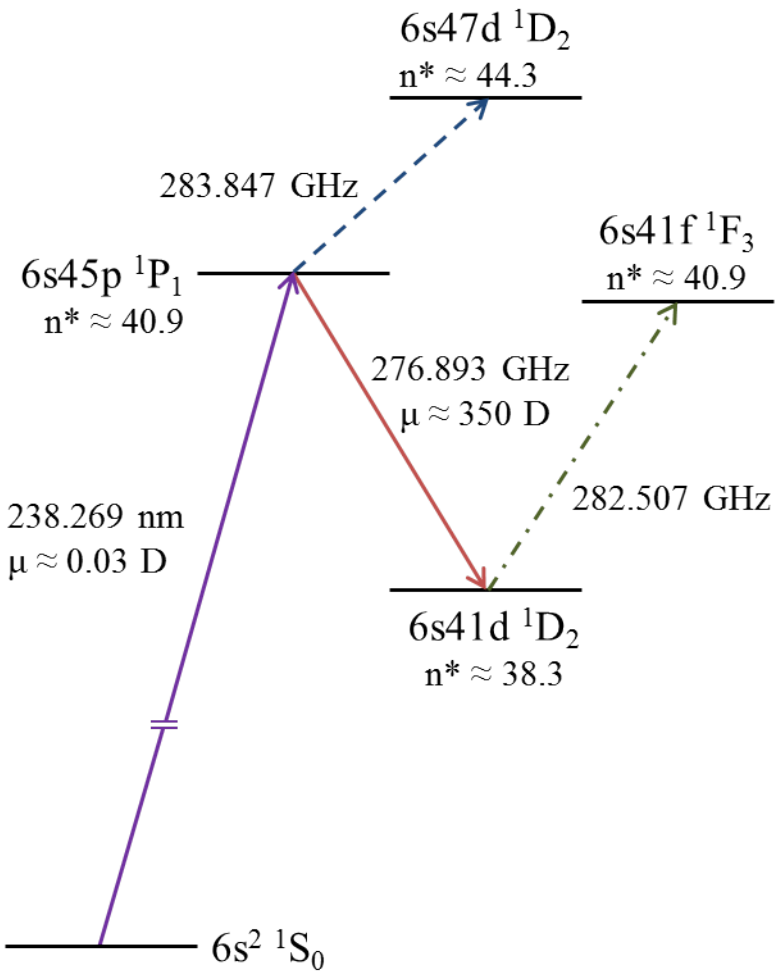

Figure 6-1: Level diagram for STIRAP experiments in barium. The Pump (purple, solid), Stokes, (red, solid) and probe (blue, dashed and green, dashed-dotted) transitions are shown along with the effective principal quantum numbers of each state and the electric dipole transition moments for the Pump and Stokes transitions.

laser pulse that transfers population to the $6s45p$ ($n^* \approx 40.9$) $^1P_1$ state and the Stokes pulse is a 276.893 GHz mm-wave pulse that transfers population from the $6s45p$ state to the $6s41d$ ($n^* \approx 38.3$) $^1D_2$ state. Population in the intermediate state is monitored by a mm-wave transition at 283.847 GHz to the $6s47d$ ($n^* \approx 44.3$) $^1D_2$ state, while population in the final state is monitored by a mm-wave transition at 282.507 GHz to the $6s41f$ ($n^* \approx 40.9$) $^1F_3$ state. The electric dipole transition moment for the Pump transition is approximately 0.04 D and the electric dipole transition moment for the Stokes transition is approximately 350 D.

This level scheme was chosen in order to take advantage of the relatively low ionization potential of barium that allows for single-photon excitation to Rydberg states, because only a single dye laser was available during these experiments. Both the Pump and Stokes transition dipole moments are smaller than they would be in an ideal experiment, because of the large change in n^* in each transition. A larger Pump transition dipole moment is available in a two-step excitation scheme to access Rydberg states, exciting from a low-lying excited state as the initial state to the intermediate state. A larger Stokes transition dipole moment is available when one chooses a set of Rydberg states that have smaller changes in n^* between them. The scheme in barium shown above has the smallest possible Δn^* for the Stokes transition while retaining probe transitions inside the bandwidth of the high frequency mm-wave system.

The laser wavelengths for two-step excitation in barium are very inconvenient, and so I looked to other alkaline-earth atoms for a simple two-step excitation scheme to Rydberg states. I focused on alkaline-earth atoms for two reasons: 1) the electronic structure of expected initial molecular targets, alkaline-earth monohalides (such as CaF) strongly resembles the electronic structure of the alkaline-earth constituent, and 2) they are easily produced in large densities in the buffer gas cooled atomic beam, unlike, e.g. alkali metals. The laser wavelengths for two-step excitation in strontium are equally inconvenient, but the required wavelengths in calcium are well suited to the available lasers. Additionally, with a two-step excitation scheme I can take advantage of either the ns or nd series when searching for a set of STIRAP intermediate, final, and probe states with small changes in n^* between them.

The level structure of the relevant states in calcium is displayed in Figure 6-2. The initial state of the STIRAP process is the $4s5p\,^1P_1$ excited state, populated by a 272.245 nm laser pulse. The Pump pulse is a 803.719 nm laser pulse that transfers population to the $4s30d$ ($n^* \approx 28.8$) $^1D_2$ intermediate state, and the Stokes pulse is a 263.876 GHz mm-wave pulse that transfers population to the $4s28f$ ($n^* \approx 27.9$) $^1F_3$ final state. Population in the intermediate state is monitored by a mm-wave transition at 282.406 GHz to the $4s30f$ ($^n* \approx 29.9$) $^1F_3$ state, while population in the final

state is monitored by a mm-wave transition at 298.011 GHz to the $4s27g$ ($n^* \approx 27$) $^1G_4$ state. The electric dipole transition moment for the Pump transition is approximately 0.4 D and the electric dipole transition moment for the Stokes transition is approximately 1000 D.

Atomic systems in electronically autoionizing states can replicate the short lifetimes of molecular states. These are Rydberg states built on an electronically excited ion-core, as displayed schematically in Figure 6-3. Energy exchange between the ion-core and Rydberg electron leads to dexcitation of the ion-core and ejection of the Rydberg electron. As in molecules, CNP states in atoms have much longer lifetimes than CP states due to the centrifugal radial barrier that prevents overlap between the Rydberg electron and the ion-core. Unfortunately, the lifetime of electronically autoionizing states is ultimately limited by the radiative lifetime of the excited ion-core state, which is often on the order of ~ 10 ns for low-lying excited states in alkaline-earth ions. Highly excited ion-core states are necessary if one wishes to detect FID from electronically autoionizing atomic CNP Rydberg states.

6.2 Experimental evidence of two-photon coherent coupling in barium

To determine the dependence of population transfer efficiency in barium on the relative delay of the Pump and Stokes pulses, I monitored the relative population of the intermediate and final states as a function of the delay between the Pump and Stokes pulse, τ. The leading edge of the Pump pulse is stepped in 500 ps increments through that of the Stokes pulse in order to observe this dependence of transfer efficiency on the Stokes/Pump time delay. The Stokes mm-wave pulse is centered 100 ns in advance of the two probe pulses. This delay between Stokes and probe pulses allows sufficient time for damping of reflections inside the vacuum chamber. The overall timing scheme is displayed in Figure 6-4. In order to obtain as large Rabi frequencies as possible in both the Stokes and Pump pulses, I used the full output of

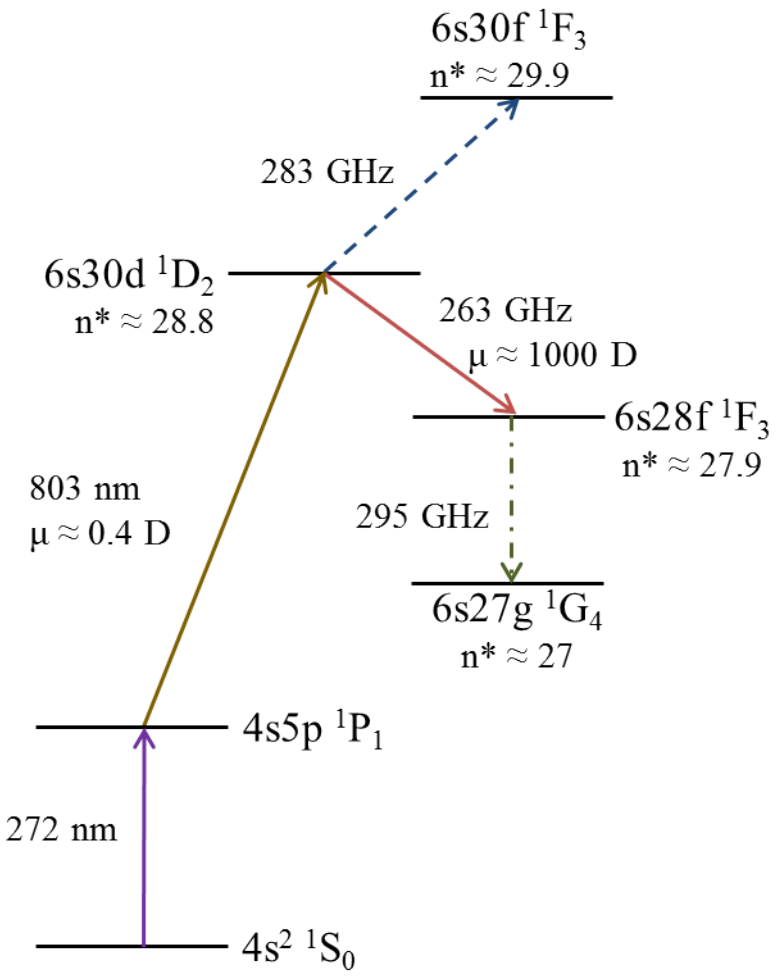

Figure 6-2: Level diagram for STIRAP experiments in calcium. The Pump (yellow, solid), Stokes, (red, solid) and probe (blue, dashed and green, dashed-dotted) transitions are shown along with the effective principal quantum numbers of each state and the electric dipole transition moments for the Pump and Stokes transitions. The initial population step into the $4s5p\,^1P_1$ state is shown as the solid, purple arrow.

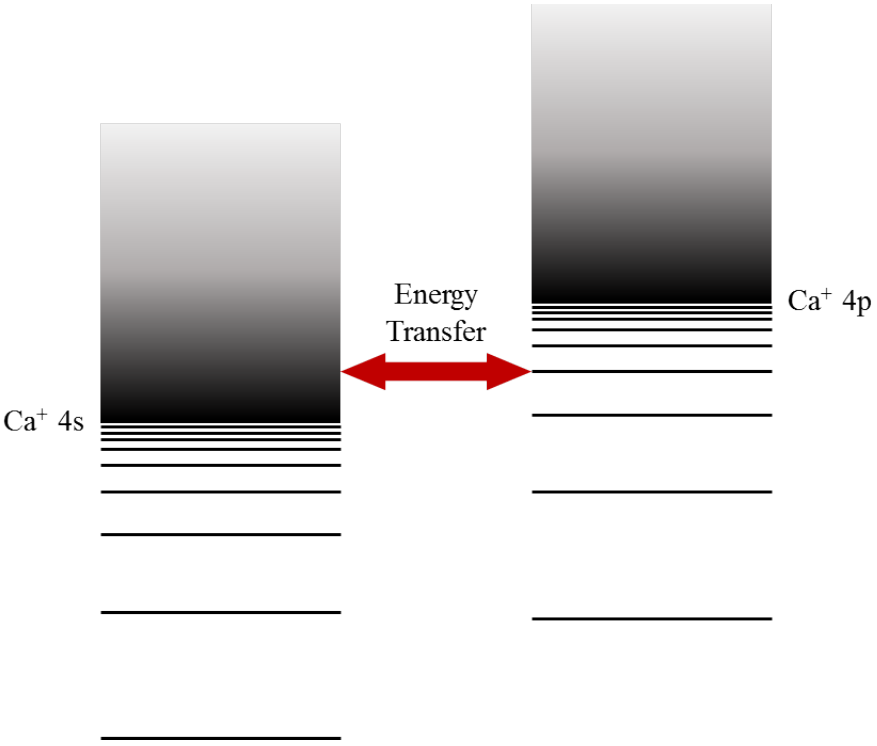

Figure 6-3: A schematic representation of electronic autoionization in the Rydberg states of calcium. The left-hand level diagram illustrates a Rydberg series converging on the $4s$ ground state of the Ca^+ ion, while the right-hand level diagram illustrates a Rydberg series converging on the $4p$ excited state of the Ca^+ ion. Rydberg states excited to the right-hand manifold at energies above the ground state ionization potential can couple to the ionization continuum, as indicated by the red double-headed arrow.

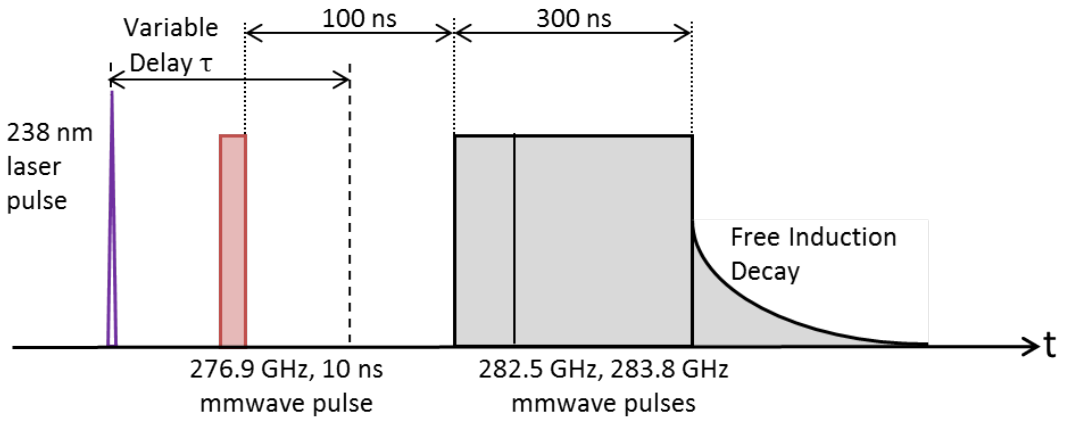

Figure 6-4: The timing sequence for the laser, mm-waves, and FID in experiments on barium. The first, purple pulse is the Pump pulse stepped through a variable delay τ with respect to the second, red, Stokes pulse. The two probe pulses occur 100 ns after the Stokes pulse.

both the Scanmate dye laser (~ 400 μJ/pulse at the chamber) and the high frequency mm-wave spectrometer (~ 13 dBm CW power in the interaction region).

Due to the large electric dipole transition moments for transitions between Rydberg states, the probe transitions can be very easily power broadened. The probe pulse used to monitor population in the $6s41d\,^1D_2$ state is attenuated by reducing the input power from the AWG to the AMC. Due to the highly nonlinear response of the AMC, changes in the input power of less than 1% can result in significant changes in the output power, as discussed in Chapter 2. I used the duration of the probe pulse as an additional variable to adjust the degree of polarization of this probe transition. The probe transition used to monitor the $6s45p\,^1P_1$ state was sufficiently weak that no attenuation was used. The two probe pulses consisted of one strongly attenuated 50 ns single-frequency pulse centered at 282.507 GHz followed immediately by an unattenuated 250 ns single-frequency pulse centered at 283.847 GHz. The first pulse induced a polarization modulo-2π of $\pi/2$ while the second pulse induced one of $\pi/4$. The ratio of these polarizations is used to normalize the two probe transition intensities and to determine an accurate pair of relative populations.

The solid curve in Figure 6-5a shows the ratio of transition intensity of the $41f - 41d$ transition (probe of final level) to the transition intensity of the $47d - 45p$

transition (probe of intermediate level) as a function of the variable delay, τ, of the laser Pump pulse. The observation of a maximum at a delay $\tau = 0$, the time at which the center of the Pump pulse is coincident with the center of the Stokes pulse, demonstrates enhanced transfer when both radiation fields are present at the same time. For negative values of τ, the center of the Pump pulse occurs before the center of the Stokes pulse, while positive values of τ correspond to the center of the Pump pulse occurring after the center of the Stokes pulse. For negative values of τ, the ratio of transition intensity is determined primarily by the efficiency of the Pump and Stokes pulses in transferring population via separate one-photon processes, while for large positive values of τ, no population is expected to be transferred to the final state. All coherent transfer processes are expected to occur when τ is small and positive, or when τ is approximately zero.

Figures 6-5b-d show the intensity of the $41f - 41d$, final state probe transition, and Figs. 6-5e-g show the intensity of the $47d - 45p$, intermediate state probe transition, at the delays indicated by the vertical dashed, solid, and dash-dotted lines, respectively. At a delay consistent with the intuitive pulse sequence, both the intermediate and final states retain population, thus probe transitions from both states are observed. As the pulses begin to overlap, the intensity in the probe transition that originates from the final state increases significantly, while that of the probe transition out of the intermediate state disappears entirely. Finally, when the Pump pulse is delayed to occur entirely after the Stokes pulse, the probe transition out of the final state disappears, while the probe transition out of the intermediate state increases significantly in intensity.

The dashed curve in Figure 6-5a shows the results of my theoretical calculations of coherent effects including phase and intensity noise effects, as outlined in Chapter 5. The dash-dotted curve in Fig. 6-5a shows the results of a calculation of an incoherent transition sequence using Einstein rate coefficients. Qualitatively, the dependence on τ of the experimental data is well reproduced in the coherent calculations, in contrast to the qualitative disagreement between experimental observation and the incoherent calculations.

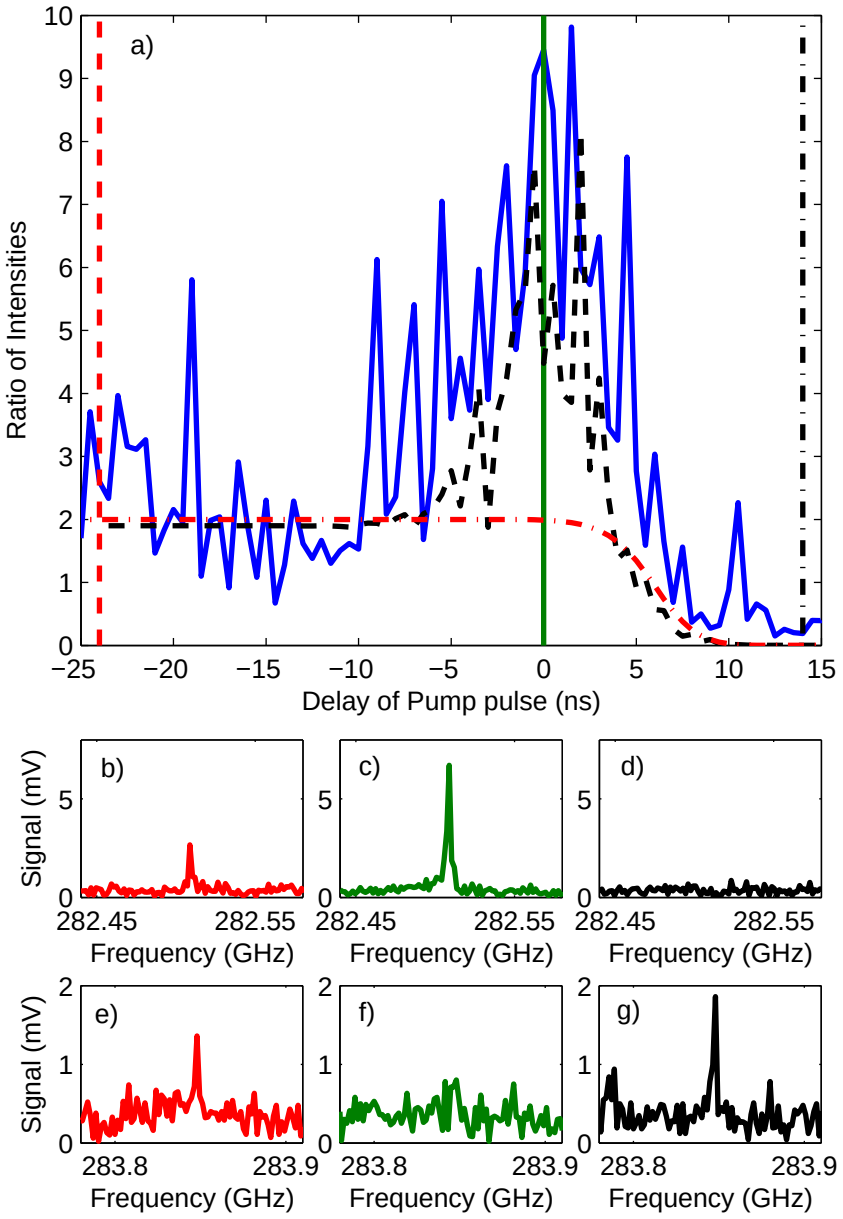

Figure 6-5: Plot (a) displays the experimental ratio of the population in the final state to the population in the intermediate state as a function of Pump pulse delay, τ, as a blue solid curve, the coherent theoretical results as a black dashed curve, and the incoherent theoretical results as a red dash-dotted curve. Plots (b) - (d) display the intensity of the $41f - 41d$ transition (probe of the final level) at Pump pulse delays given by the red dashed line, the green solid line, and the black dash-dotted line in plot (a), respectively. Plots (e) - (g) display the intensity of the $47d - 45p$ (probe of the intermediate level) transition at the same pulse delays.

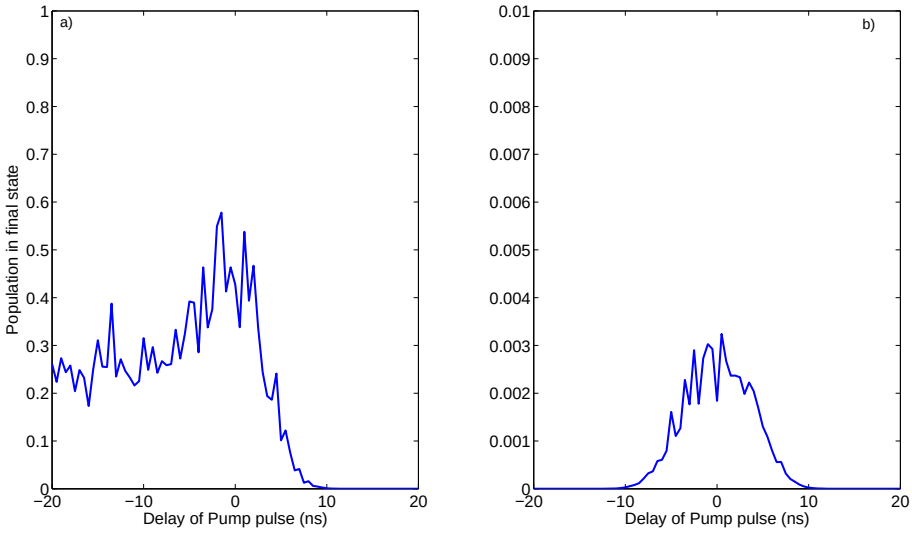

Figure 6-6: Theoretical population of the final state as a function of Pump pulse delay, τ, without (a) and with (b) intermediate state decay for barium. Note the 100% difference in scales between (a) and (b).

This agreement of the coherent theoretical calculations for the ratio of final to intermediate populations supports the validity of my calculation of the population transferred into the final state when the pulses are overlapped and I expect to find good agreement with my experimental results. The model system shows a population transfer to the final state of 50% during exact overlap, compared to a transfer of 20% for both the intuitive and counter-intuitive pulse sequences. The calculated variation of the final state population with delay time of the Pump pulse is shown as the solid curve in Figure 6-6a.

The primary factor that limits the efficiency of the two-color two-photon process is the phase fluctuations associated with the Pump pulse generated by the pulsed dye laser. Previous theoretical and experimental studies of the use of pulsed dye lasers in coherent population transfer techniques have shown that the Rabi frequency required to drive these processes scales as $N^2_{Fourier}$ [170], wher $N_{Fourier}$ is the ratio between the bandwidth of the dye laser to the Fourier-transform limited bandwidth. In this system, $N_{Fourier} \approx 4$ for each longitudinal mode [36], leading to a $\sim 16\times$ effective reduction in the Rabi frequency for the Pump pulse. The absence of an improvement

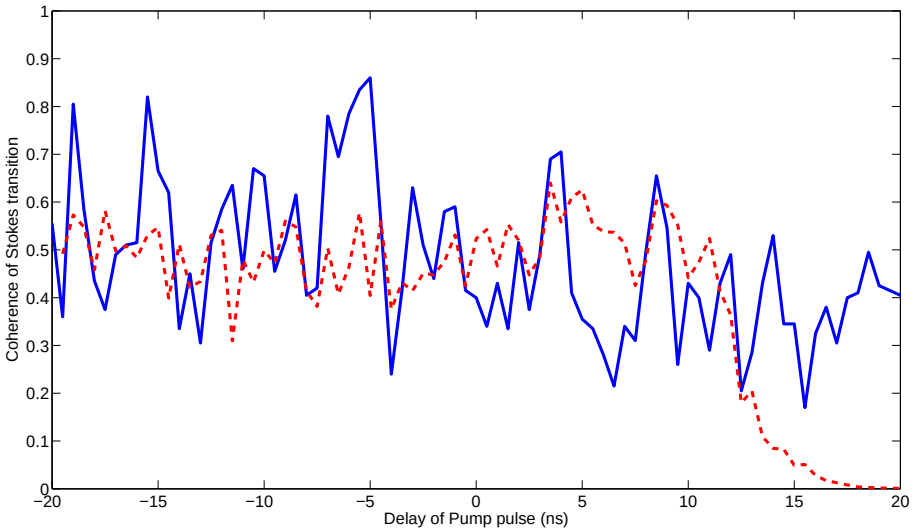

Figure 6-7: Coherence between the intermediate and final states as a function of Pump pulse delay, τ, for barium. The blue solid line is the experimental value of the coherence, and the red dashed line is the calculated value of the coherence.

in population transfer for the counter-intuitive pulse sequence as compared to what we observe for completely overlapped pulses, as well as a maximum population transfer efficiency of only 50% imply that STIRAP is not occurring in the barium system. With the limited power available from the dye laser in the UV, I cannot reach the regime of STIRAP because the effective Rabi frequency for the first transition is too low. This conclusion is experimentally supported by the observation of the remaining coherence between the intermediate and final states, in the form of FID radiation. The solid curve in Figure 6-7 shows the FID associated with the $41d - 45p$ transition as a function of the delay of the laser Pump pulse, while the dashed curve shows the calculated coherence (as in Chapter 5) between the two states. The decrease in coherence near small, positive delays characteristic of the STIRAP process is absent in both of these curves.

The increase in amount of population transferred to the final state when the Pump and Stokes pulses are overlapped can be understood with the same mathematics as those described in Section 5.1.2. In this case, however, the detuning of the Pump pulse, Δ_{12}, is zero, and so population is transferred through the intermediate state on

the way to the final state. With the appropriate Rabi frequencies, this method can provide 100% population transfer to the final state in the atomic case, but is not a useful method for molecular Rydberg states for two reasons. First any fluctuations in either laser or mm-wave power will lead to deviations from 100% population transfer. Second, since population travels through the intermediate state en route to the final state, any decay from the intermediate state becomes important. In typical molecular Rydberg states with predissociation lifetimes on order of $T_1 = 100$ ps, essentially no population survives to be transferred to the final state. This is shown as the dashed curve in Figure 6-6b. Note the 100% difference in scale between Figs. 6-6a and 6-6b.

6.3 Optical-mm-wave STIRAP in calcium

In order to determine whether optical-mm-wave STIRAP is feasible using a pulsed dye laser similar to the one available for my experiments, I calculated the results of using the calcium level scheme presented in Section 6.1. This scheme provides a much larger effective Rabi frequency due to the larger Pump laser electric dipole transition moment. The effective Rabi frequency was the main limiting factor in the experiments performed on barium.

When calculating the population transferred to the final state in the calcium system, I observe a maximum associated with STIRAP that occurs at an optimum Stokes/Pump delay of the counter-intuitive pulse sequence, as shown in Figure 6-8a. Additionally, I observe a characteristic decrease to zero in the coherence at the same pulse timing, as displayed by the dashed curve in Fig. 6-9. The solid curve in Fig. 6-9 shows the system discussed in Section 5.2.2 (and is the same curve as in Fig. 5-7d). These clear decreases in coherence between the intermediate and final states at ~ 5 ns delay in both curves are associated with the STIRAP mechanism of transferring population directly from the initial to the final state without placing any population in the intermediate state. The final test to ensure that STIRAP is occurring is to introduce a rapid decay to the intermediate state, as in a molecular case. After setting $T_1 = 100$ ps again in order to replicate typical predissociation lifetimes in the

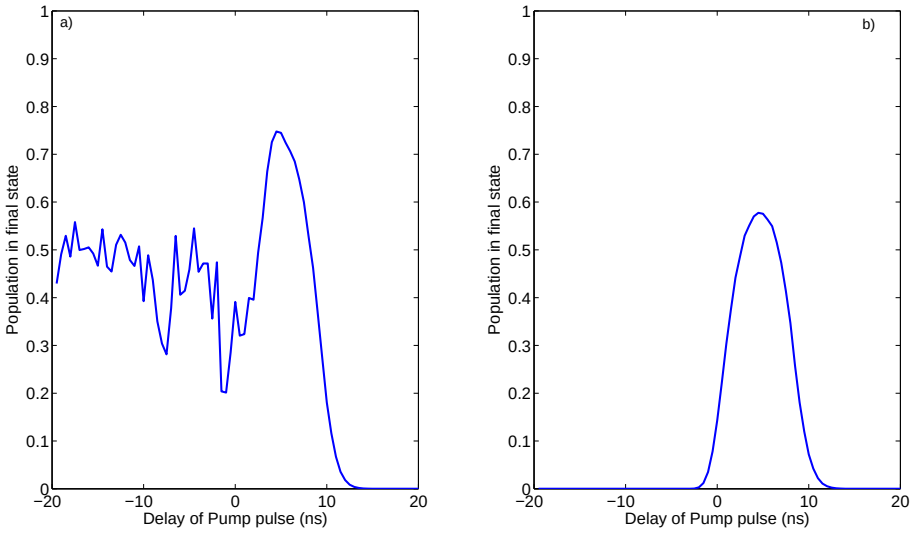

Figure 6-8: Computed population of the final state as a function of Pump pulse delay, τ, without (a) and with (b) intermediate state decay for calcium. Note the maximum at small, positive values of ÏĎ in each plot.

intermediate state, I recalculate the population transferred to the final state with the calcium experimental parameters. The population of the final state as a function of Pump laser delay is shown in Fig. 6-8b, and shows a maximum of $\sim 60\%$ population transfer at the counter-intuitive pulse timing. These three calculations demonstrate that the primary obstacle remaining to achieve optical-mm-wave STIRAP is to increase the Rabi frequency for the Pump transition, either by increasing the laser power, changing the excitation scheme to exploit a larger transition dipole moment (as done here), or improving the coherence properties of the laser.

The failure to achieve near 100% transfer of population from the initial to the final state in the calcium system is due to other experimental imperfections in our system, such as non-adiabatic losses inherent in the sharp turn-off of the mm-wave pulse. The transfer efficiency may be modeled as a function of the mm-wave pulse shape (Square wave, Gaussian, triangle pulse) and the results are shown in Figure 6-10. As expected, a Gaussian pulse provides the most efficient transfer, but a triangle pulse provides nearly the same efficiency and is technically easier to implement. Shaping the high frequency mm-wave pulses on a time scale shorter than $\sim$ 30 ns remains

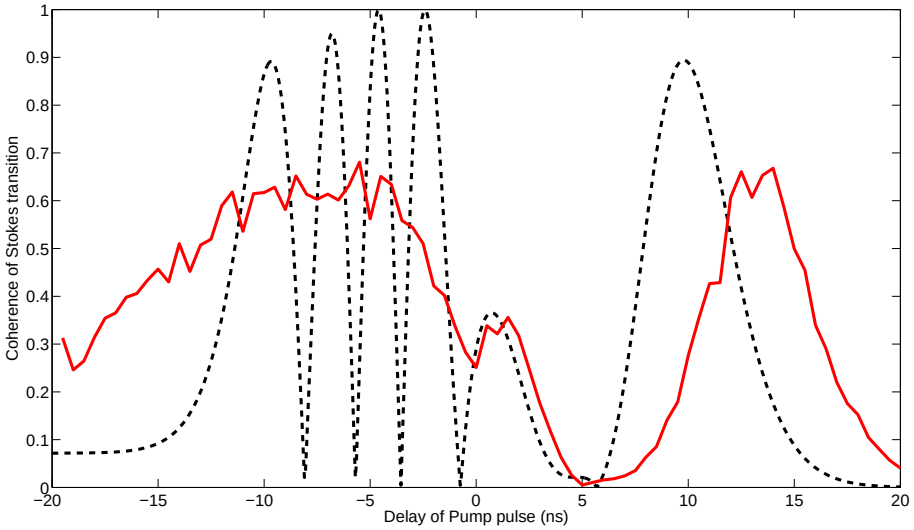

Figure 6-9: Coherence between the intermediate and final states as a function of Pump pulse delay, τ. The red solid line is the calculated value for the calcium system, and the black dashed line is the coherence expected for the system described in Chapter 5, Figure 5-6 (without an intermediate state decay). The absence of oscillations at negative values of τ in the calcium system is due to the inclusion of phase and intensity fluctuations in the Pump pulse, while the shift in the maximum at positive values of τ are due to the square wave envelope of the Stokes pulse in the calcium system.

technically difficult, and all of the experiments reported in my thesis use a square wave Stokes pulse.

As the frequencies of the laser and mm-wave photons are different by a factor of $\sim 10^4$, the Doppler shifts of the two transitions are quite different and result in a two-photon detuning that cannot be compensated by choice of experimental geometry. For a Λ-type transition, co-propagating beams of similar frequency cancel the majority of the Doppler shift, while for a ladder-type transition, counter-propagating beams of similar frequency have the same effect. In my case, the Doppler width associated with the optical photon ($\sim$ 800 MHz) is much larger than the Doppler width associated with the mm-wave photon ($\sim$ 250 kHz). These small Doppler widths are due to the use of a buffer gas cooled beam source in our experiments. Typical Doppler widths in a supersonic expansion are $\sim 5\times$ larger. I calculate the efficiency of STIRAP transfer in calcium (with a short lifetime intermediate state) for both a slow buffer gas expansion and a fast supersonic expansion as a function of radial distance from the center of the beam. The results of this calculation are shown in Figure 6-11. For systems with a large frequency mismatch between Pump and Stokes pulses, it is clear that a slow beam expansion, such as is obtained from buffer gas cooling, is essential to achieve efficient population transfer across the entire molecular beam.

At the time of the writing of this thesis, experimental investigations of STIRAP in calcium atoms are currently underway.

6.4 Applications of STIRAP to molecular systems

One of the primary obstacles to STIRAP in molecular systems is the reason for performing STIRAP in the first place: the short lifetime of the intermediate state. The lifetimes of predissociating states can range over several orders of magnitude, depending on the details of the molecular potential energy surfaces and the coupling of the Rydberg states with dissociative electronic states. In the sections above I used 100 ps as a representative predissociation lifetime, but the lifetime can be much shorter than 100 ps in certain cases. Autoionization typically is a much faster process

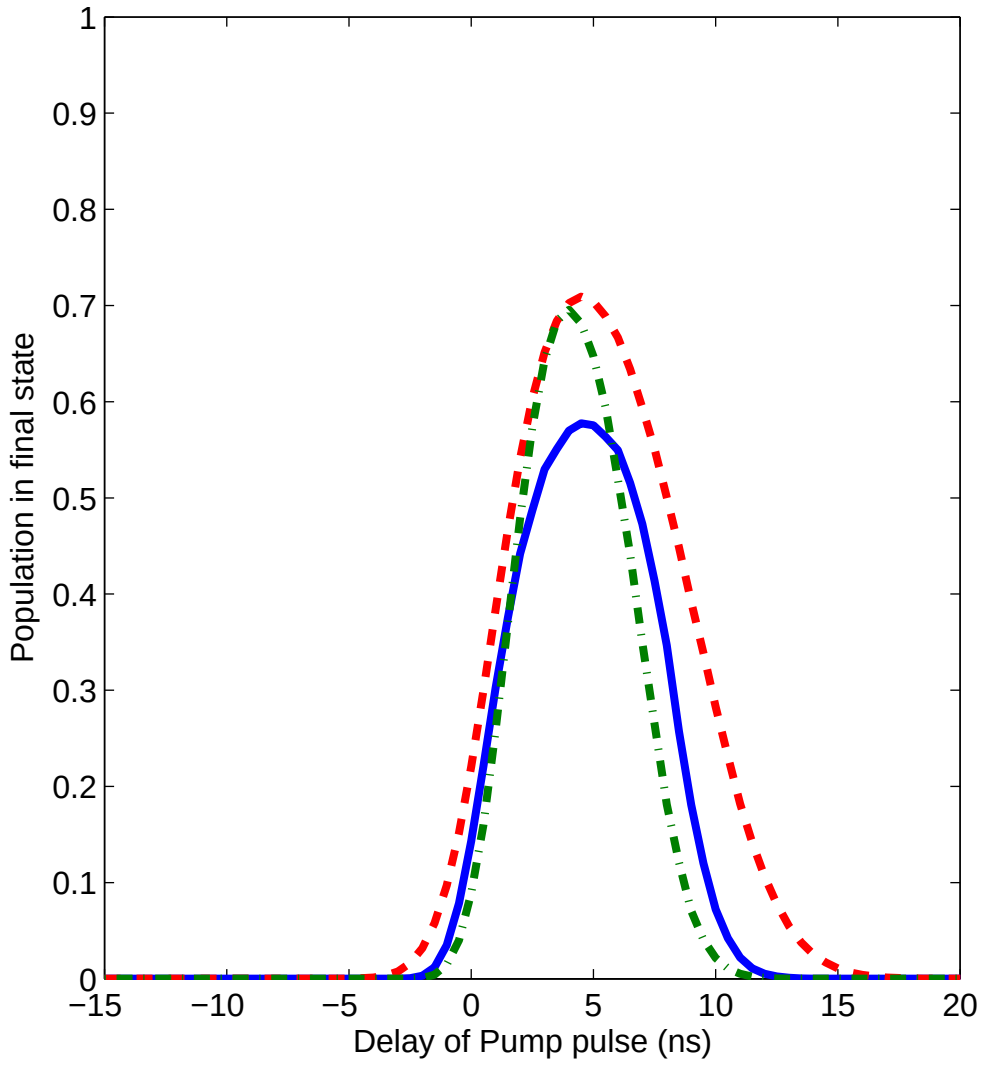

Figure 6-10: Computed populations of the final state as a function of the Stokes pulse envelope. The blue solid curve represents a square pulse envelope, the red dashed curve represents a Gaussian pulse envelope, and the green dash-dotted curve represents a triangular pulse envelope. All calculations were performed for the calcium system.

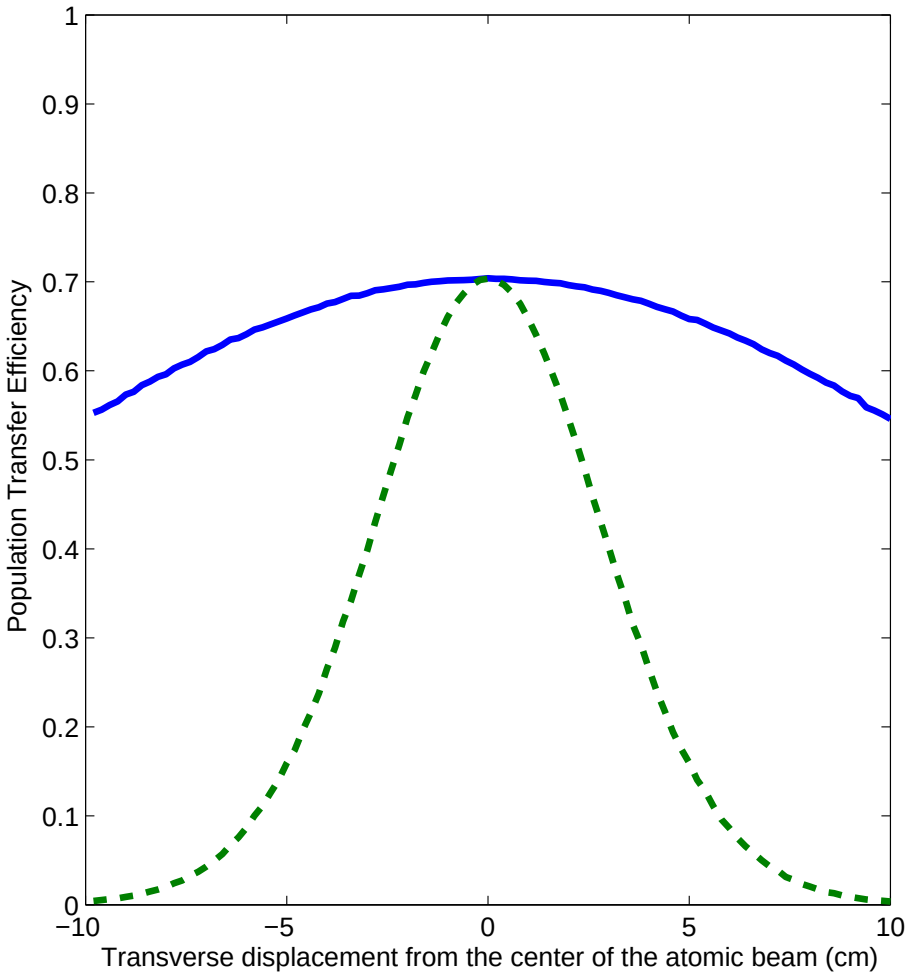

Figure 6-11: Computed population transfer efficiency as a function of transverse distance from the center of the atomic beam. The blue solid curve represents a slow buffer gas cooled expansion and the green dashed curve represents a fast supersonic expansion. The arbitrary units in both cases cover the entire transverse extent of the atomic beam. All calculations were performed on the calcium system.

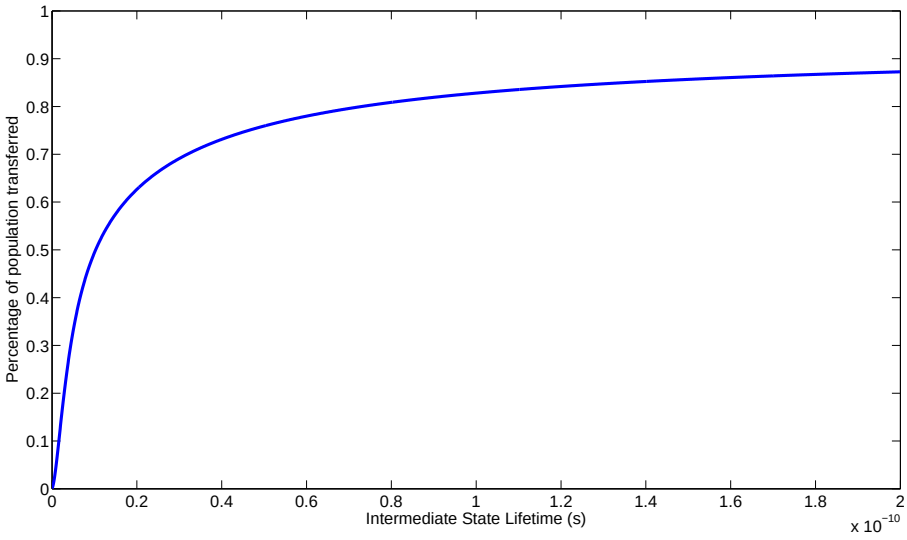

Figure 6-12: The population transfer efficiency of a generic STIRAP scheme with 10 ns pulse duration Pump and Stokes pulses for a variety of intermediate state lifeteimes. Note that even at relatively long lifetimes the efficiency does not increase to greater than 0.9 due to the square wave envelope of the Stokes pulse.

than predissociation. An intuitive reason for this is that instead of breaking a chemical bond and moving heavy nuclei apart, autoionization ejects a light electron from the molecule. In order to populate CNP states that autoionize into a single quantum state of the molecular cation, autoionizing states must be traversed via STIRAP, a more challenging requirement than for predissociating states. STIRAP efficiency for typical values of transition dipole moments (0.5 D for the Pump pulse, 3000 D for the Stokes pulse) and pulse energies (2 mJ for the Gaussian Pump pulse, 13 dBm for the square Stokes pulse) is displayed as a function of intermediate state lifetime in Figure 6-12. This calculation assumes a Fourier-transform limited Pump pulse.

A second difficulty with molecular targets is that the proper intermediate state for accessing CNP states is often not known to the same accuracy as for atomic targets. Only the Rydberg states of H_2, NO, and CaF have levels of characterization that approach that of atomic Rydberg states [77]. As such, some spectroscopic preparatory work may need to be performed to determine the appropriate CP intermediate state for STIRAP in order to have strong electric dipole transition moments to CNP states. CNP states, however, uniformly have near-integer principal quantum numbers and

are easily identified in the spectrum.

An additional challenge, in both molecular and atomic systems, is unintentional multi-photon ionization. The fundamental problem is that when driving transitions that have small electric dipole transition moments, the natural way to improve STIRAP efficiency is to use more power in order to increase the Rabi frequency. For mm-wave Stokes transitions, this is not a problem, because many mm-wave photons are required to ionize Rydberg states at the values of n^* that I work at (generally $>$10). However, for the optical Pump transition, a single additional photon can easily ionize a Rydberg state. In certain molecules, the optical cross section for ionization can be even larger than the optical cross section for excitation to the intermediate state (as observed in BaF experiments), in which case increasing Pump laser power is counter-productive to creating CNP Rydberg states.

A conceptually straightforward way of solving both this complication and the complication of Stokes pulse non-adiabaticity is to use longer Pump and Stokes pulses. This decreases the required Rabi frequency of each pulse to satisfy the adiabaticity criterion from Chapter 5, and allows for simple mm-wave shaping of a smooth turn-off of the Stokes pulse. Pulsed lasers, unfortunately, typically have maximum pulse durations of $\sim 10 - 20$ ns. One potential method of producing a long duration pulse is to introduce a build-up cavity around the sample, allowing the natural filling and ringing-down of the cavity to form the pulse. This would also benefit from the use of phase-coherent CW lasers as the Pump source, further increasing STIRAP efficiency. STIRAP efficiency as a function of intermediate state lifetime with 100 ns Pump and Stokes pulses, using the same transition dipole moments as above and a Gaussian envelope of the Stokes pulse, is shown in Figure 6-13.

Despite the many obstacles to performing optical-mm-wave STIRAP to populate CNP states of molecules, the path forward is promising. Experiments currently underway on atomic systems can be easily extended to molecular systems to demonstrate population transfer with a decaying intermediate state. The technology and techniques required to effectively drive STIRAP currently exist, and simply need to be applied to the systems in question.

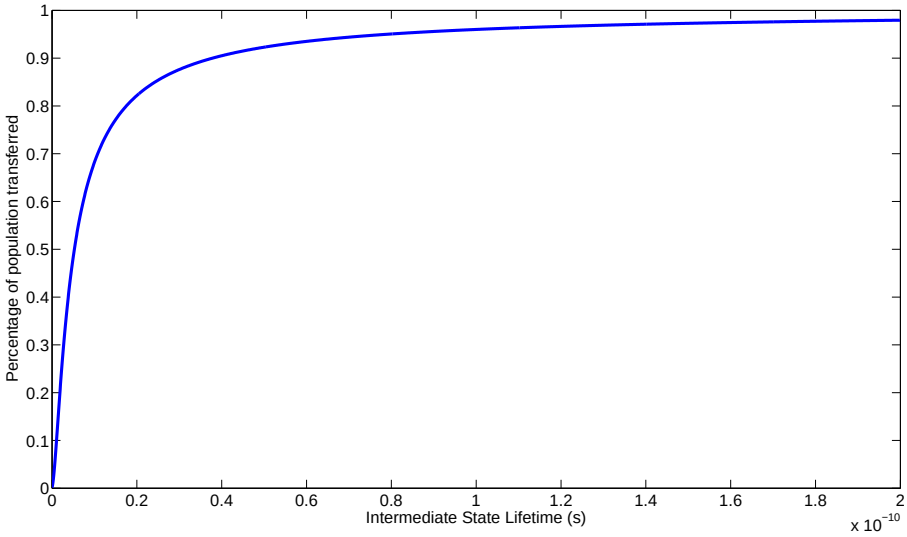

Figure 6-13: The population transfer efficiency of a generic STIRAP scheme with 100 ns pulse duration Pump and Stokes pulses for a variety of intermediate state lifeteimes. Note that the increase is much more rapid, and the efficiency is nearly unity even for a 200 ps intermediate state lifetime.

Chapter 7

Conclusion and future directions

The experiments described in my thesis demonstrate the potential of mm-wave spectroscopy of Rydberg states to both investigate the dynamics of strongly cooperative systems and to develop efficient schemes to control coherent population transfer between Rydberg states. The single-shot observation of free-space mm-wave superradiance provides a window into quantum many-body effects at much higher optical depths than other gas phase superradiance experiments. The free-space nature of this experiment allows for investigation of cooperative frequency shifts and broadenings. I have observed frequency shifts and broadenings $10^5\times$ larger than the natural lifetime of the transition and $20\times$ larger than the Doppler broadening of the experiment. Additionally, after the superradiant emission, I have observed long-lived, coherent emission, the source of which remains to be conclusively determined.

I have also demonstrated the potential to populate high orbital angular momentum CNP states via coherent population transfer techniques. First, using barium and relatively low Rabi frequencies, I performed coherently enhanced population transfer directly from the ground state to an *nd* Rydberg state. Second, using calcium and relatively high Rabi frequencies, I have shown that STIRAP is possible with a standard pulsed dye laser in combination with a CPmmW spectrometer, and characterized the parameters necessary for applications to molecular systems.

7.1 Investigations of cooperative radiation effects

While there are many potential experiments that lend themselves well to investigations with highly cooperative ensembles of Rydberg states, two directions stand out for initial work. First, investigations of superradiance with simultaneous monitoring of the absolute density of Rydberg states is essential to provide an independent determination of the optical depth of each shot as well as the relative density of each shot. This information will enable a more complete comparison with theoretical models, especially for determination of the scaling of the induced cooperative frequency shift. Second, investigations of superradiance in the absence of an untriggered competing superradiant transition must be performed in order to disentangle effects of the triggered and untriggered processes.

Ideally these two sets of new experiments could be performed at the same time. Calcium provides a useful test system for both of these experiments. First, an excitation to an ns Rydberg state eliminates competing untriggered superradiance. Second, there are convenient transitions (either $4s5p \rightarrow 3d4s$ at ~ 670 nm or $4s5p \rightarrow 4sns/nd$ Rydberg states at ~ 805 nm) that would enable monitoring of population excited from the $4s5p$ intermediate state to the ns Rydberg state via changes in absorption/stimulated emission.

Once these experiments have been performed, there are a variety of more exploratory experiments that can be performed. Investigation of the properties of the emitted radiation, such as the polarization of the light and presence of any diffraction patterns (associated with the spatial mode of the radiation), in both triggered and untriggered experiments, provides important confirmations of fundamental theories of cooperative radiation. Precise determination of the frequency domain lineshape as a function of preparation geometry, as illustrated by Figure 7-1, will provide a revealing demonstration of the importance of relative phase in superradiance experiments. The experiments described in my thesis are all initiated in the "Timed Atomic State" from Figure 7-1, but by exciting the atoms to Rydberg states from a direction perpendicular to our mm-wave propagation axis, we can approach a "Symmetric

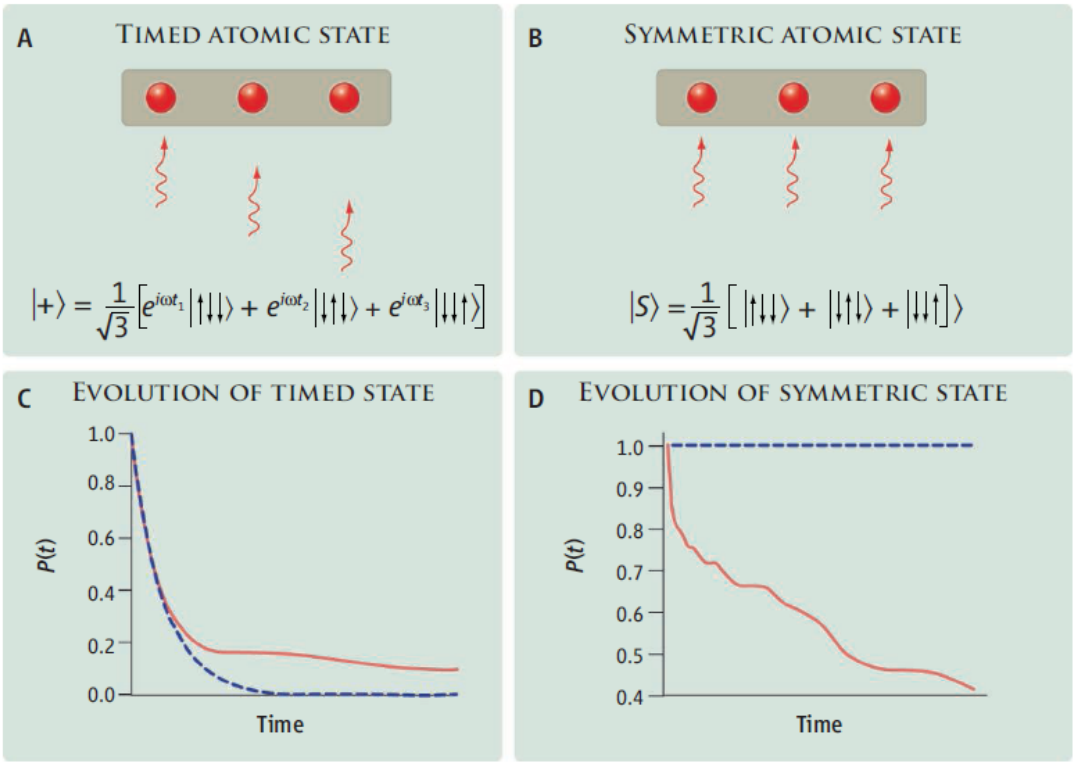

Figure 7-1: Parts (A) and (B) demonstrate two different initial phase conditions of a superradiant sample, the "Timed Atomic State" and the "Symmetric Atomic State." Parts (C) and (D) show the predicted evolution of these states in the presence (solid lines) or absence (dashed lines) of virtual photons, where $P(t)$ is the probability that atoms are excited as a function of time t. Reprinted from Ref [3]

Atomic State." Finally, determination of the source of the long-lived radiation, and whether it is attributable to subradiance, is essential for a quantitative and useful understanding of the evolution of the highly cooperative sample.

7.2 Future applications of core-nonpenetrating Rydberg states of molecules

The demonstration of optical-mm-wave coherently enhanced population transfer and STIRAP in atoms opens the door to routinely being able to populate CNP Rydberg states in molecules. CNP states are themselves interesting as the Rydberg electron can act as an embedded reporter of the multipolar moments and polarizabilities of the ion-core. Exciting CNP states based on different vibration-rotation states of the ion-core allows for determination of the dependence of these electronic properties on the internal structure of the ion-core. Determining and understanding this electronic structure is the first step toward understanding the global structure of Rydberg states and connecting a purely electrostatics-based long-range model to a full Multichannel Quantum Defect Theory (MQDT) model. Further, stroboscopic resonances between the electronic and rotational/vibrational motion of the ion-core permit detailed study of the mechanisms of transfer of energy between the Rydberg electron and the ion-core.

CNP states can be used as a tool in a variety of other experiments. The exceptionally large polarizability of Rydberg states makes them exceptionally sensitive to electric fields, and so molecular beams of CNP states can be slowed to a stop in the lab frame with a single stage of Stark deceleration, leading to very slow moving (in the laboratory frame) molecular ensembles. Further, as a CNP state is a Rydberg electron bound to a single vibration-rotation-M_J state of the ion-core, autoionization of CNP states results in molecular ions prepared in that same single vibration-rotation-M_J state. These state-selected ions can then be used in either quantum computing schemes, or used for investigations of ultracold chemical reactions.

Bibliography

[1] M Gross and S Haroche. Superradiance: An essay on the theory of collective spontaneous emission. *Physics Reports*, 93(5):301–396, December 1982.

[2] Gray Putnam, Guin-Dar Lin, and S. F. Yelin. Collective induced superradiant lineshifts, 2016.

[3] Marlan O Scully and Anatoly A Svidzinsky. Physics. The Lamb shift-yesterday, today, and tomorrow. *Science*, 328(5983):1239–41, June 2010.

[4] Thomas F. Gallagher. *Rydberg Atoms*. Cambridge University Press, 1994.

[5] J. R. Rydberg. XXXIV. On the structure of the line-spectra of the chemical elements. *Philosophical Magazines Series 5*, 29(179):331–337, 1890.

[6] Helene Lefebvre-Brion and Robert W. Field. *The Spectra and Dynamics of Diatomic Molecules*. Elsevier, 2004.

[7] T. F. Gallagher. Rydberg Atoms. *Reports on Progress in Physics*, 51(2):143–188, 1988.

[8] Kirill Prozument, Anthony P. Colombo, Yan Zhou, G. Barratt Park, Vladimir S Petrović, Stephen L. Coy, and Robert W. Field. Chirped-Pulse Millimeter-Wave Spectroscopy of Rydberg-Rydberg Transitions. *Physical Review Letters*, 107(14):143001, September 2011.

[9] Anthony P. Colombo, Yan Zhou, Kirill Prozument, Stephen L. Coy, and Robert W. Field. Chirped-pulse millimeter-wave spectroscopy: Spectrum, dynamics, and manipulation of RydbergâĂŞRydberg transitions. *The Journal of Chemical Physics*, 138(1):014301, 2013.

[10] Yan Zhou, David D. Grimes, Timothy J. Barnum, David Patterson, Stephen L. Coy, Ethan Klein, John S. Muenter, and Robert W. Field. Direct detection of Rydberg-Rydberg millimeter-wave transitions in a buffer gas cooled molecular beam. *Chemical Physics Letters*, 640:124–136, 2015.

[11] R. Friedberg, S. R. Hartmann, and J. T. Manassah. Frequency shifts in emission and absorption by resonant systems of two-level atoms. *Physics Reports*, 7(3):101–179, March 1973.

[12] Robert S. Mulliken. The Rydberg States of Molecules . Parts I-V. *Journal of the American Chemical Society*, 86(16):3183–3197, 1964.

[13] Robert S. Mulliken. The Rydberg States of Molecules. VI. Potential Curves and Dissociation Behavior of (Rydberg and Other) Diatomic States. *Journal of the American Chemical Society*, 88(9):1849–1861, 1966.

[14] F. Merkt. Molecules in high Rydberg states. *Annual Review of Physical Chemistry*, 48(2):675–709, 1997.

[15] E. E. Eyler. Autoionization of nonpenetrating Rydberg states in diatomic molecules. *Physical Review A*, 34(4):2881–2888, 1986.

[16] M. Bixon and Joshua Jortner. The dynamics of high autoionizing Rydberg states of Ar. *The Journal of Chemical Physics*, 103(11):4431–4446, 1995.

[17] M. Bixon and Joshua Jortner. The dynamics of predissociating high Rydberg states of NO. *The Journal of Chemical Physics*, 105(4):1363–1382, 1996.

[18] S. T. Pratt. Vibrational autoionization and predissociation in high Rydberg states of nitric oxide. *The Journal of Chemical Physics*, 108(17):7131–7140, 1998.

[19] F. Remacle and Marc J. J. Vrakking. Decay Dynamics of the Predissociating High Rydberg States of NO. *The Journal of Physical Chemistry A*, 102(47):9507–9517, 1998.

[20] K. Bergmann, H. Theuer, and B. W. Shore. Coherent population transfer among quantum states of atoms and molecules. *Reviews of Modern Physics*, 70(3):1003–1025, 1998.

[21] Klaas Bergmann, Nikolay V. Vitanov, and Bruce W. Shore. Perspective: Stimulated Raman adiabatic passage: The status after 25 years. *The Journal of Chemical Physics*, 142(17):170901, 2015.

[22] C. Fabre, S. Haroche, and P. Goy. Millimeter spectroscopy in sodium Rydberg states: quantum-defect, fine-structure, and polarizability measurements. *Physical Review A*, 18(1):229–237, 1978.

[23] M. Gross, P. Goy, C. Fabre, S. Haroche, and J. M. Raimond. Maser Oscillation and Microwave Superradiance in Small Systems of Rydberg Atoms. *Physical Review Letters*, 43(5):343–346, 1979.

[24] P. Goy, C. Fabre, M. Gross, and S. Haroche. High-resolution two-photon millimetre spectroscopy in sodium Rydberg states: possible applications to metrology. *Journal of Physics B: Atomic, Molecular and Optical Physics*, 13(3):L83–L91, 1980.

[25] L. Moi, C. Fabre, P. Goy, M. Gross, S. Haroche, P. Encrenaz, G. Beaudin, and B. Lazareff. Heterodyne detection of Rydberg atom maser emission. *Optics Communications*, 33(1):47–50, 1980.

[26] J. M. Raimond, P. Goy, M. Gross, C. Fabre, and S. Haroche. Statistics of millimeter-wave photons emitted by a Rydberg-atom maser: An experimental study of fluctuations in single-mode superradiance. *Physical Review Letters*, 49(26):1924–1927, 1982.

[27] P. Goy, J. M. Raimond, G. Vitrant, and S. Haroche. Millimeter-wave spectroscopy in cesium Rydberg states. Quantum defects, fine-and hyperfine-structure measurements. *Physical Review A*, 26(5):2733–2742, 1982.

[28] P. Goy, L. Moi, M. Gross, J. M. Raimond, C. Fabre, and S. Haroche. Rydberg-atom masers. II. Triggering by external radiation and application to millimeter-wave detectors. *Physical Review A*, 27(4):2065–2081, 1983.

[29] Thomas R. Gentile, Barbara J. Hughey, Daniel Kleppner, and Theodore W. Ducas. Microwave spectroscopy of calcium Rydberg states. *Physical Review A*, 42(1):5327–5332, 1990.

[30] P. L. Jacobson, D. S. Fisher, C. W. Fehrenbach, W. G. Sturrus, and S. R. Lundeen. Determination of the dipole polarizabilities of H_2^+ (0,0) and D_2^+ (0,0) by microwave spectroscopy of high-L Rydberg states of H_2 and D_2. *Physical Review A*, 56(6):4361–4364, 1997.

[31] P. L. Jacobson, R. A. Komara, W. G. Sturrus, and S. R. Lundeen. Microwave spectroscopy of heliumlike Rydberg states of H_2 and D_2 : Determinations of the dipole polarizabilities of H_2^+ and D_2^+ ground states. *Physical Review A*, 62:1–12, 2000.

[32] A. Osterwalder, R. Seiler, and F. Merkt. Measurement of the hyperfine structure in low-l, high-n Rydberg states of ortho H_2 by millimeter wave spectroscopy. *The Journal of Chemical Physics*, 113(18):7939–7944, 2000.

[33] F. Merkt and A. Osterwalder. Millimetre wave spectroscopy of high Rydberg states. *International Reviews in Physical Chemistry*, 21(3):385–403, July 2002.

[34] G. Barratt Park, Adam H. Steeves, Kirill Kuyanov-Prozument, Justin L. Neill, and Robert W. Field. Design and evaluation of a pulsed-jet chirped-pulse millimeter-wave spectrometer for the 70-102 GHz region. *The Journal of Chemical Physics*, 135(2):024202, July 2011.

[35] Hyunwook Park and T. F. Gallagher. Measurement of the dipole-dipole interaction of Rb nsnp states by microwave Ramsey interferometry. *Physical Review A*, 86(5):052510, November 2012.

[36] T. T. Kajava, H. M. Lauranto, and R. R. Salomaa. Mode structure fluctuations in a pulsed dye laser. *Applied Optics*, 31(33):6987–92, 1992.

[37] Jens-Uwe Grabow. Fourier Transform Microwave Spectroscopy Measurement and Instrumentation. In Martin Quack and Frédéric Merkt, editors, *Handbook of High-resolution Spectroscopy*, pages 723–799. John Wiley & Sons, Ltd., 2011.

[38] Gordon G. Brown, Brian C. Dian, Kevin O. Douglass, Scott M. Geyer, and Brooks H. Pate. The rotational spectrum of epifluorohydrin measured by chirped-pulse Fourier transform microwave spectroscopy. *Journal of Molecular Spectroscopy*, 238(2):200–212, August 2006.

[39] Gordon G Brown, Brian C. Dian, Kevin O. Douglass, Scott M. Geyer, Steven T. Shipman, and Brooks H. Pate. A broadband Fourier transform microwave spectrometer based on chirped pulse excitation. *The Review of Scientific Instruments*, 79(5):053103, May 2008.

[40] G. Barratt Park and Robert W. Field. Perspective: The first ten years of broadband chirped pulse Fourier transform microwave spectroscopy. *Journal of Chemical Physics*, 144(20):200901, 2016.

[41] Michael A. Duncan. Invited review article: laser vaporization cluster sources. *The Review of scientific instruments*, 83(4):041101, April 2012.

[42] J. K. Messer and Frank C. De Lucia. Measurement of pressure-broadening parameters for the CO-He system at 4 K. *Physical Review Letters*, 53(27):2555–2558, 1984.

[43] Daniel R. Willey, Richard L. Crownover, D. N. Bittner, and Frank C. De Lucia. Very low temperature spectroscopy: The pressure broadening coefficients for COâĂŞHe between 4.3 and 1.7 K. *Journal of Chemical Physics*, 89(4):1923, 1988.

[44] Christopher D. Ball, Frank C. De Lucia, Dipesh Risal, Alan Ruch, Hua Sheng, Yilma Abebe, Paula A. Farina, and Arlan W. Mantz. Performance Characteristics of a Low Temperature Cell for Collisional Cooling Experiments. *Proceedings of the Society of Photo-Optical Instrumentation Engineers*, 2834(1):102 – 109, 1996.

[45] S. E. Maxwell, N. Brahms, R. DeCarvalho, D. R. Glenn, J. S. Helton, S. V. Nguyen, D. Patterson, J. Petricka, D. DeMille, and J. M. Doyle. High-Flux Beam Source for Cold, Slow Atoms or Molecules. *Physical Review Letters*, 95(17):173201, October 2005.

[46] David Patterson and John M. Doyle. Bright, guided molecular beam with hydrodynamic enhancement. *The Journal of Chemical Physics*, 126(15):154307, April 2007.

[47] David Patterson, Julia Rasmussen, and John M. Doyle. Intense atomic and molecular beams via neon buffer-gas cooling. *New Journal of Physics*, 11(5):055018, May 2009.

[48] David Patterson, Edem Tsikata, and John M. Doyle. Cooling and collisions of large gas phase molecules. *Physical Chemistry Chemical Physics*, 12(33):9736–41, September 2010.

[49] Nicholas R. Hutzler, Maxwell Parsons, Yulia V. Gurevich, Paul W. Hess, Elizabeth Petrik, Ben Spaun, Amar C. Vutha, David DeMille, Gerald Gabrielse, and John M. Doyle. A cryogenic beam of refractory, chemically reactive molecules with expansion coolings. *Physical Chemistry Chemical Physics*, 42(13):18976–18985, 2011.

[50] Hsin-I Lu, Julia Rasmussen, Matthew J. Wright, Dave Patterson, and John M. Doyle. Cold and Slow Molecular Beam. *Physical Chemistry Chemical Physics*, 13(42):18986–18990, 2011.

[51] J. F. Barry, E .S. Shuman, and D. DeMille. A bright, slow cryogenic molecular beam source for free radicals. *Physical Chemistry Chemical Physics*, 13(42):18936–18947, November 2011.

[52] Nicholas R. Hutzler, Hsin-I Lu, and John M. Doyle. The buffer gas beam: An intense, cold, and slow source for atoms and molecules. *Chemical Reviews*, 112(9):4803–4827, 2012.

[53] A. L. Goodgame and T. P. Softley. Control of atomic and molecular motion via the Stark effect in Rydberg states. *Journal of Physics B: Atomic, Molecular and Optical Physics*, 32(20):4839–4857, 1999.

[54] S. D. Hogan and F. Merkt. Demonstration of three-dimensional electrostatic trapping of state-selected rydberg atoms. *Physical Review Letters*, 100(4):043001, 2008.

[55] S. Hogan, Ch. Seiler, and F. Merkt. Rydberg-State-Enabled Deceleration and Trapping of Cold Molecules. *Physical Review Letters*, 103(12):123001, September 2009.

[56] Ch. Seiler, S. D. Hogan, and F. Merkt. Trapping cold molecular hydrogen. *Physical Chemistry Chemical Physics*, 13(42):19000–19012, 2011.

[57] S. D. Hogan, P. Allmendinger, H. Saß mannshausen, H. Schmutz, and F. Merkt. Surface-Electrode Rydberg-Stark Decelerator. *Physical Review Letters*, 108(6):063008, 2012.

[58] S. D. Hogan, J. Agner, F. Merkt, T. Thiele, S. Filipp, and A. Wallraff. Driving Rydberg-Rydberg Transitions from a Coplanar Microwave Waveguide. *Physical Review Letters*, 108(6):063004, February 2012.

[59] D. A. Anderson, A. Schwarzkopf, R. E. Sapiro, and G. Raithel. Production and trapping of cold circular Rydberg atoms. *Physical Review A*, 88(3):031401, September 2013.

[60] P. Allmendinger, J. Deiglmayr, J. A. Agner, H. Schmutz, and F. Merkt. Surface-electrode decelerator and deflector for Rydberg atoms and molecules. *Physical Review A*, 90(4):043403, October 2014.

[61] S. D. Hogan. Rydberg-Stark deceleration of atoms and molecules. *EPJ Techniques and Instrumentation*, 3(2):1–50, 2016.

[62] W. Sandner, K. A. Safinya, and T. F. Gallagher. Forced autoionization. *Physical Review A*, 33(2):1008–1019, 1986.

[63] Hongkun Park, David J. Leahy, and Richard N. Zare. Extensive electron-nuclear angular momentum exchange in vibrational autoionization of np and nf Rydberg states of NO. *Physical review letters*, 76(10):1591–1594, March 1996.

[64] Hongkun Park and Richard N. Zare. Molecular-orbital decomposition of the ionization continuum for a diatomic molecule by angle- and energy-resolved photoelectron spectroscopy. I. Formalism. *The Journal of Chemical Physics*, 104(12):4554–4567, 1996.

[65] Hongkun Park and Richard N. Zare. Rotationally resolved photoelectron spectra from vibrational autoionization of NO Rydberg levels. *The Journal of Chemical Physics*, 106(6):2239–2247, 1997.

[66] Hongkun Park, Ian Konen, and Richard N. Zare. Partial-Wave Decomposition of the Ionization Continuum Accessed by Vibrational Autoionization of the NO 14s (v = 1, N = 20, $N_R^+ = 20$) Level. *Physical Review Letters*, 84(17):3819–3822, 2000.

[67] Huanqian Loh, Jia Wang, Matt Grau, Tyler S. Yahn, Robert W. Field, Chris H. Greene, and Eric A. Cornell. Laser-induced fluorescence studies of HfF^+ produced by autoionization. *Journal of Chemical Physics*, 135(15):154308, 2011.

[68] D. DeMille. Quantum Computation with Trapped Polar Molecules. *Physical Review Letters*, 88(6):067901, 2002.

[69] Daniel Weidinger and Martin Gruebele. Simulations of quantum computation with a molecular ion. *Chemical Physics*, 350(1-3):139–144, 2008.

[70] M. Saffman, T. G. Walker, and K. Mølmer. Quantum information with Rydberg atoms. *Reviews of Modern Physics*, 82(3):2313–2363, August 2010.

[71] P. M. Dehmer and W. A. Chupka. Very high resolution study of photoabsoprtion, photoionization, and predissociation in H_2. *The Journal of Chemical Physics*, 65(6):2243–2273, 1976.

[72] Dan Dill and Ch. Jungen. Quantum-defect functions. Interconverters of electronic and nuclear motion. *The Journal of Physical Chemistry*, 84(17):2116–2122, 1980.

[73] P. Labastie, M. C. Bordas, B. Tribollet, and M. Broyer. Stoboscopic effect between electronic and nuclear motion in highly excited molecular Rydberg states. *Physical Review Letters*, 52(19):1681–1684, 1984.

[74] M. Lombardi, P. Labastie, M. C. Bordas, and M. Broyer. Molecular Rydberg states: Classical chaos and its correspondence in quantum mechanics. *The Journal of Chemical Physics*, 89(6):3479–3490, 1988.

[75] Christian Jungen and Stephen C. Ross. Unified quantum-defect-theory treatment of molecular ionization and dissociation. *Physical Review A*, 55(4):2503–2506, 1997.

[76] Jeffrey J. Kay, Serhan N. Altunata, Stephen L. Coy, and Robert W. Field. Resonance between electronic and rotational motions in Rydberg states of CaF. *Molecular Physics*, 105(11):1661–1673, 2007.

[77] Jeffrey J. Kay, Stephen L. Coy, Bryan M. Wong, Christian Jungen, and Robert W. Field. A quantum defect model for the s, p, d, and f Rydberg series of CaF. *The Journal of Chemical Physics*, 134(11):114313, March 2011.

[78] Joseph E. Mayer and Maria Goeppert Mayer. The polarizabilities of ions from spectra. *Physical Review*, 43(8):605–611, 1933.

[79] P. W. Arcuni, E. A. Hessels, and S. R. Lundeen. Series mixing in high-L Rydberg states of H_2: An experimental test of polarization-model predictions. *Physical Review A*, 41(7):3648–3662, 1990.

[80] James K. G. Watson. Effects of a core electric dipole moment on Rydberg states. *Molecular Physics*, 81(2):277–289, February 1994.

[81] S. R. Lundeen. Fine structure in high-ℓ Rydberg states: A path to properties of positive ions. In *Advances in Atomic, Molecular and Optical Physics*, volume 52, chapter 4, pages 161–208. Elsevier Inc., 2005.

[82] Jeffrey J. Kay, Stephen L. Coy, Vladimir S. Petrović, Bryan M. Wong, and Robert W. Field. Separation of long-range and short-range interactions in Rydberg states of diatomic molecules. *The Journal of Chemical Physics*, 128(19):194301, May 2008.

[83] D. Sprecher, M. Beyer, and F. Merkt. Precision measurement of the ionisation energy of the $3d\sigma$ GK state of H_2. *Molecular Physics*, 111(14-15):2100–2107, August 2013.

[84] Daniel Sprecher, Christian Jungen, and Frédéric Merkt. Spectrum of the Autoionizing Triplet Gerade Rydberg States of H_2 and its Analysis Using Multichannel Quantum-Defect Theory. *The Journal of Physical Chemistry A*, 117(39):9462–9476, 2013.

[85] Daniel Sprecher, Christian Jungen, and Frédéric Merkt. Determination of the binding energies of the np Rydberg states of H_2, HD, and D_2 from high-resolution spectroscopic data by multichannel quantum-defect theory. *The Journal of Chemical Physics*, 140(10):104303, March 2014.

[86] D. Sprecher, J. Liu, T. Krähenmann, M. Schäfer, and F. Merkt. High-resolution spectroscopy and quantum-defect model for the gerade triplet np and nf Rydberg states of He_2. *The Journal of Chemical Physics*, 140(6):064304, February 2014.

[87] Paul Jansen, Luca Semeria, Laura Esteban Hofer, Simon Scheidegger, Josef A. Agner, Hansjürg Schmutz, and Frédéric Merkt. Precision Spectroscopy in Cold Molecules: The Lowest Rotational Interval of He_2^+ and Metastable He_2. *Physical Review Letters*, 115(13):133202, 2015.

[88] Christa Haase, Maximilian Beyer, Christian Jungen, and Frédéric Merkt. The fundamental rotational interval of para-H_2^+ by MQDT-assisted Rydberg spectroscopy of H_2. *The Journal of Chemical Physics*, 142(6):064310, February 2015.

[89] J. M. Rost, J. C. Griffin, B. Friedrich, and D. R. Herschbach. Pendular states and spectra of oriented linear molecules. *Physical Review Letters*, 68(9):1299–1302, 1992.

[90] Bretislav Friedrich and Dudley Herschbach. Enhanced orientation of polar molecules by combined electrostatic and nonresonant induced dipole forces. *The Journal of Chemical Physics*, 111(14):6157–6160, 1999.

[91] Burkhard Schmidt and Bretislav Friedrich. Topology of surfaces for molecular Stark energy, alignment, and orientation generated by combined permanent and induced electric dipole interactions. *Journal of Chemical Physics*, 140(6):064317, 2014.

[92] A. Salam. Intermolecular interactions in a radiation field via the method of induced moments. *Physical Review A*, 73(1):013406, 2006.

[93] J. P. Clemens, L Horvath, B. C. Sanders, and H. J. Carmichael. Collective spontaneous emission from a line of atoms. *Physical Review A*, 68(2):023809, 2003.

[94] A. H. Safavi-Naeini, T. P. Mayer Alegre, J. Chan, M. Eichenfield, M. Winger, Q. Lin, J. T. Hill, D. E. Chang, and O. Painter. Electromagnetically induced transparency and slow light with optomechanics. *Nature*, 472(7341):69–73, 2011.

[95] Joel A. Greenberg and Daniel J. Gauthier. Steady-state, cavityless, multimode superradiance in a cold vapor. *Physical Review A*, 86(1):013823, 2012.

[96] Juha Javanainen, Janne Ruostekoski, Yi Li, and Sung Mi Yoo. Shifts of a resonance line in a dense atomic sample. *Physical Review Letters*, 112(11):113603, 2014.

[97] W. R. Anderson, J. R. Veale, and T. F. Gallagher. Resonant Dipole-Dipole Energy Transfer in a Nearly Frozen Rydberg Gas. *Physical Review Letters*, 80(2):249–252, 1998.

[98] T. Wang, S. F. Yelin, R. Côté, E. E. Eyler, S. M. Farooqi, P. L. Gould, M. Koštrun, D. Tong, and D. Vrinceanu. Superradiance in ultracold Rydberg gases. *Physical Review A*, 75(3):033802, March 2007.

[99] Yan Zhou. Cooperative effects in a dense Rydberg gas. *Molecular Physics*, 110(15-16):1909–1915, 2012.

[100] Jianing Han and H Maeda. Super-radiance-cascades and multimode superradiance oscillations in a cold ^{85}Rb Rydberg gas. *Canadian Journal of Physics*, 92(10):1130–1134, 2014.

[101] Michelle O. Araújo, Ivor Krešić, Robin Kaiser, and William Guerin. Superradiance in a Large and Dilute Cloud of Cold Atoms in the Linear-Optics Regime. *Physical Review Letters*, 117(7):073002, 2016.

[102] Tao Zhou, B. G. Richards, and R. R. Jones. Absence of collective decay in a cold Rydberg gas. *Physical Review A*, 93(3):033407, 2016.

[103] C. M. Gittins, N. A. Harris, R. W. Field, J. Vergès, C. Effantin, A. Bernard, J. D'Incan, W. E. Ernst, P. Bündgen, and B. Engels. Analysis and Deperturbation of the C $^2\Pi$ and D $^2\Sigma$ States of CaF. *Journal of Molecular Spectroscopy*, 161:303–311, 1993.

[104] Christopher M. Gittins, Nicole A. Harris, Ma Hui, and Robert W. Field. Ionization-detected optical-optical double resonance spectroscopic studies of moderate energy Rydberg states of calcium monofluoride. *Canadian Journal of Physics*, 79(2):247–286, 2001.

[105] Nicole A. Harris and Robert W. Field. The core-penetrating Rydberg series of the CaF molecule: At the borderline between valence and Rydberg states. *The Journal of Chemical Physics*, 98(4):2642–2646, 1993.

[106] Zygmunt J. Jakubek, Nicole A. Harris, Robert W. Field, James A. Gardner, and Edmond Murad. Ionization potentials of CaF and BaF. *The Journal of Chemical Physics*, 100(1):622–627, 1994.

[107] Zygmunt J. Jakubek and Robert W. Field. Core-Penetrating Rydberg Series of BaF : New Electronic States in the $n^* \sim 4$ Region. *Journal of Molecular Spectroscopy*, 179(1):99–124, 1996.

[108] Zygmunt J. Jakubek and Robert W. Field. Rydberg series of BaF : perturbation-facilitated studies of core-non-penetrating states. *Philosophical Transactions: Mathematical, Physical and Engineering Sciences*, 355(1729):1507–1526, 1997.

[109] Zygmunt J. Jakubek and Robert W. Field. Core-Penetrating Rydberg Series of BaF: Single-State and Two-State Fits of New Electronic States in the $4.4 \leq n^* \leq 14.3$ Region. *Journal of Molecular Spectroscopy*, 205(2):197–220, February 2001.

[110] Vladimir S Petrović, Jeffrey J. Kay, Stephen L. Coy, and Robert W. Field. The Stark effect in Rydberg states of a highly polar diatomic molecule: CaF. *The Journal of Chemical Physics*, 131(6):064301, August 2009.

[111] Michael D. Morse. Supersonic Beam Sources. In *Experimental Methods in the Physical Sciences*, volume 29B, chapter 2, pages 21–47. Academic Press, 1996.

[112] W. Hogervorst. Diffusion coefficients of noble-gas mixtures between 300 K and 1400 K. *Physica*, 51(1):59–76, 1971.

[113] W. A. Hamel, J. E. M. Haverkort, H. G. C. Werij, and J. P. Woerdman. Calculation of alkali-noble gas diffusion cross sections relevant to light-induced drift. *Journal of Physics B: Atomic and Molecular Physics*, 19(24):4127–4135, 1986.

[114] Giacinto Scoles. *Atomic and Molecular Beam Methods: Volume 1.* Oxford Universtiy Press, 1988.

[115] Hans Pauly. *Atomic, Molecule, and Cluster Beams I.* Springer, 2000.

[116] N. E. Bulleid, S. M. Skoff, R. J. Hendricks, B. E. Sauer, E. A. Hinds, and M. R. Tarbutt. Characterization of a cryogenic beam source for atoms and molecules. *Physical Chemistry Chemical Physics*, 15:12299–12307, 2013.

[117] R. H. Dicke. Coherence in Spontaneous Radiation Processes. *Physical Review*, 93(1):99–110, 1954.

[118] N. Skribanowitz, I. P. Herman, J. C. MacGillivray, and M. S. Feld. Observation of dicke superradiance in optically pumped HF gas. *Physical Review Letters*, 30(8):309–312, 1973.

[119] J. C. MacGillivray and M. S. Feld. Theory of superradiance in an extended, optically thick medium. *Physical Review A*, 14(3):1169–1189, 1976.

[120] Guin-Dar Lin and Susanne F. Yelin. Superradiance: An Integrated Approach to Cooperative Effects in Various Systems. In *Advances in Atomic, Molecular, and Optical Physics*, volume 61, chapter 6, pages 295–329. Elsevier Inc., 2012.

[121] A. Icsevgi and W. E. Lamb Jr. Propagation of light pulses in a laser amplifier. *Physical Review*, 185(2):517–545, 1969.

[122] R. Bonifacio, P. Schwendimann, and Fritz Haake. Quantum statistical theory of superradiance. I. *Physical Review A*, 4(1):302–313, 1971.

[123] Nicholas E. Rehler and Joseph H. Eberly. Superradiance. *Physical Review A*, 3(5):1735–1751, 1971.

[124] Frederic A. Hopf, Robert F. Shea, and Marlan O. Scully. Theory of Optical Free-Induction Decay and Two-Photon Superradiance. *Physical Review A*, 7(6):2105–2110, 1973.

[125] R. Bonifacio and L. A. Lugiato. Cooperative radiation processes in two-level systems: Superfluorescence. *Physical Review A*, 11(5):1507–1521, 1975.

[126] A. Crubellier. Level-degeneracy effects in superradiance theory. *Physical Review A*, 15(6):2430–2438, 1977.

[127] E. Ressayre and A. Tallet. Markovian model for oscillatory superfluroescence. *Physical Review A*, 18(5):2196–2203, 1978.

[128] Q. H. F. Vrehen and M. F. H. Schuurmans. Direct measurement of the effective initial tipping angle in superfluorescence. *Physical Review Letters*, 42(4):224–227, 1979.

[129] A. Crubellier, S. Liberman, and P. Pillet. Superradiance and subradiance in three-level systems. *Optics Communications*, 33(2):143–148, 1980.

[130] A. Crubellier, S. Liberman, D. Pavolini, and P. Pillet. Superradiance and subradiance. I. Interatomic interference and symmetry properties in three-level systems. *Journal of Physics B: Atomic and Molecular Physics*, 18(18):3811–3833, 1985.

[131] A. Crubellier and D. Pavolini. Superradiance and subradiance. II. Atomic systems with degenerate transitions. *Journal of Physics B: Atomic and Molecular Physics*, 19(14):2109–2138, 1986.

[132] A. Crubellier. Superradiance and subradiance. III. Small samples. *Journal of Physics B: Atomic and Molecular Physics*, 20(5):971–996, 1987.

[133] A. Crubellier and D. Pavolini. Superradiance and subradiance. IV. Atomic cascades between degenerate levels. *Journal of Physics B: Atomic and Molecular Physics*, 20(7):1451–1470, 1987.

[134] Tom Bienaimé, Nicola Piovella, and Robin Kaiser. Controlled Dicke subradiance from a large cloud of two-level systems. *Physical Review Letters*, 108(12):123602, 2012.

[135] Marlan O. Scully. Single Photon Subradiance: Quantum Control of Spontaneous Emission and Ultrafast Readout. *Physical Review Letters*, 115(24):243602, 2015.

[136] Vasily V. Temnov and Ulrike Woggon. Superradiance and subradiance in an inhomogeneously broadened ensemble of two-level systems coupled to a low-Q cavity. *Physical Review Letters*, 95(24):243602, 2005.

[137] E. Akkermans, A. Gero, and R. Kaiser. Photon Localization and Dicke Superradiance in Atomic gases. *Physical Review Letters*, 101(10):103602, 2008.

[138] William Guerin, Michelle O. Araújo, and Robin Kaiser. Subradiance in a Large Cloud of Cold Atoms. *Physical Review Letters*, 116(8):083601, 2016.

[139] S. L. Bromley, B. Zhu, M. Bishof, X. Zhang, T. Bothwell, J. Schachenmayer, T. L. Nicholson, R. Kaiser, S. F. Yelin, M. D. Lukin, A. M. Rey, and J. Ye. Collective atomic scattering and motional effects in a dense coherent medium. *Nature Communications*, 7:11039, 2016.

[140] P. R. Berman. Energy conservation in collective coherent emission by dipole oscillators. *American Journal of Physics*, 78(12):1323–1330, 2010.

[141] Jin-Hong Chen and Xi-An Mao. Experimental verification of the relation between the delay time and the tipping angle for a superradiant pulse. *Journal of Physics D: Applied Physics*, 32(7):764–768, 1999.

[142] Xi-An Mao and Jin-Hong Chen. Relation between the delay time and the tipping angle for superradiance. *Physical Review A*, 60(6):5140–5143, 1999.

[143] C. H. Keitel, M. O. Scully, and G. Sussmann. Triggered superradiance. *Physical Review A*, 45(5):3242–3249, 1992.

[144] R. Friedberg and S.R. Hartmann. Temporal evolution of superradiance in a small sphere. *Physical Review A*, 10(5):1728–1739, 1974.

[145] Marlan O. Scully. Collective Lamb shift in single photon Dicke superradiance. *Physical Review Letters*, 102(14):143601, 2009.

[146] Marlan O. Scully and Anatoly A. Svidzinsky. The Super of Superradiance. *Science*, 325(5947):1510–1512, 2009.

[147] Ralf Röhlsberger, Kai Schalge, Balaram Sahoo, Sebastien Couet, and Rudolf Rüffer. Collective Lamb Shift in Single-Photon Superradiance. *Science*, 328(5983):1248–1252, 2010.

[148] Anatoly A. Svidzinsky, Jun-Tao Chang, and Marlan O. Scully. Cooperative spontaneous emission of N atoms: Many-body eigenstates, the effect of virtual lamb shift processes, and analogy with radiation of N classical oscillators. *Physical Review A*, 81(5):053821, 2010.

[149] Z. Meir, O. Schwartz, E. Shahmoon, D. Oron, and R. Ozeri. Cooperative Lamb Shift in a Mesoscopic Atomic Array. *Physical Review Letters*, 113(19):193002, 2014.

[150] S. J. Roof, K. J. Kemp, M. D. Havey, and I. M. Sokolov. Observation of Single-Photon Superradiance and the Cooperative Lamb Shift in an Extended Sample of Cold Atoms. *Physical Review Letters*, 117(7):073003, 2016.

[151] David D. Grimes, Stephen L. Coy, Timothy J. Barnum, Yan Zhou, Susanne F. Yelin, and Robert W. Field. Direct single-shot observation of millimeter wave superradiance in Rydberg-Rydberg transitions. *Physical Review A*, 95(4):043818, 2017.

[152] V. M. Akulin and N V Karlov. *Intense Resonant Interactions in Quantum Electronics*. Springer-Verlag, 1992.

[153] Robert C Hilborn. Einstein coefficients, cross sections, f values, dipole moments, and all that, 2002.

[154] R L Shoemaker. Coherent Transient Infrared Spectroscopy. In J. I. Steinfeld, editor, *Laser and Coherence Spectroscopy*, chapter 3, pages 197–371. Plenum Press, 1978.

[155] E. B. Treacy. Adiabatic inversion with light pulses. *Physics Letters A*, 27(7):421 – 422, 1968.

[156] Michael M. T. Loy. Observation of population inversion by optical adiabatic rapid passage. *Physical Review Letters*, 32(15):814–817, 1974.

[157] Michael M. T. Loy. Two-photon adiabatic inversion. *Physical Review Letters*, 41(7):473–476, 1978.

[158] J. Baum, R. Tycko, and A. Pines. Broadband and adiabatic inversion of a two-level system by phase-modulated pulses. *Physical Review A*, 32:3435–3447, Dec 1985.

[159] H. Maeda, J. Gurian, D. Norum, and T. F. Gallagher. Coherent Population Transfer in an Atom by Multiphoton Adiabatic Rapid Passage. *Physical Review Letters*, 96(7):073002, February 2006.

[160] Martin Oberst, Holger Münch, and Thomas Halfmann. Efficient Coherent Population Transfer among Three States in NO Molecules by Stark-Chirped Rapid Adiabatic Passage. *Physical Review Letters*, 99(17):173001, October 2007.

[161] H. Maeda, J. Gurian, and T. F. Gallagher. Population transfer by multiphoton adiabatic rapid passage. *Physical Review A*, 83(3):033416, March 2011.

[162] Jan R. Rubbmark, Michael M. Kash, Micahel G. Littman, and Daniel Kleppner. Dynamical effects at avoided level crossings: A study of the Landau-Zener effect using Rydberg atoms. *Physical Review A*, 23(6):3107–3117, 1981.

[163] Carter Kittrell, Evan Abramson, James L. Kinsey, Stephen A. McDonald, David E. Reisner, Robert W. Field, and Daniel H. Katayama. Selective vibrational excitation by stimulated emission pumping. *The Journal of Chemical Physics*, 75(5):2056–2059, 1981.

[164] Charles E. Hamilton, James L. Kinsey, and Robert W. Field. Stimulated emission pumping: New methods in spectroscopy and molecular dynamics. *Annual Review of Physical Chemistry*, 37:493–524, 1986.

[165] Thomas R. Gentile, Barbara J. Hughey, Daniel Kleppner, and Theodore W. Ducas. Experimental study of one- and two-photon Rabi oscillations. *Physical Review A*, 40(9):5103–5115, 1989.

[166] A. F. Linskens, I. Holleman, N. Dam, and J. Reuss. Two-photon Rabi oscillations. *Physical Review A*, 54(6):4854–4862, 1996.

[167] C. E. Carroll and F. T. Hioe. Analytic solutions for three-state systems with overlapping pulses. *Physical Review A*, 42(3):1522–1531, 1990.

[168] U. Gaubatz, P. Rudecki, S. Schiemann, and K. Bergmann. Population transfer between molecular vibrational levels by stimulated Raman scattering with partially overlapping laser fields. A new concept and experimental results. *The Journal of Chemical Physics*, 92(9):5363–5376, 1990.

[169] B. W. Shore, K. Bergmann, J. Oreg, S. Rosenwaks, and S. Rosenwaks. Multilevel adiabatic population transfer. *Physical Review A*, 44(11):7442–7447, 1991.

[170] A. Kuhn, G. W. Coulston, G. Z. He, S. Schiemann, K. Bergmann, and W. S. Warren. Population transfer by stimulated Raman scattering with delayed pulses using spectrally broad light. *The Journal of Chemical Physics*, 96(6):4215–4223, 1992.

[171] B. W. Shore, K. Bergmann, and J. Oreg. Coherent population transfer: stimulated Raman adiabatic passage and the Landau-Zener picture. *Zeitschrift für Physik D*, 23(1):33–39, 1992.

[172] S. Schiemann, A. Kuhn, S. Steuerwald, and K. Bergmann. Efficient coherent population transfer in NO molecules using pulsed lasers. *Physical review letters*, 71(22):3637–3640, 1993.

[173] Szczepan Chelkowski and George N. Gibson. Adiabatic climbing of vibrational ladders using Raman transitions with a chirped pump laser. *Physical Review A*, 52(5):3417–3420, 1995.

[174] T. Halfmann and K. Bergmann. Coherent population transfer and dark resonances in SO_2. *The Journal of Chemical Physics*, 104(18):7068–7072, 1996.

[175] N. V. Vitanov and S. Stenholm. Properties of stimulated Raman adiabatic passage with intermediate-level detuning. *Optics Communications*, 135(4-6):394–405, 1997.

[176] N. V. Vitanov and S. Stenholm. Population transfer via a decaying state. *Physical Review A*, 56(2):1463–1471, 1997.

[177] Moorad Alexanian and Subir K. Bose. Population transfer in a three-level atom. *Journal of Luminescence*, 76&77:674–676, 1998.

[178] Mark N. Kobrak and Stuart A. Rice. Coherent population transfer via a resonant intermediate state: The breakdown of adiabatic passage. *Physical Review A*, 57(2):1158–1163, 1998.

[179] A. Kuhn, S. Steuerwald, and K. Bergmann. Coherent population transfer in NO with pulsed lasers: the consequences of hyperfine structure , Doppler broadening and electromagnetically induced absorption. *The European Physical Journal D*, 1(1):57–70, 1998.

[180] E. Paspalakis and P. L. Knight. Population transfer via an autoionizing state with temporally delayed chirped laser pulses. *Journal of Physics B: Atomic, Molecular and Optical Physics*, 31(12):2753–2767, 1998.

[181] R. Unanyan, S. Guérin, B. W. Shore, and K. Bergmann. Efficient population transfer by delayed pulses despite coupling ambiguity. *The European Physical Journal D*, 8(3):443–449, 2000.

[182] N. V. Vitanov, L. P. Yatsenko, and K. Bergmann. Population transfer by an amplitude-modulated pulse. *Physical Review A*, 68(4):043401, 2003.

[183] G. S. Vasilev, A. Kuhn, and N. V. Vitanov. Optimum pulse shapes for stimulated Raman adiabatic passage. *Physical Review A*, 80(1):013417, July 2009.

[184] Iavor I. Boradjiev and Nikolay V. Vitanov. Transition time in the stimulated Raman adiabatic passage technique. *Physical Review A*, 82(4):043407, October 2010.

[185] M. Scala, B. Militello, A. Messina, and N. V. Vitanov. Detuning effects in STIRAP processes in the presence of quantum noise. *Optics and Spectroscopy*, 111(4):589–592, October 2011.

[186] M. Scala, B. Militello, A. Messina, and N. V. Vitanov. Stimulated Raman adiabatic passage in a Λ system in the presence of quantum noise. *Physical Review A*, 83(1):1–8, January 2011.